Development of RF-MEAM interaction potentials for Fe-Y

zur Erlangung des akademischen Grades eines

Doktors der Ingenieurswissenschaften

von der KIT-Fakultät für Maschinenbau
des Karlsruher Instituts für Technologie (KIT)

genehmigte

Dissertation

von

M. Sc. Sascha Koch

geb. am 11.02.1991
in der Hansestadt Rostock

Tag der mündlichen Prüfung: 27. August 2019

Erster Gutachter: Prof. A. Möslang

Zweiter Gutachter: Prof. G. J. Ackland

Widmung

Papa, warum ist das so?

Komm, lass uns auf die Suche gehen, Sascha!

Und so begann eine lange abenteuerliche Reise voller Überraschungen…

In immer währender tiefer Dankbarkeit für meinen Vater
Hilmar Torsten Koch

Zusammenfassung

Der Fokus dieser Arbeit lag zunächst auf einer simulationsgestützen Untersuchung über die Entstehungsmechanismen von Oxidteilchen in ODS-Stählen. Hierbei bilden empirische Wechselwirkungspotenziale von Eisen-Yttrium-Sauerstoff (Fe-Y-O) die Grundlage für eine Beschreibung dieser Oxidteilchen-Bildungs-Prozesse in Molekulardynamik (MD) Simulationen, die auch Eigenschaften von Versetzungen und anderen Bestrahlungs-Pänomenen detailiert zur weiteren Aufklärung behandeln können.

Zu diesem Zweck ist das speziell auf die Simulation zugeschnittene Anfitten der o.g. MD Potenziale (hier für Fe-Y-O) notwendig. Hierzu dienen die zuvor durchgeführten ab-initio (DFT) Rechnungen als Datenreferenzgrundlage (z.B. von Phasen oder Defekten) zur Optimierung der Potenzialparameter während des Anfittens, um ein möglichst exaktes MD Potenzial zu erzeugen, dass die ab-initio Daten auf größeren MD Skalen detailgetreu abbildet. Im ersten Drittel dieses Projektes wurden mehrere Potenziale für die einzelnen Metall-Komponenten, Fe-Fe und Y-Y, erzeugt. Dabei stellte sich heraus, dass etablierte Standardmethoden nicht in der Lage sind genaue Fe-Y Potenziale als Teillösung für das Fe-Y-O Problem zu erzeugen. Dabei wurde eine Kombination aus dem (M)EAM Modell und zur Optimierung eine LSM gestützte Software (*POTFIT*) genutzt. Die Komplexität des Problems liegt in den richtungsabhängigen Atombindungen, die die hier entwickelten fortgeschrittenen Simulations- und Fitmethoden benötigen.

Im ersten Schritt von drei Schritten (chapter 3) wurden zunächst einmal die Defizite der Standard-Fittechniken evaluiert, indem die während des Fitting-Prozesses gefundenen Parametersets im EAM Formalismus mit der flexiblen Software *POTFIT* auf ihre Eignung hin gründlich untersucht worden sind. Die hierfür genutzten Fitfunktionen wurden ursprünglich Anfang 2000 von Zhou und Wadley entwickelt. Hierbei liegt die Ursache für die dann entdeckte Parameterset-Problematik darin, dass zur Beschreibung des Fe-Y Systems das Model aus drei Potentialkomponenten besteht: Fe-Fe, Y-Y und Fe-Y. Für diese einzelnen Komponenten sind die Potentialparameter erfolgreich angefittet worden mit Bezug zur Gitterkonstante und Bindungs- bzw. Kohäsionsenergie (beides mit 1% Genauigkeit bezgl. DFT Rechnungen) sowie zu allen elastischen Konstanten (5% Genauigkeit bezgl. Experimente). All dies unter Zuhilfenahme von Parametersuchraum-beschränkenden Techniken, die zur Einhaltung der oben genannten Eigenschaften dienen und urspürnglich von Johnson & Oh sind. Selbst kompliziertere Defekteigenschaften, wie Zwischengitter- und Leerstellenbildungsenergien wurden erfolgreich angefittet. Das hier entwickelte EAM Potenzial für Y-Y ist z.B. in der Lage bei Eigenzwischengitteratomen die basal oktaedrische Position von Zwischengitteratomen (ZA) im Yttrium hcp-Gitter als Grundzustand und die Transition eines jeden ZAs aus einer anderen Position, wie zuvor in DFT berechnet, zu reproduzieren.

Zur Bildung des angestrebten Fe-Y Potenzials wurden diese beiden Komponenten, Fe-Fe und Y-Y, zum weiteren Fitten in dem weitgefächerten und komplexen Fe-Y Potzenzialsuchraum genutzt. Die Parametersets wurden mit sogenannten hier entwickelten Hauptparameter (*Key Driver*) systematisch untersucht. Ein flexibleres Konzept statt der starreren *Universal Binding Relations* in Abhängigkeit von der Rose Gleichung. Dieser Hauptparameter zeigte eindeutig, dass die Nutzung der Rose Gleichung zur Parametersuchraum-Minimierung den Suchraum dahingehend einschränkt, sodass ein akkurates Anfitten der hier genutzten 900 DFT Datensets nicht mehr möglich ist. Allerdings ist die Orientierung im Parametersuchraum mit dieser Rose Gleichung bei standardmäßigen Optimierungsmethoden (wie LSM) unabdingbar, da ohne diese die benötigten globalen Optima für die Parameter nicht auffindbar sind.
Als aufklärendes Testverfahren zur weiteren Ergründung dieser Problematik und Prüfung zur Eignung für Fe-Y Potenziale und den anschließenden Simulationen diente der Versuch, 9 verschiedene Bindungsenergien von Yttrium-Leerstellenclustern mit ansteigender Leerstellenzahl zu reproduzieren. Dieser Test konnte von diesen Potenzialen nur teilweise erfüllt werden und wurde auf die fehlende Beschreibung der Bindungswinkelabhängigkeit im Modell zurückgeführt. Die Erweiterung von EAM durch MEAM mit

Winkelabhängigkeit ist jedoch keineswegs eine zufriedenstellende Lösung, da MEAM alternativlos auf der irreführenden Rose Gleichung beruht. Daher war die Benutzung des übersichtlicheren EAM Typs aus zwei Gründen nützlich: 1. MEAM braucht die Rose Gleichung um diesen komplexen Formalismus zu beherrschen mit denselben Problemen wie in EAM, aber dieses grundlegende Problem ist in MEAM deutlich schwerer zu identifizieren als in EAM. 2. Die mit EAM gefundenen, angefitteten Parameter sind eine hervorragende Startparameter-Grundlage für den verbesserten darauffolgenden RF-MEAM Typ.

Im zweiten Schritt wurde das Problem aus dem ersten Schritt gelöst, indem ein modifizierter MEAM Spezialtyp im referenzlosen Format (RF-MEAM) angewandt worden ist. Im Gegensatz zum herkömmlichen MEAM wird hier die Rose Gleichung durch mehr DFT Daten und insbesondere einer intelligenteren *Machine Learning* ähnlichen Genetic Algorithmus (GA) Optimiertechnik ersetzt, die allerdings eine bedachte Startparameterwahl vorraussetzt, womit Schritt 1 wieder *ins Spiel kommt*. Die genutzte fortgeschrittene *MEAMfit* Software, die per GA funktioniert, wurde zwischen 2016 und 2017 funktionierend eigens dafür implementiert. Mit den in Schritt 1 gefitteten Parametern und Set-Auswahltechniken konnten die weiterführenden Fits mit optimalen Startparametern durchgeführt werden. Auf dieser Stufe waren diese Fits mit der speziell verbesserten Technik in der Lage ein detailgetreues Fe-Y Potenzial zu generieren, das sowohl alle Phasen (Fe_2Y, Fe_3Y, Fe_5Y, $Fe_{23}Y_6$ und $Fe_{17}Y_2$ sowohl als auch reines Fe und Y) als auch die gesamte Defektdatenbasis mit einer durchschnittlichen Abweichung von ≈11% erfolgreich abbildet. Zusätzlich bestätigend zu dieser allgemeinen Übereinstimmung wurde konsequenterweise der in Schritt 1 entwickelte Test hervorragend mit einmaliger Genauigkeit bestanden, mit max. 5% Abweichung von den komlexen o.g. Y-Leerstellen Bildungsenergien. Allerdings konnte ein systematischer Fehlertrend aufgespürt werden, der Schwächen in der Fe-Fe Komponente offenbarte. Als Folge dessen wurde umgehend diese Komponente durch ein anderes etabliertes Fe-Fe Potenzial von G. Ackland mit einer extrem genauen Schmelztemperatur (nur 3% Abweichung vom Exp.) ausgetauscht. Mit diesem genauen Potenzial konnte zum ersten Mal die Clusterbildung von gelösten Yttrium Atomen in einer Eisenschmelze erfolgreich per MD Simulation auf atomarer Ebene nachgestellt werden oberhalb von 1750 K. Temperaturen darunter hatten eine Ausscheidungsbildung von Y mit sehr geringer Y-Löslichkeit (<0.1%) in Übereinstimmung mit den Experimenten zur Folge. Dies wurde durch den Pot. Typ A ermöglicht, der aber die energetische Reihenfolge bei den Fe-Y Phasen nicht ganz genau einhält. Typ B hingegen hält diese ein, dort fehlt aber die Y-Clusterbildungsneigung. Durch den gebotenen Praxisbezug zur Metallurgie müssen die Löslichkeit und Clusterbildung gleichzeitig in der Simulation genau reproduzierbar sein, was aber weder Typ A noch B kann, was zum Typ A/B Dilemma führt.

Dieses Typ A/B Dilemma (Phasen oder Defekt Genauigkeit) führt zum letzten dritten Schritt (chapter 5). Darin ist zusätzlich die Strukturaufklärung von der $Fe_{17}Y_2$ Phase mit Vergleichen zu exp. *EXAFS* Spektren unserer Kollaborationspartner vom *ISSP* (Riga) enthalten. Diese Aufklärung dient auch dazu die fehlenden magnetischen Abhängigkeiten im Potenzial zu kompensieren, da die Phasenreihenfolge mit sehr feinen Energieunterschieden wohl stark von magnetischen Wechselwirkungen geprägt ist. Obwohl Potenzial Typ B diesen (Magnetismus) nicht direkt beachtet, ist es in der Lage das tatsächlich gemessene *EXAFS* Spektrum größtenteils genau wiederzugeben. Allerdings offenbart eine einzige ausgeprägte Phasenverschiebung, dass die angenommene hcp Struktur durch eine unterschwellige rhombohedrale Komponente, die sporadisch in der *c*-Gitterrichtung auftritt, korrigiert werden muss. *AIMD* (DFT) Berechnungen in Kooperation mit der *University of Edinburgh* bestätigen dies und zeigen sogar, dass magnetische Wechselwirkungen diese Strukturmischung stabilisieren. Endgültig bestätigt werden konnte dies mit der genauen *EXAFS* Spektren Reproduktion mit dem durch *AIMD* verbesserten nochmals gefitteten Potenzialtyp B, der als neuer Typ C durch *AIMD* indirekt den Einfluss der magnetischen Wechselwirkungen mit einschließt. Diese erstmalige nahezu deckungsgleiche MD Simulation eines EXAFS Spektrums von einem komplexen metallischen Alloy, hier Fe-Y, stellt eine bisher unerreichte Verbesserung dar. Schließlich löst Typ C das Typ A/B Dilemma und ernöglicht eine genaue *gleichzeitige* MD Modellierung von Phasen- und Defekten in Fe-Y – ein Durchbruch in der MD-Potenzialentwicklung.

Abstract

This work was initially aiming for the explanation by MD simulations for the oxide particle formation mechanisms during the production of ODS steels. Empirical Fe-Y-O interaction potentials are required for a description in MD of the associated oxide particles nucleation and growth, modelling of dislocation interaction with oxide particles as well as for the simulation of various phenomena occurring under irradiation in ODS steels.
For this purpose the specifically tailored development of a corresponding MD interaction potential (for Fe-Y-O) by fitting is necessary. Ab-initio calculations are used as atomic references (such as phases and defects) for the optimisation of potential parameters during the fitting process leading to an as accurate as possible representation of the properties predicted by DFT on the broader, more meaningful MD scale.
Relatively quickly after various fits for the single metals, Fe-Fe and Y-Y during the first third of this work, it turned out that the established methods, a combination of the chosen potential formalism (EAM & MEAM) and available fitting tools (POTFIT with LSM), fail to reproduce reliable (Fe-Y) alloy potentials. Therefore, this work focuses on the essential preliminary steps to model and understand Fe-Y -– complexity of Fe-Y lies in a high amount of directional bonding (with covalent character) requiring the development and validation of such advanced models.

The first step out of three (chapter 3) was to understand and overcome the fitting limitations by a systematic in-depth evaluation of the corresponding parameter sets by using the EAM formalism by Zhou & Wadley (ZWF) [96] in the flexible fitting software POTFIT. Both EAM and (RF-) MEAM potentials of Fe-Y consist of three interrelated potential components: Fe-Fe, Y-Y and Fe-Y. For EAM potentials of the single components, Fe-Fe and Y-Y, the key parameters were successfully determined by computing the lattice constant, cohesion energy, elastic constants and various vacancy formation energies analytically (by constraining parameter space in “Johnson & Oh style” [55], resulting in exact lattice constants and cohesion energies (both within 1% wrt. previous DFT calculations) as well as in the various elastic constants (within 5% wrt. experiments)). Even more complicated features were successfully fitted: defect properties, such as interstitial and divacancy formation (and binding) energies, were reproduced more accurately. The here developed EAM potential accomplished for the first time the MD simulation of self-interstitial atoms (SIA) taking the basal octahedral (BO) configuration as the ground state (GS) as previously predicted by DFT [85], which, as reproduced too, every interstitial atom regardless of its initial position is eventually transforming to.

For the compilation of the desired Fe-Y alloy potential these two previously mentioned elemental potentials were used. Different parameter sets were investigated with the help of the in this work developed more flexible key driver concept, which replaces the previous compulsory universal binding relations (UBR) rigidly restraining the parameter space by exact matching to the Rose eq. to support the parameter optimisation. This newly developed key driver varies in a flexible range, which is determined by considering the sub-lattice relaxation energy in hcp Y (with all additional, necessary parameter-space restrictions as a whole concept some inevitable similarities to the Rose eq. still occur). This key driver is used to scan systematically through the available parameter sets. These scans revealed that the necessary affiliations to the Rose eq. impede finding convincing Fe-Y potentials during the search, which accurately represents all 900 atomic configurations of the extensive DFT data base consisting of Fe-Y clusters with different vacancy and interstitial configurations. These observed similarities to the Rose eq. to some extent are inevitable when using LSM optimisation techniques in POTFIT due to the local minimisation leading to an inability to find global minima without these parameter-space-reducing restrictions, which always exhibit the aforementioned parallels to the Rose equation (which will be described and overcome).

A decisive testing procedure, which enabled these findings and thoroughly checked for suitability for the specific requirements by Fe-Y alloys was developed. The test included the try to reproduce 9 binding energies of 9 Y-vacancy defect clusters with an incrementing number of vacancies. This test was partly failed and problems were attributed to the use of the Rose eq. and additionally due to the missing angles between the bonds in the model. However, MEAM, which seems to be a solution, is not a suitable alternative for that, because it also relies on the Rose eq. The resulting findings in EAM turned out to be invaluable because of two reasons: 1. MEAM is inevitably relying on the Rose eq. to kind of handle the somehow over-complex formalism. So, in MEAM the same issues and underlying problems would have occurred (but would have been much harder to follow and realise). 2. these EAM fits produced supportive start parameters for the next stage in RF-MEAM.

In the second step out of three (chapter 4) the previous problem was resolved by the use of an adapted MEAM type as the reference free format, RF-MEAM. In contrast to *standard* MEAM techniques this approach, simply speaking, compensates the Rose eq. by fitting to more DFT data and using more intelligent global optimisation algorithms in the form of genetic algorithms (GA), which works apart from the high sensitivity on the start parameters quite well. The associated tool MEAMfit became available as an unstable trial version in 2016 and as a stable version 1.2 in 2017. In version 1.2 the problem about start parameters was simply resolved by adopting the previous EAM parameters as starting points in the RF-MEAM potential fitting. These points were carefully selected as opposing parameter sets with the help of previously developed key drivers, implying linearly decoupled sets with significantly reduced parameter correlations leading to a wider more thoroughly coverage of the sampled parameter space.

This procedure generated successful RF-MEAM potentials, granting an accurate modelling of all Fe-Y phases, Fe_2Y, Fe_3Y, Fe_5Y, $Fe_{23}Y_6$ and $Fe_{17}Y_2$ (and naturally pure Fe and Y) as well as the defects leading to an overall agreement with the fitted data within ≈11%. In addition to the general agreement the previously developed Y-vacancy test was passed excellently, yielding 5% agreement in the binding energies of Y-vacancy cluster, an unparalleled accuracy. However, identifying a systematic pattern in parts of the deviations leads to awareness for an improvement of the Fe-Fe part, as done by exchanging this part with another established Fe-Fe potential by G. J. Ackland [76] with an extremely accurate melting temperature (T_m within 3% wrt. experiments).
With this potential and its improved T_m it was possible for the first time to reproduce by pot. type A the clustering of dissolved Y atoms in liquid Fe (at 1750K with 2.5 % Y forming clusters of few nm) and consequently model precipitation of the Y-clusters, confirming the experimentally observed low solubility of Y in Fe, around 0.1%. The used RF-MEAM potential type A, which puts more focus on defects and less on the phases, has at least one considerable shortcoming in the energetic sequence of the Fe-Y phases: the cohesion energy of $Fe_{23}Y_6$ is not greater (more negative) than the one of $Fe_{17}Y_2$. When modelling the formation and transformation of phases this turns out to be problematic. The second potential type, type B, is successful in phases but cannot represent the clustering behaviour by pot type A (supposedly because defect properties are traded in for fine subtleties by magnetism). All in all, for ODS or Fe-Y, the simultaneous accurate modelling of phase and defect processes at the same time in the same simulation is desirable, leading to the type A/B dilemma, choosing between defect and phase accuracy in these MD potentials.

This dilemma initiates the third and last step (chapter 5) which aims at the fine structure clarification by comparisons with EXAFS spectra of $Fe_{17}Y_2$, which were measured by our collaborators from ISSP in Riga. This fine structure clarification is applied to visualise qualitatively the influence of the missing magnetic components in the model. Interestingly, the magnetic energy contribution, by up to 0.05 eV per Fe atom, could make up a significant part of the energy gap between these two adjacent phases ($Fe_{17}Y_2$ & $Fe_{23}Y_6$). Though potential type B has no intrinsic dependence on magnetism, it already yields a surprisingly good agreement with the experimental EXAFS spectra at 300K.

One distinct phase shift in the EXAFS-MD comparison clearly reveals that the assumption by experiments that the $Fe_{17}Y_2$ phase exists as pure hcp has to be corrected by additional minor rhombohedral components as sporadic layers in c direction. Further simulations by AIMD confirm this interpretation of the previous EXAFS-MD comparison and even link qualitatively the occurrence of rhombohedral layers to magnetism – the flipping of spins which corresponds to a change in magnetisation of $0.13\mu_B$ (cell of 38 atoms) changes the volume by 2-3% corresponding to single layers transforming into rhombohedral structure. A clear mixture, consisting of hcp as main component and rhombohedral as minor component, has been identified by these simulations.
This was further confirmed by improving potential type B using the recently obtained AIMD data in cooperation with Prof. Ackland's group at the University of Edinburgh leading to potential type C, which indirectly includes magnetism by these references (containing states (energy vs. structure) which depend on magnetism). Potential type C reproduces the first simulated EXAFS spectrum of a complex metallic alloy (such as the here considered $Fe_{17}Y_2$) accurately with an excellent agreement, giving a strong indication for a structure of $Fe_{17}Y_2$ at room temperature, which has to be verified by further experiments.

Finally, as an invaluable conclusion of this work, pot type C is able to overcome the type A/B dilemma for Fe-Y phases with up to 20% Y content (overall agreement 7.8% to fitted DFT data) – the use of AIMD during the fitting links the phase and defect properties in the resultant MD potential. So, this previously presented threefold development constitutes a path-breaking technique, which is successful in Fe-Y and is able to reproduce current findings in ODS.

Acknowledgements

This present work has been conducted within the Institute of Applied Materials – Applied Material Physics (IAM-AWP) as part of the engineering faculty of the Karlsruhe Institute of Technology. This work is part of the former Helmholtz Russia Joint Research Group, HJRG 411, "ODS steels for High Temperature applications (ODS-HiTs)" and our collaborating partners from ISSP (Riga), who were also associated to the fusion program with the EUROfusion programme by the European Union.

Without the following persons this project would have been impossible and I want to thank them warmly for their incessant support at all stages and challenges of this longsome project:

Prof. A. Möslang for admitting me to the institute, granting outstanding research conditions, for being an exceptional, accommodating and dedicated supervising Professor and responsible first referee of my PhD project On top of that, he generously enabled several helpful visits to numerous conferences and other research groups, which provided essential impulses for this project.

Dr. P. Vladimirov for admitting me to his group and being an excellent PhD supervisor, who during all possible eventualities of this project always remained calm, reassuring and patiently pulled me through all challenges, no matter what happened – it is nearly impossible to put all of his generous, constant and loyal support into words.

To both also special thanks for letting me participate in their superb researching network, which provided an invaluable assistance and extension to the project horizon (as listed below).

Prof. G.J. Ackland for agreeing to act as second referee of my PhD project after countless patient and supportive guidance in many subtleties of potential fitting during various visits to his group in Edinburgh. Thank you kindly for candidly hosting me during my last two prolonged visits in previous autumn – it was an important final pivotal impulse to settle this project. In addition, I hope that all the previously invested patience and effort during your supervision of my Master project also pays off now by some rewarding outcomes of this work.

Best thanks to the brilliant IBM associated researcher *A. I. Duff*, who can be called a real savior of my project, because he is the developer of MEAMfit, which made the difference to my project. All the advanced results, starting from section 4, are due to his countless endurance during the 8 year long development of MEAMfit and due to his generosity to share this masterpiece of fitting software with us.

Special thanks to my vibrant colleague *Dr. Yuri Mastrikov*, who is kind of a founding father to this project, because his engaged pioneering ab-initio calculations did not only provide a splendid fitting data-base but also acted as a first orientation in the complicated "ODS mystery". I will always remember the great time during his visits at KIT and my visits in Riga, during which he patiently worked through all my DFT questions and fulfilled my "tedious DFT extra wishes".

Another special thanks to *A. Kuzmin and Y. Purans* from ISSP (Riga) – Purans kindly provided our group with the invaluable experimental EXAFS data, which were generously enabled by

measurements with the synchrotron organisation ELETTRA in Italy. On top of that, Purans allowed me to participate in a week-long EXAFS measuring session at ESRF in Grenoble, an important insight.
A. Kuzmin from ISSP is the mastermind behind EDACA and gave numerous practical advises.

Boundless thanks to the senior scientist and one of the best and most rigorous MD potential checkers, *Dr. V. Borodin*, who taught me to distinguish good MD potentials and showed me the necessary checking techniques. Besides, especially in the field of analytic restraining techs he granted crucial impulses.

Dr. P. Brommer, who developed POTFIT and frankly discussed some points with me.

Also boundless thanks to *M. Marques*, who was the brilliant mind behind the used helpful AIMD calculations and let me have a little insight into her cutting edge AIMD techniques.

Dr. Rieth as leader of the High Temperature Materials Division for admitting me to his division with a pleasant and constructive atmosphere. He provided various practicaly motivated impulses and helped me to gain track with respect to experimental issues in addition to his reliable and smooth administration.

Dr. D. Scopece for sharing with me the underlying blueprint of his CTIP LAMMPS module.

Prof. Wangyu Hu and Prof. Fei Gao for vivid, open and helpful discussions about AMEAM.

To all other colleagues at the institute for a pleasant and innovative atmosphere and for a smooth IT-operation to the admins *S. Enke & M. Klotz,* as well as for the general administration to our secretaries *J. Howell & C. Schuler*.

And finally, the Helmholtz foundation for granting the financial support and the trust in my research project.

On a personal note I want to wholeheartedly the following persons:

My family, my grand-parents, mother, my sister and brother, step-mother, step-father and two step-brothers for their constant support to pursue my dreams and master these challenges.

My wife, Victoria, probably prefers some proper actions after PhD completion instead of these bare words. Though, I could not always be the husband and father I wanted to be during these 5 years, full of total time consuming challenges in the parallel universe of science, she blessed me with generous and unconditional support and love, always saving me out of the deepest graves of doubts and sorrows. She took care, that our three wonderful kids did not suffer any deprivations from their overly busy father – I can never repay this, just showing my eternal gratitude for my breathtaking and strong wife, whom I do not deserve.

When thinking of my role model, my father, the merited inventive Dipl.-Ing. Torsten Hilmar Koch with numerous developed patents, the first impression is endless sadness, that my loved one and most influential motivator is gone. I wanted to make you proud, Papa. I hope you are, even though you cannot witness directly this final completion of my PhD project anymore.
But what outweighs the sadness is the universe of endless happy memories of our great time together, Papa. Because you were so much more than the respected engineer – you are the pivotal point of my life, Papa. Foremost, I am eternally thankful for all the exciting adventures we had together. Whether it be, when you showed little Sascha with 7 years with the rpm-measurement devices you brought home from work, how fast our washing machine is spinning, or when I was a querulant student and we discussed Thermodynamics together (engineer vs. student: is the concept of entropy useful?) – behind all the professionalism was our deep bond and curiosity for refreshing discoveries, which always motivate me to fill your shoes and go further, consequently pass this unique deep-going curiosity to my kids and always remember my first steps with you.

All of this is for you, Papa!

Table of contents

List of figures and tables

List of abbreviations

A

a_0	lattice constant
ABOP	Analytic Bond Order Potential ab-initio → *DFT*
at. (%)	atomic percent (relative to number of atoms)
AIMD	Ab-initio Molecular Dynamics dynamic DFT calculations at T≠ 0

B

Bcc	body centred-cubic, denotes a structure with an atom in its unit cell centre (in material science often labeled ferritic)
B	bulk modulus (macroscopically [GPa], nanoscale ev/Å^3
BO	Basal Octahedral, most stable SIA position in hcp Y (used once in 2.3 for Born Oppenheimer approximation)
Btw.	between

C

C_{ij}	elastic modulus in *ij* direction
Calc./calcs.	calculation/calculations
CJG	Conjugate Gradient method (local optimisation method in POTFIT)
CM	Continuous motion
COMB	Charge optimised many body pot., extension to ABOP→2.2.4
Contr.	Contribution
CP	Car-Parinello (Method= decoupling atomic and electronic motion)
CTIP	Charge Ionic Transfer Model

D

DB	Daw & Baskes, EAM method developer
DFT	Density Functional Theory,

NO

NN	Nearest Nieghbour (useful concept in the description of atomic clusters)
N-W	Nishiyama Wassermann (orientation of interphases during phase transition in Fe K-S another one)K
ODS	oxide dispersion strengthened→1.1

PQ

Para-set(s)	Parameter-set
PBE	Perdew-Burke-Ernzerhof XCF
Pot./pots.	potential(s)
P63	→hcp

R

RAFM	Reduced activation ferritic martensitic (steels)
Reac.	Reaction
RF	Reference-Free (type of MEAM)
RHS	Right hand side (opposite LHS)
$R\bar{3}m$	index for rhombohedral groups

S

SCD	solute centred divacancy
SIA	Self Interstitial Atom

atomistic calcs. based on exact description on fundamental level, also called *ab-initio* = from the start

DOF Degrees of freedom

Sim. simulation

E

EAM Embedded Atom Method

E_c cohesion energy, describing how much energy is needed to vacate one atom out

Elec-dens (also e-dens, ρ, ρ_e) electron density, hypothetical concept in MD as a functional for EMB part, subscript e, denotes equil.

EMB embedding-energy (part)→ 2.2(.1)

EOM/EOS eq. of motion / eq. of state

Eq./eqs. equation

Equil. equilibrium

Exp. experiment(al)

EXAFS Extended X-Ray Absorption Fine Structure (Spectroscopy)

T

T/T_m Temperature/melting Temperature

TB Tight Binding (approximation)

Tech/Techs. Technique(s)/technical

Ti Titanium

TMT Thermo-mechanically treated, relatively simple method for improved properties (good compromise for less irradiated areas for instance)

Type A/B dilemma – means the dilemma to chose between defect accuracy by pot type A and phase accuracy by pot. type B (no high defect and phase accuracy in the same pot)

FG

GA Genetic Algorithm (globaloptimisation)

GGA Generalised-gradient-approximation

GS Ground state

UVW

Vac vacancy

Wrt with respect to

HIJ

Hcp hexagonal (structure)

HIP(ping) Hot isostatic pressing→1.1

HSC High-Speed-Cutting

Ht high-temperature (in the context of the Fe-Y phase diagram >1000K

XY

XCF Exchange-correlation-functional

Y-vac test Yttrium vacancy test for suitability of pots. to describe Fe-Y alloys

Y2O3 chemical composition of yttria

KL

KS Kohn & Sham developer of KS theorems, foundation of DFT

K-S Kurdjumov-Sachs (→ N-S)

LHS Left Hand Side (pointer for reader)

LSM Least Squares Method (local optimisation)

Z

ZW(F) Zhou and Wadley formalism, Zhou and Wadley improved the Johnson and Oh method further and extended it with CTIP

M	
MD	Molecular Dynamics →2.1
MEAM	Modified EAM
Mech.	Mechanical
MeV	Mega electron Volt
Mat	Material
ML	Machine Learning

1 Introduction

The examined material of interest in this work is iron-yttrium (Fe-Y). This chapter deals with the related background of Fe-Y to ODS steels and provides an overview of the relevance of ODS steels and thereby occurring challenges. In the second half of this chapter the question, how to search for answers to these challenges, will be pursued by considering the abilities and limitations of MD simulations as a review and the fathomed capabilities of MD are then at the end used to set up the targets and aims of this work.

1.1 Key background aspects of this work

The worldwide energy consumption and the implied need has more than quadrupled since 1965 [1]. This poses a kind of all or nothing challenge for humanity in the 21st century. The development of new generations of power stations, implying the near time further development of nuclear power stations such as the IVth generation in the US and the long term goal of Fusion power plants, is inevitable [2]. However, such challenging ambitions implicate fundamentally different and increased requirements for the necessary applied materials in question [2]. For instance in potential fusion reactors the plasma reactions cause the reactor walls to face a high-flux of neutrons with high energies (14.1 MeV) [3, 4]. As a result, the used materials have to withstand to much higher irradiation loads than before (the requirements before, as in common fission reactors, envisaged only neutron energies of the order of magnitude of few hundreds of keV [2]). This promotes the development of reduced activation ferritic martensitic (RAFM) steels, which can be further upgraded either by TMT or strengthened by adding oxide particles leading to oxide-dispersion-strengthened (ODS) steels [5–7]. The addition of these oxide particles enable higher operating temperatures, as a rough orientation up to 100° C increase in operational temperatures or higher [7]. This advantage promotes applications of these (ODS) steels not just for the "far away" goal fusion but also for other high-temperature applications: for instance the increase in operation temperatures of gas turbines in electrical power plants leading to better efficiency and thus protecting the environment by reducing CO_2 emissions [8]. One of the first ODS steel batches was developed in the aerospace industry for the air-plane turbines (Ault and Burkle on a Gordon conference [9]), but due to the intense manufacturing effort (will be deepened below) for these steels, super alloys produced by solid solutions with the help of sintering (pressing at high pressure below the melting point) became more popular [10]. In the 80's, around 30 years ago, Fischer et. al. discovered that best results were obtained when using Y_2O_3 (yttria) as the added oxide, since yttria are among the most stable "ODS steel-utilizable" oxides with highest melting temperatures [11]. On top of that, these particles improve mech. and creep properties supposedly due to the rather unique defect formation behaviour of Y with its ability to occupy by one Y atom two vacant lattice positions at the same time [3], which up today leaves many questions unsolved. Later Ukai discovered that the extra addition of Ti reduces the oxide particle size and improves the mechanical properties, especially the mech. stability further [12]. In addition, ODS steels also raised widespread attraction in the fusion materials researcher community due to the vast improvements in irradiation resistance [6, 7, 13], as a further outlook an extracted graph is in the appended (A.1 in 7.1). But, as too often encountered by innovations, these improved qualities of ODS steels *come at a price* [6].
In contrast to the classical procedures in metallurgy to produce alloys, which are normally just melting and mixing in molten state [14], these standard fabrication routes prove to be unfit in ODS steels [8]. These standard procedures fail to integrate the yttria particles into the base alloy due to the extremely low solubility of Y in Fe (<0.6% at.% at 1350°C) [15] in addition to the to the very different densities of Fe and Y(≈7780 vs. 4472 kg/m^3 [16]). Consequently, the production of ODS steels require more laborious approaches, as shown schematically on the RHS in Fig. 1.1: the yttria particles are incorporated into the

steel matrix by mechanical alloying (MA)[1], which enforces an integration of the yttria particles (and as well Ti-yttria) into the steel matrix [13]. Due to the need of a fine-coarsed matrix with homogenously distributed yttria precipitates of few nm [7, 15] the requirements to this MA-technique are challenging and impose an extensive multi-step process [6], which is presented vastly simplified with the help of Fig. 1.1 (further details in J. Hoffman's Thesis [17]):

1. Mechanical alloying by ball milling: the initial components, roughly speaking a base alloy and yttria powder, are mixed for several tens of hours in a fast spinning mill with very hard, considerably large, metal-balls. By the resulting frequent and severe impacts with high kinetic energy between these balls the powder particles are significantly deformed and fragmented. Most state of the art experiments indicate that the yttria particles are already disintegrated and kinetically dissolved into the steel matrix at that stage, yet to be entirely resolved. But what can be said that both powders are fully mixed by this process – but "the exact how" remains unclear [13].
2. HIPping (Hot isostatic pressing): the resulting processed and mixed powder is then HIPped at parameters, which are around 1000°-1200°C and high pressures of around 100 MPa for several hours. This stage acts as a consolidation to support the final densification of ODS steels. What is still discussed is the question, whether in addition to this stage the yttria particles are formed by solute Y and oxygen atoms, which after the likely disintegration from the yttria particles in the previous step can potentially diffuse and eventually re-precipitate [7].
3. Hot Rolling – this is one of the last steps to further stabilize and improve the microstructure.

In order to enhance the ODS particle formation by improved parameters during the production process an exact in-depth knowledge about the underlying processes would be desirable. Although this technique has now been applied and examined for the development of ODS steels for about 25 years the mechanisms of oxide particle formation are still not understood at a satisfactory level [7, 13, 18]. Numerous experiments performed in the last decade have unambiguously shown that a variety of models of oxide particle formation is not able to describe all experimental findings [6, 7, 13, 18, 19].

It was commonly assumed that yttria particles in ODS steels are the remnants of the brittle oxide powder, crushed and incorporated in the ductile steel matrix in the first step during mechanical alloying and that HIPping is only consolidating [18]. Admittedly, later findings discovered strikingly disagreeing facts to this – if pure Ti was added to the powder mixture before mechanical alloying (MA), the oxide particle size was drastically reduced [12]. This and the quantification, that the oxide particles consisting of Y, Ti and O reduced their size by ten times [13], are an evidentiary indication that the final smaller oxide particles are formed after MA during or shortly after the powder consolidation step as HIPping [4]. Motivated by additional observations of coherence between small ODS particles by Klimenkov`s TEM analysis [20], the inevitable conclusion drawn by these surprising findings is that, in spite of being one of the most stable oxides, yttria particles are indeed disintegrated as an actual break-up into its components (otherwise no coherence would occur). And, at least parts of "freed-up" Y (and Ti) atoms are dissolved in the steel matrix during mechanical alloying, probably acting as mobile solutes for the following oxide formation [7, 20]. Consequently, mixed Y-Ti-O particles are formed by re-precipitation of these dissolved atoms [4]. This formation of these supposedly newly formed smaller (2-20 nm) oxide particles homogeneously distributed over all grains by the multi-step procedure positively affect mechanical properties of the ODS material increasing substantially their resistivity to high-temperature creep, decreasing ductile to brittle fracture transition temperature and increasing their resistance to neutron irradiation [10, 13, 15].

Atomistic simulations by Molecular Dynamics (MD) are a promising assistance to clarify this question by possible continuous and expanded insights at exactly controlled conditions. The underlying problem

[1] not to be confused with mechanical milling, which is only changing the microstructure but not the material composition as MA [8]

causing the above mentioned confusion is the ubiquitous challenge all experiments face: a lot of the relevant processes, such as the MA and HIPping, are (nearly) impossible to consequently monitor *in-situ* by experiments [21–23] – in other words in-situ measurements during the production processes are missing. MD simulations and their characteristics seem like an ideal tool to fill this gap for new insights.
But, why MD? One straight approach to answer this, is just considering the "length-timescale rule" of all simulations: the more detailed and exact the simulation becomes the smaller and shorter the time scales become. The most detailed and exact level, ab-initio (DFT) calcs. have a rather too limited length and time scale – only few 10s of Å and ps. If the microstructure with its grains and defects are considered, as said before, defects are important for the mobility of the dissolved Y atoms [3, 24, 25], these characteristic DFT scales are definitely too low. The time and length scale of MD on the other hand spans up to few hundreds of nm (even few µm) and few hundreds of ns up to few µs are possible [22] allowing the consideration of the formation and diffusion mechanisms related to defects [14] and as well the transformation of existing Fe-Y phases, which could act as Y-solute donors, *at the same time*. As always the price is related to accuracy: instead of exact description of the atomic interactions in MD these are approximated by empirical potentials, fitted with the help of DFT [26] (so, MD is kind of a bridge for DFT to larger scales). The empirical potentials are based on specific assumptions causing restrictions, which prove to be the pivotal point of MD simulations limiting the possible properties and processes to be modelled, further details in the next chapter. As a result of this, for new complex questions as this one here the time consuming requirement to develop an individual, specifically tailored MD potential arises. The complexity of Fe-Y-O is related to the fact that both metallic and ionic (ceramic) bonding should be included. Although good interatomic potentials exist for single component metals (e.g., those based on the embedded atom method (EAM) and MEAM) [27] and for *pure* oxides (without metallic bonds) [28], the mixed potentials including both parts or even just Fe-Y are practically non-existent [29](→lit-review). Already Fe-Y turns out to be a complex and hard to model due to the significance of directional bonds. Therefore, this project focuses on the MD potential development for Fe-Y with the resulting useful, unprecedented capability to model very accurately defect and phase properties at the same time.

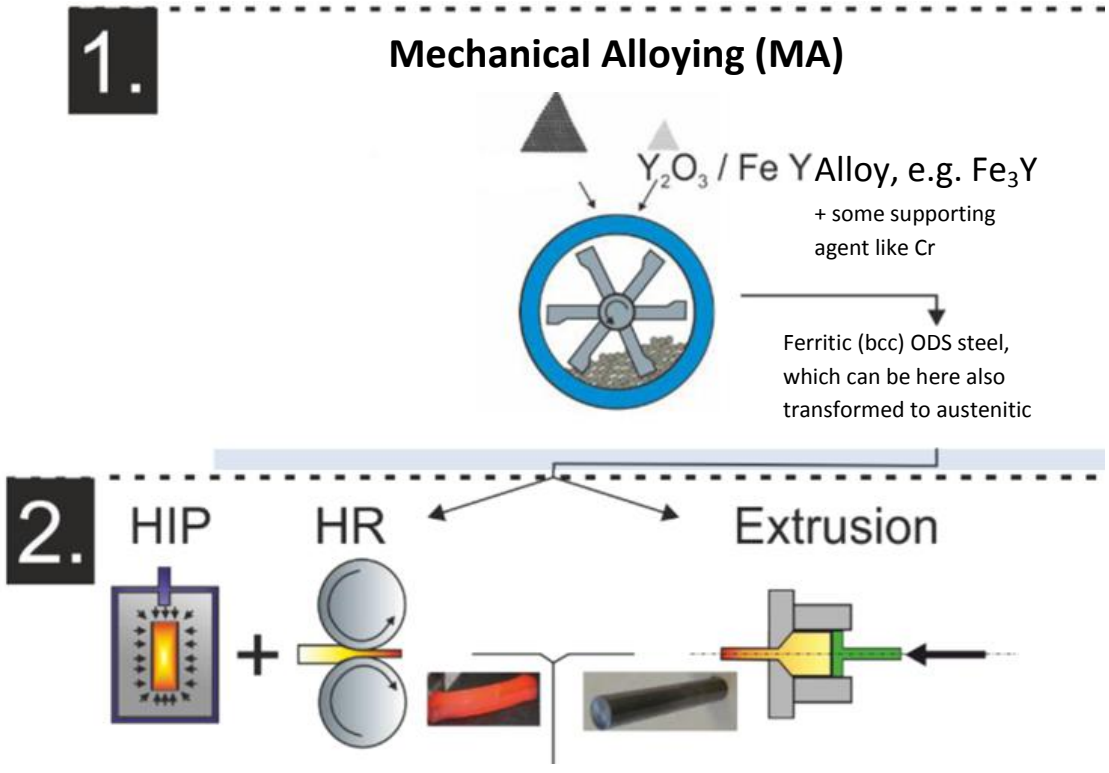

Fig. 1.1 Extract of illustrated processes during ODS steel production – courtesy from T. Gräning (KIT) [8]

1.2 Literature review - putting MD potentials into context

Before directly investigating cutting edge developments of suitable MD potential types and their associated implementation-techniques, which can adequately address the previously mentioned challenges, some relevant extracts of the history of MD are discussed in a goal-orientated manner – in order to get a constructive overview for a better classification and assessment of the suitable techniques.

1920-1955: Too theoretical non-dynamic models in the *early history* and a missed opportunity for MD

The history of MD goes back over 100 years at the beginning of the 20th century, although, at that time there were no computational resources for a dynamically calculated simulation [21]. Instead of these, theoretical consideration and "hands on simulations" like by actual rubber balls in a box (as a model for mixing behaviour) were dominant [22]. The first potential models, which sustained till now, were developed as pair potentials by Lennard-Jones (LJ) [30] and Morse [31]. At this time, in the 1920s, the aim were theoretical estimations with noble, closed shell, gases (Xe, Ne, Ar and Kr). In defiance of its short-comings (see 2.1 & 2.2) both potential types are still used nowadays or at least as a part of an enhanced model (like ZWF (3.1), which uses a modified Morse type form). One of the reasons for that are related to the ability of these potentials to determine equilibrium bulk properties for some material classes pretty accurately, such as the lattice constant and/or relate cohesive energy and lattice constant. Admittedly, one of the most interesting questions at that time, the examination of defects, exceeded the capability of them. In the 1920's Frenkel [32] tried to calculate yield stresses of steels and introduced the possibility of important influences by defects and dislocations. The major questions were, how defects affect mechanical properties and how they form and whether they exist at all [33]. Most of the "elucidation" was yielded by experimentalists – a missed opportunity (for MD). Due to the challenges experiments had to face, the proof of the existence of defects took till the 50's with prominent findings by IR micrographs [34] and by Hirsch's discovery by TEM in 1956 [35]. By that time it could be proven that dislocations drastically lower the yield stress, an invaluable finding for the material research and development [34]. Nevertheless, the quantitative answer, by how much dislocations actually lower the yield stress remained still an open one [14]. But to that point, where MD simulations are able to answer such questions, another 30-40 years passed till the 90's [36].

1955-1980: First dynamic MD models and the difficult start for MD until the emergence of EAM:

After some preliminary *groundwork*, like the influential Los Alamos report in 1955 by Fermi and Pasta et. al. [31], the first actual dynamical MD computer-run was implemented in 1957 by Alder & Wainwright simulating perfectly elastic collisions between hard spheres [37]. This and critical improvements by L. Verlet [38], who later also laid the ground work for simulations with more particles [39], initiated first research activity in a small and specialised community, like the Vineyard group with simulations of damaged Cu crystal [40]. But due to the rather quite limited computational capabilities (few hundreds of particles) and the resulting shortcomings in accuracy, these rudimentary models were very skeptically perceived by the broader scientific community and lead to a niche existence of MD during that time [41]. Fortunately, 15 years later in the beginnings of 1970, a few great *coups* have brought MD "back into the game": Rahman used effective LJ-liquids simulations for a chemical landmark map for liquid argon [21], followed by simulation of water in 1971 by Rahman and Stillinger [42], initiating the more chemically minded Stillinger Webber potentials [22]. The real breakthrough followed one year later in 1972 by experimentally verified simulations of self-diffusion processes in water by Rahman and in another publication by R. Mills [43]. In the physical minded material science community, focused on metals, D. E. Harrison was one of the pioneers, who can be claimed to be the first one, who performed successful and meaningful MD simulations about atomic collisions [44] – MD was established. However, common *MD potentials* in the 70's were yet not good enough to consider mech. processes and defects [39].

1980 -1995: EAM emergence and its breakthrough in popularity[2]

Right from the beginning (see 1920) the quantification and in-depth insight into defects was a central desire of material science. It became an even more pressing question with the emergence of nanocrystalline materials at the beginning of the 80's and discovery of the inverse Hall-Petch relationship [45], essentially pushed by Gleiter at KIT, who can be called the father of these new materials [46].
This time the developments in MD, particularly with regard to potentials, were able to keep pace with the needs by these emerging questions. A corner stone for the necessary fundamental improvements in MD (regarding metals) is the initialisation of the embedded atom method (EAM) in 1983 by Daw and Baskes (DB)[47][3], which applies the concept by Kohn and Sham of electron density functionals [48](→2.3) in an elegant way to MD – this marked a new era in MD modelling. The great strength of this approach, simply stated, lies in the significant boost in accuracy by including the electronic DOF with relatively little effort (as explained in 2.2) by numerous flexible and versatile ways to implement this method. The versatility is due to the fact, that numerous different approaches were found to set-up and fit the EAM potential.

Around the same time in 1984 Finnis and Sinclair (FS) derived based on the tight binding (TB) model, in a somewhat more rigorous way focused on theory, so called tight binding second moment potentials [49], which are in fact, though with a different interpretation, arriving at the same idea as DB to include the electron density as a functional [50, 51]. Nowadays both types (FS pots. & EAM by DB) are grouped together into the wider defined class of EAM potentials [22].[3] Thus, already the derivation of EAM can be approached from many different angles. Accordingly, the analytical parametrisation functions and fitting procedures can be chosen by individual preferences – the same applies to the parameter fitting of the analytical functions forming the shape of the EAM potential, which can be fitted to various inputs, like DFT data computations or directly to certain experimental quantities [52]. In the 80's when computing capacities for DFT computations were still severely limited, the latter possibility to directly fit to experimental quantities was an extremely useful asset of EAM (while at the same time keeping a lot of room for improvement by more detailed data (see force matching below)) [21]. While FS linked their fitting input from bottom to top by orientating their fitting around phonon dispersion and considering these in detail by linear combination of atomic orbitals (LCAO) models, DB had a more empirical from top to bottom view, directly connecting the pot. curve with observable quantities as fitting targets [22].

Both methods by FS and DB became quickly very popular [53], but already at that time, one of the central themes in this work, parameter sets, caused some confusion among the broader scientific community and inhibited wider applications[4]. Some standardisations and more clarity about the fitting and what the functions and the parameters actually mean were needed (and also how to obtain the explicit functions). It took till 1988, when Johnson and Oh started to put the various fitting procedures with its many functional forms in order by developing a kind of a universal (explicit) form of EAM (motivated by difficulties to model BCC metals) [55, 56], which is characterised by some normalisation features, such as the requirement for the first derivative of the EMB function to be zero. This standardisation procedure can also be interpreted as a comprehensive guide, how to fit or at least set up an EAM potential. These basic ideas for implementation are still reused in many EAM potentials (like in the latter ZWF [57]). At the same time the notion to use empirical relations, labeled as universal binding relations (UBR) mostly in the form of the Rose eq., discovered in 1984 [58], to assist the fitting processes, even to the point to fit the whole EMB function by the Rose eq., became popular [52]. Unfortunately, this is a double-edged sword: on the one hand this makes the fitting faster and easier[5], but at the same time it has consequences for accuracy [22], which were ignored for too long in further pot. formalism developments (→MEAM).

[2] same time in the 80's by popularity more techs such as ensembles&espacially car-parinello – refer for details to my Master thesis!
[3] It is a bit tideous to argue, whether Daw and Baskes first paper in 1983 introducing EAM, applying the idea of EAM to hydrogen in steels, was actually already a *proper* description of the formalism and not till their following paper in 1984 as the same time as FS
[4] One of the first ones to publish this phenomenon was Johnson in [54], who encountered this when applying EAM to alloys. What is meant in detail, is the fact, that the parameter sets (explained in 2.2.3 and 3.3.6) can drastically limit the transferibility of pots..
[5] The fact, that this increased the number of available and „OK" pots. and established EAM further should not be overlooked, too.

A third major class of EAM interpretation as glue potentials (abolishing the original, descriptive interpretation of the embedding term by Daw and Baskes [47]) followed at the beginning of the 90's, linked to an improved fitting scheme in the form of force matching (2.2.2) developed by Ercolessi [59], which made use of the better availability of reliable and useful DFT data [27]. As a consequence, EAM potential fitting got more involved with atomic references (model is matched to computed accurate forces by DFT). This and extensions (p. 7) started a creation of a universe of results, which can't be overviewed.

Fruitful effects on Fe-based material science by the success of original EAM and limitations in alloys
The aforementioned vast number of results are narrowed down to a selection focusing on some of the major successes related to Fe.[6] Ultimately, already these developments up to the 90's provided the foundations for the invaluable insights up to now on hidden processes by classifying these processes and by revealing the necessary conditions to observe them in reality, with the following selected "highlights":

- phase transitions, investigation of the underlying processes taking place, e.g. in 2008 in the FCC->BCC transformation the exact atomic orientation at the interfaces were identified as N-W and K-S [62], EXAFS spectra confirmed this in 2017 [63], also in polycrystalline Fe [64]. Further examinations lead to some interesting findings about martensitic transformations [65].
- effects of impurities:
    - hardening effect of impurities by initiating dislocation glide and climb by Bacon [66]
    - special focus on He in Fe, as He plays an essential role in irradiated reactor mat.
        - diffusion coefficients of He in α-Fe and He-clustering by Osetskiy [67]
        - interaction of He with defects in-depth considered by Nordlund in 2008 [68]
        - dilation of He bubbles after vac.-clustering depends on He/vac. ratio [69]
    - one of the origins is the AMS pot. by Ackland [70], initially considered P in Fe and showed a critical reduction in the ductile to brittle transition temperature
- underlying analysis of defect formation processes & classification (after the discovery in 1956):
    - discovery of the most stable SIA position to be the <110> dumbbell followed the <111> dumbbell by Ackland [27] and Wirth [71] around the same time in 1997
    - vacancy diffusion is in steels with C impurities (for better tensile strength) is faster than the diffusion of soluble C atoms by B.J. Lee [72], it's important under irradiation
- displacement cascades in irradiation (particularly in Fe-Cr) [73]
- "Real life" machining processes – e.g. determination of conditions in HSC when chipping occurs, where EAM is still very accurate in description of met. bonding in workpieces [74, 75]

During these developments one particular EAM potential, that can be called a fundament in this work, emerged as an unparalleled work showing the *true art of fitting intuition* – the Fe-Fe EAM potential for liquid and crystalline Fe by Ackland and Mendelev in 2003 [76], which even after 15 years of further developments can still be claimed to be one of the best MD potentials to describe defects and melting processes in Fe (→ 4.2.2)[7]. An extensive Fe MD pot. summary with ABOP is given by Müller in [78].

What is striking, is the pattern that EAM and MEAM seem to be only capable of systems with one metallic component and a gas or with Cu and Cr (which can be treated as a solution with Fe since it forms few directionally dependant bonds), alloys with low amounts of such bonds are rare. The answer to this was already given in a review of 1993 by Baskes: "it [EAM] works best for purely metallic systems with no directional bonding; it does not treat covalency or significant charge transfer" [36]. The keywords are *covalency* (=directional bonds) and *charge transfer* – this marks two separate levels of complexity: level one is just covalency, which is the case for Fe-Y (see 3.3.5) and is manageable by nowadays techniques (see next page) and level two, covalency and charge transfer as in ODS, is not really manageable, yet.

[6] Two other central developments in the infrastructure during that time, crucially contributed to these successes, the LAMMPS MD simulation software tool [60] and the Common neighbor analysis (CNA) algorithm for structure analysis by Schiotz in 1997 [61]
[7] There is two specific exception in accuracy: 1. Bain path (BCC->FCC)&2. screw dislocations, improved by Proville [77](2008/12)

1995 to 2005: a quite difficult start for MEAM, ABOP & Co

Some of the presented highlights used extensions by the ABOP and MEAM formalism, which were developed in parallel. The previous review distinguished between the TB based approach by FS and the "pure" EAM method – an important distinction, since it essentially affects the following trends in the ongoing developments up to now. Improvements in the accuracy of covalency in FS pots., originating from the TB approach, lead to the class atomic bond order pots. (ABOP) [79], closely related to DFT.

In 1990 Baskes himself extended EAM by the Modified Embedded Atom Method [80] (MEAM, which compared to ABOP is a more empirical and intuitive model). What both have in common is the inclusion of angles making the formalism vastly more evolved and quite hard to follow and fit. Simply speaking the formalism is too difficult to fit with the commonly used non-intelligent techniques without Machine Learning (ML) traits [81]. The reason for this assessment lies in the fact, that the patterns and fitting relations to properties and physical properties are not anymore traceable [82]. ABOP and MEAM also represent two opposing "fitting philosophies" to handle such an overwhelming complexity:

ABOP just treats the potential fitting as kind of a "Black Box": the explicit functions are fitted regardless of the meaning of the parameters to match the desired properties and quantities and the form is orientated to theory to the disadvantage to comprehensibility.[8] Without ML this makes the fitting with respect to phases and defects (see 1.3) nearly impossible [86]. The further developments to include charges by COMB models [87] look promising, but as laid out in footnote 8 already the related simpler ABOP formalism has serious short comings in Fe-Y without ML optimisation techniques, so the next level should be only tackled with ML and will, therefore, not be used in this work.

MEAM, on the other hand, tries to simplify the fitting processes by keeping close links between properties (physical quantities) and parameters to make the fitting more controllable [22]. However, in the original MEAM form this does not work, as shown by one of the most successful MEAM pot. developers (for metals) Lee: these links are only in a too approximate and inextricable manner correlated [82, 88], which cannot be used for fitting. The intention to make the fitting *that easy* turned out to be illusive, failed and even made the original MEAM somehow ill-suited [22] (→ following theory chapter).

As a last resort to compensate this kind of *unfittable* formalism up to ≈2010 the Rose eq. has been used in most MEAM pots. to replace the fitting of the pair part, since it allowed direct input of physical quantities for the fitting [89]. But this relation is too inaccurate and drastically limits the parameter space during the fitting, which is especially problematic for multicomponent systems, such as in the case of Fe-Y, treated in this work.[9] This dilemma leads to quite severe consequences – a low number of accurate applicable metal-alloy potentials (between 1995 and 2015): while the AFLOWLIB library lists 500 (metallic) alloys of interest [53], the MD potential repositories, NIST and OPENKIM, listed up to 2016 only 50 available MD potentials (of all kinds, in MEAM it is just 14!) [28, 53]. Therefore, it is not surprising that there is no readily Fe-Y pot., except of the aforementioned but dismissed ABOP one[10] and even no *suitable* (M)EAM Y-Y pot[11], so these interactions need to be fitted from scratch to pursue the questions of 1.1.

2005 to now: Genetic algorithms – bridging a time gap without pattern recognition by Machine Learning

Fortunately, after some time, starting from 2005 some serviceable developments for improvement were undertaken: around 2010 B. Thijsse's group successfully abolished the Rose eq. in MEAM by the formulation of the *Reference-free (RF) MEAM* formalism, which will be discussed in the second half. Timonova verified this approach by developing an improved RF-MEAM silicon potential [94].

[8] As a result, no ABOP potential up to now is suitable for the desired applications in Fe-Y, the most recent Fe-Y ABOP pot. by M. Mock [83] misses the melting temperatures (especially in Fe, is orientated to Müllers Fe pot., but at least is pretty good in defects). The only available pure Y-Y ABOP potential by Kai Min Fan [84] crucially lacks defect accuracy as shown by Borodin [85].

[9] Numerous tries with „MEAM-like" modification to EAM, like AMEAM by Hu [90], but did not resolve this underlying problem

[10] Hammond [23] tried to model Fe-Y-O by Buckingham pots, but has all the shortcomingss as a pair pot.. So, it is too inaccurate.

[11] Available Y pots: 3x MEAM Y-Y pot. (alloy), 2x (A)MEAM (pure) & 1x EAM pot. (alloy) appear in the literature [83, 84, 90], but these are not suitable (obviously since intended for different alloys), more in 3.3 and OPENKIM and NIST have none [28] The most promising candidate, the recent MEAM Y-Y pot. by B.j. Lee [92] misses the melting temp. by nearly 300K (1505 K)!

The next surpassing step was taken by another group member, Laszic, who fitted an impressive RF-MEAM Al-O potential with an additional included charge transfer ionic potential (CTIP) [95]. The later part, *CTIP* technique, has been refined before, around 2005 by Zhou and Wadley (ZW) [96]. In addition ZW develop an extremely useful fitting scheme to form Universal Relations (*not Universal Binding Relations (UBR)*, see chapter 3) for parameter set control, which do not depend on the Rose eq. but only orientate to the Rose eq. (=more accuracy and flexibility with tolerable higher fitting effort) [97]. Laszic's work was influenced by these ideas and this work also facilitated these ideas in the first half and made use of the resulting parameters for start parameters in RF-MEAM in the second half. Both works were still based on classical fitting techniques, e.g. LSM, and led to fixed screening factors. Unfortunately, under these conditions CTIP turns out to be quite unstable [98], even more so for alloys with Y-Y interactions, essentially caused by enhanced requirements for the global optimisation techs..[12]

This pushed for *more sophisticated fitting codes* with better optimisation schemes: inspired by RF-MEAM, A. Duff and Finnis published in 2016 with the assistance of Genetic Algorithms (GA) the first publically available full scale (RF-)MEAM fitting tool: *MEAMfit* [99]. The Genetic algorithms are capable of global minimisation without use of the Rose eq., provided suitable starting parameters are given and the fit references as DFT data are extensive (AIMD is of excellent help, too). However, the current performance optimised implementation has to turn the screening factors off, which eliminates the possible stable inclusion of a CTIP extension to RF-MEAM potentials in MEAMfit.

This general framework of suitable models (RF-MEAM) and fitting tools (MEAMfit) at the time around 2015 narrowed this project down to the development of a Fe-Y potential (wrt. to feasibility as a PhD project in 4-5 years). The use of Genetic algorithms can be interpreted as bridge for fit-techniques until more reliable ML techniques become available in the next 5 years. Currently, ML techniques in MD pot. development are still in the *fledgling stages* [81] – a useful possible benchmark to determine the readiness of ML approaches for the here presented applications about ODS steels would be the reproduction of the accuracy of Ackland's Fe potentials. At the moment ML techniques cannot replace the great amount of wise and dedicated human intuition contained in these pots., not yet (the best ML pot. for Fe at the moment, is the one by D. Dragoni [100] (2018), which misses the melting point by up to 250 K, this is not enough improvement, *yet*). Once this challenge is "cracked", ML is a serious competitor in the race in the field of Fe-Y(-O) MD potential development. Until then GA based approaches, yielding acceptable results and revealing invaluable insights into the fitting techniques and models, are a suitable alternative.

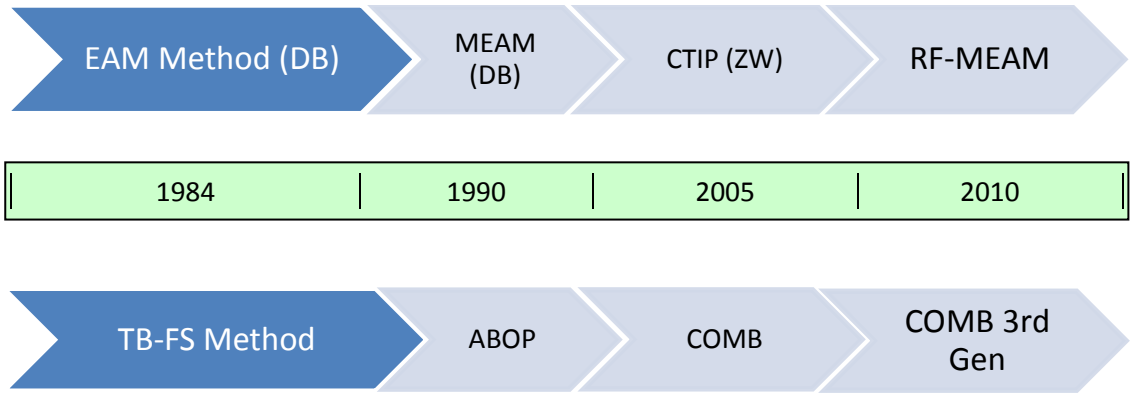

Fig. 1.2 Overviewing Timeline for the Development of the two major MD potential groups for mechanical process characterisations in metals and metallic alloys: Up to now, 2019, RF-MEAM, originating from Daw and Baskes EAM & MEAM, and COMB, which originated from Finnis Sinclair via ABOP, are competing against each other. Within the next 5 years, as a careful estimation, ML based techs. might take over replacing these two in metals.

[12] The use of standard LSM techniques turned out to be problematic and even lead to correctum of their published paper [98]

1.3MD Potential fitting as a process – methodology & aims

Fitting in principle is simply a process to find in a selected model suitable parameters, which yield the best agreement between the results reproduced by the model with a given set of training data, which are in MD potential fitting mostly (atomic) fitting references. Although the principle seems quite easy, in reality it actually proves to be rather difficult because a suitable model has to be found (see chapter 2.2) with flexible, precise but at the same time fittable analytical functions (see 3.1). Subsequently, the right set of empirical data (=fitting references) must be fitted to the function, such as cohesive energies (E_c), lattice parameters (a_0) and defect energies. Ab-initio (DFT) simulations are mainly used here. By performing for instance basic least-square fitting (LSM), the parameters can be adjusted to yield the best results for all references. The references usually need to be weighted differently. This is called optimisation. On top of that, stability of the potential has to be maintained at all times, which can prove difficult because of the unforeseeable possible events in an MD simulation. Yet, checking model data against some of the predetermined test reference sets is compulsory [26, 52].
So, for a successful fitting procedure resulting in powerful potentials, simply speaking, three "ingredients" are needed: powerful fitting software, a suitable model with functions and boundary conditions and detailed DFT fitting references. This work will focus on the first two, the DFT references are briefly summarised here (and some characteristics of the DFT fitting references are in the appendix). This focus is simply due to the fact that this work focuses on the rigorous in-depth explanation of the used EAM and RF-MEAM formalism with its functions and analytical techniques plus the optimisation methods (provided by the fitting software). Already the literature review revealed that the models and optimisation techniques are a kind of the pivotal point during the fitting, but another reason for this focus becomes apparent when considering the fitting references in principle: the fitting references can be separated into three main classes: <u>defect clusters, phase- and migration references (refs).</u>

<u>The defect clusters are needed to describe for instance:</u>

- description of the binding energy for the defects, for instance vacancies or interstitial atoms, interstitials can be either self- interstitials (like Y in Y) or more interestingly Y atoms in an Fe lattice, because of their importance the detailed tables of included energies are appended in 7.2.
  ➔ for example binding energies control when and how clusters are formed
- these references also contain information about the most likely location of the defects – this includes the "specialty" of Y, the double occupancy behaviour, which will be deepened in 3.3.6
- together with the details about migration (for instance moving from one defect position to another, as for instance in self-interstitials: from an exited state to the GS state (BO in hcp Y [85])) information about diffusion is also incorporated – this means for instance diffusion coefficients, directions of diffusion [83] and also diffusion barriers, which are very interesting when considering necessary temperatures to initiate desired diffusion processes.

A detailed report, describing the used defect clusters, has been already given by the author and Y. Mastrikov in the publication *"Ab-initio modelling of the initial steps of the ODS particle formation process"*[5], for any further specifications in detail it is referred to this paper. Beside the physical interpretations of the findings, a nomenclature has been developed (measuring distances as Nearest Neighbours) and the database was sorted to find a suitable weighting during the fitting in chapter 3-5.

<u>Phases</u> are included in the fitting data base to ensure correct reproduction of the equilibrium properties of different configurations (phases, especially lattice parameters and cohesion energies) and as well correct behaviour around the equilibrium (distortion up to 10% so from a_0 0.9-1.1). For single phases, here Y and Fe, the hcp, bcc and fcc as well as diamond structures with their energies were used, also liquid like states for better behaviour at higher temperature. It has to be remarked that for Y the database is extensive, the one for Fe, however, is more basic (leading to the adaption of an existing potential in chapter 4).

For the two component Fe-Y phase, there are much more references, since there are different possible chemical compositions, from here on labelled as phases (Fe_2Y, $Fe_{17}Y_2$, $Fe_{23}Y_6$, etc. more details in 4.2.3) and each phase is included in different structural variants (hcp, bcc, fcc but also rhombohedral and other) with the corresponding energies. In this multicomponent system three properties are essential: correct reproduction of the structure of the phase (including lattice parameter within 5% or up to 10% for negligible phases), correct cohesion energy (E_c within 5%) of the phase and on top of that correct energetic sequence/order of the phases (wrt. to E_c), ensuring that under certain circumstances/conditions the correct phase is reproduced. Especially the latter point proves to be challenging, sometimes (as shown in chapter 4 & 5), just slight subtitles by magnetism separate different phases or even structures.
Accurate DFT references are just the very first step. As said before in the definition of fitting, these references need to be mapped onto the MD potential models, concretely the fitting parameters. And even the best MD potential models need strong fitting software. The used software are POTFIT [101] and MEAMfit [99] with individual modifications – these will be explained in more detail "on the fly" at the corresponding parts in this work, namely 3.1.4 and 4.1. But what can be said in general here about the fitting is the important difference between a global and a local minimum [40, 102] – this point will appear frequently in this work. The optimisation is a minimisation of some quantity which measures the disagreement of the model with the references data [53]. The simplest and in the first half used technique is the least squares method (LSM) [102]: the deviation in energy is measured and is summed by quadratic weight. But, the great issue with LSM lies in the fact that it cannot distinguish between a local and global minimum. Local simply means that in the surrounding parameter space of that minimum the minimum appears to be the only existing minimum. Since LSM methods mostly follow some kind of a gradient, this gradient inevitably leads only to local minima. But, it is very likely that in the whole parameter space there is another minimum, which is smaller. The global one is the best one of all seemingly minima [40].
This parameter space surface can be illustratively visualised as standing in a valley and being surrounded by hills, which hide the next deeper neighbouring valley. While being in that valley, the deeper valley cannot be seen. With some constraints the parameter space can be limited in a way to avoid this problem [52, 90, 97, 103]. But, in opposition to the still wide spread conception that this is possible too for alloys, in fact this approach quickly reaches its limits in alloys, as shown in the second half of chapter 3. This requires the use of techniques which are more capable to locate global minima – one of these techniques are Genetic Algorithms (GA) [102], which are incorporated by the combination of RF-MEAM and MEAMfit (chapter 4). The scheme of a GA in the context of MD potential fitting can be simply summarised as: instead of just following a gradient (the change of the parameters leading to better target values, minimised), a GA actively recognizes kind of parameter subsets (explained in second half of chapter 3) and shuffles and adapts these with respect to global minimisation, by so called GA operators. The shuffling of different parameter sub-sets causes the mixing of different local minima and therefore enforces the wider search towards global minima (few more facts about that in 4.1.2).

Having underlined in 1.1 the importance of the simulation of phases and defects (p&d) at the same time and based on these considerations and the literature review (1.2), this work aims for an overall agreement of 10% for both p&d (measured as an R value, introduced in 3.1.4) – mastering this challenging compromise is the goal of this work. It necessitates the development of an advanced model and fitting technique which is able to reproduce the structures very accurately to a level, which even agrees with state of the art EXAFS experiments. All of this requires a threefold technique: development of the fitting technique (mainly analytical constraints and in-depth understanding of the model) and suitable testing methods in chapter 3 by pure EAM, then applying these findings (and the found EAM parameters as start parameters) to a more advanced model in RF-MEAM, with further software tool developments such as a LAMMPS module. The developed technique with RF-MEAM is then shown to overachieve the 10% goal for phases and defects. And the third step is then performed by a broad discussion in chapter 5 resulting in the first successfully simulated EXAFS spectra of a complex alloy (what complex means is illustrated in 2.2.2). Further introductions are given separately at the beginning of each chapter and section.

2 Theoretical Background & Methods

After having set up the targets of this work to examine Fe-Y by the development of (RF)-(M)EAM potentials for MD simulations, these theoretical concepts are introduced in detail in this chapter. After an explanation of the functionality of MD, the pivotal point of MD simulations, the underlying ideas of the used empirical potential formalism (EAM & MEAM) are explained. For an easier understanding a top to bottom approach is used – starting from intuitively clear pair pots. to describe the simulated interactions towards the advanced cluster functionals (MEAM) by highlighting the motivation for each method-upgrade (pair->EAM->MEAM). At the end all these types will be compared. One of the central themes of this work, *parameter sets*, stands out and will be revisited in the in-depth development of the formalism with its functions in chapter 3 (here it is only the general formalism, not the explicit analytical functions). The theory in this chapter already indicates as underlined in the lit. review that in the development of metal alloy pots. one cannot simply mix two elemental pots. – here the reasons for this are explicated and substantiate the need for the specifically tailored potential development for Fe-Y. For the sake of completeness the main ideas of the used DFT technique for the fitting references are explained.

2.1 Introduction to the principals of Molecular Dynamics

A comprehensible description of a molecular dynamics simulation represents MD as a computational method calculating equilibrium properties of atoms or atomic configurations. Such configurations are treated like a classical many body system, which is controlled by a dynamic potential energy distribution (can be assumed due to the small de Broglie length, $\lambda = \sqrt{\frac{h^2}{Mk_B T\, 2\,\pi}}$). Appearing as the gradient of a potential, the forces are thus defined by the potential, see below on LHS. [21, 60]

$$\overrightarrow{F_{ij}} = -\overrightarrow{\nabla}\,\Phi\left(\overrightarrow{r_{ij}}\right) \qquad \overrightarrow{a_i} = \frac{\overrightarrow{F_i}}{m_i} = \frac{d^2\overrightarrow{r_i}}{dt^2} \qquad (2.1)$$

The left equation represents the force, F acting on atom *i* and atom *j* as the corresponding counterpart for this pairwise interaction. Φ(r) describes the potential as an analytic function (more details on p. 12).

It can be easily recognised, that eq. (2.1) is just the classical equation of motion (EoM), the key to the position and velocity by integration [38]. Consequently, a position can be obtained by the following steps:

1. Determining the atomic positions and using the potential to obtain the force for each atom (taking atom *i* and then considering all interactions with N-1= j remaining atoms).
2. Using integration of (2.1) to solve the EoM and thus obtaining velocity.
3. Establishing the new position t+Δt, based on the calculated velocity.
4. Repeating step 1-3 for the new position.

The foundation of successful MD simulations is an accurate MD potential, systematic inaccuracies have to be avoided at any cost. Instead of the aforementioned length-time scale problem, the problem is now a kind of shifted to the potential development. Once a suitable MD potential is developed, care has also to be taken to have a correct setting of the MD simulations to prevent utterly unrealistic calculations [21]. Unsound choices in the intervals of the time steps poses as an illustrative example: overly short intervals are not necessary and lead to excessive effort in the computation. Excessively outstretched intervals on the other hand generate unphysical situations (e.g. resulting in breach of the confinement of particles

inside the simulation cell). More details about the basics for accurate MD simulations are described in the author's Master thesis [104] and is taken for granted from here on.

Since the underlying initial problem is the same as in the previous master project the problem description is directly cited from the author's master thesis: "*When developing a MD potential, intuitively before the necessary fitting (see 1.3), one would try to take a classic pair potential format to model the interatomic interactions in an MD simulation, such as the Lennard-Jones (L-J) potential form (V= A/r^6 [=attraction] – B/r^{12} [repulsion]). This however, comes about as impossible[21, 52]. Firstly, because of the two fitting parameters (A and B) that do not contain the more versatile material parameters of metals [105]. The second, more acute reason for which these pair potentials are ill-suited lies within the complex interactions of the electron structure in metals [106, 107]. This generates many electronic degrees of freedom [106].One way to capture this complexity are ab-initio simulations [39, 53, 108]: they quantum mechanically solve the backbreaking computational Schrödinger equations for this many electron system, as described in 2.4. This method may be very exact, but has the disadvantage of limiting the number of simulated atoms to a few hundreds, and of shortening the accessible time spans to picoseconds (ps, while MD simulations cover nanoseconds (ns) [22]) – again the aforementioned length-time scale problem.*"

(cited text taken from p. 14 in [104])

This necessitates the use of more accurate methods, which include the effects of the electron interactions. Motivated by DFT one of the most effective approaches resides in the embedded atom method (EAM) [50] or in the tight-binding method [39].With little additional effort impressive improvements, clearing the limits of pairwise potentials in metals, are obtained. The improvement in EAM is based on the acknowledgement, that electrons are strictly delocalised and these electronic degrees of freedom cannot be integrated out as it is tried in a pairwise treatment (=potential) – this will simply not work. A closer look at this delocalisation reveals: the atomic bonds interact with each other and a form of electron screening takes place [80, 107]. One important consequence is that the vacancy formation is intertwined with the cohesive energy (=E_C, i.e. bonding energy of the crystal) and thus represents up to one third of E_C [105, 106]. Macroscopically this can be nicely illustrated by totally wrong melting temperatures stemming from missing screening by using a pairwise potential: L-J potentials propose melting temperatures for metals of the order of $\frac{E_C}{k_B T_m} \approx 13$ [52, 65]; other pair potentials are similar. Comparing this ratio to real materials it turns out that this ratio is actually around 30 [65]. Simply speaking, two fitting parameters, one for the repulsion and another one for the attraction, are not sufficient[13].

2.2 Putting the EAM and MEAM method into perspective

2.2.1 General (simple) idea of EAM

An elegant approach to overcome the previously raised problem, is to include the electron density as an *electronic energy functional* depending on the electron density as DFT [36]. This density is a hypothetical concept and will be expressed as the rather fictitious electron density function. Notwithstanding, the potential still consists of two short-ranged parts [49]: 1. the potential part for the atomic cores (U_R). This part is only depending on the position and has a distinct repulsive and attractive part as a *classical* pairwise potential. 2. The electronic part depends on the electron density, also including repulsion and attraction. All of this forms a so called pair functional in eq. (2.2) on the next page:

[13] "Trying to fix this by perturbation theory does not work, since the electron density cannot be assumed to be constant in space and time. Nevertheless for a *hypothetical* defect free crystal such potentials could work" (author's Master thesis p. 14 in [104]).

$$U_{Tot} = F_{Se} + \Phi_{pair} \quad \leftrightarrow \quad U_{Tot} = \frac{1}{2}\sum_{ik}\phi(r_{ik}) - \sum_{i}F_{Se}(\rho_i) \quad (2.2)$$

$$where: \quad \rho_i = \sum_{k} f(r_{ik}) \quad \& \quad \Phi = \frac{1}{2}\sum_{ik}\phi(r_{ik}) \quad \& \quad -\sum_{i}F(\rho_i) = F_{Se} \quad (2.3)$$

Part one, Φ_{pair}, the mainly repulsive term, is set up as an independent sum of individual pairwise core interactions, each described by the pair function $\phi(r_{ik})$. The input solely depends on the atomic position between atom i and k . The influence of the electrons is handled by the function F_{Se}, summing up all interactions caused by 'changing electron clouds'. The embedding function $F(\rho_i)$ describes each electron which interacts with the cloud (see Fig. 2.1 below, the "se" index of the sum denotes the species/metal). $f(r_{ik})$ describes the highly varying electron density and is thus called electron density function (see comment below). It is also short-ranged and quickly diminishes with increasing interatomic distance. This is one reason for the short-ranged nature of this interaction [21]. Considering many atoms (10^6) and billions of electrons, the above sums can be turned into integrals, which reliably fix the electronic degrees of freedom in the EAM model [26, 65]. The functions $f(r_{ik})$, $F(\rho_i)$ and $\varphi(r_{ik})$ should be fitted to parameters (but before fitting an explicit analytical form has to be found, as done in 3.1) [22, 52].

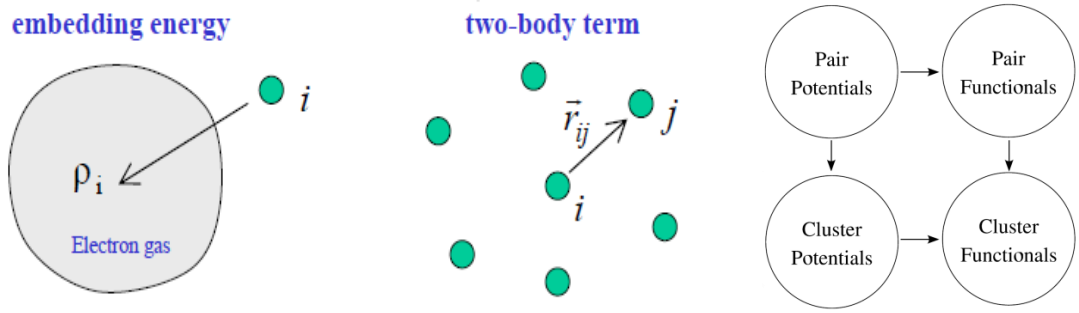

Fig. 2.1 On the LHS a schematic illustration of EAM, the EMB term describes the interaction of one electron with the other electrons, characterised by an electron density of an electron gas. The two body term treats pair-wise interactions of the atoms. RHS: Classification of pot. classes, EAM is a pair functional, more in 2.2.4.

Now, from a conceptual point of view this method with this understanding seems to be a handy solution – with a little additional term at nearly no more computational effort most of the previously mentioned problems are resolved, like in the elastic constants and regarding the vacancy formation energies. And indeed, remembering the literature review in chapter 1, EAM provided a great success to describe many single metals [50]. It can be even claimed that in single metals this interpretation is sufficient.

2.2.2 Closer look at EAM with glue potentials

However, when it comes to alloys, the fitting successes become rare and there seem to be not many accurate (pure) EAM alloy potentials and it seems to be much more effort to fit alloys.
In order to find the reasons for this, taking a step back and a look at the broader picture helps: the previous explanation of EAM followed the rather simplified interpretation as the so called EAM model. As said before the key point, and also its *beauty*, of the idea is to assign the pair and EMB term a specific and unique physical meaning (like an empirical relationship). But since the electron density is a rather hypothetical concept, the meaning of these terms is in fact not unique, which can be easily shown analytically in the glue model (interpretation). Before doing so by mainly analytical considerations, an insight into the physics provides a better and even deeper understanding of the origins of this ambiguity.

The main idea of the EAM method (interpretation) that the electrons act as a homogenously distributed electron gas with a specific electron density and this electron density can be linked to an energy by the idea of embedding, see 3.1.1 description of embedding function. This originates from DFT, where the energy can be specified by the electron density (functional) [52, 108].
This electron density, acting on one atom, is caused by the neighbouring atoms and the EAM method assumes a linear superposition of the contributions to this density by each neighbouring atom, which is purely distance dependant [22] – that's the difference between a pair and a cluster functional, see Fig. 2.1. As an irreversible consequence, the electron density and its functions are simplified as a spherically-averaged electron density field. Comparing this with the actual *real* electron orbitals the striking difference is, that in reality it is not just the distance but also the direction [109] (leading to a consideration of angles in triplets, as in the cluster functional potential type MEAM which is more complex and is explained below). Conveniently, in single metals, these orbitals[14] can be approximated as spherical averaged distributions [107], simply because of the absence of distinct influential bonding angles. This stems from the fact, that in a single metal the charges between the individual metal atoms are the same since they are the same species. And bonding angles and their non-uniform electron distribution are caused by differences in the charges [107] (as in yttria for instance, visible by EXAFS [110]).

All in all, for single metals this approximation by EAM is reasonable [49]. However, this approximation causes a very meaningful phenomenon – parameter sets [54]. These occur due to the interplay of the electron density function and the embedding energy function (EMB) [40]. The trick of EAM is that the fitting process is only dependant on the resulting energies of averaged spherical symmetries and not to the underlying exact electron densities, which are not explicitly included in the fit. This leads to the possibility of choosing different electron densities for the same potential [53], as said at the beginning in the EAM context the electron density is a hypothetical concept (and not exact as in DFT).

This phenomenon, lead to the glue potential interpretation [22], which illustrates, explains and tries to handle the concept of parameter sets. These originate from the fact that EAM potentials are invariant under the following transformation, as already pointed out Johnson in 1989 [54]:

$$\phi(r) \;\rightarrow\; \phi(r) + 2\xi\,\rho(r) \quad (2.4)$$

$$F(s_{si}) \;\rightarrow\; F(s_{si}) - \xi s_{si}, \qquad \text{with} \;\; s_{si} = \sum_k \rho(r_{ik}) \quad (2.5)$$

Eq. (2.4) and (2.5) describe a transformation simply controlled by ξ, which represents any real number, which controls the potential transformations which yield exactly the same energies as the original one.

In other words, the splitting up of the energy by EMB and pair part can be chosen without affecting the total energy of the potential. So, when a potential is transformed, the split up of the total energy between pair and EMB part changes, this leads to different parameters but does not change properties of the potential (since the total energy is the same). The deeper meaning of this transformation is, that this split up is an artificial one, the fitting is only concerning the total energy – but this split-up is a helpful assumption. Another important transformation with strong links to the previous considerations on p. 13, is the invariant transformation of the electron density:

$$\rho_{si}(r_{ik}) \rightarrow \lambda\,\rho_{si}(r_{ik}) \quad (2.6)$$

$$F_{se}(\rho_i) \rightarrow F_{se}(\rho_i/\lambda) \quad (2.7)$$

This mathematically formulates, what was mentioned before about the electron density as a hypothetical concept and that the electron density can be chosen freely. The proof is simply performed by eq. (2.6) and (2.7), if ρ is scaled by λ, than only a kind of normalisation for the ρ in the EMB changes (F_{se} where the "se" means species)– but this scaling changes parameter sets (which are irrelevant in single metals).

[14] some orbitals are a particular good match to EAM, like the d-band or especially the s-orbital, which has no angular dependence

So, interestingly, the parameters are changed, but apparently with the same physics. In principle any number of transformed potentials can be generated, all of them with different parameters but with the same properties and thus the same physics. All the different parameters of these potentials of such a group are defined as a parameter set, each set belongs to one transformed potential in the same group.

This phenomenon is the *Achilles' heel*, weak spot, of the EAM formalism and requires a rigorous control and a more thorough interpretation.

Claiming all these sets have the same physics, though, is a *double-edged sword*, because the resulting energies are indeed the same but not necessarily the resulting derivatives of the potential function[15], this helps to distinguish parameter sets and handle them by different fitting techniques which are closely linked to the different interpretations of EAM. A first overview of the various interpretations:

- In the glue potentials (interpretation) the electron density function is interpreted as a function to match or glue the pair and EMB part. This provides, beside the degrees of freedom (DOF) for the fitting of the pair and EMB part, one gauge DOF by the additional electron density function (for a monoatomic system). Preferentially, in this interpretation the force matching method by Ercolessi and Adams [53] is applied: the potential is fitted to the forces, therefore also the derivative of the energy is considered[16]. On top of that for each gauge degree of freedom an additional fitting target property is included to fix this gauge DOF (and this depends on the system, in quasicrystals stresses caused by atomic forces are chosen or in bcc materials with open electron shells the change in the atomic configuration with pressure was taken as an additional constraint, both represents successful approaches (by Fellinger [40]&Brommer [101]).
- In the pure EAM method several analytical constraints are applied directly to the parameters (and less focus is put on parameter sets), the first convenient and transparent (thus very popular application) constraint applications in EAM were described by Johnson and Oh [55]. These results resemble UBER and the Rose eq. though not directly fitted to it.
- In FS such constraints can be also used, but the difference here is a characteristic $\sqrt{\rho}$ dependence of the energetic contribution by the EMB part, which changes the explicit analytical expressions a bit. This approach originates form the tight binding approach (instead of DFT) - where $\rho(r_{ik})$ is defined as 'the square of the tight-binding hopping integral between [atom] j and i.' [39, 49]. Here, particularly phonon dispersion spectra are a common fitting target, as described by Mishin and Farkas [26], and which lead to many successful potentials, for instance to one, which stands out, the Al-Ti alloy pot. by Mishin [111], which handles very well the parameter sets by considering phonon spectra (in Y-Y, though, parameter space is more complex).

In the last two approaches, FS and EAM method, so called Universal Binding Energy relations can be applied to avoid fitting of the EMB and instead to analytically determine the parameters of the embedding function with the help of the Rose eq.. Interestingly, it has to be noted that some analytical restraints have a very similar effect as the Rose eq., this will be described in detail in chapter 3 and in particular in section 3.2. All these subgroups belong to the bigger group of pair functionals. The choice of the subgroup, does not just influence the fitting technique, but also the explicit analytic expression for parametrisation (the here used form will be explained in 3.1) – but this section here underlines, the formalism has to allow a combination of the fitting technique with a rigorous control of parameter sets (see chapter 3&4).

[15] In general the function must be stable, and the potential energy has to be of a form that can be differentiated to get the forces (i.e. there must be no singularities). To name two examples of the additional requirements: the 2nd derivative has always to be positive, this rules out some parameter sets (see 3.2.2) or the first derivative of the EMB function has to be zero for transferibality (see 3.2.4).

[16] The forces are computed twice in the glue approach, once for the pair part, then the electron densities and then the EMB contribution (per atom pair i wrt. j) by $Force_{i_{EMB}} = -\sum_{i \neq j}\left[F_i'(n_i)\rho_j'(r_{ij}) + F_j'(n_i)\rho_i'(r_{ij})\right]\frac{(x_i - x_j)}{r_{ij}}$

2.2.3 Fitting alloys – *a bottleneck for EAM*

The simplification by a linear superposition of spherically symmetric electron density averages in EAM causes the challenge of parameter sets on the one hand, but on the other hand it provides an additional powerful advantage. By extending the previous presentation (2.2.1 & 2.2.2) of applied super position in monoatomic systems to systems with different species (alloy fitting) significantly can be simplified, *in principle* (the "superposition argument" also applies to MEAM but without spherical symmetry).
This can be better understood, when considering, how many potential functions, consisting of electron density, pair- and EMB function, are needed in alloys. In a diatomic system (A and B) for instance each function describes the interaction between a specific set of two species. So namely, for A-A, B-B and the mixture A-B. Thus, clearly for the A-A and B-B interactions, all three functions (pair, elec-dens, EMB) are needed. This is like two separate potentials, one for A-A and one for B-B, each with three functions. For the mixture in addition to these functions, one pair potential is needed to describe the interaction between the mixed components A-B [52, 54]. But, conveniently for the electron densities and embedding energies no additional separate functions are needed. Practically, the EMB energy contribution is determined by an independent superposition of the EMB contributions of species A and B – this is a significant advantage of this (EAM) method and makes the mixing of two potentials to obtain an alloy potential easier. In theory, if two elemental EAM potentials already exist, just one more (pair) potential is needed to describe the resulting two component alloy [52]. Applying this to the alloy of interest in this work, Fe-Y, only 7 functions are needed (and not 9 functions), namely: three pair pot. for Fe-Fe, Y-Y and Fe-Y, two separate embedding function and two electron density functions for Fe and Y (4 functions). The Fe-Y interaction pot. is described by an additional pair potential, resulting in the following functions:

$$U_{Tot}^{Fe-Y} \rightarrow \Phi_{Fe-Fe};\ \Phi_{Y-Y};\ \Phi_{Fe-Y};\ F_{Fe};\ F_Y;\ \rho_{Fe},;\rho_Y \ \rightarrow 7x \text{ functions} \quad (2.8)$$

Now, it seems like two single metal potentials can simply be mixed with just one additional pair potential for a new alloy pot.. But, in fact such *wild* mixing fails most of the time, because only a fraction of the possible parameter sets are suitable in alloy potentials. The fitness of the corresponding para-sets depends on the composition of an alloy potential. So, a potential set for species A, which works well in an alloy potential A-B, is not necessarily a good candidate for another component C. What has been previously an enormous simplification, superposition based on spherical symmetry, turns out to be a quite problematic *additional challenge* in alloy fitting, because parameter sets have to be matched for the alloys (pots.) [54].
In order to fully understand this, the previous "atomic view" of page 14, is applied again as a helpful illustration: in monoatomic systems, in principle any random parameter set can be chosen[17] (allowed due to the spherical symmetry of EAM, electrons assumed to be symmetrically distributed). In intermetallics this assumption is no longer self-evident – in some alloys it can be made but in many it is not possible.[18] This is simply due to the fact, that the components of the alloy represent different charges and these charges can cause drastic breaks of the symmetries in the electron distribution. In practise, alloys which could be simplified as dilute solution are potential promising candidates for such a simplification and alloy fitting in EAM (such as Fe-Ni). Complex intermetallics, such as Fe-Y, possess a weighty number of covalent bonds which are dominated by bonding angles. Now, this shapes the electron distribution to be non-spherical symmetric. Consequently, any random spherical symmetric electron distribution, represent by the numerous parameter sets, cannot accurately represent this situation any more. One relatively simple "hotfix" for this problem is, to control (at least partially) the parameter sets by a scaling factor, f_e, and enforce a match in parameter sets. ZW were quite successful with this technique [96]. Similar other techniques exist [112]. Their common denominator is the underlying assumption, that the amount of covalent bonding character has to be rather small. Since that is not the case in Fe-Y, these do not work and EAM is rather limited (but still useful, e.g. as a first step, see end of 2.2,4 &chapter intro 3).

[17] As long as additional checks ensure the previously mentioned conditions (2.2.2) – even after such checks many para-sets fulfil these.

[18] On top of that additional degeneracies occur, illustratively described in the glue interpretation as additional gauge DOF [101].

2.2.4 MEAM – a better solution for complex alloy fitting?

The problem of the combination of parameter sets and a dysfunctional assumption of spherical symmetry in alloys with a significant covalent bonding character lead to the extension of EAM to the Modified EAM (MEAM), which is simply speaking just an extension of EAM by the inclusion of angles in the calculations of the electron density in the formalism (while keeping the functional for the EMB part). Introducing an embedding part as a functional is an upgrade to the pair functional group (→ Fig. 2.1). Extending the considered atomic pairs by including additional three body interactions as triplets (and thus including angles & directions) leads to cluster functionals (where clusters denote a three body character).

This extension leads to a drastically higher complexity in the formalism, especially with regards to the fitting process (as seen in the second half of this section, 2.2.4), but the expectation in alloy fitting is a significant reduction of parameter sets to the extent of lifting the parameter set degeneracies.[19]

In order to impose the triplet description, the electron density is split into a sum of electron density contributions from the individual orbitals, distinguished by an angular momentum index 'l' and each of these is, mathematically, a function of tensor invariants (depending on the direction, expressed as distance and angle of an triplet *ijk*). In order to set this sum up, a simplified version at equilibrium is considered:

$$at\ eq.:\ (\rho_i)^2 = \sum_{l=0}^{3} \left(\rho_i^{(l)}\right)^2 = \left(\rho_i^{(1)}\right)^2 + \left(\rho_i^{(2)}\right)^2 + \left(\rho_i^{(3)}\right)^2 + \left(\rho_i^{(0)}\right)^2 \quad (2.9)$$

The sum in eq. (2.9) with *l* ranging from 0 to 3 resembles the contributions of the orbitals s, p, d and f to the electron density [52] – this was only a rather symbolic interpretation for the first establishment of MEAM by Mehl [113]. Whereas $\rho_i^{(0)}$ can be interpreted as the standard EAM contribution (mainly by s-orbitals). However, the missing exact connection of all these terms as a unity to electron orbitals in actual metals is underlined by the correspondingly developed expression for the partial electron densities, $\rho_i^{(l)}$:

$$(\rho_i^{(l)})^2 = \sum_{j,k(\neq i)}^{N} S_{ij} S_{ik} f^{(l)}(r_{ij}) f^{l}(r_{ik}) P^{l}\left(\cos\theta_{ijk}\right) \qquad with \sum_{j,k(\neq i)}^{N} \equiv \sum_{j\neq i}^{N} \sum_{k\neq i}^{N} \quad (2.10)$$

The $f^{(l)}(r_{ij})$ is the classical electron density function as seen in EAM, which is extended by the additional Legendre polynomial function[20] with $\cos\theta_{ijk}$ as an argument and the screening functions S_{ij} & S_{ik}. Before getting into the details, the principal idea is laid out: the angular dependant Legendre polynomial is supposed to impose the non-spherical electron distribution caused by the bonding angles. But, it can be immediately seen that these are not in one-to-one relation to the orbitals. These expressions were matched to the data and first principle data. Since this again, is only an averaged, but this time more detailed as overlapping clusters, representation of the actual electron density, a many body screening is necessary, controlled by the screening functions S_{ij} & S_{ik}, [78, 95]. In other words, the individual contributions do not perfectly add up and partially, in simple words, overlap. And in order to avoid the "double counting" screening has to be included. This point is closely connected to the fitting and is one of various reasons leading to a specific implementation of the Reference Free MEAM method [99], which abolishes the screening factors, see section 4.1.1 (beside the need to replace the Rose eq., see below in this section). This rather non-intuitive summing up requires for better fitting an summation procedure which is additionally controlled by tuneable partial electron density weighting parameters $t_i^{(1)}, t_i^{(2)}, t_i^{(3)}$:

$$\rho_i = \frac{2\rho_i^{(0)}}{1 + e^{-\sum_{l=1}^{l=3} t^{(l)} (\rho_i^{(l)}/\rho_i^{(0)})^2}} \quad (2.11)$$

[19] In the original development it was even not an alloy, but a monoatomic system, Si (with known covalent character), which necessistated the development of MEAM (first MEAM paper by Baskes [80]) and also lead to RF-MEAM by Thijsse [94]

[20] Legendre polynomials are taken for granted, but an expanded expression for $(\rho_i^{(l)})^2$ can be found for instance on p. 278 in [22]

And with the final ρ_i of this expression in eq. (2.11), covering all orbitals from *l*=0-3, an *ordinary* electron density is obtained which can be used in MEAM in the same manner as in EAM to compute the EMB energy and then the total energy. This more detailed computation of the electron density in clusters slows down the computational performance of MEAM in comparison to EAM up to a factor of 6 [22, 52] – this in-depth description comes at a certain cost.

Unfortunately, there is another cost in the form of complications during fitting, causing fitting problems in MEAM (introduced in the previous literature review 1.2). Here, the reason why seemingly only the Rose eq. is available for support in the fitting procedure of standard MEAM will be highlighted:
As said before, MEAM is much more complicated, but resuming the previous discussion in chapter 2.2.2 about the essential necessity of fitting constraints provides a more precise picture: fitting constraints, which have many possible forms as said before, such as fixing the parameters to physical quantities, analytical conditions or force matching, are always necessary to control the fitting process by limiting parameter space and parameter sets. But in the kind of non-transparent formalism of MEAM it is rather impossible to apply these helpful constraints, as expanded in detail in the following.
A simple reasoning in the spirit of glue potentials is that no explicit analytical parametrising form (function) for both the pair and EMB part is able to fulfill the above mentioned formalism of MEAM (*with screening factors*). Only the partial electron densities can be parametrised and fitted but not at the same time with the pair functions (cannot be fitted but only fixed). From another perspective this has to do with the screening functions[21] but a more illustrative explanation is found with the help of para-sets:
Simply speaking the introduction of the angles limits parameter sets but at the same, since these angular-dependant triplet characterisations are also an (simplifying, but less as in EAM) average, parameter sets are possible due to different angles leading to the same results. Scaling the electron density by a parameter α and scaling simultaneously the angular dependant Legendre polynomial by parameter β leads to a MEAM potential with the same properties but a different parameter sets, namely, this is done by:

$$\rho\ \ (r_{ij}) \rightarrow \alpha\ \rho\ \ (r_{ij}) \qquad ;\quad f_{elec-dens}(r_{ij}) \rightarrow {f_{elec-dens}(r_{ij})}\Big/{\beta}$$

$$g(\cos\theta_{ijk}) \rightarrow \alpha\beta^2\ g(\cos\theta_{ijk}) \ ;\ \ F\ \ (\rho_i) \rightarrow\ F\ \ (\rho_i/\alpha) \qquad (2.12)\ \ with\ g = S_{ij}S_{ik}P^l(\cos\theta_{ijk})$$

In contrast to EAM, the degeneracy (in a monoatomic system) is not anymore controlled simply by one but by two parameters, α and β. And both parameters apply to one part (EMB) but not both (in EAM to scaling parameters applied to both parts). The degeneracy in eq. 2.5 and 2.6 is no longer valid in MEAM, with drastic consequences, this can be even called another (much more complicated) level of degeneracy. While in EAM a certain parameter set uniquely defines EMB and pair part, this is not anymore the case in MEAM – here one parameter set, controlled by either α or β, is intrinsically degenerate, too.
Summarising, the inclusion of angles reduced types of degeneracies (in eq. 2.5 and 2.6), as anticipated and expected, but it failed eliminating *all* degeneracies, it has left at least one double-folded degeneracy ruling out the existence of a general function to simultaneously fit both parts. The momentous consequence of this is that the very helpful and even essential constraining mechanisms of section 2.2 are no longer effective. Without general analytical parameterisations of both parts at the same time constraints cannot be enforced – for instance enforcing a bulk modulus as done in chapter 3 for EAM, applies to both parts and both functions need to belong to a definite parameter set for a definite selection. Even force matching is not possible anymore (since the pair pot. function cannot be manipulated to a definite inferable form for the necessary derivatives– no analytical force calculation during fitting) [22]
As explained in general in the literature review different simplifying techniques have been developed to perform the necessary limitation onto the fitting complicating influence of this double-folded degeneracy.

[21] which are abolished in RF-MEAM → lifting the double degeneneracy in eq. 2.13→ enabling a full parameterisation for both parts
[22] Though, one could try to transform an RF-MEAM potential for this – but no GA fitting techs. in POTFIT, therefore it is not done.

The simplest idea is to reduce complexity by the inclusion of angles by reformulating and limiting the Legendre polynomial part (leading to EMD techniques by Pasianot [114] and the Lenosky fitting scheme [115], which is used in POTFIT and alloy applications [113]). This, however, kind of "goes too far".

The most commonly used, somehow more accurate, technique is to fix the pair potential by exactly matching it to the universal binding energy relation (UBER) with the help of the corresponding Rose eq. [94]. The pair part is one-to-one expressed by the Rose eq., which has certain physical quantities as input parameters. This technique is popular in the MEAM potential developer community, since it critically simplifies the fitting[23]. So, the physical properties are enforced by rather approximate empirical relations (UBER) instead of exact analytical constraints (since they cannot be applied). As a direct consequence of this approximate character, the input parameters which represent certain physical quantities (such as *B*) are not exactly reproduced by the resulting MEAM potentials. Instead the used parameters have interdependent, even highly complex entangled parameter influences on the resulting physical quantities, as shown in a detailed paper by Lee [88] and Moore [82]: only principal contributions of parameters to physical quantities can be identified but not direct influences, which can be analytically described.[24]
On top of it, apart from the general inaccuracies as shown in chapter 3 specifically in section 3.3.6 this rigid application of the Rose equation is far too inflexible (no general fitting possible), especially for alloys (with covalent bonding, for which MEAM was designed for) such as Fe-Y, as it will be shown in the next chapter (3.3.5), which then leads to RF-MEAM techniques overcoming this issue.[25]

All in all, as said before MEAM is simply too complicated for fitting, the patterns to control the parameter space are hardly recognisable by human intuition. One out of many reasons was given here, which lies in the double-folded degeneracy caused by the rather ill-suited and illusive split up of the partial electron densities into these illustrative but incorrect orbitals (eq. 2.9, standard MEAM is based in that, ABOP follows a more rigorous path). All of this causes a non-transparent and difficult to handle formalism (the classical non-RF-MEAM one is meant), which leaves to little room for improvements in the fit. Therefore helpful (fitting) constraints and techniques are developed in EAM for a solid starting point in the application in the more flexible RF-MEAM formalism (which is more challenging for the optimisations techniques though, as introduced in the literature review).

2.2.4 Concluding comparison of potential classes

In the previous sections the implications of the different potential classes with the relevant formalism groups were described wrt. to single atomic interactions as the origin of the bulk properties. This view is dominated by the application to monoatomic systems. However, when considering alloys, this view should be extended to the general description of configurations. A configuration is a specific set up of atoms with a definite energy. Especially in alloys different configurations of the two species are possible with different energies – figuratively speaking the different energies could be easily linked to temperature. So the different configurations with different energies cover the spectrum of all the possible structures at different temperatures – that is exactly what a MD potential should cover. This general view easily gets overviewed when one has to focus on the accurate description of atomic interactions.
Exactly with such a more general view the different potential classes are in principle compared in Fig. 2.2, which is brilliantly shown schematically in the comprehensive textbook by Tadmor [22]. The comparison focuses on the question, how good the various energies of the different configurations can be reproduced in principal by the previously presented potential classes (pair pots., pair - (EAM) & cluster functionals (MEAM)). The following points in conjunction with this schematic illustration can be made:

[23] By simplified it is meant, that basic simplex techniques with some physical intuition, which are more or less LSM like techniques (explained in see 3.1.4), are sufficient for the fitting and leads to convincing potentials – simply by local optimisations (see 2.5)
[24] B.J. Lee can be called the father of the best available MEAM potentials– so, this *verdict*, there are no definite links, is terminal.
[25] The transformation to RF-MEAM is rather a result. Therefore, it will be presented in the Results part in Chapter 4.

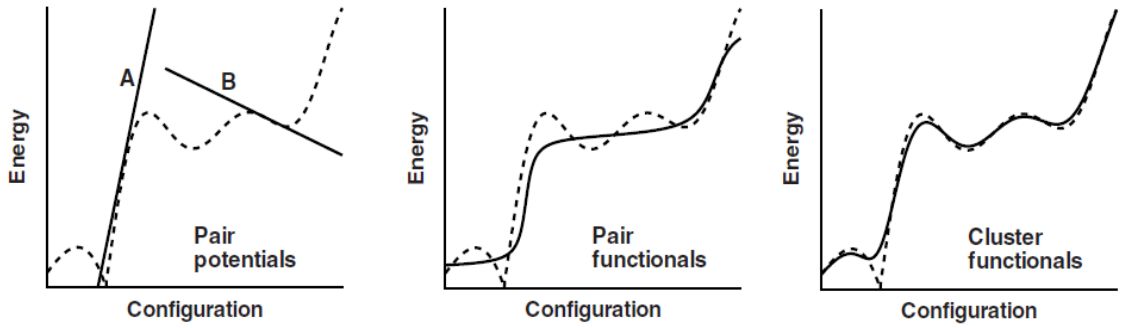

Fig. 2.2 Illustration of the principal differences in accuracy as a map of the different energies vs. the possible atomic configs. (dotted actual energies, line refers to the pot.) btw. the different potential classes: EAM is a pair functional & (RF-) MEAM a cluster functional, taken with permission from p. 282 of textbook by Tadmor "Modelling Materials" [22]

- As seen on the LHS, the simple pair potentials contain only two linear representations of the energies, A and B, which correspond to the repulsive and attractive term in the pair potential. This behaviour stems from the fact, that a pair potential assumes sole linear dependence of the atomic distance on the resulting energy, just as said before as a core to core interaction. But here the reality of electronic interactions altering the energies is well shown (see dashed line). The influence of these electronic interactions is in reality not linear and causes significant deviations.
- EAM in the middle as a pair functional includes these in addition to the pair potentials *A* and *B* on the LHS in Fig 2.2. However, the curves/lines *A* and *B* are much less step in EAM. The interplay of EMB part (which is not a straight line) and these pair pot. lines forms this slowly increasing plateau. This plateau is caused by the assumed centrosymmetric electron density distribution in EAM, as described in 2.24 in detail. In real alloys, there are small wiggles. But apart from these EAM already describes the energies pretty well. However, it can be easily imagined that many similar curves are a good match, which gives a rough simplified idea about the high number of possible parameter sets in EAM.
- These wiggles are represented MEAM and reduce the degeneracy because the potential becomes more distinct. The wiggles are caused by angular dependant symmetries of the electron orbitals, which differ from configuration to configuration. These cause only minor energy differences. EAM ignores these and MEAM includes these.
- Even in MEAM little deviations to reality exist – this is because the triplet clusters are also a simplification (and magnetic dependencies are mostly missing too[26]). For an exact match DFT, as shown next in 2.3, considering all interactions is required.

This is an overviewing summary of the previous discussion about MD potential classes and provides all principal knowledge about the pot. models. Besides, this overview enables two short *fetch-ahead*:

1. knowing that in pure iron these wiggles are not very distinct and only minor, provides an explanation why good results can be also yielded in pure EAM (as mentioned in the literature review). This also leads to a kind of "hybrid" set up of the final Fe-Y potential in chapter 4&5. The Y-Y and Fe-Y potentials are in the RF-MEAM form but the Fe-Fe is in "plain" EAM. This is also due to practical reasons and will be explained in detail 4.2.2.
2. Hypothetically, one could also split up a (RF-)MEAM potential into a non-angular part (representing the plateau without the wiggles) and an angular part to reproduce these wiggles. This idea will be picked up again in the discussion in chapter 5 and helps for the precise reproduction of EXAFS spectra.

[26] including magnetism could potentially lead to higher deviations. E.g. in bcc Fe some defect properties are essentially formed by these magnetic influences as shown in [116], lead to some pot. development with magnetism (Dudarev [117] , Ackland [118])

2.3 Brief description of DFT and AIMD

2.3.1 Limits of MEAM, Schrödinger eq. and why it is "incomputable"

The description by grouping the interactions into triplets as in MEAM is, as discussed in 2.2.4, a very accurate representation. However, not all atoms can be entirely included. Outside the triplets there are always few atoms, which are not completely covered by the electron density and the screening functions in MEAM – fortunately, this minor inaccuracy by the triplet assumption in MEAM is rather small. Thus, the exact description can only be yielded by the (less intuitive, thus presented after (M)EAM) density functional theory (DFT or called ab-initio, implying from the "start" (=fundamental atomic interactions)), which basically is a way to replace the Schrödinger eq. in a computable manner to material systems.
Any system can be exactly described by the following Schrödinger eq. (eq. (2.13)), which depends on R (atomic (ionic) distances), r (electron distances) and t (time):

$$i\frac{h}{2\pi}\frac{d}{dt}|\Psi(r,R,t)\rangle = \widehat{H}|\Psi(r,R,t)\rangle \quad (2.13)$$

This formula has been found in 1925 by Schrödinger [119], and is principally a Hamiltonian "$\widehat{H}$" acting on the wave equation, describing the quantum system, yielding the evolution in time of the system with respect to the energy – which is the same as the derivative wrt. time of the wave equation. This eq. can be also understood as a condition, which must be fulfilled, for the exact and correct wave equation, which includes and describes all details of the atomic system. As a direct consequence this exact description has to take into account all electrons interacting with each other [41] and it is obvious, that the number of necessary variables is enormous – all distances between all atoms and the higher number of electrons need to be described leading to exponential complexity. Concretely, for a system with N particles with the three necessary variables "r, R, t" (variable triplets) with p values per dimension p^{3N} values need to be calculated [120]. A typical number for "p", for instance, would be 1600 for a system with 100 atoms with 15 considered electrons (considering 2 orbitals), with N=1600 (1500 electrons, 100 atoms), the number of values to compute easily reaches the 10^{1000} threshold. And this is only for 100 atoms with few considered electrons – clearly this exponentially increasing complexity quickly rules all accessible computing capacities out [121]. This simple example sufficiently illustrates, why the pure one-to-one application of the Schrödinger eq. is practically impossible. It took 40 years until 1965 to develop the Kohn-Sham theory (KS) leading to DFT [48][27] to handle this complexity and make it computable.

2.3.2 Overcoming barriers by DFT and KS Theory

Simply speaking, the central theme of KS theory are two theorems. The first one drastically simplifies the problem by reducing the number of variables by summarising the electronic interactions as a functional dependant on an electron density shaped by their configuration. So, instead of looking at the individual configuration of electrons, just their effect, described by an electron density, is considered [48, 108].[28]
This idea is implemented by the first of the two theorems by KS, which results in:

1. The central Hamiltonian operator in eq. (2.13) can be expressed in a way, so that it is only directly dependant on the electron density as a functional in a similar manner as previously presented in 2.2 (which replaces all the r variables for the electrons) – in order to enable this form the definition of a flexible so called external potential is necessary, which is specifically

[27] Before that Fermi and Hartree Fock [122] also developed some schemes with few results [120] , but these were approximations.
[28] It also served as the inspiration for functionals in EAM, only hypothetically and not exactly calculating the elec-dens as in DFT.

formulated in a manner which makes it dependant on the electron density, too. Unlike in EAM, this manipulation is not an approximation as before, but an exact and unique method to express the energy wrt. electron density, as shown by Kohn Sham in 1965 [48], who used a proof by contradiction, which is nicely illustrated in many textbooks, for instance in [41].

2. The second theorem leads to the variational principle, which more or less states that every external potential yields a ground state (electron) density, ρ_{GS}, which is inherently linked to the ground state (GS) energy – effectively the energy functional $E(\rho)$ always yields the GS energy, if the ground state density is known [120] leading to the reformulation of the GS energy as:

$$E_{GS} = \min_{\rho \to \rho_{GS}} \left[F(\rho) + \int \rho(\vec{r}) V d\vec{r} \right] \quad (2.14)$$

Now, as before, this functional needs to be determined. In 1965 KS accomplished it with some *ingenious tricks* [48]. The first step is to split the Functional "F" in eq. 2.14 into three terms: kinetic energy T, Coloumb interaction $J_{e,e}$ (between the electrons inspired by Hartree-Fock) and the exchange-correlation functional (XCF). Only the Coloumb interaction is actually known. In order to describe the kinetic energy of the electrons in a computable manner (see 2.3.1) effective potentials are established [124], which are describing a non-interacting reference system of fermions, which can be elegantly described by Slater determinants [122]. But the consequence of this is that this kinetic energy is no more exact but only approximate (=T_S and T is the exact one). This inaccuracy is compensated by the following XCF:

$$E_{XC}(\rho) \equiv \big(T(\rho) - T_S(\rho)\big) + \big(V_{ee}(\rho) - J_{ee}(\rho)\big) \quad (2.15)$$

Where the first difference describes the deviation in kinetic energy and the second describes the mutual self-interaction and correlation energy contribution btw. the electrons (since effective potentials are based on non-interacting fermions (s.a.) ignoring this effect). The *trick* in the KS functionals is to put these deviations of the previous convenient analytic expressions into a separate functional, which is dealt with later. This allows the expression of the functional by an approximate kinetic energy, exact columbic interaction and XCF as:

$$F(\rho) = T_S(\rho) + J_{ee}(\rho) + E_{XC}(\rho)$$

$$with \quad T(\rho) = \langle \Psi_i | \nabla^2 | \Psi_i \rangle \;\; \& \;\; J_{ee}(\rho) = \frac{1}{2} \iint \frac{\rho(\overrightarrow{r_i}) \rho(\overrightarrow{r_j})}{r_{ij}} \, d\vec{r_i} d\vec{r_j} \quad (2.16)$$

Using the reformulated *F* (eq. 2.16) with the help of the XCF (eq. 2.15) and inserting it into (eq. 2.14) and applying this to the Schrödinger eq. in eq. (2.13) leads to the more explicit expression for the energy:

$$\left(-\frac{1}{2}\nabla^2 + \left(\int \frac{\rho(\overrightarrow{r_j})}{r_{ij}} \, d\vec{r_j} + V_{XC}(\vec{r_i}) - \sum_A^M \frac{Z_A}{r_{iA}} \right) \right) \phi_i = \varepsilon_i \varphi_i \quad (2.17)$$

The solution of this eigenvalue (energy)/eigenvector(wave function) using different methods is the central idea of practical DFT calculations in actual DFT codes, one of the most prominent and used codes is VASP [124]. Mentioning few of the relevant methods and approximations: the PAW (Projector-Augmented-Wave method) [125] was applied in all calculations for stability of the pseudo-potentials. For the XCF numerous methods were developed, the most basic one is the local density approximation (LDA). The Generalized Gradient Approximation (GGA) [126] serves as a reasonable compromise between accuracy and performance. However, for more accuracy in most of the used DFT fitting reference the PBE XCF with GGA by Perdew & Burke [127] was used, though it is slower. Another *trick* to enhance performance is the common technique to only consider the most relevant electrons, the idea of

effective potentials allows this significant performance boost. Interestingly, though XCFs are used, the KS approach for itself is exact, no approximations are in the underlying theorems and descriptions. However, when the XCF is implemented in a computable form, then some compromises have to be taken. Up to now numerous research is done to find better approximations [120]. Nevertheless, the accomplished XCF functional methods, such as PBE, turn out to be very exact in many applications. The more relevant issue is high computational effort for DFT calculations, limiting DFT to few hundreds of atoms, as said before.

In addition to this outline about the general idea of DFT, the computational effort is highlighted by the following schematic steps – these are actual operations, performed to obtain DFT fitting references [124]:

1. The modelled system, consisting of N particles, is redefined as a non-interacting reference system with orthogonalised wave functions, which form a single Slater determinant yielding exactly the same elec-dens as the real (interacting) system (but not the energy, this follows).
2. For each single electron the kinetic energy can be determined by a one-electron KS operator, this allows the determination of T_S (in eq. 2.16), by this the corresponding electron density is determined, which is then used to define the boundaries for the external potential in the one electron KS operator scheme to resembles the real (electron) density.
3. Having obtained the density and the approximate kinetic energy, the exact Coloumb correlation term is determined and the energy due to the nuclei are considered, and now the energies are split up according to the previous outline – and this allows to identify the remaining XCF.
4. Now as the components of the KS functional are identified, eq. (2.17), these will be subjected to the variational principle, which is linked to the 2nd KS theorem, and an effective potential is yielded, which exactly matches to the KS functionals and reproduces the correct atomic orbitals.
5. These explicit forms of step 4 and boundaries of step 2 allow the exact quantitative knowledge about the single electron external potential (and thereby the form is fixed), with these the non-interacting reference system is defined as KS orbitals – these KS orbitals help to find quantitative values of XCF by a chosen approximation scheme, such as (GGA)-PBE.
6. Having determined the XCF, ρ_{GS} is determined and then used to determine the GS energy.

This in a short context is a DFT calculation – looking at the actual operations, one new issue becomes apparent. The final results are always the ground states – in practice this corresponds to T=0. So, thermal vibrations and their effects are excluded. Standard thermal vibrations in a lattice are not included by this pure DFT technique – an extension is needed.

2.3.3 Ab-initio Molecular dynamics (AIMD)

The main idea of AIMD is to model the acting forces by performing electronic structure calculations in DFT *on the fly* and to update the exact force-field with every step [41] instead of using fixed potentials as in EAM. A suitable first step is considering the Hamilton-Jacobi eq. describing CM on a GS surface[121]:

$$\dot{P}_i = -\nabla_i E_{GS}(R) \quad with \quad \dot{R}_i = \frac{P_i}{M_i}$$

$$and \quad E_{GS}(R) = \varepsilon_0(R) + V_{NN}(R) \qquad with \quad \nabla_i \varepsilon_0(R) = \langle \varphi_0(R) | \nabla_i H_{elec}(R) | \varphi_0(R) \rangle \qquad (2.18)$$

So, the top of eq. (2.18) is the modified EOM in the framework of DFT, a force by the gradient of the energy (where ε_0 labels the GS energy eigenvalue, and the capital *R's* are vectors (the arrows are left out)), which contains the electronic influence and V_{NN} the potential for the nucleus-nucleus interactions. This provides exact forces by a constantly updated pot. in contrast to EAM, as graphically summarised below:

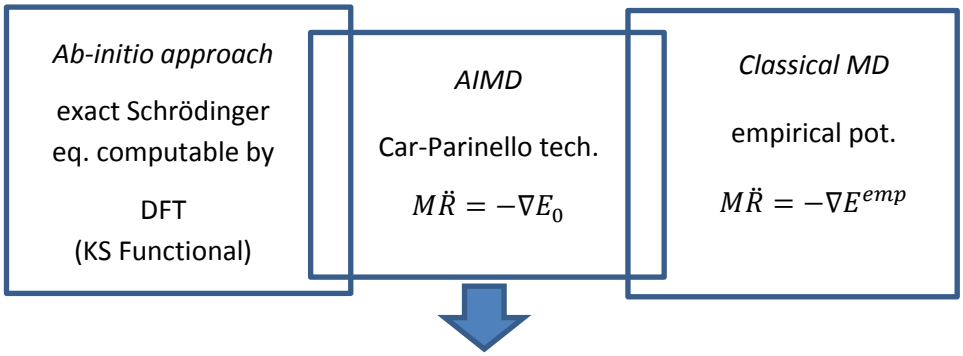

Fig. 2.3 diagram illustrating the differences in the underlying ideas of MD and AIMD and similarities

Now, with this approach in theory a minimisation to determine the solution to eq. (2.18) should be carried out for each MD step and at each nuclear configuration – a time intensive approach, especially when the convergence criteria in DFT are strict. Fortunately, already in 1985 Car and Parinello [128] had an idea of similar impact as the KS theorems: they simply decoupled the nuclear time evolution and electronic minimisation by an implicit adiabatic dynamics approach (not to be confused with BO). This decoupling is performed by introducing a separate fictitious dynamics for the electronic interactions only (orbitals respectively) as given in eq. (2.19) below. By using the suitable adiabatic assumption at the determined minimum of the initial nuclear configuration, the fictitious temperature of the electrons is computed by:

$$K_{hypo} = \mu \sum_i \langle \dot{\psi}_i | \dot{\psi}_i \rangle \quad (2.19)$$

where $\dot{\psi}_i$ labels the orbital velocities of the electrons and the result is a fictitious kinetic energy of the electrons (which should not be mixed up with the actual *true* QM kinetic energy *T*, therefore, the index "hypo" (=hypothetical) μ, in the units of energy x time^2 , acts as a decoupling parameter in the form of a hypothetical mass. In order to include the nuclear minimisation, this expression (eq. 2.19) is incorporated into a practical form of Lagrangian dynamics, uniting electronic and ionic dynamics, as

$$\mathcal{L} = \mu \sum_i \langle \dot{\psi}_i | \dot{\psi}_i \rangle + \frac{1}{2} \sum_{I=1}^{N} M_I \dot{R}_I^{\,2} - E[\{\psi\}, R] + \sum_{i,j} \left[\Lambda_{ij} \left(\langle \psi_i | \psi_j \rangle - \delta_{ij} \right) \right] \quad (2.20)$$

As said before this term includes the ionic interactions by the term in the middle (*E*). The whole scheme in eq. (2.20) is enforced to be computable by the Lagrangian matrix Λ_{ij} ensuring orthogonality by $\langle \psi_i | \psi_j \rangle = \delta_{ij}$. All of this unites the adiabatic fictitious electron and true ion dynamics. Employing the known Euler-Lagrange eq. (Lagrangian dynamics) yields the coupled EOM, known as CP eq.:

$$ions\ (I): \quad \mathrm{M}_I \ddot{R}_I = -\nabla_I E[\{\psi\}, R] \qquad electrons: \ \mu\, \ddot{\psi}_\iota(\vec{r}) = -E[\{\psi\}, R] + \frac{\delta}{\delta \psi_i^*(\vec{r})} \sum_j \Lambda_{ij}\, \psi_j(\vec{r}) \quad (2.21)$$

This quite complete EOM scheme by considering electrons and nuclei in eq. (2.21) would be ideal for the performed final AIMD calculations in chapter 5 but it is too slow and instead the faster adiabatic Born Oppenheimer (BO) approximation excluding the electron dynamics from the EOM (eq. 2.18) is used.

Summarising, in this theory section the computable MD technique with its effective potentials and the exact, but resource intensive, DFT have been introduced.

This AIMD approach as a kind of fusion of both (MD & DFT) has to be viewed with some "*healthy skepticism*": obviously AIMD is even more resource intensive than DFT – only up to 100 atoms and a few ps can be modelled. So, MD is still needed as a *bridge* (for instance for the concluding EXAFS calcs. in chapter 5, *pure* AIMD contains too few atoms).

3 Development of Fitting Strategies for basic properties & results

By utilising the previous theory, it can be immediately seen, that the development of a suitable MD Fe-Y interaction potential is an active interplay of guessing and fitting and then the cycle of checking and improving (as presented in general in 1.3, details see 3.1, 3.3 and its appendix). This guessing has to be "smart"– the first models should not be too far from the fitting targets, the global minimum. Otherwise a local minimum could mistakenly be seen as a global minimum [26]. This is ensured by the correct analytic formalism for MD potentials and a sensible (=justified) choice of initial parameters and by the appropriate application of the fitting techniques as presented here. In particular, the fitting technique should ensure enough degrees of freedom (DOF) but also avoid overfitting. This can be also expressed as: *The fitting program does not know whether an optimised potential is physically unrealistic - by boundary conditions and fitting targets (atomic references/configurations and physical properties) potentials have to be enforced to be physically sensible.*

The choice of the correct fitting method and technique, including knowledge of the obstacles within established methods, is necessary as illustrated in this chapter. A profound example of not paying enough attention to such systematic inherent obstacles of fitting models is one of the first tries to model ODS, the readily presented Ti-Y-O potential by Hammond [23]: polynomials seem to be chosen a bit too arbitrarily and the physical reasoning appears non-transparent and the whole complex Ti-Y-O system was fitted with too few degrees of freedom. The resulting potential seems to have the smallest mean square deviation – a seemingly good fit in the sense of section 1.3. But own preliminary tests suggested that it cannot confirm many of the crucial phenomena of interest, for example the typical migration of Y atoms within defect clusters [3][25]. It can be said beforehand, that as a first step stepping down to the embedded atom method, EAM (from the modified EAM (MEAM)) *before using MEAM* is suitable, because fitting techniques, which are then also used for MEAM, can be better investigated and established more reliably.

In this chapter, by the EAM approach a reliable fitting technique for the basic materials properties (obtained at the equilibrium distances of the potential), such as crystal structure and elastic properties, is established. Initially, MEAM seems to be a better starting point, because it can fit more than just these *basic properties*. But, MEAM seems not useful for systematic "problem spotting" in the used fitting technique, because of the somewhat harder to follow formalism with regard to physical origins. Contrary, in EAM the parameters in this framework can be linked on a one-to-one basis to its physical counterparts in a universal manner as presented here. This has the following three advantages. Firstly, these findings, linking the potential parameters to properties, will be used in an applied manner for refined fits in RF-MEAM. These links do not just help to save time and effort in the RF-MEAM fitting (since the basic properties can be already fixed) it can also ensure that the goals for the basic properties are always met in the resulting RF-MEAM alloy potentials when fitting to advanced properties, like EXAFS in chapter 5. Secondly, these examinations of the fitting problem with these more transparent and simple tools, presented in this chapter, allow to detect some fundamental fitting problems. Using the Rose eq. [58] (→ 3.3) for the Fe-Y alloy was found to be a substantial limitation, see 3.3.4 & 3.4. The standard MEAM scheme also extensively relies on the use of the Rose eq. [52] - RF-MEAM on the other hand represents a better technique abstaining from the Rose eq.. These findings were only possible in simpler EAM. And thirdly, the extensive work in this chapter on the fitting formalisms and their application in MD provided an essential set of starting parameters for RF-MEAM (see 4.1.2). All of this embodies the fundamental step toward the development of the subsequent adapted Fe-Y RF-MEAM potential.

3.1 Method Applying the ZW EAM model to POTFIT

Like mentioned before (in 2.2) the EAM formalism consists of the pair potential function ($\varphi(r)$) and embedding energy function ($F(\rho)$) directly depending on the electron density function ($\rho(r)$). The actual "art" of potential development is finding the right analytical expression for these functions, matching $\varphi(r)$ and $F(\rho)$ and mastering the fine tuning of the corresponding parameters in these analytical expressions (by appropriate fitting software tools and techniques). Before jumping into various details of this rather technical chapter 3.1, these few remarks might provide a helpful introduction: when choosing analytical expressions, these crucially depend on the physical interpretation of the potential functions $\varphi(r)$, $F(\rho)$, $\rho(r)$. While the fundamental principle of EAM leading to the total energy as Φ (see 2.2) is always the same, the expression of the energy as pair functionals allows different mathematical formulations. each of them is linked to different physical interpretations. As a recap, the major groups are, the glue potentials with strong ties to force matching (POTFIT is based on this form), effective medium theory, the Finnis Sinclair method (using the p-th moment approximation) and finally the EAM method by Daw and Baskes.[29]

In particular, at the beginning of the 90's this aforementioned EAM method has become popular because of Johnson's and Oh's further development of a simple analytic formalism to derive EAM potentials from Daw's and Baskes' principles and reduce fitting work drastically [56], as well as many parameter will be fixed analytically later in this chapter (3.2). One of the major characteristics is the use of the BJS formula [129] in this approach, describing the embedding energy (more details in 3.1.3) – as a consequence the electron density curves stem from a density functional scheme (more details see 3.1.3). Because of its mathematical convenience and intuitive interpretation, as presented in 2.2, this form of the EAM method is one of the widest used schemes for the application of pair functionals [22].

Zhou and Wadley modernised it by adapting this analytic formalism [57] in modern fitting methods, while partly sticking to the BJS formula with special emphasis to a sensible cut-off behavior. On top of it, they designed it in an extensible manner, for instance by CTIP or to the analytic modified EAM (AMEAM) technique [90], which is like a predecessor of RF-MEAM (application of it in chapter 5). Hence, this reproducible[30] formalism (ZWF) is used as a basic sketch and will be presented in the first section (3.1) by exactly describing the parametrisation functions: firstly, the pair function, $\varphi(r)$, (3.1.1) covering the interactions of the atomic pairs in the convenient form of exponentials based on Morse potentials [52]. Secondly, the electron density function, $\rho(r)$, associated to the electron cloud of each atom, described in 3.1.2, which can be conveniently expressed in the same form as $\varphi(r)$. And thirdly as mentioned above in 3.1.3 the EMB function. Then this presented formalism is linked to the fitting tool POTFIT [101], which is presented in 3.1.4. The focus of this description lies on the explanation why the developed analytic EAM formalism without force matching is used in POTFIT, though POTFIT is designed and intended for the glue potential formalism by force matching (see 3.3.4).

In order to adequately apply this analytic fitting formalism for Fe-Y, the following modifications in 3.2 of the "*Zhou and Wadley form*" (ZWF) are necessary. Another introducing overview about the use of fitting constraints will be given in the intro of 3.2.

And after all these preparations, finally, fitting in POTFIT within this developed scheme (3.3) can be performed resulting in some first findings in MD. The fact, that the MEAM implementation in POTFIT using the Lenosky scheme [115] fails to produce suitable MEAM fits for complex alloys, substantiates the necessity of these lengthy modifications and deviations in 3.2. Therefore, the next steps of this chapter building on the here presented formalism in this section are necessary for the transition to the more suitable RF-MEAM formalism (suitable for Fe-Y).

[29] For convenience often all potentials of these groups are called EAM potentials (like in LAMMPS they are all labelled EAM) – though in fact each group should have his own declaration, but since the basic idea is the same this convention is used

[30] By reproducible it is meant that the developers of the tested and used potential publish the parameters in a clear manner.

3.1.1 Form of the pair potential and understanding its purpose

The pair potential part represents the distance dependant repulsion and attraction between the atomic cores. The Morse potential type has been successfully applied to a wide range of materials and served in this adapted form, presented in this chapter, as a backbone in Zhou's and Wadley's formalism (ZWF) [57, 96]. For this purpose it consists of a short-range repulsive part, expressed as an exponential with an exponent α multiplied by factor *A*. For the long ranged repulsion part the same exponential form is used, but with different parameters: *B* as a multiplication factor and β for the exponential. The important difference to the original Morse potential is, that both parts are controlled by a normalised distance, r_e, which will be explained here in an illustrative way. In 3.2 its theoretical origin and links to α and β by the idea of universal (binding) relations, matching pair and EMB part, will be shown. Furthermore, the description of the attraction by the electrons (clouds), represented by the parameters *B* and β, is chosen in a way that it can be partially transferred to the electron density parameters, simplifying the fitting. However, fitting the genuine Morse potentials to metals generates much too long-ranging potentials (caused by the slopes which are associated with the elastic constants [21, 52, 97]. So, an "automatic" cut-off, acting at higher distances, controlled by λ, κ and the exponent in the denominator, is necessary as an adaption to the genuine format (inspired by Morse pots.) [52]:

$$\varphi(r) = \frac{Ae^{-\alpha\left(\frac{r}{r_e}-1\right)}}{1+\left(\frac{r}{r_e}-\kappa\right)^{20}} - \frac{Be^{-\beta\left(\frac{r}{r_e}-1\right)}}{1+\left(\frac{r}{r_e}-\lambda\right)^{20}} \quad (3.1)$$

Each part, repulsive and attractive, has 4 parameters: r_e, α, *A*, κ and *B*, β, λ and again r_e. So, in total 7 parameters (since r_e is the same for both parts). Since λ and κ are kept fixed, only five of them are flexible, each can be either fitted or analytically fixed. The constants λ and κ are determined empirically for a suitable and stable cut-off behavior before fitting leading to a self-regulating *natural* cut-off[31]. r_e is tuning the equilibrium distance and can be fixed depending on the behavior of α and β (more details in 3.2). The stability of lattice equilibria, phases and as well spacing of other atomic configurations are mainly governed by the ratio of α and β. In addition, the structures as well as the energies and the elastic constants are influenced by the ratio of *A* to *B*.

This aforementioned "natural cut-off" implies, that when computing the total energy by summing up the interactions of all atoms[32] (see 2.2), only the interactions up to the 3NN for bcc/fcc materials and up to the 4NN for hcp materials need to be considered (sufficient for the aims of this work). Using this fact and that at equilibrium and even around it (max. 5% distortion) all the same neighbors of the same order (1st NN, 2nd NN, 3rd NN (NN=Nearest Neighbour)) have the same specific distance from the considered atom, the summation (for the pair potential and the electron density) as shown in 2.2 can be efficiently simplified. Instead of summing over j atoms it can be summed over all NN, counted by the index *m*, where:

$$\sum_{ij} \varphi\left(\overrightarrow{r_{ij}}\right) = \sum_{im} a_m \varphi\left(\overrightarrow{r_{NN}}\right) \quad (3.2)$$

[31] since as r increases the denominator gets very large. For nearly all chosen parameter this is the case already after the 4NN

[32] It is important to keep in mind, that the contributions of pair potential to the total energy are sums over all atoms (as shown in 2.2):

$$\sum_{ij} \Phi\left(\overrightarrow{r_{ij}}\right) = \sum_{ij} \varphi\left(\overrightarrow{r_{ij}}\right) \; where \; \varphi\left(\overrightarrow{r_{ij}}\right)$$

Hence, the one atom i is chosen and then the distance to all surrounding atoms j are measured. For each atom j the distance $\overrightarrow{r_{ij}}$ is plugged in the pair potential formula and then all resulting potentials for the distances are summed up. Normally the number of included atoms is limited by a cut-off. Here this is not necessary, since the denominator automatically acts as a cut-off as explained.

Where NN_{mi} is the m-th nearest neighbour distance of atom i. In bcc for example there are 8x 1st NN, 6x 2nd NN, 12x 3rd NN to consider. So, for instance to compute the contribution of all atoms in the 1st NN distance, the contribution of one single atom at 1st NN distance ($\varphi(\overrightarrow{r_{NN}})$) are just multiplied by the number of NN (a_m). This yields the same result as using the tedious summing up of each NN individually, since all eight 1st NN are at the same distance in equilibrium (and have the same contribution). The number of NN varies in the structures and is expressed as a_m. In simulations this is not done, but for calculations by hand at equilibrium this is a pleasant simplification for analytic determinations of potential parameters. (This will be deepened by the analytic calculation in chapter 3.2, which were then adapted in POTFIT).

Before moving on to the electron density function(al), the shape of this pair function will be presented and its links to its parameters and the resulting properties of the modelled material in question explained.
Below is a schematic sketch of a pair potential function in the aforementioned parametrisation with suitable parameters for (bcc) Fe-Fe interactions. The red curve are the parameters determined by Zhou and Wadley [57], the blue curve represents the fitted parameters which were established in this work (the details about the actual fit are in chapter 3.3). The schematic purpose is immediately visible by all the annotations in the graph for the resulting properties of the potential. Before explaining these annotations it is important to properly understand the axes of the potential function. This graph shows the pair potential interaction energy per atom – recognisable by the range of the energy scale, a few 0.1 eV.[33]

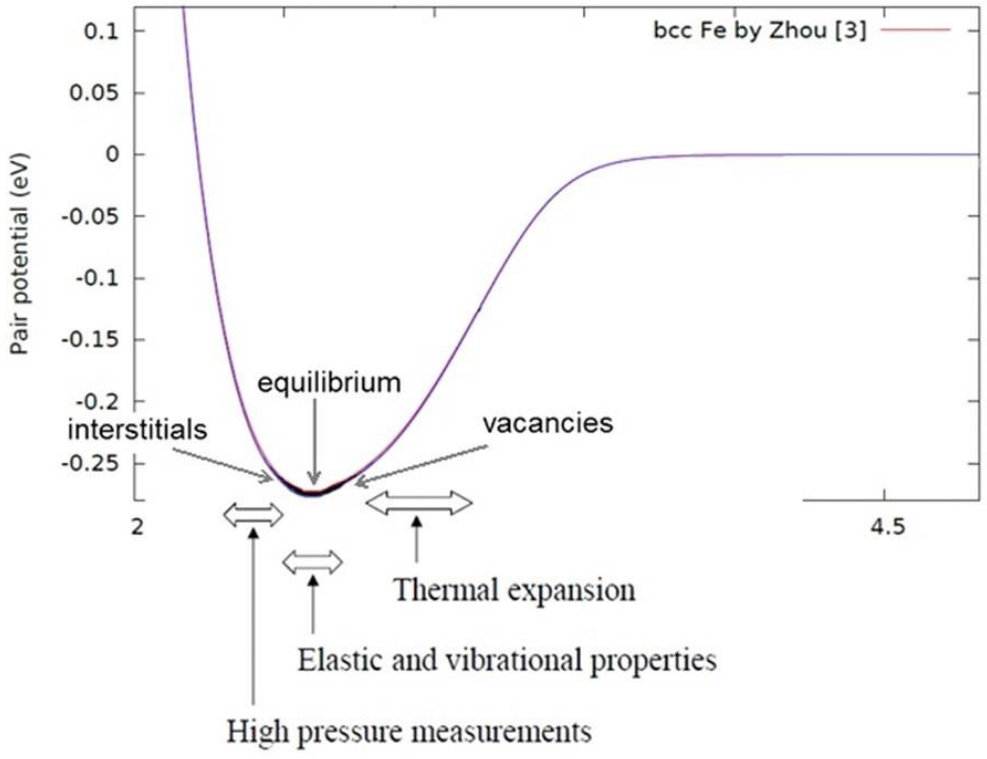

Fig. 3.1 A principal representation of a pair energy function per atom in eV vs. Å – it shows the energy per atom vs. the distance of the atom pair of ZW bcc Fe and own fit (blue). For a principal understanding its highlighted which regions of the potential shape which properties – discussed on p. 30. The black marked region covers the fine tuning differences in the fitting process and this will be reviewed in 3.2.1 (p. 38).

[33] The scale representing the energy of all pair interactions at a given distance would be approximately ten to twenty times higher. It is important to distinguish which scale is used, all atoms or per atom. Considering all atoms provides a better overview (assuming equal spacing of all atoms by equilibrium), the *pure* function per atom allows an easier understanding of potential functions and the used parameters. (generally speaking, the first one is of greater interest for users, the second one for potential developers/checkers)

Having understood shape & purpose of this graph, the following potential properties can be illustrated:

- Equilibrium position: This is one of the most important features of the potential, because the distance at which the minimum occurs controls the lattice constant, because the lattice constant represents the equilibrium of the atomic positions. In addition to that, the depth of the potential well represented by this minimum also controls the cohesion energy. The position of this equilibrium crucially depends on r_e and the ratio of α and β. r_e scales the exponentials in both parts (repulsion and attraction), which is one of the main influences on the lattice constant. The ratio of α and β significantly forms the proportion of attraction to repulsion, which is the driving influence on the depth of the potential well and thus on the cohesion energy. Since the lattice constants of common metals and their cohesion energy are related and occur in a limited range (Zhou Wadley paper), universal relations can be established to control these parameters. One very convenient consequence of one possible set of universal relations is, that r_e can be set to the 1st NN (as done by Zhou and Wadley and mostly in this work).
- Steepness: The ratio controls the depth of the potential well, the values of α and β are the main influence on the steepness of the potential well around and also farer away from the equilibrium, they are one of the major influences on the general shape of the potential. The direct and simplest indicator of a correct shape and steepness (and thus appropriate values for α and β) around the equilibrium is the bulk modulus as one of the most basic indicators for a good fit of the mechanical properties. After an accurate fit to the bulk modulus, another more sensitive property is represented by vibrational modes, which can be checked by phonon spectra and/or other spectra like EXAFS, IR, etc. Here in addition to a precise gradient the anharmonicity of the well, the different slopes on both sides, is very important for a suitable representation. The ratio of α and β is again one of the main controlling influences. A sensible representation of the vibrational properties and bulk modulus normally results in a more or less suitable gradient for the thermal properties (thermal expansion). The fine tuning for the thermal properties can be controlled by changing λ and a suitable λ can be determined by using the anisotropy ratio (while the ratio of κ and λ is controlled by the universal relations, see 3.2). The properties for high pressure measurements are in theory influenced by the gradient located on the LHS of the minimum – However, in practise the EMB function has a bigger influence on the high pressure properties (particularly η) , but they are of lower interest in this work.
- Fine tuning of steepness for elastic constants and defects: A more refined influence on the steepness around the equilibrium exert the parameters *A* and *B*. These parameters also control the position of the minimum (s.a.). However, this influence is insignificant compared to the effect on the steepness particularly around equilibrium. Therefore, the elastic constants which are directionally dependant (more details 3.2.3) are very sensitive towards these parameters. In addition to that the parameters *A* and *B* can be linked to the EMB part as an interplay of A, B and the EMB part the representation of defects is shaped (e.g. defect formation energies).
- The cut-off is mainly impacted by λ, κ and the power of the denominator – the value of 20 for the denominator was just chosen by experience and trial and error. Values below 16 yield an insufficient cut-off (the pair pot. is not vanishing fast enough at higher atomic distances, which is unphysical), values greater than 20 result in a too sharp cut-off and as a consequence lead to an inaccurate description of long range interactions.

When considering these links between the properties of the modelled material (in this case bcc Fe) and the shape of the corresponding pair potential function, it has to be kept in mind that for the total energy the EMB part additionally contributes to the total energy. Therefore, the conclusions for the properties cannot be directly in a one-to-one relationship be drawn from the pair potential. This is immediately stressed by

the fact that the Fe-Fe pair potential as shown in figure 3.1 suggests a minimum at the 1NN distance around 2.48 Å, but the lattice constant of bcc Fe is around 2.86 Å. Adding pair and EMB part, the minimum of the total energy is located at the correct lattice constant. (As shown in 3.2 this functional form allows fixing parameters in a way that the minimum of the pair potential is always at the 1NN, in a pure pair potential this minimum would be the lattice constant.) Nevertheless, just looking at the pair potential provides a first reliable estimate for the lattice constant. The main influence on the basic parameters stems from the pair potential part, the EMB part acts as a correcting contribution (roughly up to 20% of the total energy around equilibrium). However, such corrections by the EMB part play a significant role for more detailed properties, such as the defects or the Cauchy relation (C_{12}-C_{44}, which would be 0 in a pure pair potential without an EMB part).

Both parts complement each other. In order to guarantee a suitable interplay between these two parts (analytical) parameter fixing or restraining and UBRs by Rose eq. are an efficient necessity (as shown in 3.2). The nature of this parameter fixing has to be taken into account when matching the two parts – there are numerous possible combinations, leading to the concept of parameter sets, which are of particular importance in alloy potentials. Once all potential parametrisation functions are set up in the following section, a suitable parameter fixing and fitting technique is established. During the fitting one obtains a closer intuition for the parameter space and for sensible restrictions of it. Using the experiences of the actual fitting in 3.3 in advance the following principal remarks for this pair potential format can be made: The whole adaption of this kind of the pair potential and EMB part to Fe-Y alloys is taking place as *fine tuning* restricted to the black marked region in graph (Fig. 3.1) – little differences in that region crucially improve the refined properties, such as defects and fine differences in the elastic constants and these enable the fitting of alloys. Changes in these differences are as well coupled to the electron density function (see 3.1.2) and by that indirectly to the EMB part. This resembles the parameter space in an illustrative way. The analytic fixing and restraining conditions in the next section 3.2 for the desired accuracy and applicability in alloy fitting are solely acting by restraining the parameter space to this black region – *that's simply speaking all these analytic relations are there for.*

3.1.2 Description of the electron density and its universality

The electron density has the same form and parameters as the long ranged attractive part of the pair potential. The parameter *B* as a factor is just replaced by f_e leaving it as an additional fit-parameter:

$$f_j\left(\overrightarrow{r_{ij}}\right) = \frac{f_e\, e^{\left[-\beta\left(\frac{r_j}{r_e}-1\right)\right]}}{1+\left(\frac{r_j}{r_e}-\lambda\right)^{20}} \quad (3.3)$$

It is assumed that the number of bonds per atom pair is similar to the number of bonds caused by a collective electron cloud [9] - hence the same summation procedure as above in 3.1.1. f_e can be freely chosen by empirical observations [57, 97] to be (proving to be a solid choice in pure metals):

$$f_e = \frac{E_c}{\Omega^{1/3}} \quad (3.4)$$

Where in eq. (3.4) E_c is the cohesion energy and Ω the atomic volume (per unit cell) of the considered metal. As explained, in EAM the electron density is a hypothetical concept, the associated embedding energies link this hypothetical concept to a more comprehensible meaning (the ratio wrt. to ρ_e is relevant, since in the embedding energy the resulting ρ_e is used for normalisation). As a consequence, in single metals eq. (3.4) can be set as an exact equation and not a suggestive estimation. However, for alloys the choice of f_e is rather more limited, since it gives a kind of weighting of the superimposed electron densities

of the alloy components [109]. Another interpretation is: this flexibility is allowed due to the spherical symmetry of EAM (electrons symmetrically distributed in pure metals, another illustrative factor for the existence of parameter sets in EAM). But since the bonds of metallic alloys have bonding angles, the electron density distribution is not symmetric anymore and f_e has to be matched to a suitable ρ_e [97]. Another interpretation: in pure metals the freedom of splitting the total energy between the pair and EMB part is greater than in alloys (less suitable parameters sets). When constructing the electron density for a potential formalism for alloys more constraints are necessary to ensure a correct splitting – this is supported by having the same parameter β in the pair potential and in the electron density funtion. By this concept *natural* matching between the EMB and pair part is established (since EMB depends on the electron density). Since β is kind of the strongest parametric influence on the functional shape of both parts and β matches them, it seems intuitively reasonable, that this parameter should not be analytically fixed (important in the next parameter fixing section, 3.2). Consequently, in 3.2 and 3.3 it will be confirmed, that β is a very sensitive parameter, meaning little changes of it, remarkably change the functional shape and its properties as said before.

For the universality of the electron density function in alloys, it has to be ensured that a broad range of metals can be covered. Here, in the graph 3.2 below, it can be seen by various EAM fits of Zhou and Wadley in 2005 [96], that all common metals can be satisfactorily represented by this form.

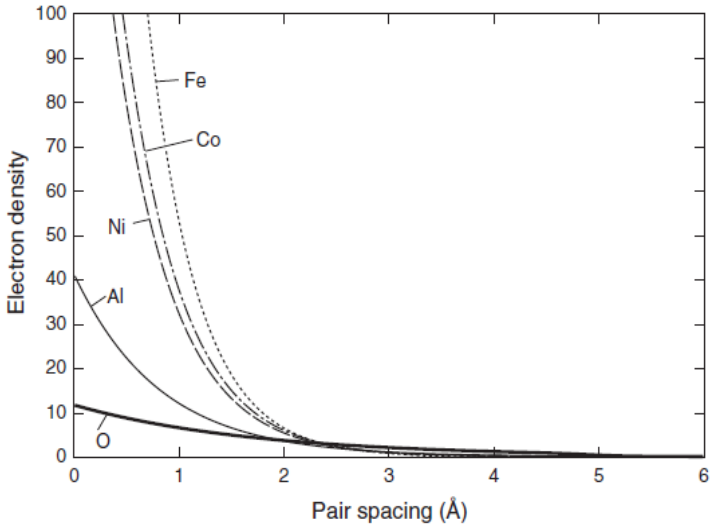

Fig. 3.2 Graph of electron density functions (in the presented form here) for various metals, taken from [96] to highlight the flexibility of this function

In the graph Zhou and Wadley's fitted electron densities (dimensionless) are shown vs. the pair spacing. It is electron density per pair spacing. In Fe at the 1NN and 2NN the electron density contribution per atom pair is around 2-3, summing up all the contributions (similar to 3.1.1) the total ρ_e for Fe (electron density at equilibrium) is around 24. This fit of the electron density provided a very helpful starting point for the fits in 3.3[34]. In this graph from a ZFW paper [96] it can be seen that many common metals in alloys can be modelled by ZFW. It is also useful to get a feeling for the range of β: it ranges from around 3.5 for Al to 6.12 for Y. This makes sense since Al has the fewest electrons in its shell and thus the lowest density and Y the most. For the fitting it has been experienced that it is sensible to restrain β to this range for the first fits (and then systematically scale with parameters set rules). The produced electron density in this range can be also linked to some DFT calculations and atomic models by Clementi providing an elegant *bridge* between theoretical DFT and more applied MD calculations [109].

[34] The actual final fits in 3.3 of this work are not that much different from these, which makes sense, since in order to stay in the black fitting region in 3.1.1, the fitting parameter β has a very small fitting range(in fact few decimal places).

3.1.3 Short description of the embedding energy

The embedding energy describes the energy necessary to insert/embed an atom into the electron sea (the local electron density at equilibrium,ρ_e). Since this is a hypothetical concept like the above mentioned electron density function, there is some flexibility in the formulation of this part. This has led to different techniques to construct it. The two major ways of building the EMB function $F(\rho)$: either with an exact analytical function, which parameters can be exactly analytically restrained or fixed for a sensible match or by establishing universal binding relations (UBR). When using UBRs an equation of state (EOS) is postulated to match the EMB part – this approach is motivated by Banerjea's, Smith's and Rose's discovered universality in cohesive energy and volumes in metals [129]. The cons and pros of both approaches are discussed in the introduction of chapter 3.2. Regardless which approach is preferred, the BJS formula is a solid starting point to describe and fit the EMB part, because it can be used as an analytic function but also as a parametrisation for the EOS match when using UBRs. All in all, the BJS formula is accurate and flexible.[12] Later, in chapter 4, a (more) exact analytic function in RF-MEAM will be used (as the two previous functions). The BJS formula expresses the EMB energy depending on the electron density ρ as:

$$F\ \ (\rho) = F_e \left[1 - ln\left(\frac{\rho}{\rho_e}\right)^{\eta}\right]\left(\frac{\rho}{\rho_e}\right)^{\eta} \quad for\ \rho > 1.15\rho_e \qquad (3.5)$$

At equilibrium (density at equilibrium structure) the energy is F_e. Hence, F_e is the energy necessary to embed an atom into a vacancy of the (relaxed) lattice. This can be just calculated by the difference of the cohesion energy and vacancy formation energy. Consequently, this parameter is primarily contributing to the cohesion energy and secondly influencing the defect properties. This fact will be used in 3.2.1. ρ_e is the normalization (which can be scaled by f_e, see eq. (3.4)) and η gives a kind of slope, which obviously depends on the atomic structure and the associated bulk modulus. (to be more precise the contribution of the EMB part to it, which is smaller than the pair part contribution.
Nevertheless this old BJS formula from 1985 [130] has some weaknesses at smaller ρ, it has an infinite slope towards ρ=0 and results in unphysical values for the pressure derivative of the bulk modulus. Hence, more accurate cubic spline equations, which are similar to a Taylor series of it, are used for lower ρ:

$$F(\rho) = \sum_{i=0}^{3} F_{ni} \left(\frac{\rho}{0.85\ \rho_e} - 1\right)^i \ ; \ \rho < 0.85\rho_e = \rho_n \qquad (3.6)$$

$$F(\rho) = \sum_{i=0}^{3} F_i \left(\frac{\rho}{\rho_e} - 1\right)^i \ ; 0.85\ \rho_e \le \rho < 1.15\ \rho_e \qquad (3.7)$$

$$F(\rho) = \ F_e \left[1 - ln\left(\frac{\rho}{\rho_s}\right)^{\eta}\right]\left(\frac{\rho}{\rho_s}\right)^{\eta} \quad ; 1.15\ \rho_e \le \rho \qquad (3.8)\ \ with\ \rho_s = \rho_e$$

Where ρ_e represents the equilibrium density and the F's are fitting parameters, as well as η, contributing 5 flexible parameters for hcp and bcc (since $\rho_e = \rho_s$, in FeY this is ok, but especially in Al alloys a distinction btw. ρ_e& ρ_s is necessary)[35], of which actually are only 2 are actually fitted (and the rest is analytically fixed for properties and matched). The shape of the actual EMB function in Fe-Fe has been significantly changed and scaled respectively (in comparison to ZWF part for Fe-Fe) for a better alloy potential tailored for Fe-Y (see 3.2 and 3.3).

[35] The number of fitting parameters is reduced by 6 parameters by continuity & boundary conditions see 3.2.7

3.1.4 Overview: possibilities and limitations of POTFIT

Now as the analytic form of the EAM model has been established, the fitting programme POTFIT by P. Brommer et. al. [101] has been chosen as a suitable fitting program for the first half of this work. It is based upon the least squares method (LSM), more details in [102] – despite its principal limitations by LSM, especially w.r.t. global minima detection, POTFIT provided an efficient starting point because:

- Variety of available potentials in POTFIT and code openly available under the GNU license
- Fast and efficient by force matching and glue potential techniques
- Extension to MEAM possible, but some principal restrictions have been observed later
- Can be readily adapted on a broad range by:
  - New potential functionals can be added to the code and easily integrated into POTFIT
  - Ideal to also include analytical parameter restraints (code extract see appendix)
  - Parameters can be easily restricted by range functions in the parameter input

The last point, the versatility and flexibility, is of particular importance and was the main reason as POTFIT can be called one of the best public fitting tools for customised MD potential models. New potential formats can be quite easily integrated in the C code (especially in comparison to the modular fitting code ATOMICREX [131]). In order to schematically understand POTFIT, the basic fitting steps and operations will be explained with the help of the following flowchart about the POTFIT fitting routine:

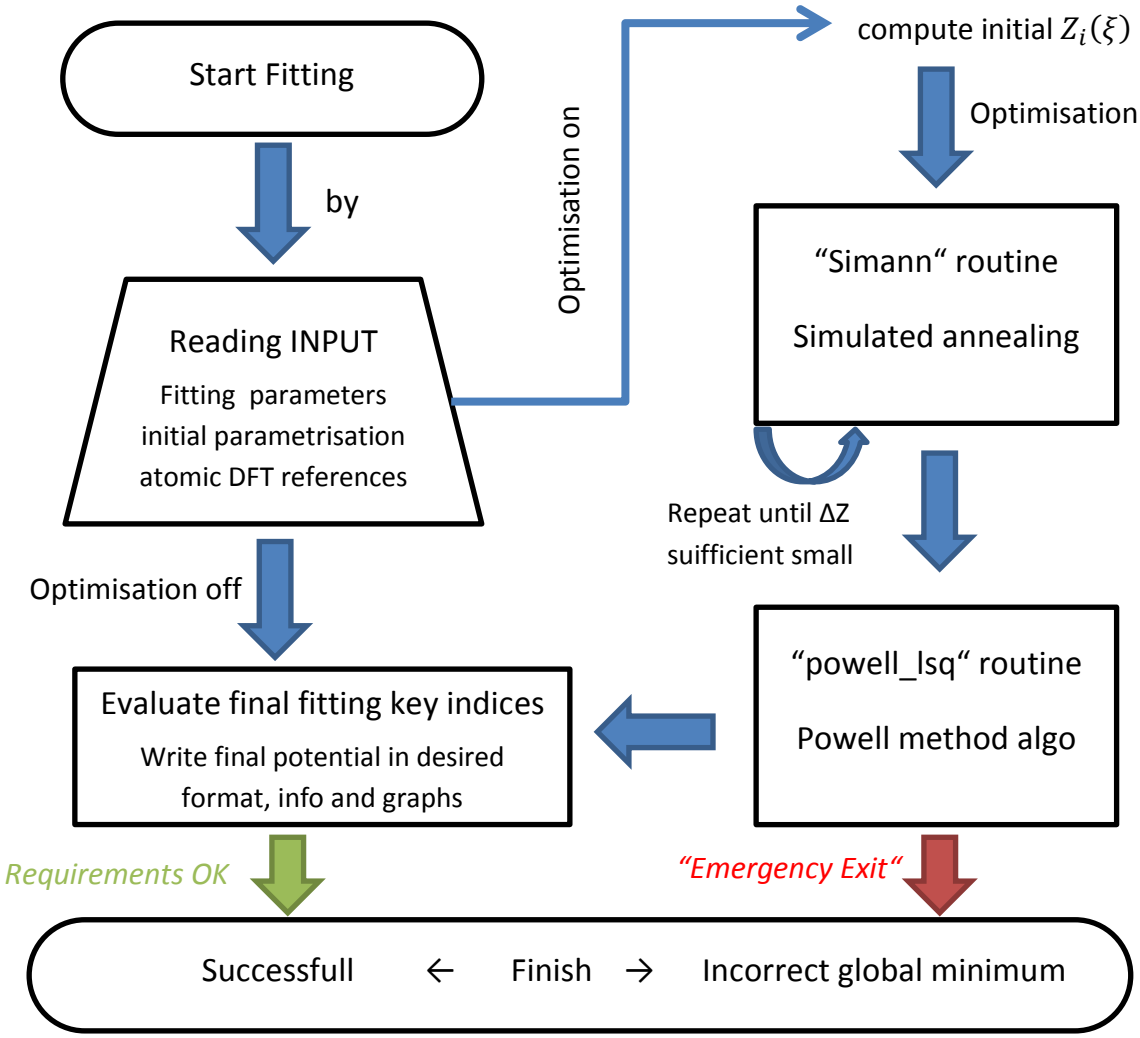

POTFIT optimises potentials by at first reading in the potential parameter starting point and fitting parameters, following the command whether to optimise and then starting the optimisation routine by fitting the parameters if the optimisation tag in the fitting parameters is turned on.

The fitting process consists of the following two major parts:

1. It starts by calculating as the first step the deviations between the data of the atomic references (includes mainly forces, energies and also atomic stresses) and the data of the same atomic references calculated by the test potential (generated by the staring parameters leading to the initial $Z_i(\xi)$). This deviation is computed by the important *Z function* describing the deviation of the parameter set as:

$$Z_F(\xi) = \sum_{k=1}^{m} u_k \, (F_k(\xi) - F_k^0)^2 \quad (3.9)$$

   This is nothing more than a LSM fitting method: $Z_F(\xi)$denotes the mean square deviation of the test function F with a parameter set ξ (which is the input), this is done by summing over k (index for each reference data point) squared differences between the forces calculated by the MD test potential each reference (DFT calculation). But special attention has to be paid to the fact, that the "F" in (9) are forces and not just energies. This crucially improves the *plain LSM* by the method of force matching by Ercolessi and Adams [59], with some consequences such as the interpretation of the EMB part as a glue function (see below).

2. After the calculation of the deviation of the starting parameters by eq. (3.9), POTFIT independently optimises the parameters by two stages: Simulated Annealing ("S*imann*" in the graph), which is finding *global* minima more or less by trial and error with LSM, and then once a *valley* has been found, local minimum optimisation by a conjugate gradient method in the Powell form is performed.
   Simulated annealing is a simple but at the same time very efficient method to scan the parameter space for *global* minima: it is a probabilistic process which is controlled by the annealing temperature, which will be decreased during the process (thus the name "annealing"). For each step, the parameter set is alternated by adding a normally distributed random number to the parameters. Then the target function $Z_F(\xi)$ of the alternated parameter set ξ is evaluated, see step 1 and eq. (3.9), and then the ΔZ between the original and alternated parameter sets are considered. If ΔZ is negative, the deviation has decreased, so the parameter set has improved and the change will be accepted and the parameters are changed. Then the cycle repeats with a new try to further alternate these accepted parameters. If ΔZ is positive, then the regressing change will only be accepted with a certain probability. If the alternation is rejected, the cycle will repeat starting from the previous parameter set before this step. The probability depends on the ΔZ and annealing temperature T, which is:

$$P(\Delta Z) = e^{-\frac{\Delta Z}{T}} \quad (3.10)$$

It can be immediately concluded: the bigger ΔZ, the less likely is the acceptance and thus the change to this parameter set. How "strict" or better the scaling of the probability is controlled by the annealing temperature T in the denominator of the exponent. At the beginning T is set high and positive ΔZ, even higher values of it (since T is high) are more often accepted – the optimisation has bigger jumps in the parameter space. This makes sense, in order to have a first thorough scan of the whole parameter space. It jumps from minima to minima and by the probabilistic process compares the minima. In possible global minima, positive ΔZ occur less often, while in a non-desired local one its more often, this will lead to the proximity of *seemingly* global minima. The ΔZ will eventually become smaller than some thresholds, then

T is decreased and the annealing becomes "stricter", the steps decrease until finally another threshold of an absolute $Z(\xi)$ value is reached– indicating the valley of the global minimum has been found and a the local minimisation with a conjugate gradient method (CJG) by Powell [102] (in the chart "powell_lsq"), will follow the *draw of the minimum*. By *draw* it is meant that the alternation of parameters towards the minimum produce a constant improvement of the deviation – the algorithm scans the surrounding parameter space and follows the direction where the decrease of the deviation appears to be the strongest. Once the improvement is smaller than a set threshold for the CJG the target function will be evaluated and the potential will be written out in the desired potential[36] format and the MD runs can be started.
Two concerns regarding this approach have to be raised from the viewpoint of this work: One of the most important weaknesses in this approach is that the simulated annealing only finds *seemingly* global minima – it is not a systematic scan for global minima, as by GAs in MEAMfit, but a probabilistic one with trial and error. One can encounter this problem by kind of knowing *what to look for* by choosing appropriate starting parameters and restrain the parameter space. This is what makes the fitting lengthy and tedious.
Without this exact knowledge wrong parameters ranges and starting points lead to a failing CJG – POTFIT has to take the "emergency exit" (see graph and appendix), like most of the time before one knows how the potentials has to look like.
Still even with a pretty exact idea how the potential and its parameters have to look like and an advanced intuition of the parameter space one will encounter the 2nd problem: parameter sets. In POTFIT this is handled by the concept gauge degrees of freedom in the glue potential interpretation. A mathematical description of some parameter set rules can be found in 2.2.2 – simply explained as before the origin of the parameter sets is caused by different possibilities to split the EMB and pair part.[37] To be more precise the problem of parameter sets describes the occurrence of a group of different parameter sets for all functions, when all of them seemingly yield the same physical results and behavior. This transferability can be found in the electron densities with different ρ_e and different scaling in EMB function (the practical consequences of this will be deepened in 3.2). In POTFIT this is called gauge degree of freedom (sets of parameter changes that do not change the phys. properties of the potential) and is controlled in the following way: the forces are computed separately for the EMB part in the following analytical manner:

$$F_{ip} = -\sum_{j\neq i}\left(F_i'(\rho_i)\rho_j'(r_{ij}) + F_j'(\rho_j)\rho_i'(r_{ij})\right)\frac{(x_j - x_i)_p}{r_{ij}} \quad (3.11)$$

And these resulting forces, F_{ip}, purely originating from the EMB part can be matched to selected DFT force references, which represent properties which can be solely represented by the EMB part – for instance $C_{12} - C_{44}$ (as mentioned before this is in a typical pair pot. zero) this is one way of force matching.[38] In 3.2 this will be replaced by analytical matching – analytical restraints and fixings. And such mechanisms are supposed to link the EMB part to the pair to complement each other for an accurate representation of the desired properties (by matching the forces and the resulting properties). In the intended use of POTFIT by force matching the EMB part is "glued" to the forces and the pair potential. Therefore, the EMB part is called glue potential in this framework. Since the fits in this work do not use force matching, this overviewing remark will be left at this stage.
Summarising, the concept of glue potentials is used to handle the parameter sets and to avoid the use of UBR or analytic restraints (which makes sense, see dilemma introduced in the intro of 3.2). Practically speaking, it can be said that UBR for matching is kind of replaced by more information in the reference data in the form of forces.

[36] POTFIT is also a great tool when turning the optimisation off to print out the shape off the potential or format the potentials

[37] And this also represents the different approach in this work to tackle the problem of parameter sets, namely by empirical physical intuition and understanding the meaning of the parameters as opposed to POTFIT.

38 Has to keep in mind force matching does not lead to one definite electron density – as in DFT

However, in this case, when fitting Fe-Y, this approach seems not to work that well[39], because

- The fitting data for this project contains mostly single energies of many clusters but not sequences of energies for processes and no forces are included (see 2.5) – so no force matching. However, there are NEB calculations for exact energies of transition/diffusion barriers (and for potential MC simulations like by Mock for Fe-Y [132])
- The extension to a full scale MEAM is not possible in POTFIT, since POTFIT uses a reduced MEAM formalism by Lenosky [115]. Nevertheless, this is logical, because the classical MEAM relies on EMB-pair matching by the use of the Rose eq. and/or analytical constraints related to rose eq.. The use of force matching is not intended in "classical" MEAM. POTFIT uses a reduced MEAM scheme by Lenosky [115], which worked for silicon [94], but seems problematic for metals (an example can be generated by trying to reproduce the Y-Y pot. in [92]).
- On top of that: the aforementioned parameter set choice by gauge DOFs in the EMB part works quite well in pure metals, but is problematic in complex metallic alloys. In alloys only a very limited range of parameter sets work for the combination in complex metallic alloys - the LSM in POTFIT is trying to do this more or less by trial and error and thus is very poorly performing in finding the very few available adequate parameter sets for alloys. (In quasicrystals by additional constraints, calculated stresses in DFT, the parameter space can be reduced and enables the appropriate use of LSM – the properties of Fe-Y are more complicated to fit though.)

Summarising: in order to use a full scale MEAM fitting and for a better control of parameter sets in metallic alloys more advanced optimisation techniques are needed than LSM in POTFIT. It should not be overseen that this drawback cannot be compensated by more and more detailed fitting data, such as having ab-initio MD and/or forces. The problem remains, that one either has to use the full scale classical evolved MEAM formalism with the matching by Rose eq. (due to the complexity of the electron density function with orbital functions see 2.2) or has to use the reduced scheme, which is not suitable for these kinds of alloys. In order to overcome this problem, as it will be discussed in more detail in the following chapter, the enhanced RF-MEAM (reference free) form will be introduced and used in a more detailed fitting procedure for Fe-Y in MEAMfit in the second half of this work[40] (chapter 4&5).
Nevertheless, before doing so regardless of these drawbacks it had to be investigated how suitable fitting with matching assisted by the Rose eq. is for accurate fits of Fe-Y (see introduction of chapter 3) – for this question POTFIT with some modifications served as a perfect tool. And as said before, one of POTFIT's great advantages is its versatility and flexibility to allow these incorporations. Moreover, the author personally likes the glue potential interpretation to get a better grasp of the parameter set concept.
In order to use POTFIT for clarifying these questions a concept of analytical parameter restraining with a deeper understanding of the meaning of the parameters (see 3.2) was used, instead of a force matching method. During the fitting this restraining is additionally supported by an available function in POTFIT to confine during the fitting the fit parameters to an allowed range for each parameter. These restraints are necessary because of these limitations in POTFIT, which were presented here. As a consequence, these restraints will be a kind of a compensating core technique for the Fe-Y alloy fitting in POTFIT – there is even more to it than just in POTFIT, these techniques essentially contribute to the successful selection of powerful and necessary start parameters for RF-MEAM (→4.1.2). During the following derivations of the rather lengthy analytic considerations in the next section (3.2) the reader is encouraged to keep in mind, that these are absolutely essential. By this the drawbacks of LSM without detailed force matching are solved leading to a solid foundation, which can be transferred to RF-MEAM, for detailed, accurate and versatile Fe-Y potentials.

[39] Has to be kept in mind, always depends on the application, e.g. for quasicrystals, Mg-Y and Al-Ni-Co it works (see [53])
[40] Just to remind: In autumn 2016 the first actually working beta version of MEAMfit was available, previous versions before had too many bugs –the development of a first wider applicable version of a first full scale MEAM fitting code took between 7 and 9 years

3.2 Preliminary Results - Handling parameter space by analytic and principal limitations

As said before the parameters space needs to be constrained for sensible and effective parameterisation schemes, in order to ensure finding a global minimum in affordable time. Chapter 3.1 has established a suitable analytic representation of the fitting functions for the EAM scheme in the fitting program POTFIT. This effective representation allows an analytic and principal reduction of fittable parameters. Analytic means fixing a parameter, and thus reducing one parameter by an exact analytic expression representing a physical property. Fulfilling this analytic condition by this fixed parameter grants that this aforementioned physical property is accurately reproduced by the fitted potential. This fixed parameter is linked to this physical property – a great advantage of EAM (and by some extension also MEAM). The typical properties for analytical fixing are the cohesion energy (E_c), lattice constant (a_0), bulk modulus (B) and the elastic constants. As mentioned in 3.1 this established, reliable and relatively simple implementation of this analytic scheme originates from Johnson and Oh in 1989 [55]. This simple but still quite exact analytic framework could even reliably link the EMB part to the pair part, in a way which granted a reliable and accurate representation of all metals (nearly, Al is in dispute [111]). Similar coupling methods are also used here and will be presented in 3.21. These analytically coupled potentials, which completely do not depend on the Rose equation [52], can extrapolate the Rose equation by the resulting energy-volume correlations (EOS) with these new forms of potentials [55].

However, this analytical fixing by Johnson and Oh turns out in many cases to be too *rigid*. Though basic properties (s.a.), are well reproduced, it bears the potential problem, that properties or behaviors which are not included in the fit (or are difficult to include in the reference set, e.g. phase formation energies or IR spectra) are less likely to be reproduced by such rigidly analytically fixed potentials [103].

The use of rather flexible principal limitations instead of analytical constraints, as in the form of the Rose equation (further discussed in 3.3.6), allows more flexibility and more transferability, but too often at an unacceptable cost of the accuracy, even of the desired basic properties.[41] In addition, this use of the Rose eq. for coupling the EMB and pair part, proves to be very problematic for the desired accurate representation of defects – and this is a grave concern for the various defect reference data points in this project, as it will be shown in this chapter.

Therefore, the Rose eq. cannot be used in this standard way here. The pure analytical approach by Johnson and Oh could be theoretically possible by introducing more parameters for matching the test data base reference points, but this leads to overfitting and solving/optimizing a difficult fitting problem (which kind of shifts the problem to the fitting scheme). Moreover, when considering an exact representation of alloys (eq. including defects, see database 2.5), like in this work Fe-Y, this notion has to be abandoned because of the following reason: parameter sets, which, to shortly recap, occur due to the different possibilities of dividing the total energy into EMB and pair part leading to several seemingly equal optimisation/fitting solutions for the same reference data set. And as explained before (in-depth), when it comes to alloys, these parameter sets are not equal. The strict Johnson and Oh formalism limits the choice of parameter sets by a rigid coupling of the EMB and pair part too much (as shown theoretically in depth by Wang in [103]). Thus, this cannot work. Fitting without any limitations of the parameter space with the standard fitting tools has little chance of finding a suitable global minimum.

A reasonable solution for this dilemma, which is kind of a compromise, was proposed by Zhou and Wadley (ZW) around 2001 [97]: keeping the analytic restraints by Johnson and Oh but allowing at the same time a bigger transferability and choice of parameter sets by using the Rose eq. as a kind of orientation by the use of URs as an alternative method [57]. Instead of applying the Rose eq. to fix the whole embedding part as

[41] It is the typical dilemma in modelling which was explained previously with the concept of DOFs. This leads to the possible solution of introducing more parameters to include these desired properties – but it makes the fitting more difficult and also could cause overfitting (some parameters have no influence on the properties) slower computers achievement simplification

explained above, Zhou and Wadley used *manually* the Rose eq. to fix two parameters in the pair potential by so called Universal relations (UR) [97], which will be proposed in the next section (3.2.1). These are called principal analytical limitations, which allow more flexibility than analytical constraints. Quite fascinatingly, the fixing of just two parameters in both parts, labeled as *key drivers*, by URs linked to the Rose eq. and fixing other parameters in "Johnson and Oh manner", ensures a suitable match with energy (E_C) and volume (lattice constants). So, all in all this works well with various metals at the cost of little inaccuracies, but by a smart choice these inaccuracies can be reduced to an acceptable level.

Summarising this general overview, the principal fitting techs. with the aforementioned explicit form are:

- A rigid pure application of Johnson and Oh's technique – but this is too inflexible
- Applying the Rose eq. (see 3.3.6) to completely formulate the EMB part empirically without fitting and rigidly fix the pair part by Johnson and Oh – very efficient, but too inaccurate
- More flexible adaptions of Johnson and Oh's restrictions but applying an *open form* of Rose eq. by universal relations (URs) – this is an optimal deal btw. accuracy and flexibility

In the following of 3.2 this idea will be pursued for a specifically tailored, exact implementation, with principal limitations by default in mind. Empirical experiences will be also utilised, especially for the universal relations and its actual meaning will be underlined (e.g. with respect to E_c and a_0 (lattice constant)). This new technique will be summarised in an overview on page 61 (3.2.9). In 3.3 this is then applied and the results are used for verification of this approach and identification for improvements.

3.2.1 Principal parameter restriction by key drivers

Principal considerations how to find suitable key drivers

Following the idea of the previous overview a fixing mechanism to ensure a fit in the proximity of the corresponding EOS is set up here. Instead of *pure* UBRs strictly adhering to the Rose eq. two flexible key drivers as open URs are implemented, which can be related to the Rose eq., as it will be shown here. This proximity can be interpreted as a kind of the correct energy-density enforcement covering the correct cohesion energies and lattice parameters.

Only two analytical restraints, here in the form of key drivers (one for each part, pair and EMB), suffice to stay close to the desired lattice constant. These key drivers are the main influencing factors to restrain the potential curve to the black marked region in Fig. 3.1 (3.1.1). Having understood the functional shape and its relations to all fitting parameters, several potential parameter candidates for these two key drivers were tried out in a target orientated manner. However, relatively quickly, as anticipated from the beginning, the ratio of α and β for the pair part and η for the EMB part were found to be suitable key drivers, similar to ZW [97]. By empirical considerations as shown in 3.1.1 β is left *untouched* as a "pure fitting parameter" for the desired flexibility, for example for the interplaying compromise between the accuracy of cohesion energy and defects. These key drivers efficiently link the EMB and pair part by analytical means, while the pure fitting parameter β links both parts by fitting. This is illustrated by this section, where the two key drivers are derived and presented in the context of the EOS curve.

Before moving on, one important distinction in the definitions, which can be slightly confusing, is highlighted: when the Rose eq. is used to approximate the equation of states (EOS) and the EMB part is determined by exactly matching pair and EMB part to the Rose eq. to fulfill the EOS, the relations between parameters satisfying the Rose eq. are called Universal Binding Relations (UBR) (at the end of this section, 3.3.6, the implications of UBRs for alloys will be further discussed). Since in the ZWF there is no exact match but only a simple empirical comparison to the EOS and parameter relations are chosen in a way to roughly satisfy these, these relations are called Universal Relations (URs, sometimes in a more confusing way called Universal Fitting Relations) and these are meant in the following section!

Finding a suitable ratio of α to β by manipulations to the lattice equil. condition:

The ratio of α to β ensures the correct order of magnitude (proximity) of the lattice constant. In the underlying original analytical formalism for ZWF by Johnson and Oh two parameters in each part, EMB (in BJS form) and pair potential part, are fixed by exact analytical calculations [55] which resemble the UBRs (they did not use these) when comparing their results with the Rose eq. (by creating an EOS curve) – this fixing technique of the parameters by conditions, which determine the cohesion energy and lattice constant, will be the starting point (since this successfully works for several metals as shown by Johnson and Oh, ZW and several others [50]) – the lattice equilibrium condition, clearly demonstrated in [52], serves as a starting point for the principal consideration:

$$\frac{1}{2}\sum_{ij}\Phi'(r_{ij})\,r_{ij} + F'(\bar{\rho})\sum_{ij}\rho'(r_{ij})\,r_{ij} = 0 \qquad (3.12)$$

In most techniques, one parameter is exactly determined by this relation and strictly fixed, but this is less flexible, especially for alloys. Zhou and Wadley (ZW) replaced this rigid parameter fixation by an UR - presumably they obtained it by starting from eq. (3.12) in a trial and error procedure. This led to what can be called the most important UR in ZWF: a ratio between α and β:

$$\frac{\alpha}{\beta} = 1.875 \qquad when \qquad r_e = 1NN \quad (3.13) \qquad URs\ for\ lattice\ equlibrium$$

It is particularly unclear how they, ZW, arrived to the second condition (eq. (3.13)), that the parameter r_e will be exactly set to the 1NN of the modelled metal, so $r_e = 1NN$. In a longer review like journal article they claim "*many ratios involving A, B, α and β in combination with r_e were tried*" [97] (here the ratio of *A* and *B* is formed by analytic determinations which are more exact) – this looks like trial and error in fact. For a more reasoned determination a step is taken back to the lattice equilibrium eq. (3.12) and the enforcement of it on the model is derived analytically – for α and β the analytic consideration arrives at the same result as ZW, but here the handy choice of r_e can be reasonibly explained. The other important difference is that the counterparts η and F_0 in the EMB part will be determined in a drastically different and more flexible way than ZW did (see next pages for η and on page 52 for F_0, which in ZWF are rigidly analytically determined before the fit and then kept fixed during the whole fitting [96]). Foremost, this difference in the EMB part is one the main reasons for the different behavior in the *pure* fitting parameter β during the optimisation (which corresponds to the black region in Fig. 3.1 (3.1.1) and has remarkable effects, like a critical improvement of vacancy (formation) energies). The necessity for this amendment can be also highlighted by the fact, that the original more static definition of the previous parameters only allowed a "*β varying between 4.0 and 5.5 (below 4.0 for gases)"* [97]. However, for hcp Y and its alloys this range for β seems too small (one possible reason why ZWF excluded hcp Y from the 16 modelled metals [57]) because fitting in that range for hcp Y works not too well – and to extend the possible range of β these URs in the EMB part need to be rearranged. This *lookahead*, the conclusions which are normally discovered during the fits, is necessary to justify the fixing procedure for the ratio α to β, η and F_0 in the EMB part with new procedures. The cut-off behavior with m=n=20 works here, too. This entity of these major changes regarding the environment of the key driver parameters (α and β with a linked r_e, η and F_0 see overview on page 61) has to be kept as an intertwined concept in mind.

By returning to the lattice equilibrium condition the derivation of the ratio α to β can be presented in shortened version as and then in the second step can be simplified by putting $\Phi(1NN, 2NN, \dots)$ into eq. (3.1), using $F_1 = 0$ and plugging in and rearranging (more details below):

$$\frac{1}{2}\sum_{ij}\Phi'(r_{ij})\,r_{ij} + F'(\bar{\rho})\sum_{ij}\rho'(r_{ij})\,r_{ij} = 0 \quad (3.14)$$

$$\frac{\alpha}{\beta} = \chi \frac{B}{A} \left(\frac{\sum e^{-\beta(\frac{iNN}{r_e})}}{\sum e^{-\alpha(\frac{iNN}{r_e})}} \right) \quad \xleftrightarrow{choosing\ r_e=1NN} \quad \frac{\alpha}{\beta} = 1.875 \quad (3.15)$$

The above condition in eq. (3.12) ensures that a minimum of the pair potential, which marks the cohesion energy, exists. In the arguments of expression (3.12) all the derivatives of the pair function wrt. r, labeled by the " ´ ", are multiplied by the corresponding distance r_{ij} of the atom pair summed over all these pairs. The same is done for the electron density function and the corresponding r_{ij}. This is then multiplied in a similar manner with the corresponding EMB function at $\bar{\rho}$ $(means\ of\ all\ atoms\ and\ implies\ \rho_e)$ respectively. This just implies that the total change of the energy in both functions, pair and EMB part, is zero. Therefore, it ensures the existence of a minimum at a specified lattice constant. If this condition is not fulfilled there is no minimum and no stable equilibrium structure with a specific lattice constant, which would be unphysical. Thus, fulfilling this eq. (3.12) is absolutely essential. Plugging in the actual expression of the energy in the presented form of the previous section, eq. (3.12), and transforming leads to the form of eq. (3.15), where one simplification (1.) and helpful assumption (2.) were used:

1. The "*simplifying trick*": like in many other cases the presented simplification (3.2) in 3.1.1 becomes very useful here: using the fact that all nearest neighbours (NN) of the same order (1st, 2nd NN) have the same distance, since eq. (1) is at lattice equilibrium, all distances are covered by all the NN distances at equilibrium. Hence, they can be just plugged in a simplified manner. The corresponding plugged in distances and multiplication factors of the NN can be just summarised as a factor χ.[42] After this an α and β dependant expression in (4) is formed.
2. Underlying assumption: $F'(\bar{\rho})$ is zero. This is only true if F_1 is set to zero. Setting F_1=0 is a kind of normalisation, which ensures the existence of a minimum in the EMB part[52].[43] Consequently, by the linked nature between pair and EMB part argument this assumption immediately raises the necessity to set r_e = 1NN[44]. The alternative is to set r_e not to the 1NN and set F_1 to nonzero, this exactly corresponds to other parameter sets – but since other pots use F_1=0 for easier comparisons this convention is *inherited*.

These two points take for granted that a correct F_0 linked to the EMB contribution for the cohesion Energy is chosen (ensured by an exact analytical *dynamic* match as by Johnson and Oh [56]). Performing this manipulation and setting r_e to the 1NN, $\alpha/\beta = 1.875$ is reached. In this way one important parameter is reduced. With the detailed analytic fixings of *A* and *B* beside all the other parameter determinations only β is left to be fitted in the pair part. For consistency a similar restriction needs to be implemented for the EMB part, η is controlled empirically for greater flexibility in alloys.

Finding empirically a suitable η with the help of the EOS to control the EMB part:

Before getting into the restraining mechanism for a suitable η in the EMB part the necessity for this restraint is highlighted: if the EMB part is not controlled in one of the different ways mentioned before, then the fit of the EMB part has a disturbing proneness to yield unphysical fit results. Namely, if η is not appropriately restrained in POTFIT, POTFIT steadily changes the parameters in an unphysical manner to drastically increase the equilibrium electron density (unrealistically decreases β below 4.0 and increases f_e in alloy fitting). As a consequence, η is (*and has to be*) restrained to avoid this.

[42] χ depends on the structure (bcc, fcc or hcp). The rather lengthy mathematical manipulation for χ was performed in mathematica.

[43] This is not strictly necessary, since only the total energy needs a minimum. But this normalisation is a common convention .

[44] re = 1NN requires F_1 to be 0, because re = 1NN means that first derivative at the 1NN is 0, then F_1 also needs to be 0, so the 1st derivative of the EMB part is also zero, otherwise if a zero resulting from one part is added to a non-zero part it cannot be 0 in total

Nevertheless, *as always in the potential business* a total rigid determination of an exact η, which is kept constant during the fit, is a too far reaching loss of flexibility (though in ZWF this was exactly done this way similar to Johnson and Oh (s.b.) to grant universality of 16 metals in the expense of accuracy [57]). Here, in this formalism η is "semi-restrained". By this it is meant that a range of possible values for the parameter η is analytically determined and constantly adapted during the fit. Within this range the best suiting η for all properties will be chosen by fitting leading to improved defect and elastic properties. In order to do so, an upper limit, η_{max}, and lower limit, η_{min}, are determined and shown (Fig. 3.3) by considering the bulk modulus and elastic properties, granting a suitable slope of the potential curvature. The correct energy, cohesion energy, is granted by a dynamic fixation of F_0 described in 3.2.5.

$\boldsymbol{\eta_{max}}$ is simply determined by using the technique by ZWF [97]: by calculating the bulk modulus analytically and plugging in the analytic expressions for the potential functions (as done in detail in the closing remarks 3.2.8 of chapter 3 with some comparisons) η can be analytically fixed to meet the bulk modulus as:

$$\eta_{max}(\beta) = \frac{1}{\beta}\sqrt{\frac{9\Omega B - 15\Omega G}{F_0(\beta)}} \qquad (3.16)$$

This eq. depends on the fitting parameter β and B, Ω and G: bulk modulus, atomic volume and the Voigt shear modulus. In eq. (3.16) it is clear, that the index "max" is the upper limit for η. The reason is, that this expression completely ignores sublattice relaxations, which play a significant role in the defects of hcp materials (with sublattices due to the a and c planes). In bcc Fe this does not occur, and η_{max}=η_{min}, significantly reducing such para-sets [112]. However, regardless of the loss of the accuracy in defects (mainly, also a few percent as well in the elastic constants, in particular C_{13}), this supports the universality of the formed potential to model various metals, or respectively compensate missing DFT references for details by simplification. All in all, this supports the fitness for alloys and is good at that.

$\boldsymbol{\eta_{min}}$, the other extreme, is represented by a fixed η in another way, which fully takes the sublattice relaxations into account. However, though the accuracy is higher for single hcp metals, the performance in alloys is severely limited (since η relates to changes in the linking btw. EMB and pair part, thus relating to parameter sets which play a significant role in the determination of alloy potentials). In eq. (3.16) the used $F_0(\beta)$ is transformed to $F_0'(\beta)$ by using (only valid for hcp metals!):

$$W = \tfrac{1}{2}\left[(3C_{12} - C_{11}) - a(3C_{13} - C_{44})\right] \quad with\ a \propto \acute{\rho}(r_{ij}) \quad \& \quad F_0'(\beta) = F_0(\beta) + W \qquad (3.17)$$

$$\eta_{min}(\beta) = \frac{1}{\beta}\sqrt{\frac{9\Omega B - 15\Omega G}{F_0'(\beta)}} \qquad (3.18)$$

Luckily the sublattice relaxation energy (W), needed to find $F_0'(\beta)$, can be calculated by using the details of the elastic constants (C_{ij}, where ij labels the directions, see 3.3.2, in eq. (3.17)[45]). After $F_0(\beta)$is replaced by $F_0'(\beta)$ eq. (3.18) is exactly the same as eq. (3.16), except of the changed F_0, leading to smaller values of η.

For a better grasp of the implications of these limits, they are shown graphically for hcp Y with the presented formalism of 3.1 in Fig. 3.3 on p. 45. This figure shows the total energy contribution of the EMB part vs. the lattice constant – lattice spacings other than at the expected minimum 3.65 Å, the lattice

[45] Details for the electron density dependant *a*, which was presented here for simplicity in a shortened manner, can be found in [112]

constant, are either an elongation or compression[46], that is what is shown on the x-axis "*a*". Logically, such a distortion leads to an increase in the energy, corresponding to a state out of the equilibrium at the minimum in energy at a_0. Attention should be paid to the fact this curve in Fig. 3.3 is only a snapshot at a fixed β during the variations of it in the fitting process (changes in β also alternate the positions, minima and slope).

Having this in mind the following points about Fig 3.3 can be made:

- The green and blue curve resemble η_{max}, the upper boarder for η during the fits – In ZWF η is set to this exact value which is ideal for metallic alloys (blue curve exact ZWF technique, green curve own technique with same determination for η as in ZWF).
- The cyan (own fit with fixed η_{min}) and magenta coloured (by ZWF) curves resemble the lower limit, with exact sublattice relaxation energy influences – ideal when considering pure metals.
- For bcc Fe $\eta_{max} = \eta_{min}$, since there is no notable sublattice relaxation energy in that sense to consider, and both curves for min and max resemble the red curve (the actual EMB curve of Fe is located at a minimum at a different x value (!), but here for illustrative concepts by different para-sets ($F_1 \neq 0$) this curve was shifted (in x-direction) to be on the same scale).
- Oddly enough, following exactly the ZWF-technique (using the bulk modulus instead of elastic constants, see next pages) for hcp Y leads to discontinuities between the splines. This can be also seen in the fit section which compares own fits to the original bcc Fe EMB function by ZW on p. 64 in 3.3.2. In the improved, more accurate technique by this work, these mistakes and discontinuities were corrected.
- The most striking fact of this consideration are the observations by including the curve of the Rose eq. into the graph, this curve simply corresponds to η as: $\eta_{Rose} = \sqrt{9\Omega B/E_C}$ and exhibits an astonishing feature: as expected, this curve, the black line is between η_{max} and η_{min} as a kind of a compromise due to the approximate character of it. However, surprisingly this curve turned out as an ultimately useful borderline: separating the area of values for η, which are more suitable for alloys (top one) and, which is more suitable for single metals (bottom one). During the fitting for alloys with hcp Y, POTFIT always chose values of η in the top area (to be more exact, reproducing these curves with the fitted η in alloys always yielded curves in that area). This is a useful unexpected use for the Rose eq.
- Additionally, the lower border can be also interpreted as another parameter set, with a different $\frac{\alpha}{\beta}$ and $r_e \approx 2NN$ (still fulfilling eq. (4)) – which exactly follows the logic of parameter sets, that some are more suitable for alloys while other are less suitable.

These key drivers are an ideal compromise of exactness and flexibility in metallic alloys. F_0 has a similar importance as r_e for the pair part – but because of the more complex determination it will be explained in a separate section (3.2.5). Moreover, as said in the beginning of this section, this limitation of η by η_{max} and η_{min} was inevitable but had drastic consequences during later fits of Fe-Y phases – this obstacle required better fitting techniques, such as MEAMfit, and an compensation of Rose by using reference-free forms.

[46] This distortion changes the electron density and as a direct consequence the EMB contribution, in energy. For this illustrative plot it was assumed the distortion was distributed normally and that all distances were distorted equally and the corresponding electron density was mapped to this distorted distance and then used in the EMB function and this energy was mapped back to this distortion.

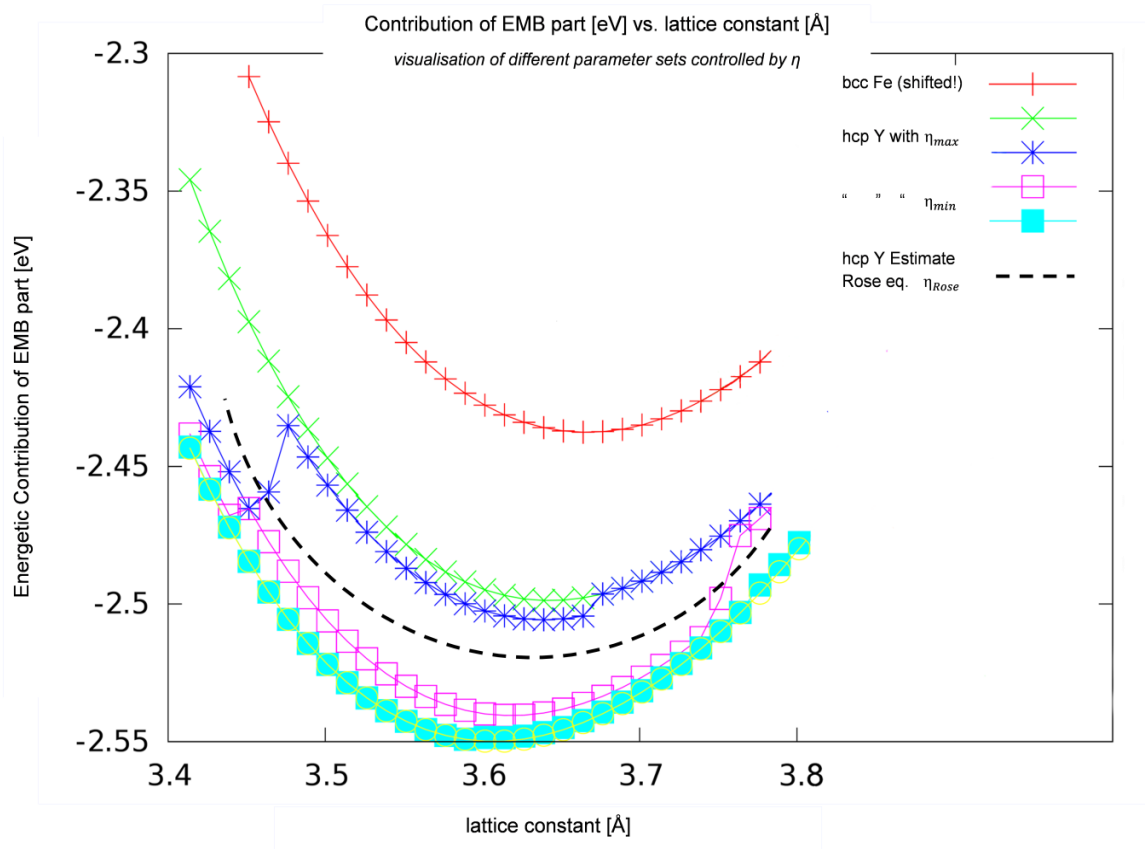

Fig. 3.3 EOS curve for hcp Y specifically for the EMB energy contribution to illustrate fine differences caused by selected choices of η (acting on the EMB part), ranging from the min. (η_{min}) at the bottom ideal for single hcp elements, since it has the exact sublattice relasxation energy W, the max (η_{max}) is better for alloys. The red curve for Fe is shifted for comparison, to show that under this parameter set distinction ther are no para-sets for Fe. Note: Å denotes from here on the atomic Unit *Angstrom* and shifted implies that the bcc curve, which is centred around 2.866 Å was shifted (transformed respectively) by 0.8 to the right to fit on the same graph as hcp Y.

Another consequence, but which can be easily overcome, is that, this flexibility of η can lead to inconsistencies in the elastic properties, when determining parameters analytically only by considering the bulk modulus in the pair and EMB part, as done originally in ZWF. Therefore, in the following section an analytical determination technique by elastic constants and continuity in the EMB splines is presented. The fitting parameters A, B and F_0, F_2 are fixed in this manner and correct these inconsistencies. This leads to more accuracy, a bit unexpectedly also for the defects. This technique also eliminates the mistake of discontinuities in the splines of the EMB functions in the original ZWF technique. On top of that, the flexibility in η solves a dilemma in the determination F_2 for hcp materials, like hcp Y. When determining F_2 by elastic constant the sublattice relaxation energy (W) should be accounted for, but this would decrease suitability of the potential for alloys when doing so. Fortunately, this fitting technique of the parameter η takes this W sufficiently into consideration, so that for F_2 the W contribution can be simply left out in F_2, while the fitness in alloy fitting is granted[47] – target fulfilled!

These key drivers ensure the right order of magnitude for the lattice constant and cohesion energy and being as well a reasonable answer to the challenging compromise of accuracy and flexibility, as mentioned before. Finally, the next section about exact analytic determinations for fine tuning follows.

[47] since the fitting of η accounts for W, the sublattice relaxation, already and corrects this little missing energy contribution

3.2.2 Linking elastic constants to the potential in general

Slope Bulk modulus elastic modulus

Now, after having ensured a satisfactory proximity to suitable energies and lattice constants, the procedure for analytically determining fit parameters by using elastic constants as rigid specifying boundary conditions for physical properties of the fitted potential follow (flexibility is granted by the aforementioned key drivers). For implementation the general definition of the elastic modulus is introduced as a starting point as (for a clearer arrangement it is done here and not in theory chapter 2):

$$E_{elas} = \frac{1}{2} C_{\alpha\beta\gamma\delta}\, \varepsilon^{\gamma\delta} \varepsilon^{\alpha\beta} \;\rightarrow\; C_{\alpha\beta\gamma\delta} = \frac{\partial^2 U}{\partial \varepsilon^{\gamma\delta} \partial \varepsilon^{\alpha\beta}} \qquad (3.19)$$

Eq. (3.19) describes the elastic energy (density) which is represented by the elongation squared and the elastic modulus. The second derivative comes originates from a Taylor expansion of the energy. It can also be interpreted as the convexity (slope of the slope) of the potential. The directional dependence is described by the α, β, γ and δ indices, where the α, β, γ and δ pairs can be summarised by the following table according to the Voigt notation:

pure strain		shear	
ij(kl)	I(J)	ij(kl)	I(J)
11	1	23,32	4
22	2	13,31	5
33	3	12,21	6

Table 3.1 Explanation of Voigt notation (I(J)) by linking the Voigt indices to the ij(kl) direction indices

The Voigt indices 1-3 describe a "pure" strain in one direction, while 4-6 describe a shear (see p.50). Elastic constants with the same indices (Voigt notation) are labeled 1-3. Combinations of these like 1-2 etc. are superpositions of one-directional strains, resulting in a two dimensional strain.
In most common metals C_{12} and C_{44} are different, so there is a difference between superposition and shear (rotational motion). This shows a certain dependence on direction which leads to a so called anisotropy. A pure pair potential can only describe non anisotropic materials, the embedding part is necessary to establish the difference between C_{12}/C_{23} and C_{44}/C_{66}. Therefore, the symmetries of linear elasticity do not apply in the case of anisotropy, like in hcp Y.
Applying the aforementioned to the potential represents one difficulty, this formula is for macroscopic measurements, which would correspond to an MD simulation of a high number of atoms, where the lattice constant is changed in the corresponding direction. The altered energy by this change is measured and then fitted to a parabola and the second order coefficient representing this parabola, the elastic modulus, can be obtained. This will be performed as a check of a fitted potentials for hcp Y in in the next section 3.3. But, staying in this definition of the elastic modulus one cannot directly deduce it by the potential parameters and its analytic form.

To do this one has to redefine the elastic modulus in terms of bonding energies, which are the equivalent to MD potential energies, enabling a direct determination of elastic constants by potential parameters (after some further transformations in the next steps). The bonding energy [52, 112] is expressed as:

$$E_b(r_{ij,0}) = \frac{\nu_0}{V} = \frac{\nu_0(r_{ij,0})}{N\Omega_0} \qquad (3.20)$$

It represents the energy between a pair of atoms at equilibrium separated by the distance $r_{ij,0}$ divided by number and volume. The N vanishes when correctly carrying out the summation as in the previous section.

When performing the calculation of lattice constants macroscopically, it is simply like a little deviation from $r_{ij,0}$ (equilibrium of a considered pair of atoms), this can be put as:

$$C_{\alpha\beta\gamma\delta} = \frac{\delta^2 \left[E_b(r_{ij}) - E_b(r_{ij,0})\right]}{\partial\varepsilon^{\gamma\delta}\partial\varepsilon^{\alpha\beta}} \quad (3.21)$$

Provided the considered difference is infinitesimally small, one can Taylor expand and gets a second order expansion around the minimum:

$$C_{\alpha\beta\gamma\delta} = \frac{1}{N\Omega}\frac{\partial^2 E}{\partial r_{ij}^{\alpha}\partial r_{ij}^{\gamma}}\bigg|_{r_{ij,0}} r_{ij,0}^{\beta}\ r_{ij,0}^{\gamma} \qquad (3.22)$$

Plugging in the formula due to the product and chain rule twice applied for the 2nd derivative as well as having an embedded and pair part it is a bit involved. One allowed simplification, since it is just the sum of the pair potential and embedding energy, is to treat both parts separately (this is because of the different directional factors, as explained later (and was also used for eq. 3.15, where the EMB part is zero by the choice of F_1). For the pair potential, φ, this results in the following formula:

$$C_{\alpha\beta\gamma\delta} = \frac{1}{2\Omega}\sum_j \left[\varphi''(r_{ij,0}) - \frac{\varphi'(r_{ij,0})}{r_{ij,0}}\right]\frac{r_{ij,0}^{\alpha}\, r_{ij,0}^{\beta} r_{ij,0}^{\gamma}\, r_{ij,0}^{\delta}}{r_{ij,0}^2} \quad (3.23)$$

Where Ω is the volume per atom and unit cell (for bcc this obviously reduces to $1/2\Omega = 1/a^3$). Then the second derivative and first derivative are plugged in with the corresponding distances between one selected atom and all its neighbours. Again, since it is at equilibrium, the sums can be simplified with the concept of m-th nearest Neighbour (which causes the differences between bcc, fcc, hcp) as done before:

$$\rightarrow C_{\alpha\beta\gamma\delta} = \frac{1}{2\Omega}\sum_m \left[\varphi''(r_{m,0}) - \frac{\varphi'(r_{m0})}{r_{m0}}\right]\frac{b_m r_{m0}^{\alpha}\, r_{m0}^{\beta} r_{m0}^{\gamma}\, r_{m0}^{\delta}}{r_{m0}^2} \quad (3.24)$$

So, the same neighbours are grouped by m groups, where m is the number of the nearest neighbour r_{m0} distance of this NN, the top indices indicate the components by the voigt notation. $a_m r_{m0}^{\alpha}\, r_{m0}^{\beta} r_{m0}^{\gamma}\, r_{m0}^{\delta}\ / r_{m0}^2$ will be simplified as a directional factor $\mu_m^{\sigma\tau}$, where m is the m-th NN and σ is $\alpha\ and\ \beta$ and τ is $\gamma\ and\ \delta$ (caused by inner derivative (chain rule) wrt. r and not the components):

$$\mu_m^{\sigma\tau} = \frac{a_m r_{m0}^{\alpha}\, r_{m0}^{\beta} r_{m0}^{\gamma}\, r_{m0}^{\delta}}{r_{m0}^2} \quad (3.25)$$

All m-th nearest neighbours will be added up and the analytic elastic constant can be summarised as:

$$C_{\sigma\tau} = \sum_m \mu_m^{\sigma\tau} * d\varphi_m \qquad (3.26)$$

Where $d\varphi_m = \varphi''(r_{im,0}) - \frac{\varphi'(r_{im,0})}{r_{ij,0}}$ (3.27)

NN/C_{ij}	C11 C_{22} C_{33}	C12 $C_{44\text{-}66}$ $C_{13,23}$
1NN	$2/(3*a_0)$	$2/(3*a_0)$
2NN	$2/a_0$	0

directional factors $\mu_m^{\sigma\tau}$ for bcc as an example

With this approach the elastic constants can be determined in a well-arranged manner. It is also computationally efficient, since for all elastic constants the derivatives only need to be computed once for the corresponding NNs. Then all these can be used for any elastic constant, since only the directional factors vary as corresponding adaptive *prefactor* (as shown in eq. (3.15)).

3.2.3 Analytic Determination of A & B in pair part by $C_{12} - C_{11}$ & C_{44}

When trying to map the elastic constants to individual potential parameters, the intertwined concept of pair and EMB function of EAM displays a significant obstacle – for full control of parameter sets it is desirable to control one physical property by one parameter. However, since for one elastic constant EMB and pair part usually contribute to the property of interest, at least two parameters are necessary, ruling out this one-to-one linking. Nevertheless, by closer looking to the determination of elastic constants and taking *smart* differences of the corresponding different elastic constants the parameters *A* and *B* can be computed solely by pair part contributions without the EMB contribution[48] and as a one-to-one mapping (one phys. property → boundary condition → one parameter –allowing a better understanding of fitting).
By evaluating the exact analytical expression for the direct calculation by potential parameters of the difference $C_{12} - C_{11}$ and considering C_{44} the usefulness of the choice of these properties becomes apparent. Expressing these as directional factors and derivatives in the formalism introduced before in 3.2.2 as a sum of the individual NN contributions $\mu_m^{\sigma\tau}$ (m= the NN and EMB_{ij} denotes the EMB contribution to the elastic constants in the *ij* indices of the elastic constants).

$$C_{11} = \mu_1^{11} * d\varphi_1 + \mu_2^{11} * d\varphi_2 + EMB_{11}$$

$$C_{12} = \mu_1^{12} * d\varphi_1 + \cancel{\mu_2^{12} * d\varphi_2} (= 0) + EMB_{12}$$

$$C_{44} = = \mu_1^{44} * d\varphi_1 + \cancel{\mu_2^{12} * d\varphi_2} (= 0) = \mu_1^{12} * d\varphi_1 = \mu_1^{11} * d\varphi_1$$

EMB (EMB_{11}, EMB_{12}) of bcc metals is for both cases the same $EMB_{11} = EMB_{12}$ by symmetry in bcc.

By additionally using $\mu_1^{12} = \mu_1^{11}$ it follows:

$$C_{11} - C_{12} = \mu_1^{11} * d\varphi_1 + \mu_2^{11} * d\varphi_2 + EMB - [\mu_1^{12} * d\varphi_1 + EMB] = \boldsymbol{\mu_2^{12} * d\varphi_2} \quad (\mathbf{3.28})$$

$$\rightarrow C_{11} - C_{12} = \mu_2^{12} * d\varphi_2 \overset{!}{\Leftrightarrow} \frac{\boldsymbol{C_{11} - C_{12}}}{\boldsymbol{\mu_2^{12}}} = \boldsymbol{d\varphi_2} \quad (\mathbf{3.28})$$

$$\frac{C_{44}}{\boldsymbol{\mu_1^{11}}} = \boldsymbol{d\varphi_1} \quad (\mathbf{3.29})$$

These relations in eq. (3.28) and (3.29) are only valid in bcc materials, because of the used relations by symmetry **(**EMB_{11}, EMB_{12} & $\mu_1^{12} = \mu_1^{11}$). For the sake of compactness and clarity in the following the simplified case of bcc is considered. More details on $\mu_2^{12}$for hcp are in the appendix in the POTFIT fitting code extract (→ A 7.3) as well as the inclusion of the 3NN, though it is negligible, see 3.2.3).
Eq. (3.28) and (3.29) are the two basic equations for the analytic determination (physical property as parameter/DOF limiting constraint) for the two parameters *A* and *B*.
The RHSs in eq. (3.28) and (3.29) are simply the derivatives with the 1NN and 2NN as input respectively. These derivatives contain all parameters of the pair potential. and reduce these by two (see overview on p. 61). The explicit derivatives in ZWF are now schematically evaluated in the following:

$$d\varphi_1 = \varphi''(1NN) - \frac{\varphi'(1NN)}{1NN} \quad (3.30)$$ with explicit distance of 1NN plugged in

$$d\varphi_2 = \varphi''(2NN) - \frac{\varphi'(2NN)}{2NN} \quad (3.31)$$ with explicit distance of 1NN plugged in

[48] This is another example of the value of the effort on the key drivers: In hcp materials there is a W contribution, since $EMB_{11} \neq EMB_{12}$ (see 3.2.1) blocking this notion as in the determination of F_2 – but by a smart key driver choice this obstacle is overcome.

The following rather lengthy derivatives will be arranged in the following way: $\varphi''(r_m)$ and $\varphi'(r_m)$ are once evaluated regardless of which NNs are plugged in (with r_m generally for 1NN and 2NN). Than for $d\varphi_1$ *and* $d\varphi_2$ 1NN and 2NN positions are plugged in successively by arranging the eqs. in a new way with the help of marked bottom brackets (see next page). Six of these brackets are used to summarise six parts of the derivative as one variable for each. In each part either the 1NN or 2NN can be plugged in, leading to 12 new variables (γ_{0-2}, $\delta_{0-2}, \xi_{0-2}, \kappa_{0-2}$for shortening) with indices running from zero to two. The new variables for better lucidity and efficiency in the POTFIT code routines are:

$$\varphi'(1NN) = A * \kappa_0\kappa_1 - B * \xi_0\xi_1 \quad (3.32) \qquad \varphi''(2NN) = A * \kappa_0\kappa_2 - B * \xi_0\xi_2 \quad (3.33)$$

$$\varphi'(2NN) = A * \delta_0\delta_1 - B * \gamma_0\gamma_1 \quad (3.34) \qquad \varphi''(2NN) = A * \delta_0\delta_2 - B * \gamma_0\gamma_2 \quad (3.35)$$

Plugging in these expressions, by eq. (3.32) & (3.33) into eq. (3.29) yielding the new expression (3.36), and eq. (3.34) & (3.35) into (3.28) yielding to eq. (3.37), leads the following clearer arrangement:

$$\frac{C_{44}}{\boldsymbol{\mu_1^{11}}} \quad = \boldsymbol{d\varphi_1} = A * \kappa_0 * \kappa_2 - B * \zeta_2 * \zeta_0 - \left(\frac{A * \kappa_0 * \kappa_1 - B * \zeta_1 * \zeta_0}{1NN}\right)$$
$$= A * \left(\kappa_0\left(\kappa_2 - \frac{\kappa_1}{1NN}\right)\right) - B\left(\zeta_0\left(\zeta_2 + \frac{\zeta_1}{1NN}\right)\right) \quad (3.36)$$

$$\frac{\boldsymbol{C_{11} - C_{12}}}{\boldsymbol{\mu_2^{12}}} = \boldsymbol{d\varphi_2} = A * \delta_0 * \delta_2 - B * \gamma_2 * \gamma_0 - \left(\frac{A * \delta_0 * \delta_1 - B * \gamma_1 * \gamma_0}{1NN}\right)$$
$$= A * \left(\delta_0\left(\delta_2 - \frac{\delta_1}{2NN}\right)\right) - B\left(\gamma_0\left(\gamma_2 + \frac{\gamma_1}{2NN}\right)\right) \quad (3.37)$$

Now each of the multiple new parameters ($\gamma_{0-2}\delta_{0-2}\xi_{0-2}\kappa_{0-2}$) will be summarised to:

$$\left(\kappa_0\left(\kappa_2 - \frac{\kappa_1}{1NN}\right)\right) = \boldsymbol{\kappa_2 - \frac{\kappa_1}{1NN} = \kappa} \qquad \left(\zeta_0\left(\zeta_2 + \frac{\zeta_1}{1NN}\right)\right) = \boldsymbol{\kappa_2 - \frac{\kappa_1}{1NN} = \xi}$$ [49]

$$\left(\boldsymbol{\delta_0}\left(\boldsymbol{\delta_2} - \frac{\boldsymbol{\delta_1}}{\boldsymbol{2NN}}\right)\right) = \boldsymbol{\delta} \qquad \left(\boldsymbol{\gamma_0}\left(\boldsymbol{\gamma_2} + \frac{\boldsymbol{\gamma_1}}{\boldsymbol{2NN}}\right)\right) = \boldsymbol{\gamma}$$

$$\Rightarrow A\delta + B\gamma = \frac{\boldsymbol{C_{11} - C_{12}}}{\boldsymbol{\mu_2^{12}}} \quad (3.38) \qquad A\kappa + B\xi = \frac{C_{44}}{\boldsymbol{\mu_1^{11}}} \quad (3.39)$$

These two equations (3.38 & 3.39) allow *A* and *B* to be calculated in a compact form as eq. (3.40):

$$\Rightarrow \boldsymbol{A = \frac{C_{11} - C_{12}/\mu_2^{12} - B\gamma}{\delta}} \quad \boldsymbol{and} \quad \boldsymbol{B = \left[\frac{C_{44} * \kappa/\mu_1^{11}}{\delta} - d\right] * \left[\frac{\gamma\kappa}{\delta} - \xi\right]^{-1}} \quad (\mathbf{3.40})$$

By this, all 7 parameters in the pair part except the one fitting parameter β, are fixed. α, κ and r_e are determined by URs, *A* and *B* are determined by this analytic method by $C_{12} - C_{11}$ & C_{44} – pair part done!

[49] *since* κ_0 & $\zeta_0 = 1 = e^{-\alpha\left(\frac{1NN}{r_e}-1\right)} = e^{-\beta\left(\frac{1NN}{r_e}-1\right)} \overset{1NN=r_e}{\Longrightarrow} e^{-\beta*0} = 1$ – Another side remark: λ is fixed by the end of the chapter.

Before moving on with the analytic methods for the EMB part, as mentioned on the previous page, here the explicit full form of the derivatives of the pair potential with the shortening variables $\gamma_{0-2}\delta_{0-2}\xi_{0-2}\kappa_{0-2}$) put under the brackets, which show what is summarised by each variable (and a visaulisation of the directions in the description of the elastic constants).

$$\varphi''(r_m) = A * e^{-\alpha\left(\frac{r_m}{r_e}-1\right)} *$$

$$\underbrace{\left[\frac{\alpha^2}{r_e^2\left(\left(\frac{r_m}{r_e}-\kappa\right)^{20}+1\right)}+\frac{40\alpha*\left(\frac{r_m}{r_e}-\kappa\right)^{19}}{r_e^2\left(\left(\frac{r_m}{r_e}-\kappa\right)^{20}+1\right)^2}+\frac{800*\left(\frac{r_m}{r_e}-\kappa\right)^{38}}{r_e^2\left(\left(\frac{r_m}{r_e}-\kappa\right)^{20}+1\right)^3}-\frac{380*\left(\frac{r_m}{r_e}-\kappa\right)^{18}}{r_e^2\left(\left(\frac{r_m}{r_e}-\kappa\right)^{20}+1\right)^2}\right]}_{\kappa_2\ for\ r_m=1NN\ /\delta_2\ for\ r_m=2NN}$$

$$- B * e^{-\beta\left(\frac{r_m}{r_e}-1\right)} *$$

$$\underbrace{\left[\frac{\beta^2}{r_e^2\left(\left(\frac{r_m}{r_e}-\lambda\right)^{20}+1\right)}+\frac{40\beta*\left(\frac{r_m}{r_e}-\lambda\right)^{19}}{r_e^2\left(\left(\frac{r_m}{r_e}-\lambda\right)^{20}+1\right)^2}+\frac{800*\left(\frac{r_m}{r_e}-\lambda\right)^{38}}{r_e^2\left(\left(\frac{r_m}{r_e}-\lambda\right)^{20}+1\right)^3}-\frac{380*\left(\frac{r_m}{r_e}-\lambda\right)^{18}}{r_e^2\left(\left(\frac{r_m}{r_e}-\lambda\right)^{20}+1\right)^2}\right]}_{\zeta_2\ for\ r_m=1NN\ /\gamma_2\ for\ r_m=2NN}$$

$$\varphi'(r_m) =$$

$$\underbrace{A\ \underbrace{e^{-\alpha\left(\frac{r_m}{r_e}-1\right)}}_{\substack{\kappa_0\ r_m=1NN\\ \delta_0\ r_m=2NN}}\left[\frac{-\beta\left(\left(\left(\kappa-\frac{r_m}{r_e}\right)^{20}+1\right)-20\left(\frac{r_m}{r_e}-\kappa\right)^{19}\right)}{a_0 r_e\ \left(\left(\kappa-\frac{r_m}{r_e}\right)^{20}+1\right)^2}\right]}_{\kappa_1\ for\ r_m=1NN\ /\delta_1\ for\ r_m=2NN} - B\ \underbrace{\underbrace{e^{-\beta\left(\frac{r_m}{r_e}-1\right)}}_{\substack{\zeta_0\ r_m=1NN\\ \gamma_0\ r_m=2NN}}\left[\frac{-\beta\left(\left(\left(\lambda-\frac{r_m}{r_e}\right)^{20}+1\right)-20\left(\frac{r_m}{r_e}-\lambda\right)^{19}\right)}{a_0 r_e\ \left(\left(\lambda-\frac{r_m}{r_e}\right)^{20}+1\right)^2}\right]}_{\zeta_1\ for\ r_m=1NN\ /\gamma_1\ for\ r_m=2NN}$$

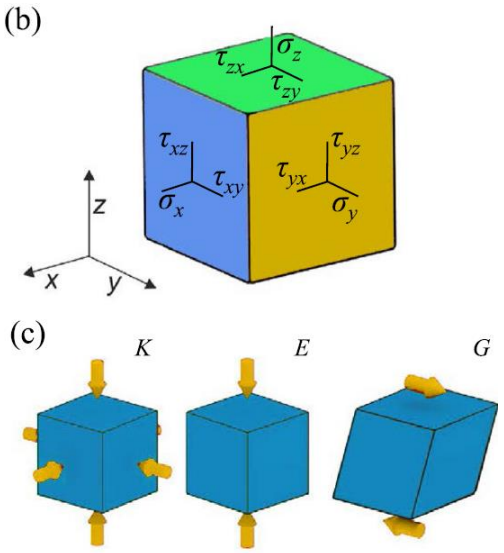

Fig. 3.4 Principal visualisation for the indexed directions on p. 46 as the strain (σ) and shear (τ), where the indices represent the direction relative to the shown Cartesian system. Below by *E* and *G* differences between strain and shear are illustrated – permitted figure extract as a courtesy by Meyers from his article in progress in material science 94 (114ff) 2018 [45].

3.2.4 Preface for F_1 and analytic determination methods in EMB part

Major determinations of F_0 and F_2

Accuracy in the embedding energy contribution is of crucial importance for the whole potential. At first the two major conditions are presented. The first one is based on the fact, that without EMB there is no difference between C_{12} and C_{44}. Using the consequence that this difference solely stems from the EMB part, this difference is used for the determination of one of the main EMB parameters, namely F_2 (3.2.5). This ensures a correct slope and is a better choice than the bulk modulus (which will be shown by a comparison to ZWF at the end of this chapter in 3.2.8). The following second condition for F_0 in 3.2.5 ensures a correct match of the EMB function for the cohesion energy and ensures a correct unrelaxed single vacancy formation energy since it originates from this, as it will be shown on the next pages.

Overview of determinations in EMB part

After these two major analytic fixings, *finer* analytic restraints in 3.2.6 are discussed such as the continuity restraints to ensure a match in value (0th order) and slope (1st order=1st derivative and once even 2nd order)[50], which **already reduces the number of EMB fit parameters from 11 to 6.** Minus two other: η is already fixed as an UR and ρ_e follows by the UR and electron density function automatically. So, 4 parameters are remaining and one of these parameters, F_1, is reserved for normalisation purposes. Leaving in principle 3 parameters F_0, F_2 (3.2.5 & 3.2.6) and the remaining determination of F_3 is used for fine tuning and compared the independently developed techniques to the ones by ZWF in the end (in 3.2.8 since it is not be used in the original sense as an high-pressure property fit parameter).

Choice of F_1:

Before starting with these three left parameters the choice of F1 with its simple physical backgrounds is repeated from the "EMB viewpoint": the $F_{\rho_n \le \rho < \rho_e}(\rho\ )$ spline describes the embedding energy around the equilibrium density. At the equilibrium density the embedding energy is supposed to have its *own* minimum, because equilibrium implies that this elec-dens driven EMB contribution is stable without external influences (as the pair part). Minimum implies zero slope (1st derivative =0) and zero slope implies no changes in the energy and the corresponding electron density, which is required since the density should not change. This implies as an analytical condition that F_1 has to be zero (the classical BJS formula cannot grant this (and requires a balancing contribution from the pair part which implies different parameter sets) this is one major reason for using splines in 3.1.3). So, F_1=0 for normalisation and all the following results are based on this common normalisation.

Side remark about choice of spline regions:

The ranges of the splines in the EMB function were simply chosen by trial and error. The only known requirements before these tries were to have a spline instead of the BJS formula around equil. and between equilibrium and zero. The following choice turned out to be reliable and efficient:

$$\text{1st spline for } \rho < 0.85\rho_e = \rho_n \qquad \text{2nd "equil. spline" for } 0.85\,\rho_e \le \rho < 1.15\,\rho_e$$

$$\text{3rd spline as "BJS spline" for } 1.15\,\rho_e \le \rho$$

Changes in this arrangement did not yield any advantages, therefore it's the same as in ZW [97]. The second and third spline are labeled by specific names (s.a.), which will be adhered to in this chapter.[51]

[50] $F_{\rho<\rho_n}(\rho_n) = F_{\rho_n \le \rho < \rho_e}(\rho_n)$ & $F'_{\rho<\rho_n}\ (\rho_n) = F'_{\rho_n \le \rho < \rho_e}\ (\rho_n)$ $F_{bjs}(\rho_0) = F_{\rho_n \le \rho < \rho_e}(\rho_0)$ & $F'_{bjs}\ (\rho_0) = F'_{\rho_n \le \rho < \rho_e}\ (\rho_0)$

[51] Remark about details: ZW used 4 splines in alloys for better high pressure properties, but this is unnecessary here (see 3.2.8).

3.2.5 Analytic Determination of F_0 in EMB part & setting F_{n3} by norming

So, in the EMB part in principle only 3 parameters left (with η and β as fitting parameters). This makes sense since the standard BJS formalism contains 3 parameters and is explaining the EMB well except of few discrepancies as mentioned in 3.1.3. Hence, in principle there should not be more parameters.

F_0 as a main driver for the correct cohesion energy contribution by the EMB part can be calculated in two ways, the first one is presumably the one which was taken by the potential developers and is further discussed at the end of this chapter. The second route developed in the 80's by Ackland, Johnson and Oh et. al. [55, 133] is by considering the unrelaxed vacancy energy, E_V, which will be used for an analytic determination. The first step is to consider the expression of total energy at equilibrium, leading to the definition of the cohesion energy, in the known EAM method:

$$E_{Tot}\ at\ equil. \overset{\text{def}}{=} E_C = \frac{1}{2}\sum_m \varphi(r_m) + F\ (\rho_e) \quad where \quad \rho_e = \sum_m \rho(r_m)$$

Where as said before at equilibrium spacing the energy required to remove one atom can be interpreted as the corresponding EMB part. Consequently, one parameter can be fixed by aligning one parameter to it – this is exactly leading to the unrelaxed single vacancy formation energy, leading to $E_V = \Delta E_i + E_C$[52], which is calculated in the EAM framework in the following (resulting in eq. 3.41): to do this, the removal of one atom from a structure at equilibrium will be analytically run through as a mental exercise. Similar to the consideration of the bonding energy concept in 3.2.1, the change of E_{Tot} by removing an atom is calculated as ΔE_i by considering the differences of E_{Tot} with and without vacancy in eq. (31):

$$\Delta E_i \quad \underbrace{-\sum_{Sij}\varphi_{Sij}(r_{ij}) - F_{Sij}\ (\rho_e)}_{\substack{pair\ part\ contr.broken\ bonds \\ \varphi_{Sij}\ expressed\ as\ \phi_e\ see\ note^{53}}} + \underbrace{\sum_{ij}\left[F_{Sij}\ \left(\rho_e - \rho_{Sij}(r_{Sij})\right) - F_{Sij}\ (\rho_e)\right]}_{\substack{emb\ part\ contr.\ by\ change\ in \\ electron\ density}} \quad (3.41)$$

$$\overset{E_V=\Delta E_i+E_C}{\Longrightarrow} \quad -\tfrac{1}{2}\sum_{Sij}\varphi_{Sij}(r_{ij}) + \sum_{ij}\left[F_{Sij}\ \left(\rho_e - \rho_{Sij}(r_{Sij})\right) - F_{Sij}\ (\rho_e)\right] \quad \overset{Taylor}{\Longrightarrow} \quad \phi_e + F_0 \underbrace{\left(\frac{\rho_e}{\rho_e} - 1\right)^0}_{\frac{\rho_e}{\rho_e}=1 \Rightarrow 0^0=1} +$$

$$\underbrace{\cancel{F_1\left(\frac{\rho_e}{\rho_e} - 1\right)^1}}_{F_1=0} + \underbrace{F_2\left(\frac{\rho_e}{\rho_e} - 1\right)^2 + F_3\left(\frac{\rho_e}{\rho_e} - 1\right)^3}_{=0\ \Leftrightarrow \left(\frac{\rho_e}{\rho_e}-1\right)^2=(1-1)^2=0^2\ and\ ...=0^3} \quad \Leftrightarrow \quad \boldsymbol{\phi_e + F_0 = E_C}$$

$$\Rightarrow \boldsymbol{E_c - \phi_e(A,B,\beta) = F_0} \quad \boldsymbol{(3.42)}$$

In eq. (3.41) the first bracket corresponds to the change in total energy caused by the broken bonds of the removed atom (at site Si, where the "S" denotes that atom i will be kept constant and all surrounding j atoms are considered with a constant e-dens. causing a loss in the EMB contribution by the electron cloud expressed as $F_{ij}\ (\rho_e)$). The second bracket considers the change in electron density by the removed atom and thus a change in the electron clouds and its energy contribution by considering the EMB part with a

[52] More details about that in the result section 3.3.4 considering defects

[53] $E_{C\ pair\ part} = \sum_m \varphi(r_m) = \frac{A}{1+(1-\kappa)^{20}} - \frac{B}{1+(1-\lambda)^{20}} + \frac{Ae^{-\alpha\left(\frac{2NN}{r_e}-1\right)}}{1+\left(\frac{2NN}{r_e}-\kappa\right)^{20}} - \frac{Be^{-\beta\left(\frac{2NN}{r_e}-1\right)}}{1+\left(\frac{2NN}{r_e}-\lambda\right)^{20}} + \frac{Ae^{-\alpha\left(\frac{3NN}{r_e}-1\right)}}{1+\left(\frac{3NN}{r_e}-\kappa\right)^{20}} - \frac{Be^{-\beta\left(\frac{3NN}{r_e}-1\right)}}{1+\left(\frac{3NN}{r_e}-\lambda\right)^{20}} = 2\phi_e$

decreased electron density $(\rho_e - \rho_{Sij}(r_{Sij}))$ in comparison to the EMB part before removal with an equilibrium ρ_e.
This second bracket in eq. (3.41) can be Taylor expanded leading to the clear expression in eq. (3.42). (incl. summary of pair. contribution as ϕ_e, see footnote on p. 52). Finally, a reliable expression for F_0 is obtained which is directly linked to the cohesion energy E_c, which serves as a known physical property for one constant input replacing one parameter. Therefore, it can be interpreted as an analytical restriction to ensure the EMB part "*keeps the correct cohesion energy in mind*". The splitting between pair and EMB part is guided by the vacancy formation energy.
The ϕ_e in eq. (3.42), which controls the pair contribution as opposed to ZWF, is not a fixed constant but a *dynamic* expression. The difference to ZWF has to be highlighted: here ϕ_e depends on the analytically restricted but varying parameters *A, B* and the fitting parameter β during the optimisation. By β, which is also a main fitting parameter in the pair part, this analytic determination is also linked by fitting to the pair part (therefore as with the key drivers, by fitting a correct match of both parts is ensured). Thus, parameter sets are dynamically changed during the fit (these changes to ZWF, as done with the variable key driver η for a more flexible technique is consequently continued), as opposed to ZWF which restricts parameter sets by keeping these three variables constant and reproducing a static ϕ_e[54] (this is connected to the determination of *A and B* by the bulk modulus see end of section, 3.2.8). Again, when considering alloys and hcp Y this is of great advantage. On top of that defect properties are improved by the procedure.
However, when trying to reproduce fits and its parameters of known potentials, for instance *A and B* or the exact F_0=2.5400 (for bcc Fe in ZW) *A* and *B* need to be accurate for 5 decimal places and β even to six decimal places. This leads as mentioned before to little inaccuracies (few 0.1 ‰), because of the varying $\phi_e - F_0$ cannot be reproduced 100%. However, fixing ϕ_e to a definite value, some potential developers take this as the unrelaxed vacancy formation energy solves this. But this *kills* flexibility, especially in alloys – thus, it is adhered to the technique in eq. (3.42).

Restraining F_{n3} for a reliable "zero level energy" in the EMB part

This aforementioned procedure requires that the EMB function is zero at ρ=0 (which is also physical). This can be simply enforced by the following eqn.:

$$F(0) = 0 \overset{plugging\ into\ spline}{\Longleftrightarrow} F_{n0} + F_{n1} + F_{n2} + F_{n3} = 0$$

$$\Rightarrow F_{n3} = -(F_{n0} + F_{n1} + F_{n2})$$

This equation can be then simply transformed to the final form for F_{n3} as shown in the next line above. This eqn. ensures that the calculated F_0 is relative to an absolute zero at ρ=0. This is important since the calculated energies for F_0 are relative to this zero level.

Nevertheless, tiny deviations (up to 0.005 - 0.01 eV) from this rule can be tolerated for the sake of the following argument: this is only an EAM potential ignoring angular dependence. Angular dependence can be artificially included without actually including it by a modification function, which is mostly applied around the equilibrium or as a "background energy" (this will be done on a bigger and more refined scale in chapter 5). The small deviation serves as a background energy, which causes more accuracy in defects– however, since this is kind of an artificial inaccuracy (for the sake of defects) the computational effort to calculate all major properties analytical and only accept tiny property deviations is taken. This additional control resulted in actual chosen deviation (at $F(0)$) of up to 0.006 eV during fitting – defect properties were improved by up to 3% and hence this was considered to be acceptable and even worth the effort.

[54] Some potential developers set ϕ_e simply (but incorrectly) even to some seemingly unrelaxed vacancy formation energy

3.2.6 Analytic Determination of F_2 in EMB part by $C_{12} - C_{11}$

As announced before by considering the embedding contribution to the elastic constants, F_2 can be fixed. Now this is done by computing the embedding contribution to the elastic constants (Emb_{Cij}) as:

$$\frac{\dot{F}(\bar{\rho}_0)}{\Omega}\sum_m(\ddot{\rho}(r_m)-\dot{\rho}(r_m)/r_m)\left(\frac{r_m^\alpha r_m^\beta r_m^\gamma r_m^\delta}{r_m^2}\right)+\frac{\ddot{F}(\bar{\rho}_e)}{\Omega}\left(\sum_m\dot{\rho}(r_m)\frac{r_m^\alpha r_m^\beta}{r_m}\right)\left(\sum_m\dot{\rho}(r_m)\frac{r_m^\gamma r_m^\delta}{r_m}\right)$$

$$\xrightarrow{\dot{F}(\bar{\rho}_0)=0}\ \frac{\ddot{F}(\bar{\rho}_e)}{\Omega}\left(\sum_m\dot{\rho}(r_m)\frac{r_m^\alpha r_m^\beta}{r_m}\right)\left(\sum_m\dot{\rho}(r_m)\frac{r_m^\gamma r_m^\delta}{r_m}\right)\qquad(3.43)$$

Whereas before Ω is the volume per atom and unit cell. For distinction of the derivatives in the pair part the dots denote the first and second (double dot) derivatives, ρ represents the electron density and r_m are the m-th-NN and the directional factors r_m^X are the same as before, see 3.2.1. The sums go over all neighbours. So, in bcc over 8 1NN and then the same for the 2NN. It has to be noted that the eq. (3.43) reduces slightly since $\dot{F}(\bar{\rho}_0)=0$ because F_1 is chosen to be 0 (which has *normalisation backgrounds*).
Using symmetries namely $\sum_m x_m^2y_m^2 = \sum_m y_m^2z_m^2$ for cubic symmetries and $\sum_m x_m^2z_m^2 = \sum_m y_m^2z_m^2$ for hcp metals one can take smart subtractions of C_{ij}, as in 3.2.1, resulting in:

$$fcc\ \&\ bcc:\ C_{12}-C_{44}\equiv(c_{1122}-c_{2323})=\frac{\ddot{F}(\bar{\rho}_e)}{\Omega}\left(\sum_m\dot{\rho}(r_m)\frac{x_m^2}{r_m}\right)^2\qquad(3.44)$$

$$hcp:\ C_{13}-C_{44}\equiv(c_{1133}-c_{2323})=\frac{\ddot{F}(\bar{\rho}_0)}{\Omega}\left(\sum_m\dot{\rho}(r_m)\frac{x_m^2}{r_m}\right)\left(\sum_m\dot{\rho}(r_m)\frac{z_m^2}{r_m}\right)\qquad(3.45)$$

Great care has to be taken that in hcp $C_{13}=c_{1133}\neq 0\neq c_{1122}=C_{12}$

Now, additional directional factors, labelled as ϑ_{XNN}^{bcc} are established as $\sum_m\frac{x_m^2}{r_m}$ for bcc and used for(3.44):

1NN - ϑ_{1NN}^{bcc}	$\frac{4a_0}{\sqrt{3}}$	$\frac{4F_2}{\rho_e^2\,a_0^3}$ (3.46)
2NN - ϑ_{2NN}^{bcc}	2*a_0	= pre-factor replacing $\frac{\ddot{F}(\bar{\rho}_0)}{\Omega}$ as pre2b

$$\xrightarrow{plugging\ factors\ for\ bcc} C_{12}-C_{44}\equiv(c_{1122}-c_{2323})=pre2b*(\dot{\rho}(r_{1NN})\vartheta_{1NN}^{bcc}+\dot{\rho}(r_{2NN})\vartheta_{2NN}^{bcc})^2\quad(3.47)$$

Similar to 3.2.1 for a clearer arrangement and better overview the more transparent case of bcc metals is considered (the more advanced but harder to follow case for hcp is in the POTFIT code routine in the appendix (7.3)). The factor *pre2b* is obtained by expanding the above formula (3.43) for the EMB part in the aforementioned formalism by ZW, simply by taking the 2nd derivative of the EMB energy (in the correct spline region $\rho_n<\rho<\rho_0$ which applies for $\bar{\rho}_e$ (calculated by summing NNs at equil., $\rho=\rho_e$)[55]

[55] $F(\rho)=\sum_{i=0}^3F_i*\left(\frac{\rho}{\rho_e}-1\right)^i=F_0+F_2*\left(\frac{\rho}{\rho_e}-1\right)^2+F_3*\left(\frac{\rho}{\rho_e}-1\right)^3\ \xrightarrow{yields}\ \frac{d^2F(\rho)}{d^2x}=\frac{2F_2}{\rho_e^2}+\frac{6F_3}{\rho_e^2}\left(\frac{\rho}{\rho_e}-1\right)^1\ \xleftrightarrow{\frac{d^2F(\rho_e)}{d^2x}}\ \frac{2F_2}{\rho_e^2}\equiv\ddot{F}(\bar{\rho}_e)$
$\xRightarrow{\frac{1}{\Omega}}\frac{\ddot{F}(\bar{\rho}_e)}{\Omega}=\frac{2F_2}{\rho_e^2}*\frac{2}{a_0^3}$

This can be plugged in but before doing so $\dot{\rho}(r_{1NN})\ and\ \dot{\rho}(r_{2NN})$ need to be computed as:

$$\rho(r_m) = \frac{f_e e^{-\beta\left(\frac{r_m}{r_e}-1\right)}}{\left(\frac{r_m}{r_e}-\lambda\right)^{20}+1}$$

$$\dot{\rho}(r_m) = \frac{\left[\beta * \left(\left(\lambda-\frac{r_m}{r_e}\right)^{20}+1\right) - 20\left(\frac{r_m}{r_e}-\lambda\right)^{19}\right] * f_e * e^{-\beta\left(\frac{r_m}{r_e}-1\right)}}{r_e\left[\left(\lambda-\frac{r_m}{r_e}\right)^{20}+1\right]^2}$$

, where r_m are for NN. Substituting the 1NN and 2NN as $r_e\ (1NN)\ and\ a_0$ into the previous eq. yields:

$$\dot{\rho}(r_{1NN}) = \frac{[\beta * ((\lambda-1)^{20}+1) - 20(1-\lambda)^{19}] * f_e}{r_e\,[(\lambda-1)^{20}+1]^2} \quad (3.48)$$

$$\dot{\rho}(r_{2NN}) = \frac{\left[\beta * \left(\left(\lambda-\frac{a_0}{r_e}\right)^{20}+1\right) - 20\left(\frac{a_0}{r_e}-\lambda\right)^{19}\right] * f_e * e^{-\beta\left(\frac{a_0}{r_e}-1\right)}}{r_e\left[\left(\lambda-\frac{a_0}{r_e}\right)^{20}+1\right]^2} \quad (3.49)$$

Knowing now $\dot{\rho}(r_{1NN})$ (3.48), $\dot{\rho}(r_{2NN})$(3.49), and ϑ_{1NN}^{bcc}, ϑ_{2NN}^{bcc} and $pre2b$ from the table, these can be readily inserted into eq. (3.44) yielding:

$$C_{12} - C_{44} \equiv pre2b * (\dot{\rho}(r_{1NN})\vartheta_{1NN}^{bcc} + \dot{\rho}(r_{2NN})\vartheta_{2NN}^{bcc})^2$$

$$\rightarrow\ C_{12} - C_{44} = \frac{4F_2}{\rho_e^2\, a_0^3} *$$

$$\underbrace{\left[\frac{4a_0}{\sqrt{3}} * \frac{[\beta * ((\lambda-1)^{20}+1) - 20(1-\lambda)^{19}] * f_e}{r_e\,[(\lambda-1)^{20}+1]^2} + 2a_0 \frac{\left[\beta * \left(\left(\lambda-\frac{a_0}{r_e}\right)^{20}+1\right) - 20\left(\frac{a_0}{r_e}-\lambda\right)^{19}\right] * f_e * e^{-\beta\left(\frac{a_0}{r_e}-1\right)}}{r_e\left[\left(\lambda-\frac{a_0}{r_e}\right)^{20}+1\right]^2}\right]^2}_{\boldsymbol{w(\beta)}}$$

$$\Rightarrow\ C_{12} - C_{44} = \frac{4F_2}{\rho_e^2\, a_0^3} * w(\beta) \Leftrightarrow \frac{(\ \boldsymbol{C_{12} - C_{44}}\ ) * \boldsymbol{\rho_e^2\, a_0^3}}{\boldsymbol{4w(\beta)}} = \boldsymbol{F_2} \quad \boldsymbol{(3.50)}$$

In this way F_2 can be calculated accurately by elastic constants, its difference respectively. For satisfactory accuracy the 3NN can be ignored (change in 4th decimal place) due to other influences by continuity restraints.[56] Now all restraints by physical properties are applied, only the continuity restrains in the next section are missing. It can be already said, that this represents an ideal compromise leading to refined elastic properties, as shown in the EAM fitting results of 3.3.

[56] The continuity conditions on the next pages, especially by F_{n2} and F_3, help to carry on the detailed properties contained in the last spline fixed by η. This *feedback* also includes W and as said before replaces the inclusion of W by these analytic considerations. to here by F3 (is not in that area but by linking allowed…)

3.2.7 Complying with continuity in splines by analytic restraints

After having performed the two major analytical determinations by physical conditions of F_2 (mainly elastic properties) and F_0 (mainly energy), the second major class of boundary conditions (BC) in the form of continuity conditions needs to be performed as introduced in the preface of 3.2.4. Continuity simply implies that the splines merge fluently without any jumps (discontinuities). This is simply done by setting up analytic constraints (BC) for matches in 0th, 1st order and partially as well in 2nd order as:

$$F_{\rho<\rho_n}(\rho_n) = F_{\rho_n\leq\rho<\rho_e}(\rho_n) \;\&\; F'_{\rho<\rho_n}\;(\rho_n) = F'_{\rho_n\leq\rho<\rho_e}\;(\rho_n) \quad F_{bjs}(\rho_0) = F_{\rho_n\leq\rho<\rho_e}(\rho_0) \;\&\; F'_{bjs}\;(\rho_0) = F'_{\rho_n\leq\rho<\rho_e}\;(\rho_0) \quad (3.51)$$

Additionally to a continuous matching, these continuity conditions also act as a kind of transmitter of physical properties, namely 0th order for energy, 2nd order for bulk modulus and/or elastic properties. This is essential for the key driver η – since η is strictly speaking only linked to the bulk modulus and not directly evaluated in the equilibrium region where the bulk modulus is affected – but by the continuity-in-value-linking of F_3 with η (see eq. (3.56)) transmits its bulk properties from the BJS spline to the second spline at equilibrium – this linking allows this consideration of B for η in the last (BJS) spline. This continuity of F_3 also ensures a kind of feedback from η on the equilibrium spline for the properties by F_2 – this feedback includes the W contribution (sublattice relaxation). Because effectively it is an interplay of F_0, F_2 and F_3, η acts as a kind of corrective for the missing W contribution in F_2 because the sum in this equil. spline of F_0, F_2 and F_3 includes W by the contribution of F_3. And this interplaying combination of F_2 and F_3 simplifies the performed determination of F_2 by a great deal.[57] So, by these links a refined sensitive system is set up (major restrains at BJS spline – 2nd equil. spline for bulk modulus and mutual feedback). These individual continuity conditions and its *global links* are a bit further discussed with the simple evaluation of them by plugging the splines into eq. 3.51, yielding the following conditions:

After the determination F_2 it will be started with the continuity eq. for F_{n2} by the second derivative since this can be interpreted as transmitting the correct bulk/elastic properties of the equilibrium spline with F_2 to the first spline by F_{n2} simply using $F''_{\rho<\rho_n}\;(\rho_n) = F''_{\rho_n\leq\rho<\rho_e}\;(\rho_n)$ the explicit second derivatives are:

$$F''_{\rho<\rho_n}\;(\rho\;) = \frac{2F_{n2}}{{\rho_n}^2} + \frac{6F_{n3}}{{\rho_n}^2}\left(\frac{\rho}{\rho_n} - 1\right)^1 \qquad F''_{\rho_n\leq\rho<\rho_e}\;(\rho\;) = \frac{2F_2}{{\rho_e}^2} + \frac{6F_3}{{\rho_e}^2}\left(\frac{\rho}{\rho_e} - 1\right)^1$$

$$\overset{\rho=\rho_n}{\underset{0=\frac{\rho_n}{\rho_n}-1}{\Longrightarrow}} \frac{2F_{n2}}{0.85^2{\rho_e}^2} = \frac{2F_2}{{\rho_e}^2} + \frac{6F_3}{{\rho_e}^2}\left(\frac{0.85\,\cancel{\rho_e}}{\cancel{\rho_e}} - 1\right)^1 \Leftrightarrow \boldsymbol{F_{n2} = 0.7225 * [F_2 + 0.45F_3]} \;\; \boldsymbol{(3.52)}$$

By this a correct slope and elastic properties in the first spline are ensured and an additional match in concavity to the equilibrium spline. Similarly, for the correct energies the continuities in 0th order transmit the correct energy level of the equilibrium spline, controlled by F_0, to the first spline by F_{n0} and to the last BJS spline by F_e, applying corresponding continuity eq. from (3.51) yields continuity condition (3.52) :

Continuity btw. 2nd equil. spline and BJS spline by value → $F_{bjs}(\rho_0) = F_{\rho_n\leq\rho<\rho_e}(\rho_0)$

$$\overset{\rho_0=1.15\rho_e}{\Longrightarrow} F_e \underbrace{\left[1 - ln\left(\frac{1.15\,\cancel{\rho_e}}{\cancel{\rho_e}}\right)^{\eta}\right]\left(\frac{1.15\,\cancel{\rho_e}}{\cancel{\rho_e}}\right)^{\eta}}_{pF} = F_0 + \underbrace{\cancel{F_1 \cdots}}_{F_1=0} + F_2\left(\frac{1.15\,\cancel{\rho_e}}{\cancel{\rho_e}} - 1\right)^2 + F_3\left(\frac{1.15\,\cancel{\rho_e}}{\cancel{\rho_e}} - 1\right)^3$$

$$\Rightarrow F_e * pF = F_0 + 0.0225F_2 + 0.003375F_3 \Leftrightarrow \boldsymbol{F_e * pF - 0.0225F_2 - 0.003375F_3 = F_0} \;\; \boldsymbol{(3.53)}$$

[57] One could insist that exactly including W in 3.2.6 is more accurate – but the insight, that an exact W is even contraproductive by decreasing flexibility for alloys justifies this approach reasonably! For more supporting facts refer to the result section 3.3.

Continuity btw. 1st[nd] spline and 2[nd] equil spline by value: $F_{\rho_n>\rho}(\rho_n) = F_{\rho_n\leq\rho<\rho_e}(\rho_n)$

$$\xrightarrow{\rho_n=0.85\rho_e} F_{n0} + \underbrace{F_{n1}\left(\frac{\cancel{\rho_n}}{\cancel{\rho_n}}-1\right)^1 + F_{n2}\left(\frac{\cancel{\rho_n}}{\cancel{\rho_n}}-1\right)^2 + F_{n3}\left(\frac{\cancel{\rho_n}}{\cancel{\rho_n}}-1\right)^3}_{=0\ since\ \left(\frac{\cancel{\rho_n}}{\cancel{\rho_n}}-1\right)^x=(1-1)^x=0^x}$$

$$= F_0 + F_2\left(\frac{0.85\cancel{\rho_e}}{\cancel{\rho_e}}-1\right)^2 + F_3\left(\frac{0.85\cancel{\rho_e}}{\cancel{\rho_e}}-1\right)^3 = F_0 + 0.0225F_2 - 0.003375F_3$$

$$\Rightarrow \boldsymbol{F_{n0} = F_0 + 0.0225F_2 - 0.003375F_3} \ \boldsymbol{(3.54)}$$

This leads to an accurate definition of F_0 and F_e by energy levels suitable for the EMB part by considering cohesion energy, vacancy formation energy and also continuity (this also improves defect properties).[58] The last point is important, because in principle this information about vacancy formation energies is missing in the pair potential. But the pair potential is as well indirectly influenced by the vacancy formation energy by the interplay of η and *A*, *B* and β – an efficient linking of pair and EMB part.
All in all, the cohesive energy and vacancy formation energy are accurately translated to all splines.

As opposed to F_1 the value of F_{n1} on the other hand is not zero, because it describes the region below the equilibrium density where no equilibrium occurs (and therefore a minimum is not necessary to by setting $F_{n1} \neq 0$). Since this is the same situation in the last spline of the BJS equation[59] it can be readily computed by continuity of the first derivative $F'_{\rho<\rho_n}(\rho_n) = F'_{\rho_n\leq\rho<\rho_e}(\rho_n)$:

$$F'_{\rho_n\leq\rho<\rho_e} = \frac{2F_2}{\rho_e}\left(\frac{\rho}{\rho_e}-1\right)^1 + \frac{3F_3}{\rho_e}\left(\frac{\rho}{\rho_e}-1\right)^2 \ \&\ F'_{\rho<\rho_n} = \frac{F_{n1}}{\rho_n} + \frac{2F_{n2}}{\rho_n}\left(\frac{\rho}{\rho_n}-1\right)^1 + \frac{3F_{n3}}{\rho_n}\left(\frac{\rho}{\rho_n}-1\right)^2$$

$$\xrightarrow{\rho_n=0.85\rho_e} \frac{2F_2}{\rho_e}\left(\frac{0.85\cancel{\rho_e}}{\cancel{\rho_e}}-1\right)^1 + \frac{3F_3}{\rho_e}\left(\frac{0.85\cancel{\rho_e}}{\cancel{\rho_e}}-1\right)^2 = \frac{F_{n1}}{0.85\rho_e} + \frac{\cancel{2F_{n2}}}{\cancel{\rho_n}}\left(\frac{\cancel{\rho_n}}{\cancel{\rho_n}}-1\right)^{\cancel{1}} + \frac{\cancel{3F_{n3}}}{\cancel{\rho_n}}\left(\frac{\cancel{\rho_n}}{\cancel{\rho_n}}-1\right)^{\cancel{2}}$$

$$\boldsymbol{F_{n1} = 0.85 * (0.3F_2 + 0.0675F_3)} \ \boldsymbol{(3.55)}$$

Except of F_3 all EMB parameters are now fixed. Before moving on, as said before, the 2[nd] order continuity between the equil. spline and BJS spline is waived for more flexibility and for the key driver η, which ensures a match to the physical elastic properties (however the continuity of the concavity between these two splines is checked during the fitting and only little tolerable deviations are accepted).

Finally, one of the most important links since it regards the key driver η as explained before – the previous considerations lead to transmitting η by continuity in first order. So, F_3 can be calculated by:

$$\boldsymbol{F_3 = \frac{-\eta * \left(\frac{\rho}{\rho_e}\right)^{\eta} ln\left(\frac{\rho}{\rho_e}\right)^{\eta}}{1.15 * 0.0225} - \frac{2F_2}{3 * 0.15}} \ \boldsymbol{(3.56)}$$

A second order continuity would interfere with the influence of the bulk modulus on η by the exact analytic expression for elastic constants in F_2. As explained in 3.2.1 this η includes the sublattice relaxation energy

[58] *And a useful amendment to the ZWF technique, which omits this by keeping these three fixed as constants*
[59] As said before that the reason why the sole use of the BJS eq. for the EMB part is problematic – since it inherently has no normalization parameter to control a minimum.

by fitting in a range restricted by analytic determinations originating from the bulk modulus. By trial and error it has been worked out that this first order continuity of F_2 and F_3 with η transmits in the best flexible way corrections for W onto the equilibrium spline. Besides, this flexibility crucially improves the defect properties (by further fine adjustment in η while fitting to defect configs.) – an ideal final amendment for the application in Fe-Y. All parameters have been considered now and are summarised on p. 61 (except λ which is simply set by anisotropy considerations, see overview).

3.2.8 Comparison

Original analytical parameter fixing methodology by Zhou and Wadley

The aforementioned technique to analytically restrict or fix parameters (6x analytic restraints, 2x URs and 5x continuity conditions for each metal see overview on. p. 61) creates a significant contrast to the fitting techniques technique of the original developers, ZW, of this kind of potential form. The original potential scheme is now presented in a comparing manner and similarities, causing systematic obstacles, are highlighted. It has to be stressed, that the scheme by ZW was adopted from Johnson and Oh [55] (this technique here could be called one potential of the 3rd generation after ZW as 2nd generation [96]). This 2nd generation produces more accurate E_c (up to 0.025 eV) but no appreciable improvements in the vacancy formation energy (or defects), which is noticeably improved by this 3rd generation and ready for implantation into the next stage of RF-MEAM, see next chapter 4.

To start with the most important feature, the first universal relation (UR, $\alpha/\beta=1.875$) in this developed scheme is the same as in ZW. This is a strength and weakness at the same time. On the one hand this helps to restrict the parameter space to a seemingly global minimum and makes fitting much simpler. Without advanced optimisation techniques this is even essential, since the plain LSM in POTFIT seems to be not working without this UR. On the other hand this greatly reduces the number of possible parameter sets and constitutes substantial challenges in alloys (see 3.3.5 and 3.3.6) since one cannot forgo fitting without this UR in POTFIT – this UR is the lynchpin in POTFIT fitting of metals.

After this main global similarity, now important differences leading to more flexibility and better defect representation are presented, one subsection about the analytic fixing in general and one specifically dedicated to the determination of F_3 (affiliated to claimed innovations in fitting which will be questioned).

Analytic Fixing in general: ZW fixed the parameters in the pair potential by using the Voigt shear modulus eq. (3.58) presumably for parameter *A* or *B*. The remaining parameter of *A* and *B* was then determined by using the bulk modulus to estimate a suitable ratio of *A/B*[60]. α or β was determined by a reduced lattice equilibrium condition eq. (3.58) and the remaining one by the aforementioned UR. The anisotropy formula served to determine λ. With r_e set to 1NN all parameters in the pair part are set.

$$0 = 4r_{1NN}^2\varphi'_{1NN} + 3r_{2NN}^2\varphi'_{2NN} \quad (3.57) \qquad 15\Omega G = 4r_{1NN}^2\varphi''_{1NN} + 3r_{2NN}^2\varphi''_{2NN} \quad (3.58)$$

However, two obvious problems have to be immediately raised: 1. There seems to be no need to fix separately by eq. (3.57) the lattice constant to a_0, since this is already set by the fixation of r_e. This is slight overfitting, reducing transferability, which is especially not desired for alloys. 2. The bulk modulus is a kind of averaged elastic constants. As a consequence the specific elastic constants are less accurate, by 5-10%. This seems to decrease the prediction about the more involved vacancy formation energies. Fitting to directional elastic constants makes these vacancy formation energies more accurate!

[60] $B = \frac{1}{9\Omega}\left[F''(\rho_e)(\sum_m r_m\hat{\rho}(r_m))^2 + \underbrace{\cancel{F'(\rho_e)*\sum_m r_m^2\hat{\rho}(r_m)}}_{since\ F1=0\ s.a.} + \frac{1}{2}\sum_m r_m{}^2\phi'(r_m)\right]$, but how they uncoupled the EMB contribution remains a *mystery*.

In the EMB part one important difference is, that instead of fixing F_e by continuity (the advantages were discussed in detail in 3.2.5), they fix it as in in the original paper of Johnson and Oh [56], by the modified BJS formula by:

$$F_e = -(E_c - E_{1V}^{UF}) \qquad with \;\; E_{1V}^{UF} = -4\varphi_{1NN} - 3\varphi_{2NN} \quad (3.59)$$

$$-4\varphi_{1NN} - 3\varphi_{2NN} = \frac{-4A}{1+(1-\kappa)^{20}} + \frac{4B}{1+(1-\lambda)^{20}} - \frac{3Ae^{-\alpha\left(\frac{2NN}{r_e}-1\right)}}{1+\left(\frac{2NN}{r_e}-\kappa\right)^{20}} + \frac{3Be^{-\beta\left(\frac{2NN}{r_e}-1\right)}}{1+\left(\frac{2NN}{r_e}-\lambda\right)^{20}}$$

E_{1V}^{UF} is the relaxed vacancy formation energy, which implies creating a vacancy and not allowing the lattice to relax. The resulting F_e is in pretty good agreement with the parameters by Zhou and Wadley [57]. Performing MD runs, it was found that the 3NN should be included, see 3.2.5, and this should be applied to F_0 in the equilibrium spline. These, apart from F_3 were the major differences to ZW causing more inaccuracies in defects and as well a decreased accuracy in elastic constants (will be shown in 3.3).
On top of that, the rigid analytical fixation instead of allowing ranges and dynamical links to changes in β (as in F_0) significantly reduces desired flexibility for alloys – ZW compensate this by their CTIP addition in their oxide alloys models [96]. However, this leads to a very unstable behaviour of the CTIP, parameters cannot be changed easily (in comparison to the Al-O model by Lazic for instance [95]).[61]
This comparison will be closed by a deeper insight into F_3 because it was linked by ZW to some significantly improve high pressure properties, which as found out seems actually not to be the case (also see results in 3.3).

F3 can be calculated in 2 ways: Calculating F_3 directly requires knowledge of the exact first pressure derivative of the bulk modulus, however this is questionable, as it will be shown.

First, the bit involved derivation of the first pressure derivative, which is given by (as explained in [134]):

$$B' = \left(\frac{\partial B}{\partial p}\right)_{T,p=0} = \left(\frac{\partial B}{\partial V}\right)\left(\frac{\partial V}{\partial p}\right) = \left({}^{1}/_{B_0}\right)\left[-V\left(\frac{\partial B}{\partial V}\right)_{V=v_0}\right] \quad (3.60)$$

Using the additional fact that it can be expressed as:

$$B = -V\left(\frac{\partial p}{\partial V}\right) \quad p = -V\left(\frac{\partial E}{\partial V}\right) \Rightarrow B = \frac{\partial^2 E}{\partial^2 V}$$

This expression for the bulk modulus can be Taylor expanded (since it is around the minimum similar to the calculation of the elastic constants but without the directional dependence), applying this to EAM:

$$9\Omega B = \frac{1}{2}\sum_m a_m \phi''(r_m)\, r_m^2 + F'(\rho_e)\sum_m a_m \rho''(r_m) r_m^2 + F''(\rho_e)\left(\sum a_m \rho'(r_m) r_m\right)^2 \quad (3.61)$$

In order to calculate the first pressure derivative of the bulk modulus, a trick, which can be yielded by expansion, is used :

$$dV = 3\, dr$$

Since this is again at the minimum, one can Taylor expand eq. (3.61):

[61] To be fair though, these efforts were taken 10 years ago with less computing capacities, ZW approach requires less comp. effort.

$$27\Omega B = \frac{1}{2}\sum_m a_m \phi'''(r_m)\, r_m^3 + F'(\rho_e)\sum_m a_m \rho'''(r_m) r_m^3 + 3F''(\rho_e)\sum_m a_m \rho''(r_m)\rho'(r_m)\, r_m^3$$

$$+F''(\rho_e)\sum_m a_m \left(\rho'(r_m)\, r_m\right)^3 \quad (3.62)$$

This result can be retrieved by "brute" force: deriving the explicit expression for the bulk modulus (so EAM potential plugged in (3.62)). Knowing all coefficients and the first pressure derivative of the bulk modulus (around 6.5) (by Raju [134]) F_3 could be calculated. However, the major problem is that there are no absolute values of this quantity, the values vary and the author ZW is not clearly referencing the origin of the value. In an review article, however, ZW is stating: „This pressure derivative is not known for all the metals being considered, so the value calculated from a universal equation of state in the literature is used" [97]. The mentioned reference is only the very general original paper about the equation of state by Rose, however a modified specific EOS was used, namely the one in the paper by YX Jian [135](Jian was so friendly to mention that this calculation was used for ZW paper [57, 96]). In a paper by J.H. Li [136] the five parameter EOS was reduced to a more comprehensive four parameter EOS and the B' were computed specifically by equating:

$$E(V) = -E_C\left[1 + \eta(\xi - 1) + \left(2(B_0' - 1)\eta - \frac{1}{3}\right) * \left(\eta * (\xi - 1)\right)^3\right] * e^{-\eta(\xi - 1)} \quad (3.63)$$

$$with \qquad \eta = \sqrt{\frac{9B_0V_0}{E_C}} \quad and \quad \xi = \left(\frac{V}{V_0}\right)^{1/3}$$

Using several E(V) points F_3 and B' can be varied simultaneously. Or alternatively knowing F_3 the resulting B' can be calculated an compared with literature values. The resulting B' was found to be around 6.0 (1) and used as a reference.
Computing the actual pressure derivative of the bulk modulus of the potential, by computing the bulk modulus for several volumes in MD a value of around 7.5 is yielded (by the analytical way too, see above). The first guess is that $dV = 3\,dr$ could be too unprecise, however running a simulation (expanding and looking at energy change) at the exact same parameters, confirms this value by yielding a value around 7.6.
Determining F_3 by continuity (to safely reliable determined parameters is a much "safer route", which presumably was also taken by Zhou (because the Input of 6.1 could not be reproduced). In case of any interest for B' the following route helps determining the resulting B' for a given parameter set: Knowing the melting temperature (for example by running an MD run with increasing T), B_0' can be extracted by:

$$\delta = \frac{B_0' - 1}{2\eta} - \frac{1}{3} \qquad \& \qquad T_M = 372.3(1 - 2\delta)E_C$$

The temperature of ≈1795 K [132, 137] yields a good agreement of 6.6 for B'. However this is not necessary at the current stage and should only act as an alternative technique, which is of special interest when modelling with a special emphasis on melting temperatures.

The route taken by the author was as explained before is to set F_3 by continuity, see overview next page. Better values for F_3 are yielded, if the linked choice of η is additionally controlled by a minor punishment considering how accurate the phase difference hcp-fcc is represented (deviation are added to Z function).

3.2.9 Summary / Overview of own fitting Routine for EAM in POTFIT[62]

$$Universal\ fitting\ rel./EOS\ \Rightarrow \alpha = 1.875\,\beta \quad \& \quad \lambda = 2\kappa \quad \& \quad f_e = E_c/\Omega^{1/3}$$

$$lattice\ equilibrium\ \Rightarrow r_e = 1NN \qquad \eta_{max}(\beta) = \frac{1}{\beta}\sqrt{\frac{9\Omega B - 15\Omega G}{F_0(\beta)}} \leftrightarrow \eta_{min}(\beta) = \frac{1}{\beta}\sqrt{\frac{9\Omega B - 15\Omega G}{F_0{}'(\beta)}}$$

$$C_{11}, C_{12}, C_{44} \Rightarrow A = \frac{C_{11} - C_{12}/\mu_2^{12} - B\gamma}{\delta} \quad \& \quad B = \left[\frac{C_{44} * \kappa/\mu_1^{11}}{\delta} - d\right] * \left[\frac{\gamma\kappa}{\delta} - \xi\right]^{-1}$$

$$Anisotropy\ ratio\ for\ \lambda \Rightarrow A = \frac{8\left(r_{1NN}^2\varphi''_{1NN} - r_{1NN}\varphi'_{1NN}\right)}{9\left(r_{2NN}^2\varphi''_{2NN} - r_{2NN}\varphi'_{2NN}\right)}$$

$$E_{1V}^{unrelaxed} \Rightarrow F_0 = E_c - \phi_e(A, B, \beta)$$

$$normalization\ "standard\ form" \Rightarrow F_1 = 0$$

$$C_{12} - C_{44} \Rightarrow F_2 = \frac{(C_{12} - C_{44}) * \rho_e^2\, a_0^3}{4w(\beta)}$$

$$Continuity\ by\ value \Rightarrow F_3 = \frac{-\eta * \left(\frac{\rho}{\rho_e}\right)^{\eta} ln\left(\frac{\rho}{\rho_e}\right)^{\eta}}{1.15 * 0.0225} - \frac{2F_2}{3 * 0.15}$$

$$Continuity\ by\ value \Rightarrow F_{n0} = F_0 + 0.0225F_2 - 0.003375F_3$$

$$Continuity\ by\ slope\ (1st\ der) \Rightarrow F_{n1} = 0.85 * (0.3F_2 + 0.0675F_3)$$

$$Continuity\ by\ concavity\ (2nd\ der) \Rightarrow F_{n2} = 0.7225 * [F_2 + 0.45F_3]$$

$$Continuity\ by\ value \Rightarrow F_e = \frac{F_0 + 0.0225F_2 + 0.003375F_3}{pF}$$

$$F(0) = 0 \Rightarrow F_{n3} = -(F_{n0} + F_{n1} + F_{n2})$$

[62] These obtained fitting relations represent the first fundamental results, because it is a discovery of new links to fitting properties.

3.3 MD Results with POTFIT

The preliminary results in 3.2 yielded during fitting lead to these MD results regarding basic properties.

3.3.1 Fitting Results for bcc Fe and hcp Y in general

Finally, the rather lengthy considerations and derivations in the last sections pay off. Fitting in POTFIT for hcp Y and bcc Fe as single metals was started with the help of the following *ingredients*:

- The previously established fitting constraints in section 3.2 reduce the number of parameters for each single metal from 15 (continuity conditions excluded) to 2 parameters: β for the pair part (and mainly as an energy correction and linked to a_0 by UR controlling α/β) and η in a limited range as a fitting parameter in the EMB part and main key driver for the parameter sets. For later alloy fitting (3.3.4) f_e is also flexible for scaling. By the change of these two parameters, β and η (restrained), all parameters change by URs and analytic constraints accordingly (except of f_e fixed in single metals and r_e fixed to 1NN).
- As a fitting database the ab-initio data introduced in 1.3 [5] served as atomic fit-references, representing the defects and Fe-Y clusters leading to better defect properties in both potentials for bcc Fe and hcp Y. For hcp Y a selection of the different phases (hcp, bcc and fcc) was also included at different elongations representing EOS curves for each phase, similar as presented on page 45. These phases ensured the potential accurately reproduces hcp Y as the stable ground energy configuration, leading to a relaxation into this phase after potential excitations.
- The parameter restrictions replaced the need to include forces (force matching by ab-initio data).
- In bcc Fe a more "rudimentary" ab-initio phase data selection was chosen because the focus was on defects and the parameters of the bcc Fe potential by ZW [57] were chosen as start parameters – this waived the necessity of an extensive ab-initio data base for bcc Fe.
- Hcp Y potential was started "*from scratch*", no suitable starting parameters were available. By taking into account the bigger electron shells and thus higher electron density [109] of hcp Y a higher value of β was chosen (6.0 with a range between 4.0 and 7.0). The starting value of η was simply chosen by the Rose eq. which served as a first good approximation. Then all other values for the starting parameter set could be calculated and used in POTFIT in the fits.

With this overview of the fitting parameters and data sets (more details in 7.2) in mind the fit results are presented: after several cycles of fitting, corrections to the analytic constraints and models (which were summarised in 3.2, see 3.2.9), the final fitting phase for accurate fits of the single metals was conducted leading to the final parameters in the appendix (7.0). Due to the consideration of a large DFT database each simulating annealing step took few minutes instead of few seconds, leading to week long fitting. After all these efforts the Z value (Z_F) could be reduced to round about 0.1 (energy RMS ≈0.01, forces to cross validation data RMS ≈ 0.05, list of corresponding parameters in the appendix) – leading to an accuracy of ≈10% on average for all data points – considering the enormous data base containing hundreds of various atomic references and energies, this is a quite good fitting result, especially considering that fitting was done with a plain LSM method. The usefulness of the detailed inclusion of defects will be shown in 3.3.4, highlighting that a reasonable compromise of basic prop. vs. defect properties has been found. Again this LSM method was the main reason for the restrictive fitting – in order to get a better overview of the fitting parameter surface, parameter sets for the individual single metals were changed by varying key drivers, α/β and r_e – but this lead to drastically different β with poor performance, especially in hcp Y., 6,1168 for β represents a "save choice". In the following the fitted potential curves are examined, the resulting physical properties (basic and defects) are discussed.

3.3.2 Basic properties for bcc Fe and hcp Y

On the following two pages the fitted resulting potentials are illustrated by plots of the corresponding pair and EMB functions and the resultant *main* properties are tabulated for comparison to the curves (energy is shown per atom as in 3.1.2).

- On the pair potential plots the steeper blue and red curve on the LHS can be instantly identified as the bcc Fe pair pot., while the flatter black and green curves with a minimum at a greater pair spacing on RHS is the hcp Y pair pot. By the detailed description of the potential shape (3.2.1) the differences can be linked to the bigger lattice constant of hcp Y (≈50% bigger than bcc Fe, shift to the RHS) and smaller bulk modulus of hcp Y in comparison to bcc Fe (≈4x), see table 3.2.
- For bcc Fe the original source potential by ZW is shown in red colour – energies of ZW are a bit lower and less steep, the fitted potential is a bit deeper and steeper – this seemingly little difference (0.003 eV per atom at minimum) and even smaller difference in the β (in 5th decimal place, see parameters in appendix) lead to significant improvements in defects (p. 68ff) and more flexibility (in addition to minor improvements of lattice and elastic constant, more on p. 65ff).
- The slope on RHS of the minimum in the hcp Y potential has a considerable different shape than the bcc Fe – the hcp Y curve fades off slower and the concavity of hcp Y seems less distinctive and also both slopes on LHS and RHS of the minimum are less symmetric than in bcc Fe – this is as it should be, since this is the typical difference in hcp and bcc. The difference in the slope on the RHS of the minimum originates from the c plane in hcp (more on defect section), which breaks cubic symmetry as in bcc structures (which lead to more symmetric slopes). The anisotropy ratio is different, leading to different λ and consequently to different cut-off behaviour (hcp Y needs a cut-off at least till the 4NN/5NN (3NN is the lattice constant in c plane (*c*), so up to 6.5 Å).
- As worked out before the minimum position of the pair potentials due to the EMB contribution is not equal to the lattice constant.
- In bcc Fe η is actually fixed, so there are no parameter sets (opposed to hcp Y in next point). It was tried to systematically swap parameter sets by changing α/β and r_e but as said before it leads to unphysical and unreasonable fitting behaviour, which is due to limitations in LSM optimisation techniques (cannot find other global minima corresponding to other parameter sets)
- For hcp Y on the other hand different parameter sets can be easily created by changes in η within the range limited by the sublattice relaxation energy (3.2.1), these potentials have very little differences and the sum of EMB and pair part seem physically identical – but in the consequent alloys section (3.3.5) these differences will be of particular importance.
- For hcp Y no comparable potentials in "plain" EAM formalism exists (the only one by Sheng (part of Mg-Y) [91] is unsuitable), only MEAM like of Baskes, B.J. Lee and coworkers [92, 93], these potentials have a considerable different shape which yields less suitable results and are therefore not considered here (see literature review, but 1-2 comparisons can be found in 3.3.4).
- In the EMB part, considering the environment around the minimum, hcp Y has a greater EMB contribution than bcc Fe (sensible due to a higher number of electron shells in hcp Y).
- Following the above logic, ρ_e for bcc Fe is around 24 and for hcp Y around 30 (can be linked to DFT calculations Roetti & Clementi [109] illustrating this as bigger electron clouds).
- Own fitted EMB curve corrects the jumps between two splines in ZW curve around equilibrium.
- Different (lower) slope in hcp Y indicates low bulk modulus and a kind of defect variety(→3.3.4).

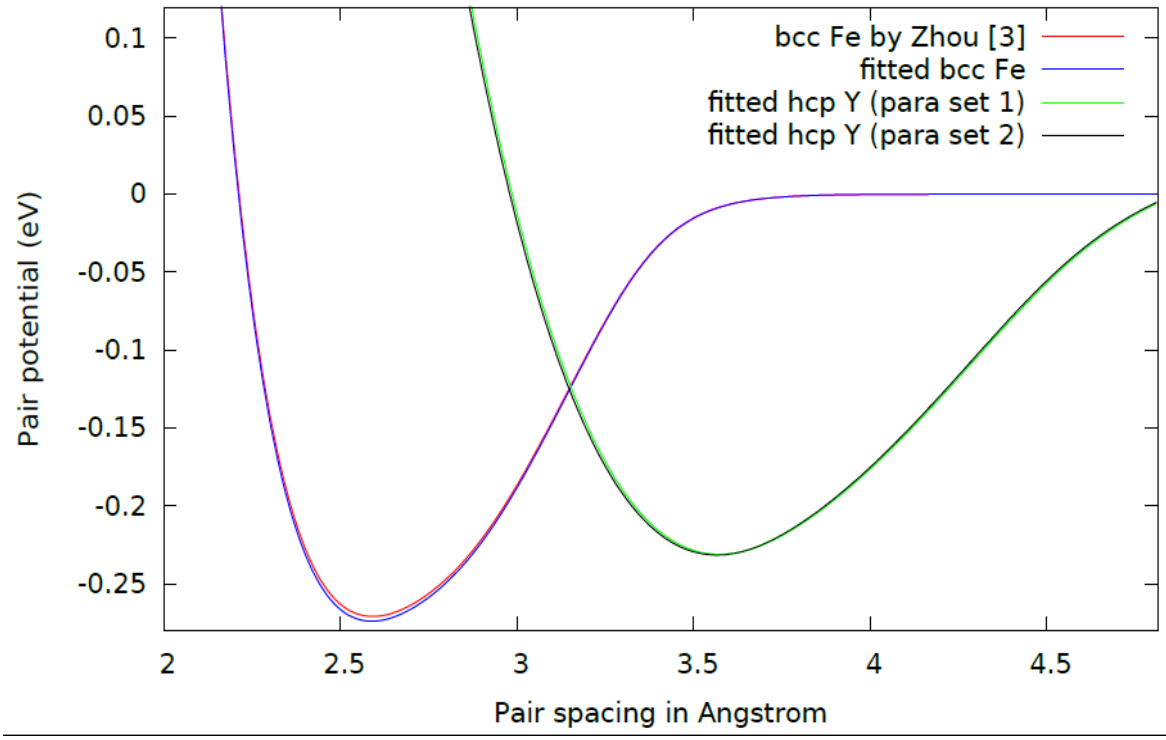

Fig. 3.5 Pair potential part for bcc Fe and hcp Y in eV vs. atomic distance. The energies are only for one atom pair (one atom has several neighbours (sum at equil. = cohesive energy). Firstly, the pair parts show the differences between Y and Fe: different lattice constants (Y is bigger) and cohesion energy (well of Y smaller). Care has to be taken that the minima are not at the exact lattice constants, since there is a contributing EMB part.

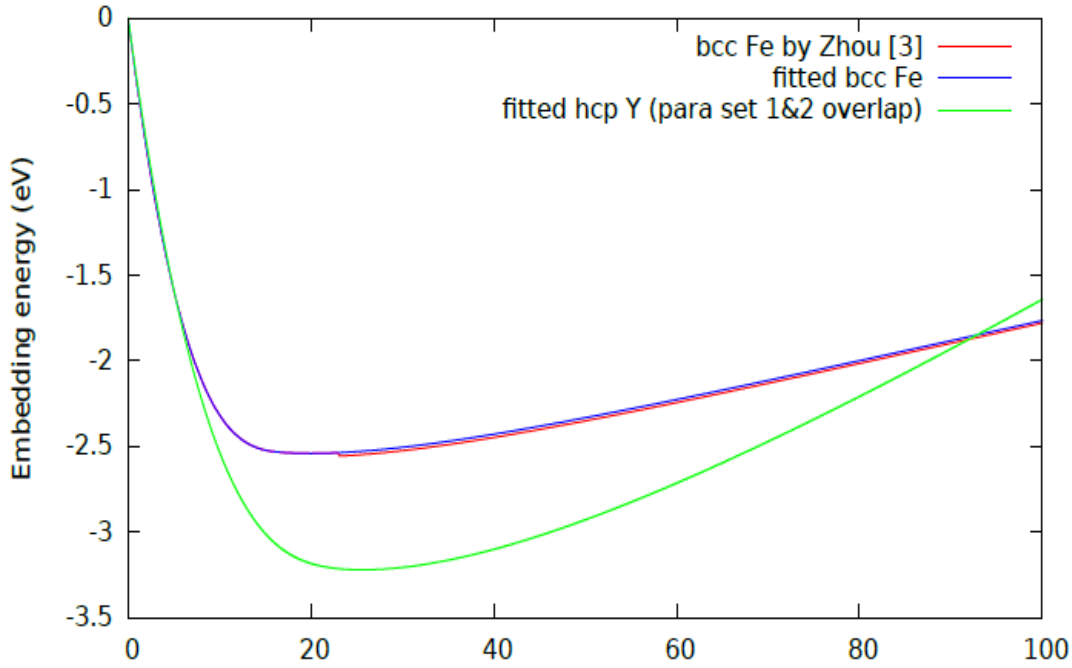

Fig. 3.6 EMB potential parts for bcc Fe and hcp Y: for Y this has been solely fitted from scratch and for Fe improvements were made by fitting (starting from the ZW potential [96]) – one very important improvement for example is the "removal" of the little jump of the original ZW EMB (red) at the elec-dens around 23.

These potential curves for bcc Fe and hcp Y result in the following property table:

Property	Potentials for bcc Fe			Potential hcp Y	
	orig. ZW	modified	exp.[138]	Fit in POTFIT	exp. [139]
a_0	2.866	2.865	2.87	3.655 c/a 1.58	3.64-3.65 c/a 1.57
E_c	-4.287	-4.291	-4.29	-4.35	-4.37
E_{1V}	1.65	1.69	1.7-1.9	1.63	1.6-1.7
E_{110i}	3.81	3.58	3.63(DFT)	Separate detailed table	
E_{100i}	4.19	4.45	4.63(DFT)	3.3	
C_{11}	1.437	1.41	1.36	0.490	0.488
C_{12}	0.85	0.838	0.837	0.170	0.164
C_{13}	0.85	0.838	0.837	0.134	0.137
C_{33}	0.7358	0.72	0.7	0.485	0.480
C_{44}	0.7358	0.72	0.7	0.133	0.145
B	1.045	1.0385	1.06	0.260	0.2571
B′	7.6	6.6	5-6.5	0.02 eV*	0.022eV*

Table 3.2 Properties of fitted bcc Fe and hcp Y potentials, corresponding fit parameters in appendix, 7.0, units for a_0 are Å, for the energies eV and for the elastic moduli eV/Angstrom^3, * bcc-fcc energy dif.

Looking at this table (3.2), it can be immediately said, that overall the main properties in both the modified bcc Fe and the "fitted-from-scratch" hcp Y EAM potential are well reproduced, specifically:

- The elemental lattice constant and cohesion energies are exactly met by these fits, within 1%, as necessary (because of the importance of these two properties). This clearly demonstrates that the URs and their key drivers are effectively working during the fit.
- All elastic const. are very well fitted (within 5%, one exception see next point) – in bcc Fe these were a little bit improved in comparison to ZW's version (original ZW pot.).
- In hcp Y the accuracy of one elastic constant stands out: C_{44} is the only one not satisfying the 5% deviation – its difference to the actual elastic constant is ≈8%. However, recapping the previous sections, especially 3.2.3, this is no surprise, since W (sublattice relaxation energy) which plays a role here is not entirely included (only by indirect fitting measures) – this was on purpose for a better representation of defects. If a more accurate W was included by a different choice of η (and thus different parameter set) would improve this (C_{44}) up to 3-4%, but defect property exactness decreases to 20% (from a maximum 10%). Since defect properties are of importance, this is a reasonable compromise. Additionally, the negative Cauchy pressure problem in EAM (which is a challenge, described by ZW in [112]) is elegantly avoided by having a nearly to zero difference in C_{13}-C_{44} (positive but small). This compromise will be substantiated in the defect section 3.3.4 showing cogent accuracy.
- In hcp Y the ratio of c/a has a satisfactory deviation of 1.5% - again another compromise which was necessary to include the other phases of pure Y (fcc, bcc) and for a more exact difference between hcp and fcc phase (listed at hcp Y instead of B'), this also helped for the next point.
- Oddly by including the phase differences with regard to the Bain path as a mild fitting target (light punishment for deviations) the first pressure derivatives of the bulk moduli in bcc Fe (here

between bcc and fcc) could be improved in comparison to ZW, though ZW claimed they included analytical determinations of the third derivative in their potentials the third derivative for B′ – a longer discussion about this was in 3.2.8, and these considerations were kind of worth the effort: improvements in B', though not having it directly included, indicates transferability.

- in bcc Fe the *basic* defects (single vacancy and interstitials in <110> and <100> direction) were significantly improved – vacancies were accurate within 5% and interstitials to 10% (which are harder to fit), giving indications that more accurate slopes by not fitting to B but to separate elastic constants also influence these properties. Defects of hcp Y are separately shown in 3.3.4 and there will be a deeper evaluation since these defects are of greater interest for Fe-Y.
- Only a single MEAM pot. by Lee [92] and AMEAM pot by Hu [90] pass these basic properties (but as ABOP have poor melting Temperatures, the MEAM one is kept for 1-2 comparisons).

3.3.3 Exact determination of lattice and elastic constants in hcp Y

As said on the tabulated property section, the lattice and elastic constants of the potential are in exact agreement with given experimental data. For an accurate determination, the sole consideration of an analytic calculation of these properties by parameters is not sufficient, because of two main reasons: 1. There could be plainly a mistake and calculating these constants by an MD can rule such mistakes out 2. There could be some relaxation energy contributions which were not accounted for – MD runs provide detailed information about this.[63]

- To start with the lattice constant (fig. 3.8) is considered: a very detailed 3D scan of the proximate energy surface around the minimum of lattice constant *a* and *c* for hcp Y is shown there (few 0,05 eV vs few 0,05 Å) – obtained by numerous MD runs of the final potential. The exact minima are determined to be 3.655 Å (a) and 5.665 Å (+/- 0.05 Å) (c), resulting in a pretty accurate c/a ratio. Steepness looks reasonable with anharmonicity as expected.
- C_{44} with the highest deviation was exactly determined by considering MD runs with the results summarised by Fig.3.7 : this shows the shear in xy direction (expressed as fraction of xy/L, 1/100 %) vs. the energy converted to Joule divided by the surface spanned by the xy plane (converted to m), this yields Pa (more experiments friendly) – corresponds to MD runs with an applied shear in the range +0.1% to -0.1% around the exactly determined minimum (with fixed c) – the resulting energies were then mapped vs. the corresponding strains yielding the quadratic points of the parabola curve. To obtain the elastic constant C_{44} this parabolic curve was purely analytically fitted by a quartic polynomial (a quadratic one is also possible, but less accurate) – the determined second coefficient of this fit represents C_{44} which could be determined to be 1.065×10^{10} Pa. This closely follows the considerations about the elastic constants in 3.2.2 namely, using the corresponding eq. 3.19 and converting it to GPa, one gets 21.35 GPa corresponding to the aforementioned 0.133 eV/ $Å^3$ (in atomic units) in satisfactory agreement with exp. data and the fit yielded a good R value for the fit (rounded in shown table, exact value 0.9776) – MD data follows predicted behaviour of 3.2.2.
- In the same manner the elastic constant for C_{11} was confirmed, this curve can be due to its simplicity directly obtained from Fig. 3.8 by extracting the curve at const. c at min=5.655.

So, the results of lattice and elastic constants in 3.3.2 are confirmed by these exact determinations.

[63] and the properties in 3.3.2 were modelled by MD, this is a "kind of catch up", how these constants were obtained

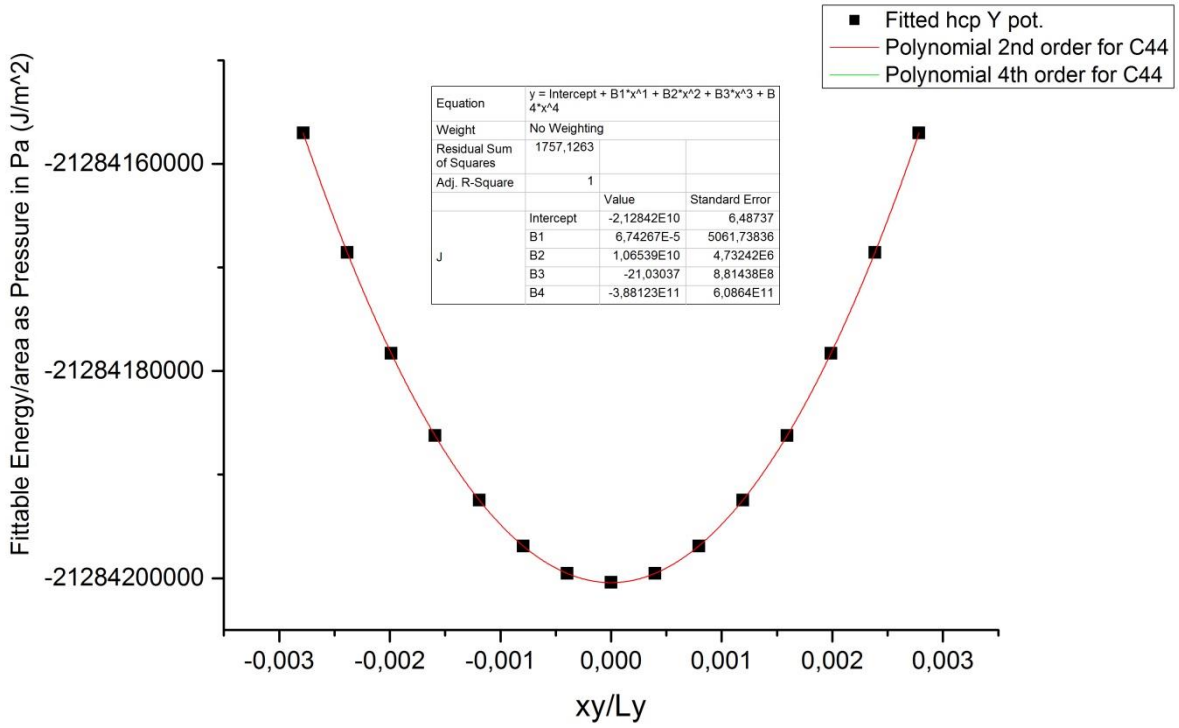

Figure 3.8 Determination curve for C_{44} in the form of shear (x-axis) vs. the energy /cross section area. The resultant fitted parabola curve with its quadratic coefficient (B2) yields the elastic modulus (C_{44}) in the units J/Pa, converting this with the help of the conversion, eV/Angstrom^3 = 160.21766208 GPa, yields the result in table 3.2.

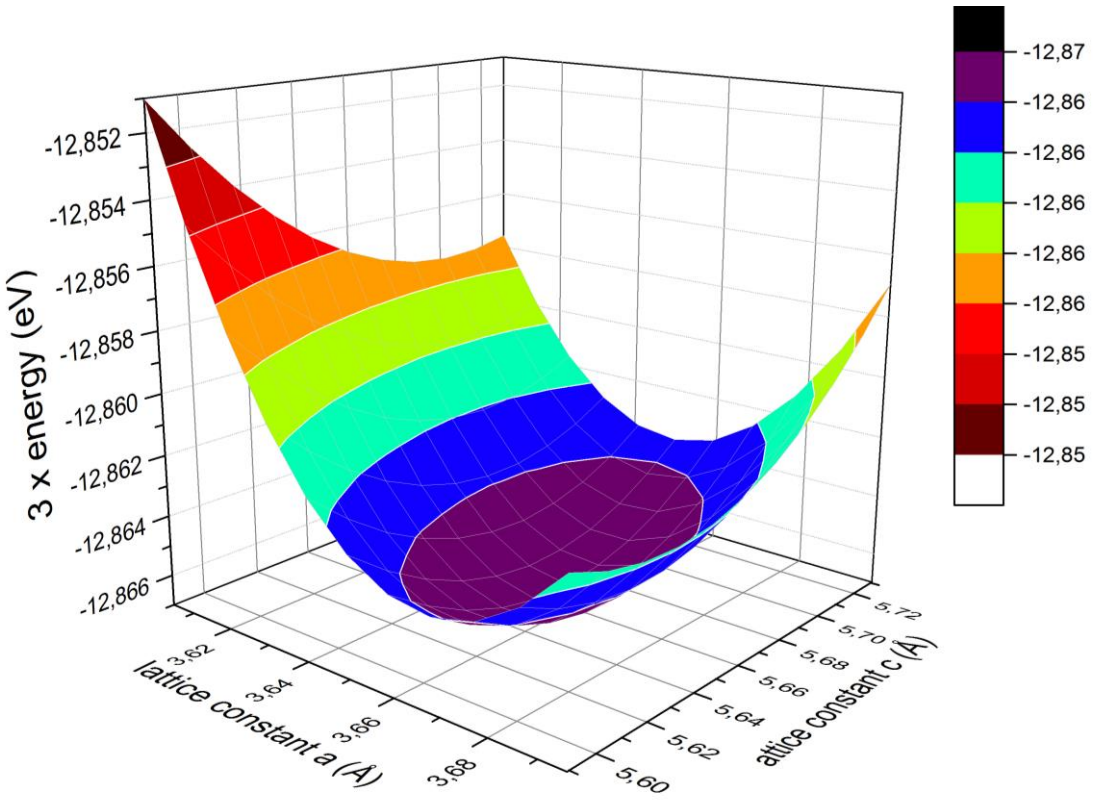

Figure 3.7 Energy surface with respect to lattice spacing in a and c direction – yields the equilibrium lattice constants

3.3.4 Behaviour of defects in hcp Y – vacancies and interstitials

Here a principal overview of the formation energies of simple point defects in hcp Y will be given.

Y is of interest because of its ability to host several different kinds of defects due to its inherent lattice anisotropy (as shown before) leading to more possible defect positions/configurations.[64] Additionally, hcp Y is a kind of special since, when filling up vacancies, it can occupy two (vacancy) sides at once [140][3]. Before looking at these subtleties, the energies need to be computed by:

$$E_{df} = E_{conf} + E_{bulk}\left(\frac{N \pm n_{def}}{N}\right) \quad (3.64) \quad where \;\; df: defect\; formation \;\; \& \;\; + for\; inter. \,|\, - for\; vac.$$

Where E_{conf} is the final energy of the configuration with defect, E_{bulk} is the energy of the configuration without the defect (relaxed bulk), N is the total number of atoms and n_{def} represents the number of defects. Eq. (3.64) assumes self-defects of one kind. Beside the energy in interstitials the following question is also of special interest: is this interstitial configuration stable, or only a transition state to other kind of interstitials? This plays an important role in diffusion. The consideration of the stability can be quite *tricky* since a seemingly stable interstitial configuration can be in fact a saddle point (as it will be shown by considering one of the very few papers about self-interstitials in Y). In order to clarify this, the stable interstitial candidates are put slightly out of equilibrium and it is checked whether the configuration retains the initial seemingly stable interstitial. This is one of the first works with accurate MD runs addressing this question, which allows a consideration in bigger simulation cells with more authentic results (with 10000s and more atoms in comparison to max few hundreds in DFT). Nevertheless, before proceeding with more details (see page 68/69) in the following the vacancies are considered:

Vacancies: The major classes of the modelled vacancies in agreement with the DFT data are single vacancies and vacancy pairs, which can further be classified as in the same basal plane (labelled as V_2^b) or in two neighbouring planes (V_2^p) as described in fig. 3.9 on the RHS and used as notation in table 3.3, where r_m denotes the number of the NN distance (as all the time before).
Considering table 3.3 the following about these groups of vacancy formation energies can be said:
Looking at the single vacancy formation energy, it is striking high – reliable DFT calculations (by Fan [84] and Borodin [85] which can be reproduced) suggest a range from 1.69 eV to 1.86 eV, which can be readily reproduced in MD by the fitted potential and which is consistent with further defect simulations (binding energies of vacancy pairs, lower single vacancy formation energies would lead to incorrect pair binding energies). Older estimates by Boer [141] wrongly assumed 1.25 eV and are used in ABOP [132].[65]
The more challenging properties are the divacancies, especially in 1NN distance since the energies are very similar (only 0.01 eV difference see table 3.3) – but this is more of a challenge for the presented results by RF-MEAM (on the RHS). As expected the accuracy of the EAM Model is not sufficient. Nevertheless it *bravely* hits by its extensive ab initio defect data base all these advanced defects with a maximum deviation of 15%. All in all, the average spreading for the defect energies is around 10% - this kind of represents one of the maximum compromises one can obtain by EAM in metals with complex defects while obtaining flexibility and an accurate representation of various phases. But this unavoidable imprecision leads to a rather unsatisfactory order in the vacancies. Therefore simply considering one specific vacancy alone can be estimated by the EAM potential, but not the migration and diffusion processes, since the binding energies are too far off. Nevertheless, this is of no surprise since covering these subtleties would require an angular dependence, as done in RF-MEAM, corresponding results are shown in advance. RF-MEAM can reasonable well cover these defects. However, it has to be highlighted, that this RF-MEAM potential has in

[64] And on top of that, contrary to bcc Fe relatively little is known about the various defects in hcp Y (and why bcc Fe is excluded).

[65] These are all recent published DFT calculations – the few older publications are rough estimates, which can't be relied on – e.g. "experiments" by de Boer [141] are in fact theoretical estimates contradicting actual measured self-diffusion energies of ≈2.6-2.9 eV

the non-angular part more or less the same EAM potential – Hence, this should illustrate that the EAM potential provides a solid first estimate which is of use and with the help of the fine tuning angular part accurate results are obtained in RF-MEAM (however, though these vacancies are quite interesting, RF-MEAM addresses more urgent questions in the later chapters 4&5).

Defect	E_f	E_{2Vb}	E_f	E_f	E_{2Vb}	E_f	E_f
	Own EAM pot.		Own DFT	Ref Borodin [85]		Own RF-MEAM	MEAM by B.J. Lee [92]
V	1.63	n.a.	1.81	1.83	n.a.	1.69	1.89
$V_2^b(1)$	3.78	0.47	3.42	3.43	0.235	*3.28*	*3.35*
$V_2^p(1)$	3.92	0.66	3.44	3.44	0.225	*3.35*	*→ E_{2Vb}=0.43*
$V_2^b(2)$	3.91	0,65	3.78	3.78	-0.115	*3.97*	*3.87*
$V_2^p(2)$	4.16	0,8	3.82	3.79	-0.121	*4.03*	*4.23*
$V_2^b(3)$	3.42	0,16	3.86	3.84	-0.179	*4.09*	*4.19*
$V_2^p(3)$	3.53	0,27	3.79	3.78	-0.118	*4.00*	*4.35*
V_2^c	4.57	1.31	3.98	3.96	-0.295	*3.93*	*3.53*

Table 3.3 Vacancy formation energies of DFT references and fitted pots.. As announced before the MEAM pot. by B.J. Lee fails in defects (particularly E_{2Vb} *is much too high)*, here a sufficient example is shown. Though EAM fails the further RF-MEAM calculations pass these challenges by the vacancies.

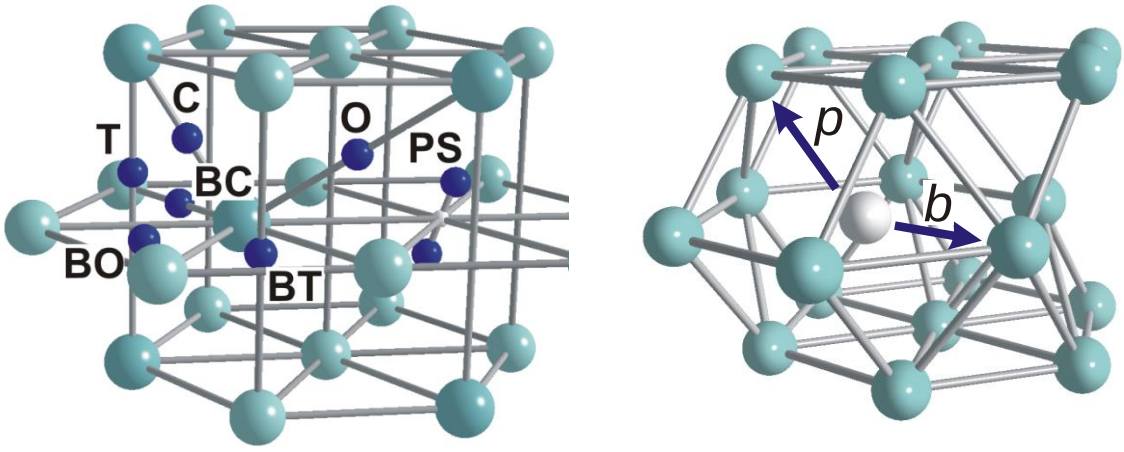

Figure 3.9 Illustration of the interstitial defect positions (LHS, relevant for p. 68) and the differences between basal plane (b) and principal plane (p) for the vacancy description as a courtesy by Borodin, whom the author assisted at the publication [85], (used abbreviations: T= Tetragonal; C= Crowdion; PS= Split Symmetric; O= Octahedral). Further information about the here rather irrelevant Split (S) and Basal Split (BS) positions can be found in the same paper [85].

In interstitials in contrast to the rather complicated behaviour of vacancies, the dynamics of inserted interstitial defects seem to be more straightforward to describe – but still challenging to model in MD. Similarly to the vacancies an interstitial can either be placed between two adjacent basal planes or in the same basal plane or additionally like in Fe in a dumbbell symmetry (S= symmetric or BS basal symmetric corresponding to that). Consequently, due to the lower interest in the modelling community for hcp Y it was unknown until Borodin and Vladimirov finally published a detailed DFT study about the interstitial behaviour in hcp Y ([85] in 2018/19) which got to the "principal bottom" of self-interstitials in hcp Y: due to the thorough and precise DFT investigations with certainty the BO configuration could be determined to be the only stable (self-) interstitial symmetry with the lowest energy, which is preferred. Considering migration and dynamics of the interstitials Borodin discovered, that all kind of interstitials eventually end up as BO interstitials and that migration of BO interstitials is a kind of a movement between different possible BO positions in the lattice (detailed DFT data was provided by Borodin and included in all final EAM and all RF-MEAM fits). Before getting into few details about the various interstitials, it can be said: the here developed EAM and RF-MEAM potentials could accurately reproduce this DFT data for the first time. In EAM, as expected, BO was reproduced as the final stable ground energy all configurations are migrating too, but with incorrect intermediate steps. In RF-MEAM these intermediate steps could be improved by the angular contribution and a principal agreement with Borodin's data could be achieved. On the RHS (next page) an extract of an MD run with the EAM potential is shown. In the same accurate manner as in Borodin's DFT calculations several distortions were tried to check for stability – it stayed in BO, test passed. Also from all other interstitial types BO was the final result, but in EAM the migration behaviour was wrong (in RF-MEAM it could be more accurately modelled). This is no surprise, since in EAM as opposed to RF-MEAM the order of the interstitials (energetic sequence of the formation energies) is incorrect: four out of eight interstitial formations are in complete wrong order with deviations of up to 20%, namely O, PS, C, T. BS is even treated like a minimum instead of a saddling point (SP), but eventually also turns into BO. Therefore, the migrations are incorrect, but the final state and minimum, BO, is correct and all intermediate interstitials are recognized as SPs. Even in EAM especially when combining with other defects, migration by jumps between different neighbouring BO positions at different distances could be achieved (not further considered since Fe-Y is of interest). Considering no free parameters in EAM were specifically fitted to these interstitials these are quite good EAM results.

Configuration	E_f	Type	E_f	E_f	E_f
Potential-type	DFT (240 atoms)		EAM	*RF-MEAM*	Ref. range [84, 85, 90] (up to 128)
BO	2.10	Min	2.17	2.03	2.07-2.12
T	2.99	Min	2.65	3.26	2.86-3.23
O	2.55	SP	2.93	2.72	2.44-2.51
PS	2.56	SP	2.86	2.69	2.52
BS	2.58	SP	2.17	2.77	2.54-2.62
C	2.82	SP	3.25	3.03	2.73-2.85
S	2.95	SP	2.36	3.12	2.85-3.01
BT	3.22	SP	4.1	3.67	3.16-3.25
BC	-	U	-	-	*2.07-3.23***

Table 3.4 Self interstitial formation energies in hcp Y

** unstable and not reproducible in all DFT and MD calcs. of this work

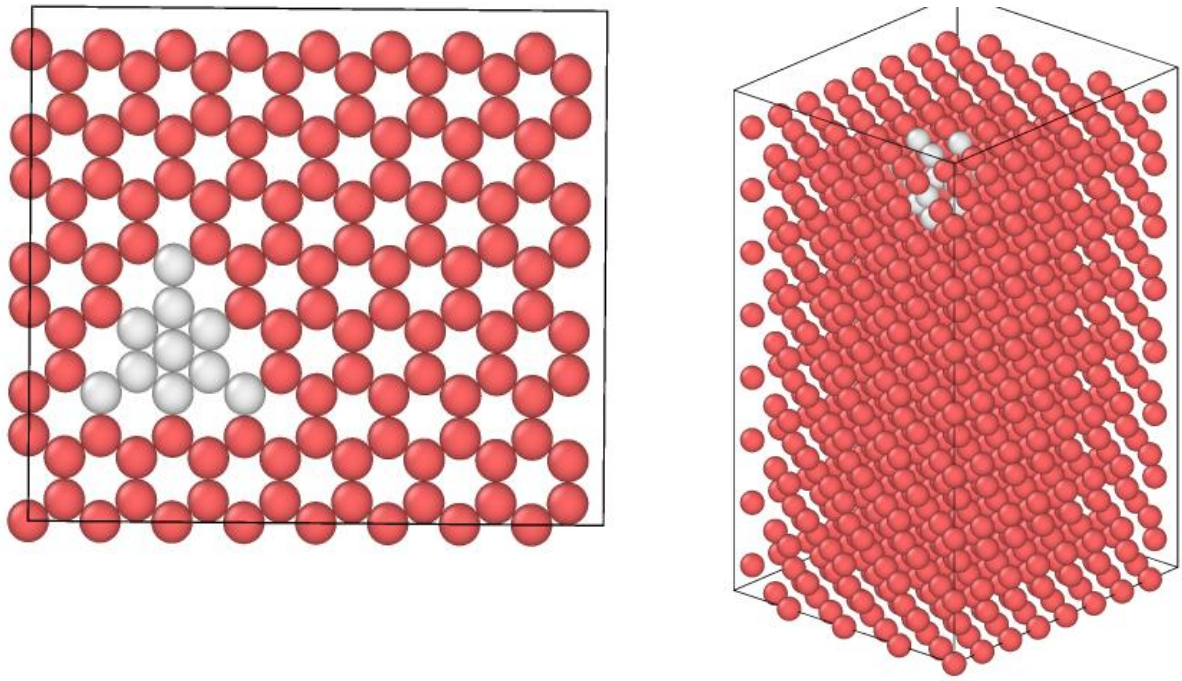

Fig. 3.10 Initial and final state of a BO interstitial in an LAMMPS MD run with the developed EAM potential the initial atomic with the help of Ovito [131]& LAMMPS [60]

LHS top: initial BO configuration (interstitial in the centre of the white atoms) bottom: final stable configuration after relaxation, the interstitial correctly stays in the BO position and just for relaxation increased few atomic spacings.

RHS top: Full overview of an 1/8 extract of the simulation cell (=one corner excavating the centered interstitial, each corner has one) of roughly 8000 atoms)

The colours correspond to the crystal structure by CNA: red= hcp, white= no structure, due to defects or distortions (as for the interstitial surrounding atoms)

3.3.5 Fitting of Fe-Y alloys in POTFIT

After the development of suitable and accurate single metal potentials in EAM for bcc Fe and hcp Y, as shown before, it was tried (unsuccessfully) to combine these in the previously described EAM technique (chapter 3) with an additional flexible pair potential function as required by EAM for the alloy fitting of Fe-Y in POTFIT. In addition to the aforementioned DFT data of numerous Fe-Y clusters (as described in 1.3) plus the DFT data of the four stable Fe-Y phases (on top of the pure metals), Fe_2Y, Fe_3Y, $Fe_{17}Y_2$ and $Fe_{23}Y_6$ in various states and elongations (atomic distances other than a_0, which were relaxed, yielding EOS curves as shown previously) were added to the data base resulting in an extensive repository with 1000s of energies in 126 configurations – which should theoretically be sufficient for a pure fitting of the additional Fe-Y pair pot. In order to do so, the following fitting procedure was conducted to examine the principal possibilities to reproduce the behaviour of Fe-Y. This inherently requires to exclude as much as possible restrictions on the fitting parameters[66] (decreasing accuracy of specific physical properties but with stable physical behaviour (satisfied at all times) to figure principal possibilities out), labeled as *pure fitting*, which is described as a retro perspective overview of the fitting activities. The best compromise of opening the previous established fitting relations vs. accuracy in alloy fitting for more flexibility is by:

For single elemental parts of the potential (Fe-Fe and Y-Y):

- URs were kept in principal: α/β was left unchanged (1.875), but r_e (1NN) was allowed to vary by 15% (so was set to a fit parameter)[67]
  The key driving UR η was set as a fitting parameter with the constraint that C_{12}-C_{44} (hcp Y) or B (for bcc Fe) was allowed to deviate up to 25% from the actual values (more did not help).
- As announced previously f_e was changed to a fully flexible fit parameter (with the original f_e as a starting value), leading to different ρ_e.
- The other analytic more specific restraints in EMB and pair part (for C11-C12 for instance in F_2 and *A&B*) were loosened up by including tolerances of 20% in the target values – leading to broader fitting ranges.
- In the fitted defects (energies) were allowed up to 20% deviation without any punishment.
- However, the restraints for continuity in the EMB part were fully kept (otherwise unphysical!).

All this easing of the analytic restraints served for better agreement with alloy phases and defects. For the additional pair potential exclusively for Fe-Y (see theory chapter 2.2.3) the following flexible fitting ensemble was set up:

- β was allowed to very as a pure fitting parameter from 4.0 to 8.5 (this is necessary due to parts of the kept restraints in the single elemental parts).
- r_e varied between 2 to 15 (but lattice constant was constantly monitored by lattice equilibrium condition, see 3.2.1 and deviations greater than 10% in single phase and 25% in alloy phases were severely punished). r_e is linked to 1NN of the lattice constant of the phases an these varied from 2.87 Å (pure bcc Fe) to 11.87 Å ($Fe_{23}Y_6$).
- *A* and *B*, since these are a kind of fine tuning parameters as previously explained, were completely flexible in a broad range (and this worked well).
- λ, shaping the cut-off behaviour, was allowed to vary from 0.1 to 1.0 (fading btw. 5Å to 10Å, physical). $\kappa/\lambda = 2$ was kept.

[66] summary of the following description: different levels of restraints (no restraints (5 fittable parameters in the pair pot and many others) to many restraints (1-2 fittable parameters in the pair pot) and few fits were tried out for each restraining level)

[67] Changes in α/β (in Fe-Fe & Y-Y) seems to be a considerable *downgrade*– results were significantly worse than with the fixed ratio

In lengthy and tedious trial and error sessions these settings have been found to be the best working and most efficient set up for this fitting environment with POTFIT for the here presented Fe-Y phases (see chapter 4 where by the use of RF-MEAM it was successfully fitted). However, the maximum fitting success in this technique of these complex phases was limited to a maximum of two specific alloy phases – a principally stable but quite inaccurate reproduction had been achieved for $Fe_{17}Y_2$ and Fe_2Y ($Fe_{23}Y_6$ is also of interest but was not working, and Fe_5Y is suitable to represent melting though its existence is in dispute (and can be excluded for now see [142])). In these at least stable modelled phases the lattice constant had deviations of up to 10%, the cohesion energy was at least within 5-7% accurate – but the more significant problem is that fact that the order of the phases is incorrect. This maximum accuracy is unsatisfactory and not usable for MD simulations (principal improvements in the technique are necessary as done in chapter 4[68]). On top of that, all the previous efforts for accurate fits of defects are kind of lost. Defect accuracy in alloys was just 15-20% and in single elements it even decreased to 20-25% (all with a lot of wrong orders/sequences!) – since these defects are essential for the stated questions in the introduction, this is unacceptable and additionally emphasises the need for an improvement in technique.

This was only a rather superficial overview, since no direct useful results of physical properties or behaviour can be obtained from these rather limited fits. But it is mentioned to highlight, that the limits of POTFIT were successively tried out – and as a preparing step to get to the bottom of the limitation in POTFIT (next section).[69] Why is that (failure)? – that's the underlying question, which will be examined in the next section by a deeper examination of the parameters sets with the help of the Rose eq. and also it will be systematically "carved" out with the help of the extensive DFT data base that hcp Y in particular involves some rather unique and challenging, hard to model, special features in alloys. In advance it can be said: it is an unlucky combination of rather limited fitting tools (LSM in POTFIT) and the challenging nature of alloys including Y. Nevertheless, these efforts provided an important fitting base for advanced fits in the next chapter (e.g. as starting parameters and parameters for basic properties) and helped to learn to obtain parameter sets for basic properties, which can be kept as a part of an alloy potential.

3.3.6 Applying the Rose eqn. and formulating a *Rose criterion*

Regardless of the unsatisfactory outcome of the previous fitting efforts by this EAM formalism in POTFIT (only approximate representation of selected phases and drastic worsening of defect properties) helpful systematic relationships in the fitting formalism were discovered. The main step, enabling these observations, was to use the key driver η not just for fixing parameters but also for distinction and control between different parameter sets – the contribution of W in the calculation of the parameter η for hcp Y (see 3.2.1) was added in a multiple of n fractions of W – such a use of η can be mapped to a systematic scan of different parameter sets (which changes the interplay of pair and EMB part by a change in the fitting behaviour of β).
This scanning by using η in this manner served two purposes: 1. The possible parameter sets were tested in a systematic and reliable manner. 2. Moreover, this scanning lead to the discovery, that only η corresponding to values greater than the estimated by the Rose eq. were chosen in fits with defects and/or alloys. Values below the "Rose estimates" were only chosen for single metals (and resulted in the best possible fits in that category). This lead to the in this work labeled *Rose criterion*: in fits with this EAM technique a choice of η and its corresponding parameter sets above the rose estimate for η is suitable for alloys and defects and a η below the estimate by Rose eq. is suitable for accurate single metal potentials.

[68] The advice of many potential experts to simply open the URs, like α/β was a „false friend" – POTFIT with its rudimentary LSM optimisation method is simply not able to find other minima (also even if force matching is applied – tried to reproduce reduced high end RF-MEAM pots. with some MD DFT data- did not work!)
[69] In addition, fitting is connected to failures, failures promoting advancement should be published to avoid further mistakes

But why do even with the best suitable parameter sets, determined by this Rose criterion in this formalism, fail to fit all phases of interest properly, and the only possible fits for alloys are a weak compromise solution with massive downgrades in the single metal properties (while in Mg-Al [91] for instance this formalism could yield more convincing results). In order to resolve this, this problem will be simplified with the help of the extensive DFT database and the simplified problem will be examined with η and the Rose eq. and compared to the DFT data, revealing the challenging (fitting) nature of some unique properties of Y in metallic alloys (which is one of the presumable reasons, why Fe-Y has not really been modelled by non-machine learning potentials before). At first the Rose eq. will be now properly introduced (it was postponed to this section, since here this eqn. is properly applied in a meaningful context). The Rose equation (eq.) is described by:

$$E_{Rose}(r) = -E_0\left[1+\alpha\left({}^{r}/_{r_e}-1\right)\right]e^{-\alpha\left({}^{r}/_{r_e}-1\right)} \; where\; \alpha = \sqrt{\frac{9B\Omega_e}{E_c}} \qquad (3.56)$$

This equation gives a kind of correct energy density at different volumes of a material (lattice constant is varied) by the lattice constant r, the equilibrium lattice constant r_e, the bulk modulus B, the eq. atomic volume Ω_e and the cohesion energy E_c. The dashed black line in Fig. 3.11 shows the corresponding curve obtained by applying the Rose eq. at different lattice constants – this curve can be also called the equation of state (EOS) curve (though strictly speaking the EOS curve is the exact curvature and not this approximation, here it is labelled like this). This equation originates from work by Rose and co-workers in the 80's [58], who discovered a remarkable pattern of cohesion energy curves vs. various volumes, or lattice constants respectively, around the equilibrium volume in a broad range of metals. By considering some derivations, they could work out, that these curves can be described by only two parameters (r_e and α) to describe the relation of energy vs. distortion (lattice constant out of equilibrium), very similar to the UR key drivers α/β with r_e (the consideration of a non-fixed η represented a further refinement of this technique). This curve by this Rose eq. as a black dashed curve vs. the total energy of Y calculated by the best hcp Y EAM pot. in alloys (red) and calculated dots by DFT (for comparison). The space between the blue EAM curve and red DFT curve (blue corresponding another parameter set for more accurate single metals) are all the possible curves by different parameter sets (driven and controlled by η). Consequently, in bcc Fe due to the cubic symmetry all the considered parameter sets (for these purposes) result in the same curve .All in all, for Y in Fe-Y alloys different parameter sets are possible and these will be compared in the next section.

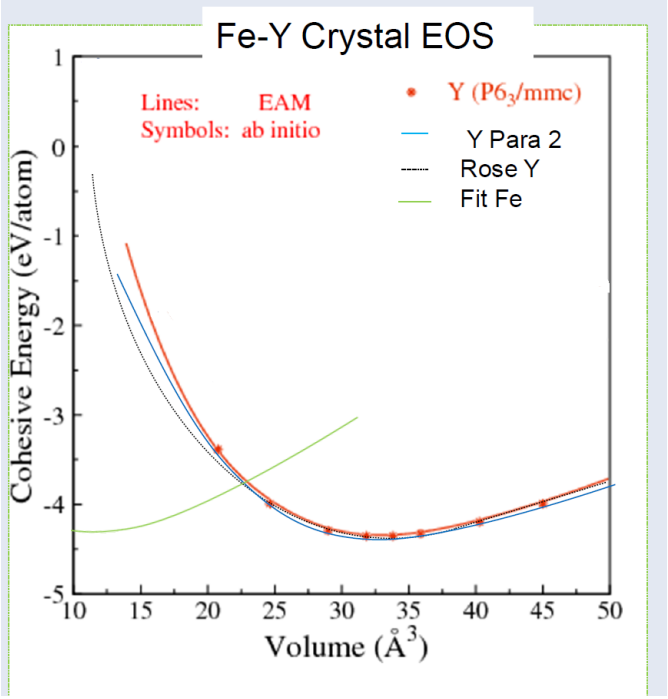

Figure 3.11 Illustration of the different parameter sets (blue and red) in hcp Y as an EOS, energy vs. a volume cell, in comparison to Rose (black) and DFT (red) data points – the parameter sets her are driven by the sublattice relaxation energy. Bcc Fe, the green curve (left) has no parameter sets from this point of view.

3.3.7 Simplification of alloy fitting identifying the underlying obstacle

In order to understand the reasons for the mismatch between the capabilities of the fitting technique (optimisation by LSM supported by UR with similarities to the Rose eq.) and the complexity of the atomic references, in particular the defects in Fe-Y, the fitting problem is simplified as: for the alloy part only selected representative defect clusters, which illustrate quite well in which way Y in Fe is unusual, are used now to check the suitability (linked to the publication by the author and Y. Mastrikov [5]).
The chosen rather specific defect cluster group describes a single Y atom in bcc Fe cluster with an increasing number of vacancies (underlying data as binding energies published in [5]). The differences between the defect clusters (as illustrated in Fig. 3.12) and ideal configurations and configurations with vacancies with no Y, representing dissolution into the isolated components, are described by these binding energies.[70] These clusters were included in the fit as the only atomic reference data for Fe-Y (8 configurations (2, 3, 4, 5, 6, 7, 8 and 9 vacancies with 1xY), resulting with different symmetries in 32 energies, see appendix A.6 in 7.1) – now the modelled EAM potential should principally be able to reproduce these.
But, surprisingly only 2-3 subsequent binding energies, shown in Fig. 3.12, out of 8 could be modelled. The remaining ones were not "hit", huge systematic errors and wild spreading of incorrect binding energies counteracted an accurate representation of these relatively basic clusters.

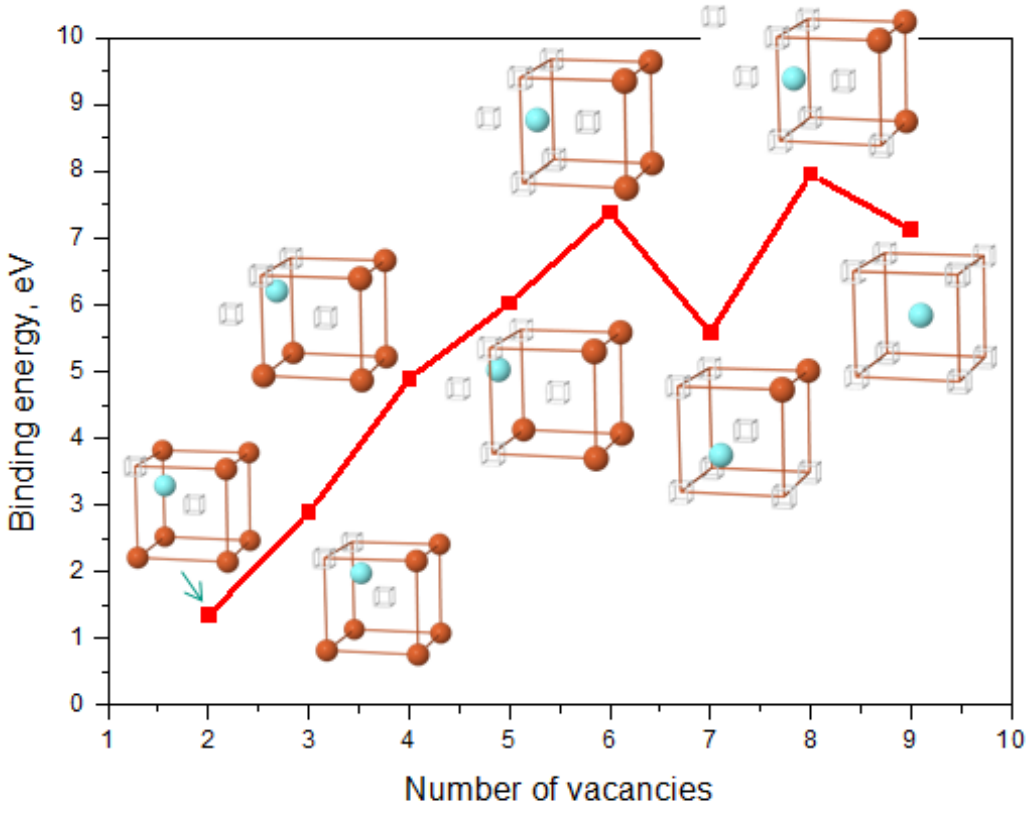

Figure 3.12 Binding energies of Y-vac. clusters with an increasing number of vacancies (red points, lowest energy by most symmetric set-up), courtesy of colleague Y. Mastrikov, who presented this graph as labelled on a conference in Tartu (2013) [144].

[70] Formula of binding energies $E_{bin} = E_{config} + E_{ideal}(N - n_{Fe} - 1) - E_{vac}(N - n_{Fe})$

The interesting fact: when swapping parameter sets (systematically controlled by η) each parameter set "hits" different points – one hits 2 and 3 of the energy data points (according to the number of vacancies in Fig. 3.12), another one 3 to 5, the other 1 and 2, another 8 and 9, but never more than three and always either between 2-6 or 8 and 9, or 7 alone. So, seemingly suitable parameter sets, which are accurate in single metals, can model small extracts of these clusters but not all. This is a simple but at the same time effective test, whether the potential model is suitable for Fe-Y, its phases and defects. Test failed (after some improvements by RF-MEAM in chapter 4, it will be passed)! The underlying cause, which can be mapped to the fitness of the whole EAM model and POTFIT, can be finally revealed by the physics and some unique anomalies in these clusters and how the Rose eq. *treats* these:
Looking at the clusters of Fig. 3.12 two facts are remarkable: 1. position of the Y atom in vacancies 2. the "valley" at 7 vacancies (see Fig. 3.12)

1. Y has the special, quite unique property of double vacancies, one single Y can occupy two vacancies at once (see Fig 3.13 in bottom corner). Even more, in the paper of the author and Y. Mastrikov [5] it could be found that: "*the lowest energy configuration for yttrium is in the middle between two vacancies on the NN sides of bcc iron lattice*", as shown in the cluster of Fig 3.13. This is in drastic disagreement with the underlying physics and assumptions of the Rose eq., lead to an universal EOS proposed by Rose, which seems to be unfit for the requirements to describe defects, especially interstitial, correctly. Already earlier investigations by Johnson and Oh [55] in the 80's distinctively showed that the Rose eq. in Fe is only suitable for distortion up to a maximum of 4% (and that is a conservative estimate!) – but for defect properties much larger deformation ranges need to be covered. In Fe and its great variety of defects for instance distortions up to 15% are common (and a suitable potential should cover at least 10% distortion satisfactorily, which Rose eq. does not). So, the Rose eq. turns out to be too restrictive. Since the defect properties with such high distortions (deformations) crucially shape this position, calculations/potentials based on the Rose eq. can hardly cover these specific positions between two vacancies, consequently not allowing such an anomaly as this kind of occupied double vacancy (or the so called *solute centered divacancy* (SCD)). This also influences the formation of phases and explains why this formalism has difficulties reproducing these Fe-Y phases.
2. This behaviour is linked to the fact that within the slope of increasing binding energy with increasing number of vacancies at the 7. vacancy position a local minimum occurs, this set up resembles the aforementioned positioning of the Y atom with two vacancies (it even resembles a kind of stable triangle), leading to significantly increased stability, alternating the binding energy drastically, causing an energy well with a characteristic barrier of approximately 1.8 eV [5]. This potentially leads to self-stabilising mechanisms in the creation of Fe-Y clusters, the number of vacancies increase up to this point, then the Y is kind of trapped. This is absolutely essential in the formation of Y defect clusters in (bcc) Fe and also for an accurate defect description in Fe-Y (which also did not work here).

Although, this technique showed good results in single metals with a promising chance for alloy potentials, the special unique behaviour of Y in alloys requires enhanced abilities of the potential formalism and fitting technique. While the potential formalism is extendable (from EAM to MEAM, great advantage of EAM) the fitting program can be even called a *dead end*, since in POTFIT at least referring to the Rose eq. is unavoidable. It is needed to stick to known global minima, proximity has to be given as input by suitable parameters and/or restraints. And in this case it can be only achieved as URs which are closely related to Rose eq. – but this has been identified as the major obstacle for fitting Fe-Y alloys! The Rose eq. needs to be replaced, but this requires enhanced optimisation techniques by a new fitting code (next chapter 4). These results can serve as a useful starting point (in the form of essential start parameters) and even as a valuable part of an advanced RF-MEAM pot. in chapter 5.

Therefore by this work in chapter 3 the cornerstone with invaluable findings for the whole project is laid.

3.4 Summary of achievements in this chapter (3)

- Set up a versatile and flexible formalism and understood its interplay with the resulting EAM pot. and material properties
- Developed *own fitting routine* in POTFIT and changed code to implement own fitting restraints (extract see appendix, 7.3)
- Set up *a changed UR method* with the key driver concept leading to significantly improved accuracy and flexibility
    - instead of rigid UBRs exactly following the Rose eq., the new independently developed URs only orientate to the Rose eq. and allow more flexibility for better defect accuracy (especially wrt. tuning of η)
    - instead of fitting to the averaged bulk modulus, specific fitting routines wrt. elastic constants are enabled
- Developed by these key drivers the *new "Rose" criterion (p. 73)*, which is able to detect the "alloy-suitability" of parameter-sets
- Formulated and implemented further *new detailed restraints* for more accurate elastic and defect properties
    - Improved bcc Fe potential
    - fitted one of the very few *EAM hcp Y potentials* with very exact elastic and defect properties, e.g. first time successful reproduction of stable BO SIA
    - more accurate vacancy formation energy in bcc Fe, satisfactory divacancies in hcp Y
    - better transferability as shown by a better match in the first pressure derivative of the bulk modulus (B'), though it was not fitted to, as opposed to ZW
- Formulated these parameter sets for basic properties in a way, which allows keeping these as a part of an alloy potential
- Established distinctions to previous potentials and described the differences e.g. to the cutting edge MEAM potentials by B.J. Lee
- Analysed the use of the Rose eq. and *discovered and explained the underlying fitting problems in Y alloys for the first time* and prepared the solutions to this in order to successfully fit Fe-Y → replacement of Rose eq., even as an orientation for the URs, absolutely necessary!
- developed a decisive and new testing procedure to check for the "Fe-Y alloy fitting suitability"
- Resultant main finding – discovery of suitable base (EAM) start fitting parameters (/sets) in an RF-MEAM fitting scheme (4.1.2) for reliable links to the most suitable parameter sets representing the best accuracy in these fundamental base properties – supplying these base start parameters is an irreplaceable necessary fundament for the following GA based RF-MEAM fit-techniques.
  It is not just simply one parameter set – but by these insights several opposing parameter sets, with systematic differences, were retrieved - the provision of such different (and not similar) parameter sets is absolutely essential for the GA based MEAMfit procedures, since the GA systematically *runs through* these sets and shuffles them in the pursuit of a global minimum –

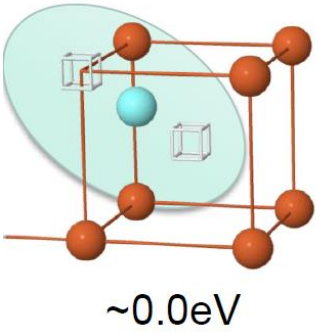

Figure 3.13: Visualisation of the specific and very stable SCD position of Y btw. two vacancies - That's kind of what all this is about! (Cluster picture extracted of a presentation [144] with permission by Y. Mastrikov)

All in all, the here obtained techniques and especially the discovery of suitable RF-MEAM compatible fitting parameter(/s) (/sets) as a solid starting point in a GA assisted fitting scheme are *the essential preliminary results for the following fitting success in chapter 4*.

Fig. 4.0 (complementing workflow Fig. 4.2 on p. 85): this is a look ahead of the infrastructure associated to the RF-MEAM formalism. This overview, though, shows that effort is drastically increased by use of this formalism, consisting of three stages: potential optimisation (left), which is launched with the start parameters bascially local and global minimsation with GAs, then the middle denotes improvements in the infrastructure, which mainly covers performance increases by GA tuning & development of LAMMPS module for the last step MD.

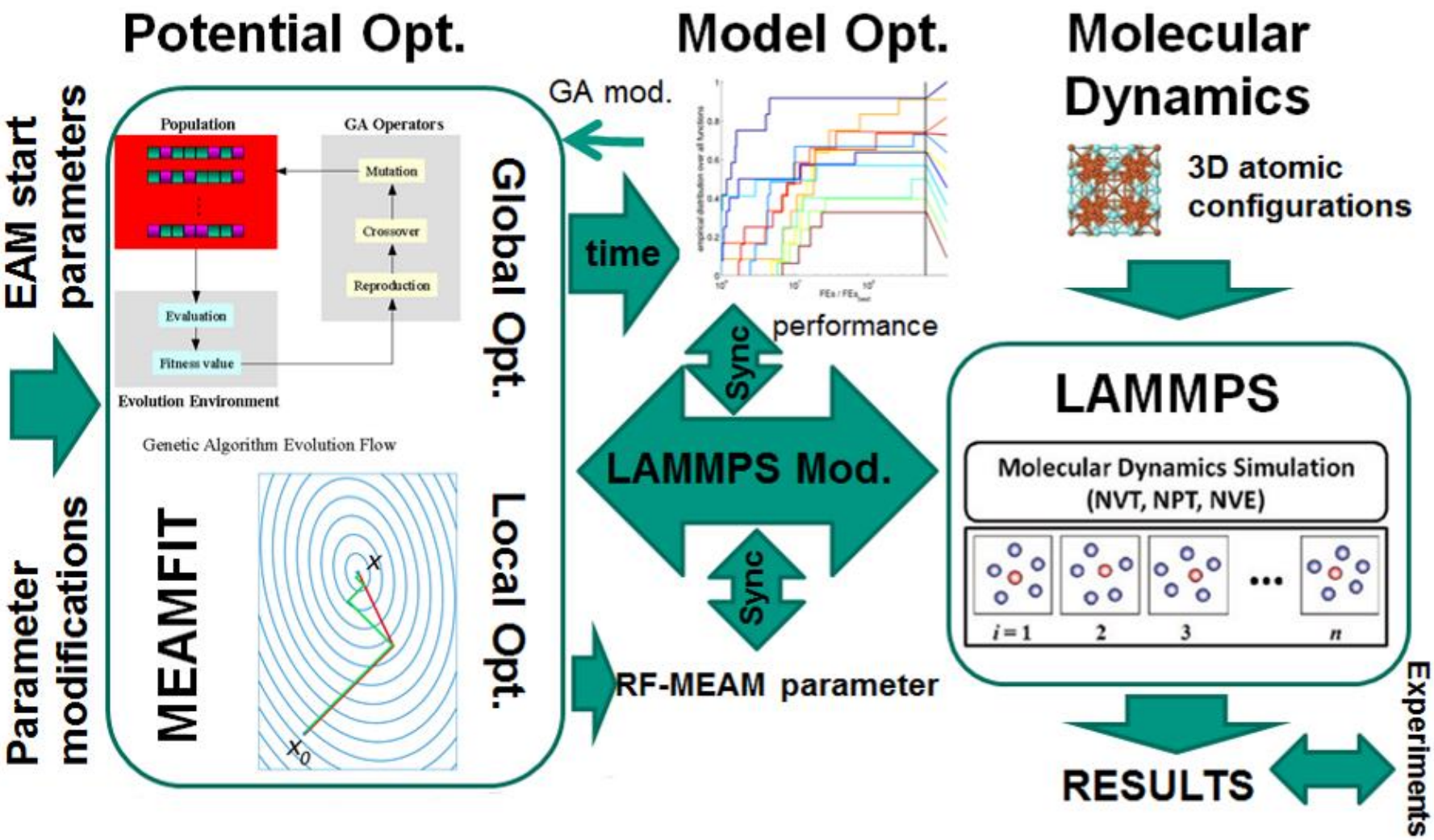

4 Fitting with MEAMfit & advanced MD results in Fe-Y

As established in chapter 3 the EMB-pair matching by the Rose eq. (*Rose matching*) needs to be replaced by a more effective and intelligent fitting technique than POTFIT for advanced results in 4.2 (by better global optimisation). In addition to a more advanced global optimisation, chapter 3 highlighted the importance of a thoroughly reasoned explicit potential formalism as an integral part of a fitting technique, which performs EMB-pair matching by fitting only without UBR/URs, Fig 4.1 provides a first overview.

This improved technique is developed and applied in the second half of this chapter with the help of the code MEAMfit [99] and a self-developed module for LAMMPS. The application for Fe-Y alloys will be further improved in the discussion of chapter 5 by linking fits to EXAFS spectra with the help of modern ab-initio MD (AIMD) techniques (enabled due to the generous help of Dr. M Marques & Prof. Ackland).
Before getting into the details of RF-MEAM and the workflow in MEAMfit (s. 4.1) few introductory remarks about RF-MEAM wrt. the question "*Why is this specific reference free (RF) form necessary?"* are raised (after MEAM has been already presented in 2.2.4). The RF-form is essential, simply speaking due to the fact that even the standard form of MEAM (*MEAM* without the prefix "RF") inevitably relies on the *Rose matching* with all its obstacles in Fe-Y, as shown by UR (linked to Rose) assisted EAM MD runs in chapter 3. The only difference in the Rose matching btw. EAM and MEAM is, that in the standard MEAM formalism the pair part is Rose matched and the EMB part is fitted (not the EMB part as in EAM, more details in 4.1.1). The detailed EMB part in MEAM (→chapter 2) solely depends on references in the fit database and the inclusion of angles in this part enables an accurate representation.
In principle the enhanced physics by MEAM allows fitting of more details by these included angles in MEAM to a point (reducing the number of possible parameter sets), at which Rose matching can be abandoned. However, this requires advanced optimisation techniques, which also compare the parameter sets as mentioned in chapter 3. In other words a fitting technique which considers the various atomic references more as a whole unity – this necessitates the conversion from MEAM to RF-MEAM. Afterwards the here applied combination of RF-MEAM and GAs in *MEAMfit*, presented in the next section 4.1, enables this for exciting results in Fe-Y.

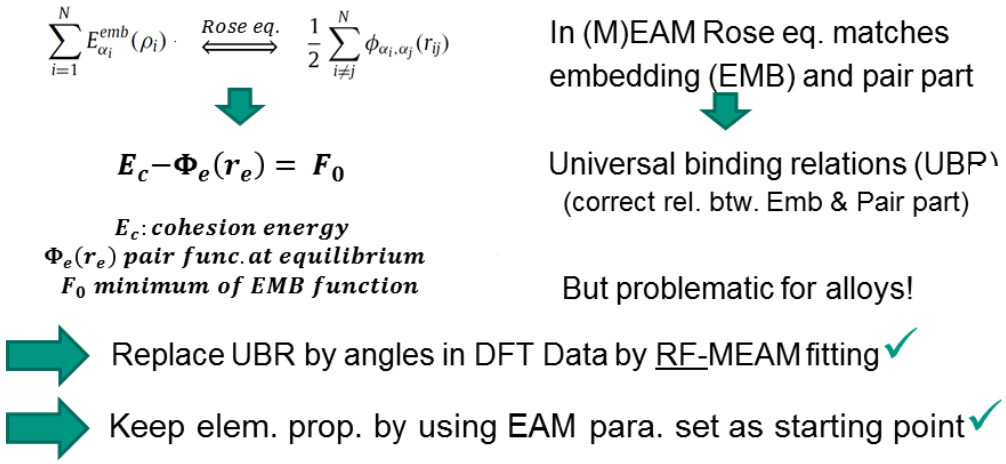

Fig. 4.1 Schematic illustration visualising general improvements by RF-MEAM: the pair and EMB part are matched by Rose eq. (top LHS) in MEAM, too (top RHS), this is characterised by UBRs – in RF-MEAM these are replaced.

4.1 Description of RF-MEAM & Workflow in *MEAMfit*

As a preparation to the rather mathematical introduction of the reference free (RF) format in 4.1.1 by transforming MEAM to RF-MEAM, some light is shed on the background of the aformentioned motivation for the use of RF-MEAM – more details how the atomic references are linked to parameter sets and how they shape the parameters during the fitting process.[71]

When fitting complex alloys[72] without the support of advanced global minimisation techniques such as GA, suppose standard LSM like techniques in MEAM, than the Rose eq. is applied in the following manner: the EMB parameters are fitted one by one to the atomic references of the fit database. Ideally, for a good fit each atomic reference consists of serveral atomic structures with one atomic reference at equilibrium as a reference structure and a set of other structures at various elongations out of equilibrium. This set is well reperesented by many parameter sets (very similar to the discussion in chapter 3 with Fig. 3.3 and 3.11). It is like the corresponding curve to one datapoint of Fig. 3.12. The distance between these atoms of the atomic references of this data point can be varied and will yield similar energy volume curves as in the aformentioned figures. Accordingly, the fitting programm finds many parameter sets (many curves), which are a suitable representation for this single curve. Crudely speaking, the shape of one single curve kind of represents the local minimisation for that atomic reference, the choice which parameter set to take corresponds to the global minimisation. And after this „local minimisation", the same is done for the next atomic reference. However, when considering this single atomic reference a plain LSM fitting code has no knowledge of the other *next* atomic references (for the here considered Fe-Y around 125 atomic references with 1500 energies are in the fit-database) with other corresponding parameter sets. Consequently, as said many times before, there is only a very small selection of suitable parameter sets for *all* atomic references. How to chose the parameter sets (without the following GA technique)? Simply by restraining the choice of parameter sets by the Rose eq. in the form if of an exact match between the pair part and the Rose eq.. As a result, in classical MEAM no parameters for the pair part are fitted but controlled by some physical input parameters of the Rose eq., as it will be shown in 4.1.1 for comparitive reasons (the UR $\alpha/\beta=1.875$ in chapter 3 is like a flexible link to the Rose eq., but still a too severe limitation for Fe-Y alloys). So, one definite parameter set is selected with the help of the Rose eq., because only one parameter set matches to the Rose eq. (by introducing the Rose criterion it has been shown that this is a compromise btw. alloy and single element properties).

It is quite challenging to find an alternative for this convenient, but at the same time too restrictive approximation by the Rose eq. as this oversimplification is especially critical when considering several phases in Fe-Y as shown in chapter 3. A good starting point for an alternative is the major simplification by the Rose eq. in MEAM in the fact of having the same equilibirum distance (r_e) in the pair and EMB part (which is a significant reduction in possible parameter sets). While this is still acceptable in EAM, in MEAM due to the bonding angles this is a kind of an oversimplification which is compensated in standard MEAM by including screening factors, which impedes the fitting substantially[73]. In RF-MEAM on the other hand this and the Rose eq. can be elegantly avoided. The use of GAs (4.1.2) and RF-MEAM (as introduced in more detail in 4.1.1) as a combination introduced by Thijsen et. al. overcomes these problems as presented in the next section 4.1.1 & 4.1.2.

[71] One could note, that this could have been discussed in chapter 2, but here its worth considering this in more depth with more concret examples for MEAM, since a solution is presented in the subsequent sections

[72] In quasicrystals or oxides the parameter space can be restrained by additional constraints (stresses) and or CTIP models [95] (in Y-O these are very unstable) – little reminder complex denotes the unusual behaviour of Y, e.g. the scd occupation

[73] In other more technical words it can be even said, the standard fitting code cannot distinguish these parameter sets resulting in a poor transferibility of the found parameters (these parameters cannot be applied for other references) – even in MEAM as said before. When using LSM techniques for MEAM the questionable Lenowsky scheme is necessary as Rose and a siginificant conern as illustrated in the extra section in the appendix.

4.1.1 Explicit form of MEAM and transformation to RF-MEAM

In RF-MEAM the EMB part is fitted in the same way as in standrad MEAM (as said before without GAs) but the pair part is matched by fitting to the whole fit database, so to *all* atomic references. In order to do so, the formalism needs to be extended to the reference free format: including another r_e for the pair part (called r_p in 4.1.1). Furthermore, this requires due to the disappearance of Rose matching (and the required flexibility for fitting) four more parameters, raising the number of parameters from 13 to 18 for a single metal (but since the *C* screening factors are waived, in fact 16 parameters remain). Values of physical properties as an input are not taken any more in the direct Rose matching form. The optimisation code *MEAMfit* exhibits the great ability to distinguish and select parameter sets by GA operations, such as cross selection and mutation (more in 4.1.2), and to translate this to the corresponding pair parameters (this is of special interest when fitting several phases). However, even with GAs the number of suitable parameter sets needs to be restrained. Thats where MEAM comes into play, by the inclusion of bonding angles in the models with more specific parameter sets in the EMB part (namely for l>0) there are less parameter sets for matching. So, the initial hypothetical idea in the introduction of chapter 4, to replace the Rose eq. by angles, can be realised with these tools. Before applying the GAs and fitting in MEAMfit (4.1.2 & 4.1.3) the aforementioned transformation will be presented in detail:
One of the first potentials using this technique was an improved MEAM potential by the at this time newly developed RF-MEAM potential by M.Timonova and B.J. Thijsee for silicon in 2010 [94]. For the transformation the explicit potential form used in that paper is resumed and is then transferred to the used form in MEAMfit. As said before in chapter 2 the total energy in MEAM can be expressed as:

$$\Phi\,(r_{ij}) = \sum_{ij,i\neq j} \frac{1}{2}\varphi(r_{ij})\,S_{ij}h(r_{ij}) + \sum_i F\,(\rho_i) \quad (4.1)$$

Where $\varphi(r_{ij})$ is the pair potential function, $F(\rho_i)$ the embedding function. $F(\rho_i)$ itself is similar to EAM, but the description of the individual ρ_i is different, as principally shown in chapter 2 (here the explicit form will be explained). $h(r_{ij})$ is a cutoff function, which is of no relevance at this point. S_{ij} are the angular screening factors, which are also not further considered, because MEAMfit allows setting them to 1 and effectively turning the screening off. Therefore, these factors are treated as being set to 1 in this work. Nevertheless, before the availability of MEAMfit in 2016, due to some shortages in the use of GAs (Timononova used some less developed evloutionary algorithms) the screening factors had to be turned on ($S_{ij} \neq 1$) to restrict parameter space by hand (alternations in a narrow range).[74]

The $F(\rho_i)$ used in RF-MEAM are very similar to the ones used in EAM (also in MEAMfit s.b.)

$$F(\rho_i) = \left(\frac{\rho_i}{\rho_e}\right)\ ln\left(\frac{\rho_i}{\rho_e}\right) \quad (4.2)$$

Little fine differences in $F(\rho_i)$ are tuned for the intended fitting purposes, here there is no η (due to the details in the electron density by l>0). The indiviual ρ_i is then expressed as a sum of different orbital contributions as said in chapter 2:

$$\rho_i = \frac{2\rho_i^{(0)}}{1 + e^{-\sum_{l=1}^{l=3} t^{(l)}(\rho_i^{(l)}/\rho_i^{(0)})^2}} \quad (4.3)$$

[74] *the same is true when charges are included in the model, e.g. by CTIP models, as done for Al-O by Laszic than as a matter of course the screening parameters should be turned on (mainly ionic not a mixture of metallic and ionic, for this CTIP is unstable).*

Eq. (4.3) can be also expressed as:

$$\rho_i = \frac{2\,\rho_i^{(0)}}{1+e^{-T_i}} \qquad with\ T_i = \sum_{l=1}^{3} t_i^{(l)} (\rho_i^{(l)}/\rho_i^{(0)})^2$$

This sum ρ_i of partial electron densities at different angular moments *l* running from 1 to 3, can be best understood by starting with $\rho_i^{(0)}$, which is the spherical electron density contribution as by common EAM potentials. By a T_i, which can be described as an angular contribution, this standard density is amended by electron orbital contributions, which are angularly dependant (see eq. (4.4) below). This T_i is a composition of the different orbitals with a weighting of each orbital by the factor $t^{(l)}$, where l is the angular momentum. These orbitals contribute a partial electron density $\rho_i^{(l)}$, which can be calculated by:

$$(\rho_i^{(l)})^2 = \sum_{j,k(\neq i)}^{N} f^{(l)}(r_{ij}) f^{l}(r_{ik}) P^{l}\left(\cos\theta_{ijk}\right) \quad (4.4)$$

What immediatelly strikes, is the $cos\,\theta_{ijk}$, which stresses that in this calculation triplets of the atoms j and k surrounding the considered atom i are taken into account, by considering the Legendre polynomial of the angle between these (for the explicit form a nice example is given by Tadmor on p. 278 [22]). The $f^{(l)}(r_{ij})$ are the electron density functions, as in EAM, but in MEAM there is one for each l (and therefore in MEAM these are called partial electron density functions. The summation here denotes the inclusion of all triplets (N), so here all atoms are considered (before that the individual atom-atom interaction was taken into account, but for the electron density all atoms need to be summed up).

The partial electron density function chosen in the RF-MEAM potential by Timonova has a very beneficial form for the transformation of the aforementioned MEAM to RF-MEAM, it is expressed by:

$$f^{(l)}\left(r_{ij}\right) = e^{-\beta^{(l)}(r_{ij}/r_e-1)}\, h\left(r_{ij}\right) \quad (4.5)$$

As before the cutoff function $h\left(r_{ij}\right)$ is of no interest. What's of interest is the fact that for each partial electron density (indexed by the l ranging from 1 to 3) there is a separate $\beta^{(l)}$ parameter. Setting $\beta^{(l>0)} = 0$ the standard EAM form can be retrieved and in fact apart from the cut-off is the same form as the EAM form in chapter 3 (this is of advantage, since it was shown that this form can be used for the here considered problem and Rose matching is possible). $\beta^{(l)}$ can be interpreted as a kind of decay parameter of each partial angular density of each orbital representing the superpositions of the different orbitals. Another important controlling parameter is r_e, which was also in EAM closely connected to the Rose eq. It's the same here, this r_e occurs again in the pair part, but here it is purely matched in the following way:

As announced in the introduction, in standard MEAM Rose matching will be conducted by equating the pair part of eq. (4.1) to the previously introduced equation of state (eq. 3.56):

$$\sum_{atoms\ (N)} \sum_{ij} \frac{1}{2} \varphi\left(r_{ij}\right) S_{ij} h\left(r_{ij}\right) = N_{atom}\, h(r\ )E_{Rose`}(r) - \sum_{atoms\ (N)} F\ (\rho_i) \qquad (4.6)$$

The RHS side is controlled as in 3.3.6 by the physical properties, namely the equilibrium lattice constant r_e, the bulk modulus B, the equ. atomic volume Ω_e (calculated by r_e,) and the cohesion energy E_c. But a slightly more detailed Rose eq. is used, the 3rd order Rose eq. ($E_{Rose`}(r)$) controlled by the parameter ϵ:

$$E_{Rose`}(r) = -E_C\,(1+\epsilon+\xi\varepsilon^3)e^{-\epsilon} \quad (4.7) \qquad \text{with } \epsilon = \sqrt{\frac{9B\Omega_e}{E_c}}\left(\frac{r}{r_e}-1\right) \quad (4.8)$$

ξ is an additional fitting parameter to control the correcting third order term in the Rose eq. for matching. The pair part of classical MEAM thus depends on three physical input values (r_e, B, E_c) and one marginal fitting parameter. Since it is matched to the Rose eq. no explicit form for a pair function is required, it is actually the form of the Rose eq. with fixed parameters. In total the classical MEAM has 3 input parameters and 13 fitting parameters for a single element: one for the pair part and 11 for the EMB part (4x $\beta^{(l)}$, 3x $\beta^{(l)}$, 2x screening parameters, two cut-off parameters. Surprisingly, it can be noted that the final RF-MEAM in MEAMfit has exactly 16 fitting parameters for one single element as MEAM, but no physical quantity input parameters, still the number of parameters is the same.

After having explained the motivation and general idea of the transformation, the actual change in MEAM to replace the Rose matching by fitting lies in the decoupling of the electron density. It can be elegantly executed in this form of the partial electron density functions by performing the following steps:

Eq. (4.5), representing this density function, is simply rewritten with the help of the new parameters $q^{(l)}$ and $p^{(l)}$, these replace $\beta^{(l)}$ and the parameter r_e:

$$f^{(l)}(r_{ij}) = e^{-\beta^{(l)}(r_{ij}/r_e - 1)}\, h(r_{ij}) \xrightarrow{q^{(l)} \text{ and } p^{(l)}} f^{(l)}(r_{ij}) = p^{(l)} e^{-q^{(l)} r_{ij}}\, h(r_{ij}) \qquad (4.9)$$

$$\text{with:} \quad q^{(l)} = \frac{\beta^{(l)}}{r_e} \quad \text{and} \quad p^{(l)} = e^{-\beta^{(l)}}$$

Now instead of separate $\beta^{(l)}$ and fixed values for r_e, r_e is automatically included in the value $q^{(l)}$, and in RF-MEAM this value is fitted. This makes the input of r_e and the associated rigid links to references redundant. The advantage here in RF-MEAM is, that each $q^{(l)}$ (for l running from 0 to 3) can have a different associated r_e (in the combination of $\beta^{(l)}$ and r_e) – leading to a significantly increased flexibility by this seemingly minor transformation (with meaningful consequences though). As said before this change requires a powerful fitting technique and here it becomes obvious: several r_e are indirectly chosen by fitting instead of setting just one r_e – since this r_e affects all references, the fitting needs to work with regard to the whole fit-database (as in GA or by manual constraints in the form of screening factors). The number of parameters is increased by the need for a fitted pair function, it is around 5 parameters for a single metal. Before coming to that, two remarks about the elegance, even beauty, of this form are made:

1. When keeping the screening factors (making the fitting harder though), RF-MEAM and standard MEAM can be simply transformed by dividing the resulting weighting factors $t^{(l)}$ for the total electron density in RF-MEAM simply by the factor $\left(e^{-\beta^{(l)}}/\rho_e\right)^2$.
2. And also in RF-MEAM as in MEAM by reducing for a monoatomic system the number of parameters in $p^{(l)}$ by restraining the index from one to zero (only for $p^{(l)}$) eq. (4.2) can be simplified as $F(\rho_i) = F_0\, ln\left(\frac{\rho_i}{\rho_e}\right)$. This second point is a useful check to get sure that the transformation kept the properties of the originating standard MEAM form.

The explicit form of the pair potential depends on the used fitting technique. Contrary to Timonova GA techniques in MEAMfit were used. So, the pair potential and the partial electron density expressions are different. In Timonova's RF-MEAM the pair function was similar to the Rose eq., controlled by the parameter $\eta_p = \left(\frac{r}{r_p} - 1\right)\alpha_p$, where, as said, before r_e is replaced by a specific pair potential parameter r_p. By using GAs and well-established choices of the two above mentioned functions screening factors could be avoided leading to different expressions (as long as no charges as in Fe-Y-O are explicitly fitted).

Having shown these originating developments and ideas (RF-MEAM transformation) the used explicit expressions for the partial electron density and pair function in MEAMfit can be better understood. In MEAMfit these are expressed as:

$$f_{\mathrm{A}}^{(l)}(r) = \sum_{n=1}^{n_{max}} a_{\mathrm{A}}^{(n,l)} \left(r_{\mathrm{A}}^{(n,l)} - r\right)^3 \Theta \quad (4.10)$$

$$\varphi_{\mathrm{AB}}(r) = \sum_{n=1}^{n_{max}} b_{\mathrm{AB}}^{(n)} \left(s_{\mathrm{AB}}^{(n)} - r\right)^3 \Theta \quad (4.11)$$

These expression can be called „the heart“ of the RF-MEAM formalism in MEAMfit. Therefore, it is not surprising that quite a lot of information is incorporated there.

It is best to start with the indices „A“ and „AB“, these simply denote the species, the metal respectively, the potential is describing. When having Fe-Y as in EAM, there are pure Fe-Fe (so A stands for Fe, B for Y) pair pots. and electron distribituion functions. The pair potential can have either the pure AA or BB functions or the additional AB (Fe-Y) mixed pair potential function. When purely considering the function (without parameters), the index will be dropped for a better overview.

The fitting parameters are simply described by $a_{\mathrm{A}}^{(n,l)}, r_{\mathrm{A}}^{(n,l)}, b_{\mathrm{AB}}^{(n)} and\ s_{\mathrm{AB}}^{(n)}$ – but to *really* understand them, it helps to link them in principle to the aforementioned original RF-MEAM: $a_{\mathrm{A}}^{(n,l)}$ are like the different $\beta^{(l)}$, where by the n a series is crudely speaking like a Taylor series of the exponential. $r_{\mathrm{A}}^{(n,l)}$ is like different r_e, important scaling of the exponential decay. In the pair pot. function the $b_{\mathrm{AB}}^{(n)}$ are like the α_p parameters and the $s_{\mathrm{AB}}^{(n)}$ are like the r_p.
Following the idea of RF-MEAM having different $r_{\mathrm{A}}^{(n,l)}$ and $s_{\mathrm{AB}}^{(n)}$ is similar as before (having different r_p and r_e) and both parts are fitted *at the same time*, the crucial idea of RF-MEAM is applied in this different expression. Concluding this comparison, it is interesting to note that there are more parameters than in the RF-MEAM of Timonova, this is to account for the omitted screening factors – these are implicitly included in these functions, an amendment of the original idea for better optimisation. Lastly, about this function, Θ is simply another cutoff function which is of no interest at this stage of description.

On top of that, the expression for the EMB energy is in RF-MEAM different, too:

$$F(\rho) = a_{\mathrm{A}}\rho^{1/2} + b_{\mathrm{A}}\rho^2 + c_{\mathrm{A}}\rho^3 \quad (4.12)$$

This EMB function is simply a sum of different polynomials, which depend on the total electron density ρ, and the function is controlled by the three fitting parameters a, b, c, where the index “A”, as before denotes the described species (which metal, s.a.). This kind of EMB energy expression belongs to the previously used expressions of the partial electron densities and this combined explicit expression of partial electron density, pair function and EMB energy is very well established (later, see result section 4.2.2, it turned out choosing this is particularly useful, since the Fe-Y potential could be significantly improved by an unmodified inclusion of G. Ackland’s detailed Fe potential [76], which is fortunately in the same explicit functions. Beside the convenience, this (same form) also ensured that no details of the Fe pot. are lost due to transformations, which would be likely in transformations between different forms).

“The rest” of the electron density calculations is the same as before. The differences in the explicit expressions are limited to the pair pot. and elec-dens (similar though) and different EMB energy (compare eqs. (4.9) to (4.10) & (4.11) and (4.2) to (4.12)) and setting the screening factors to 1 – these are all the differences to the in detail presented RF-MEAM formalism. However, the correlated “screening factor simplification” complicates the application in standard MD simulation programmes, as shown next.

4.1.2 Workflow: implementing GAs by MEAMfit & LAMMPS Module

Obviously, the previously introduced formalism (4.1.1) shows some challenging implementation aspects, since much more data, reference files, need to be handled in a multi-layered evolutionary algorithm (with the sub-class GA), representing a new fitting technique. A compact summary of the necessary workflow on the GA assisted fitting in MEAMfit is presented in Fig. 4.0 (p. 78) & Fig. 4.2, the 3 main tasks are:

1. Model optimisation: a substantial part of the potential optimisation is performed by the GA (top in the corresponding box on LHS, below a schematic sketch of a local CJG minimisation). This GA, however, necessarily needs to be fine tuned, synchronised respectively, with the analytical functions of the optimisation model (what has been essentially presented before in 4.1.1). The GA is extremely sensitive towards the linear coupling between the parameters [102] – by improvements with the *OGOLEM* GA code base [143] performance increased by a factor of 20.
2. Pot. Optimisation/Fitting cycles: on the very LHS the arrow indicates the input of the start parameters, which are the obtained fitted EAM parameters from chapter 3 (the great advantage of EAM and MEAM (also in RF-MEAM) these are compatible, as explained before). Surprisingly, the GA fitting stage fails without these reliable start parameters – these act as a kind of orientation for different local minima, by the aforementioned fitting mechanism a variety of parameter sets can be generated (which should be linearly mutually decoupled!). Considering how a GA works, this necessity can be reasoned (scheme on the RHS in Fig. 4.2):
    - Selection: The first step is exactly the same as in non-GA techniques: suitable parameter sets, passing the requirements, need to be found. Most of this step was already accomplished using the previously presented EAM formalism.
    - Cross-over: This is the improvement, now the provided parameter sets will be selected in pairs and with a probability *p* both sets will be mixed. The *Machine learning like* feature is, that the GA keeps track of the mixing processes and redistributes the probabilities according to the success. However, this mixing is highly sensitive towards the mutual (linear) dependence of the parameter sets – that's why the rigorous parameter set selection in chapter 3 kind of *pays off now*.
    - Mutation: Individual parameters are randomly changed and the result is checked, and the cycle starts again and is repeated until a fitted potential reaches the targets.
3. LAMMPS Module: To yield the desired MD results a module was developed to integrate the fitted RF-MEAM pot. into LAMMPS (*translates* RF-MEAM parameters to the implemented 2NN MEAM interface), based on previous results by Scopece [98].

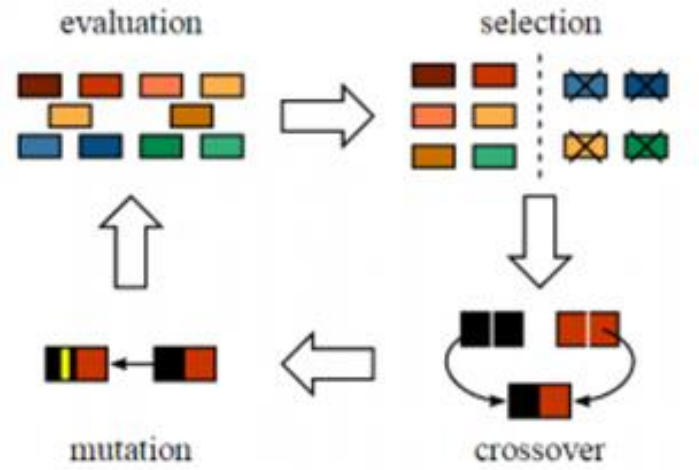

Fig.4.2 LHS: About infrastructure around MEAMfit an additional chart beside the *look-ahead* Fig 4.0. on p. 78 explaining the principals of GA with friendly permission by Vidhya [163]: the boxes denote parameter sets and at the first step (top RHS) suitable parameter sets are selected – a pre-selection for linear decoupling was done in chapter 3, these states are then mixed by crossover and eventually mutated, and then evaluated – one cycle.

4.2 Results with *MEAMfit*

Now, having significantly improved the fitting techniques of the established MEAM formalism by the use of RF-MEAM and GAs in MEAMfit (after a rigorous analysis of the problems in EAM in the previous chapter) finally the fitting of Fe-Y with all its details, mainly information about phases and defects, has been successfully performed. In 4.2.1 a broad general overview of the achieved accuracy of the fits (= fitness) will be given, which already reveals an interesting tendency: in the performed RF-MEAM optimisations the fit database entries containing details about phases and defects (in the form of clusters as shown in chapter 2) can be separated into two „kind of conflicting" classes – all fits obtained by this aforementioned technique bear the challenge of finding a compromise between the accuracy of the phases and the defect cluster accuracy. This results to two different potential types: type A, superior in (point-) defects and only satisfactory in phases, and type B, which is good for phases and acceptable for defects. This point is deepened by showing the surprisingly very accurate performance in defect clusters of pot. type A (using the original developed test in Chapter 3, in 3.3.7). However, when considering phases in 4.2.3, though in general also well performing in phases, unfortunatelly pot. type A bears one vital shortage describing a subtle, but at the same time essential, detail about one particular phase difference (which is hard to model, though). Pot. type B on the other hand masters this and many tremendous challenges in the description of phases. The consequences of this compromise are illustrated by considering the first succesful MD simulation of dissolved Y in melted bcc Fe, a mixture of liquid Fe and Y – the outcomes are influenced by the choice of pot. type A or B. Since for every specific application one cannot know beforehand, which properties are more important in this complicated Fe-Y system, one needs to fit both phase and defect processes accurately *in the same potential*. Only such a potential can *really* contribute to the wider goal of this work: understanduing ODS steels and its formation or at least parts of it (in form of Fe-Y interactions). In the following discussion, chapter 5, this pathbreaking step for ODS will be consequently taken by including additional EXAFS data for combined *dual* high accuracy.

4.2.1 Overview of fitting success – all fit data

Already the general key performance fitting indices, simply the R value as introduced in 3.1.4, show that in principle this fitting technique is working, as shown in Fig. 4.3. The blue curve in this figure shows the R value for all atomic references wrt. the number of energies used in the fit database. Since as said before between 1500 to 2000 energies of approximately 125 configurations were used, an overall R value of 0.11 to 0.12 could be achieved – that's on average an agreement within ≈10%. Considering the variety of used data this is a remarkable achievement of the RF-MEAM formalism and the advanced implemented optimisation techniques in MEAMfit. However, this R value only gives a first overviewing insight, whether the fit is useable at all. Only if the R value is below 0.15, as said before, more detailed investigation as in the next chapters can be performed. A better idea, of how well the data is fitted can be obtained by looking at a histogram, listing the deviation of each reference. Performing various fits and looking at these, it quickly became obvious that all potentials can be divided into the two classes A and B (see introduction/foreword of chapter 4.2). More specifically by looking at the histograms it could be found out, that potentials of type A are in general agreeing with the defect clusters within 8-10% (0.08-0.1) and the phase data on average to 15% with occasional outliers of about 20%. Pot B on the other hand agrees with the phases on average within 5% (with outliers up to 10%) but is only accurate in clusters about 13%-15% on average. The complexity regarding the increased inaccuracy in defects in pot. type B is nicely illustrated by the vacancy-yttrium binding energy wrt. the mutual distance as NN. These energies substantially control the movement of dissolved Y atoms in Fe. Thus, an accurate representation is of enormous interest (there are more detailed clusters such as the VYV-VYV clusters as shown in the underlying paper [5], but these (VY) are the fundamental ones, which should be fitted first). Pot. type B can model the binding energies of

the first two NN (1NN and 2NN) within 15%, which is acceptable. Unfortunately, interactions of the 3rd to the 5th NN are weak energies (>0.25 eV), but which have to stay positive, representing attraction and the tendency to form clusters. Regardless of the fitting effort (while keeping the phase details accurate) no potential of type B could yield positive energies, all were negative energies of up to -0.1eV (detailed table see appendix, A.11 in 7.1, top RHS p. 124). This has severe consequences for the aforementioned broader view and is unacceptable when considering solute Y in Fe (above T_m), this point *recurs* in the advanced result section 4.2.4. Pot. type A is right there but on the other hand has unavoidably a wrong order of the first first Fe-Y phases with low Y content ($Fe_{17}Y_2$ & $Fe_{23}Y_6$), see 4.2.4.

In addition to the aforementioned general considerations, fig. 4.3 shows another hidden issue (which is well known in the fitting-community): overfitting. This is checked by applying a testing data set. The testing data set are atomic references which are not included in the fit, but after the fit these are compared to the results predicted by the fitted potential (and then a new R value is calculated which includes that). Looking at the red curve, including the testing data set, it has been found, that the optimal number of energies (linked to 125 references) is around 2000, leading to an R of around 0.1 ∓ 0.015. The location of this threshold crucially depends on the model and the *nature* of the data. The nature of the data simply implies the correlation between the fitted energies and the connections between the atomic configurations – either too specialised (like one configuration with 1000 energies leading too little transferability) or various totally incoherent configurations, both cases are not desirable considering overfitting and its threshold. Since the fit database is extensive and has many variations, 2000 references as a threshold seems reasonable (and further tries for more accuracy, for instance for defects by including more references/energies, are not advisable, that's why this should be checked). In the discussion in chapter 5, when energies of an ab initio MD run are included, the threshold shifts to much higher values, allowing minor improvements – but for the general purposes these 2000 suffice (however when looking into detail in some process related to "broader ODS tasks", as discussed later, these 2000 energies are not enough).

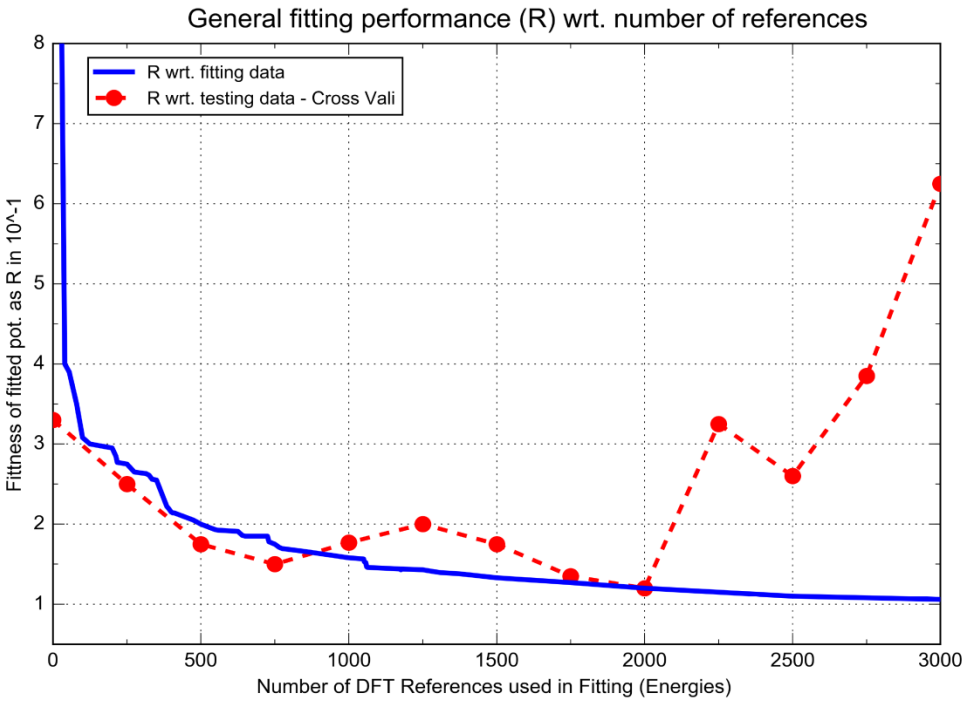

Fig. 4.3 Relationship between fitness of the potential as an R value and number of references in the blue curve wrt. to the fitting data. Additional testing cases, red curve, reveal the onset of overfitting (at ≈2000 references)

4.2.2 Binding energy test and improvement of Fe-Fe component

After the general examination, revealing the challenging limitations by the compromise btw. phase and defect accuracy in the potentials fitted by MEAMfit (labelled from here on (pot) type A/B dilemma), it is worth illustrating, that in either defects or phases these potentials are very successful. Both pot. types, Pot A and Pot B, are able to pass the previously in 3.3.7 developed test for defects and the principal ability for representation of alloys superbly, as shown in Fig. 4.4. This shows significant improvement.

Fig. 4.4 shows the results by potential type A, type B is not included due to its higher deviations, but it still matches the binding energies within 15%, which is acceptable (the systematic trend at the first three iron dominated points (number of vacs. 2-4) leads to larger deviations) .
Such an accurate agreement to this extent for these vacancy defect cluster binding energies with pot A is quite a surprise. The main reason for this lies in the detailed and accurate DFT data base and that the powerful combination of GA and RF-MEAM in MEAMfit was capable of these details (the surprise also stems from the fact that this is one of the first times MEAMfit is applied for such a complicated test set). Standard EAM or MEAM are not able to reproduce these binding energies that accurately. EAM with the Rose eq. (see 3.3.7) is not able to reproduce all energies and standard MEAM techniques without RF-MEAM and GA leads to deviations of at least 30%.[75] This clearly proves that the implementation of these rather evolved techniques were worth the great effort.
Returning to a more critical observation, Fig. 4.4 also reveals that the deviation of the RF-MEAM pot. type A to the true binding energy follows a systematic trend, the gap to the actual binding energy increases systematically with a decreasing number of vacancies, starting at four vacancies to two vacancies where the iron interactions dominate in that cluster (see dashed line in Fig. 4.4). This clearly indicates some deficits in the Fe-Fe interaction and raises the question how to improve these. Since the DFT database is not as detailed for Fe-Fe as for Y-Y and Fe-Y clusters, it is rather obvious that the fitted Fe-Fe interactions in this work are not as detailed and accurate as Y-Y and Fe-Y.

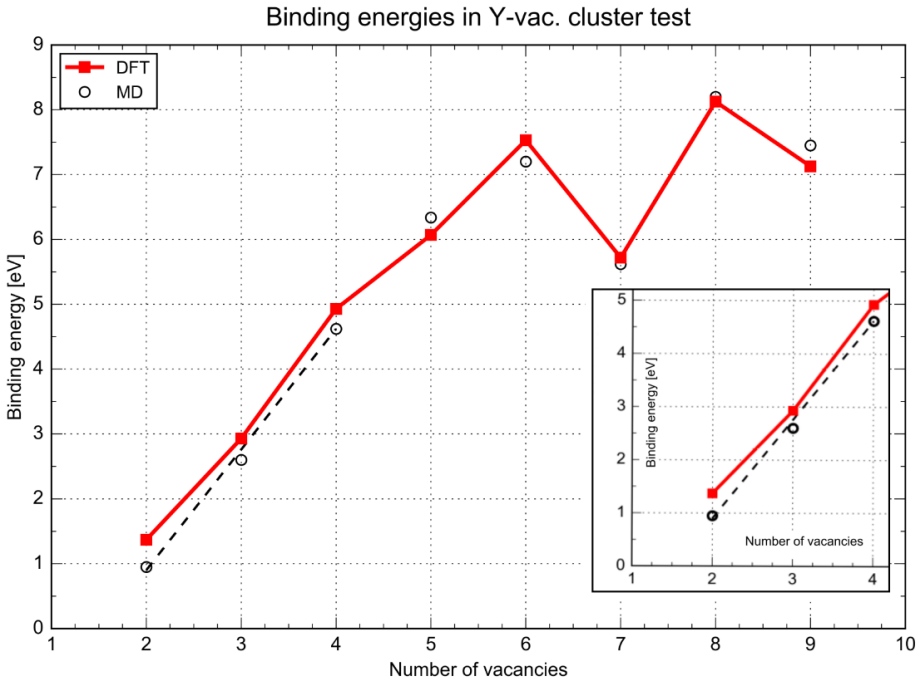

Fig. 4.4 Passing the set up test of chapter 3 – the circles show the great agreement of pot. type A in the binding energ- ies, type B is similar: below a close-up of an improvement by adapting the Fe-Fe part as done here in 4.2.2

[75] Though no suitable other hcp Y MEAM potentials are available, the available Fe MEAM potentials (e.g. Lee [92]), will at least contribute to deviations of up to 25% due to the inaccuracies of the description of disordered molten phases in FeY→following text.

This Fe-Fe potential, as part of Fe-Y pot., is replaced instead of performing lengthy DFT recalculations for the Fe-fit-database. The renown Fe-Fe potential by Mendelev and Ackland, called potential 2 in a publication of 2003 [76], serves here as a well-established, detailed and accurate potential replacement (a later improved magnetic version turned out to be less suitable [118], supposedly because included magnetic states in that pot. are not a good match to actual magnetic states in Fe-Y). Having replaced the Fe-Fe part, the extract on the lower RHS in Fig. 4.4 shows a satisfying improvement of the iron dominated domains. With this improvement all energies are reproduced more accurately within 10%.

This convincing improvement raises the following question, how an EAM potential without the inclusion of the angular influence performs that extraordinarily well. The "trick" of Ackland's potential is the inclusion of ab-initio calculations of "liquid-like" states with forces in the atomic references (further annotated as melted), with some similarities to the aforementioned force matching method in POTFIT (chapter 3). This allows avoiding the use of the Rose eq. (but the universal binding relations can be reproduced by this EAM potential, in fact even better than by the Rose eq.). The same underlying idea, replacing the Rose eq., has been applied in MEAMfit, but with different replacements for Rose Matching. Namely, beside these force matching like techniques, additional constraints are required in the form of additional fitting targets, which are mostly energies, forces or properties of additional atomic references. This can be better understood by using the interpretation of EAM as the previously introduced glue potential: force matching ensures the right potential function (including its parameters), but this function has several gauge DOF (=parameter sets) which need to be reduced by the additional fitting constraints.

Supposedly in Ackland's potential these additional restraints were applied by using a detailed database for (self) defects in Fe (and some fitting target parameters, such as energy differences in phases) similar to the one for Fe-Y described in chapter 2. Now, the *actual art of potential fitting* is using a reasonable complementing combination of force matching and additional restraints — parameter sets chosen by force matching and sets selected by wisely chosen additional restraints have to suit each other, even harmonise.

As a matter of fact, the defect clusters and forces of the melted states/configurations are a particular good match, because these defect clusters show some meaningful similarities to the melted states. The defect clusters have a very high density of defects (even higher than in a real solid bulk) — this high density very well resembles the characteristic *disorder* in a liquid. Thus, it (defect clusters with such a high defect density) is similar to the liquid state, leading to available, fittable parameter sets of the forces and clusters.

Concretely, by considering the resulting electron densities parameter sets can be conveniently distinguished, especially by the maximum and the equilibrium density. It can be interpreted, that the inclusion of the melted, liquid like configurations, particularly limits the range of possible electron densities (compression in liquids are rather limited, this is also reflected on the atomic and elec-dens). Thus, drastically reducing possible parameter sets (because many include unrealistic high elec-dens), which corresponds to a limitation by the maximum electron density of $\rho_{max} \cong 33$ [76].

Since interstitial defect clusters lead to higher electron densities and the additional atom causes some small atomic separations to the NN of the interstitial, such interstitials are similar to compressions. These interstitial clusters improve the description in the potential function on the LHS of the minimum, for compressed lattice parameters, namely $r/r_0 < 1$ (as explained at the beginning of chapter 3 in 3.1.1 & 3.12.). These compressions by defects also imply higher electron densities (as for melting). It can be said that at $r/r_0 = 0.95$ the maximum electron density is reached, ρ_{max}. Both in the liquid-like melting configurations and in the (interstitial) defect clusters similar electron densities are yielded supporting the hypothesis of similarities between these (since the region of the potential formed by the interstitial defect clusters belongs also to melting properties). As mentioned in [76] such interrelations were already at the historical beginnings of EAM, ≈30 years ago, theoretically considered by Carlson [144, 145], who considered the physical implications of the electron density as a parameter. Following these considerations (effectively implicating $\Phi''(\rho) > 0$), a physically sensible EAM model in Ackland's pot form should not exceed electron densities of ≈50. And indeed, all defects and liquid-like states are limited to the aforementioned 33 (ρ_{max} at T = 1820° K≈30 and at 2200°K ≈33, <100> interstitial in bcc ρ_{max}=30.7 [76]).

Firstly, this further confirms the hypothesis, that the liquid-like states are similar to (interstitial) defect clusters and that they suit each other. Secondly, this fixes the maximum density to around 34 and narrows down the selection of available parameter sets to the ones, which are linked to a physical sensible behaviour in this respect. Thirdly, this also confirms that this particular combination of defects and liquid states in a fit-database can act as a good replacement for Rose matching. So, the defect clusters describe the behaviour at compression well and are on top of that able to support the match of the pair potential curve to the EMB part (because the defect clusters are linked to the liquid like references which as said in point two reduce parameter sets in the EMB part). And fourthly, these considerations also help to approximate limitations in EAM, for compressions leading to a ratio below $0.95a_0$ (upmost 0.9) the pot. behaviour becomes rather unphysical (but <0.9 is not needed for the intended purposes of this work, otherwise pot. 4 is a better choice but not in this context). Summarising, all of this provides some detailed reasons, why Ackland's potential is able to improve the iron dominated binding energies in Fig. 4.4.

Naturally, the Fe-Fe potential is capable of much more *interesting* tasks than these rather theoretical considerations (which are nevertheless important for functionality). Before addressing these tasks, from the perspective of potential development, which this work is mainly about, there is even much more to these aforementioned thoughts than that. The use of the electron density as a *parameter set distinguishing indicator* is perfectly capable to explain, why it is not just a coincidence that this particular Fe-Fe component fits into the previously developed RF-MEAM Fe-Y potential (see 4.1) as a replaced by pot. 2 [76] for the Fe-Fe part in the Fe-Y pot.[76] Though, the reduced analytical form of RF-MEAM and Ackland's pot. are the same (reduced = obtain EAM by turning off the angular part in the RF-MEAM by setting all $t_{Fe}^{l>0} = 0$) the exactly adopted parameters do not necessarily need to match. Again, parameter sets – the parameter set of Ackland's Fe pot. could potentially belong to completely different, incompatible (to the Y-Y pot. developed in this work) parameter sets. Usually, two single metal ((M)EAM) potentials cannot simply be added together to form an alloy pot., as said in chapter 2. Fortunately, here, as a surprising exception, it does work because of one simple reason (apart from the same analytical form): both Fe-Fe pots., the one of Ackland and the one developed in this work have similar equilibrium electron densities (ρ_e), 26 vs. 24-25, indicating as explained before similar, at least suitable, parameter sets, which are capable of forming an alloy pot. with the Y-Y component.
As a result of these previous insights, the following guiding *rule of a thumb* becomes apparent, (M)EAM potentials with similar explicit analytical expressions and similar electron density parameters ($\rho_e, \rho_{max}, \rho_{defect}$ in this case) are promising candidates to set up an alloy potential. Besides, all of this also has to do with the fact, that when comparing the underlying paper to chapter 3 it can be even said this match stems from similarities in the fitting logic and using the parameters of chapter 3 as a starting point.
All in all, the Fe-Fe component was crucially improved by these efforts and it was explained why this match is possible. On top of that, the R value of the total Fe-Y pot. was improved from 0.11 to 0.09-0.10.

More generally, apart from the rather narrow minded binding energies, the greater benefits of this inclusion can be very well illustrated by considering the structure factor as done in the original paper [76]. Fig. 4.5 (RHS), taken from Ackland's paper [76], shows the structure factor obtained slightly above the melting temperature of 1811 K by the aforementioned Fe-Fe potential (pot. 2 in the paper and shown as the dotted line) vs. "standard potentials" (pots. which do not have these detailed forces in the fit-database as said before). It can be immediately seen, that even the first peak, is greatly overestimated by non-force fitted potentials, the dotted line, pot. 2, on the other hand very well matches to the experimental data (represented by the continuous line obtained by Il'inskii et. al 2002 [146]). This also reflects the accurate representation of the correct energies in the relaxation curve (see LHS), the graph even suggests that down to $0.85a_0$ energies are appropriately mapped. But at a closer look, below $0.90\ a_0$ it gets rather unphysical, some of the interstitial energies are not 100% correct, for instance the dumbbell formation with very close atomic separations, the repulsion acts kind of too strong. Another potential of the paper, pot 4, overcomes this

[76] Obviously, for a complete inclusion of the Fe-Fe pot, another fit cycle with fixed Fe-Fe paras (but selected flexible Y-Y & Fe-Y) was performed.

problem. However, it did not match the Y-Y pot as well as pot. 2 (presumably due to a lower transferability).

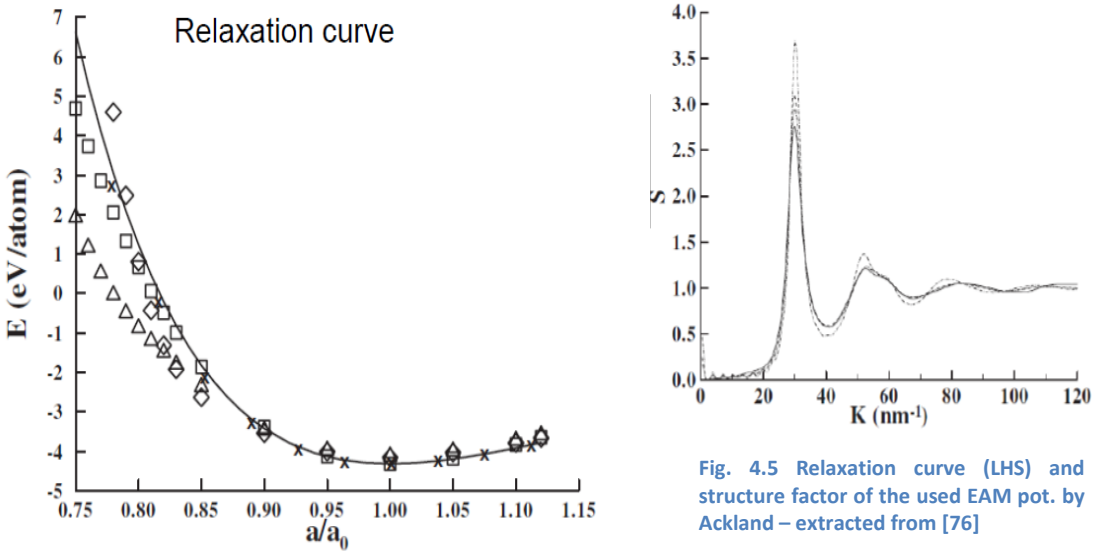

Fig. 4.5 Relaxation curve (LHS) and structure factor of the used EAM pot. by Ackland – extracted from [76]

Nevertheless, the accuracy of pot. 2 is sufficient and the accuracy in melting and the liquid state is outstanding. This is backed up by considering the melting temperature T_m: 1772 K by the EAM pot. vs 1811 K in experiments [137], this is an agreement within 2.5% (and pot. 4 is less accurate here (1753K) and this is for the wider use in an Fe-Y a considerable disadvantage, beside the fact that pot. 4 does not match well). This represents a kind of an all-time record for all empirical and semi empirical MD potentials (pair and cluster functional) – the widely renown MEAM potentials for Fe by Lee [88] and also ABOP potential by Müller [78] are far from this accuracy for T_m, their estimate is around 2200°K, the deviation is one order of magnitude higher, around 22%! Even M. Mock's ABOP potential for Fe-Y [132], as far as the author knows the only other one for Fe-Y, could not resolve the inaccuracy in Müller's Fe-Fe ABOP pot.. Consequently, it also has this wrong T_m of around 2200K (to be fair though, the phase transitions, especially from α to γ Fe are more accurate there, but in 2007 Ackland improved the potential by inclusion of magnetic properties (but this one did not fit into the fits of this project at all)).

Summing up, luckily this Fe-Fe pot by Ackland [76] fits into the Fe-Y pot. of this work (for the aforementioned detailed reasons). This accurate Fe potential provides an invaluable foundation for experimentally interesting calculations of dissolved metals in molten Fe with links to ODS – only with a correct T_m the melting behaviour of Fe is reliable. Though, this is one of the *first* and simplest questions for modelling ODS on a bigger MD scale, this has never been done before, no MD investigation about dissolved Y in molten Fe. With the help of this pot. to ensure accurate Fe-Fe interaction, pot. type A reproduced accurate findings of melted Y in Fe, see 4.2.4.
Before doing so, in the following section 4.2.3 a few remarks are made about the phases and about one seemingly tiny inaccuracy but with important consequences for pot. A in 4.2.4, stimulating further discussions involving the use of EXAFS in the next chapter.
Another final (side) remark here: one could also suggest to fit the potential for the whole Fe-Y system with the same technique as for pot. 2, which kind of brings it back to force matching in "POTFIT style" – it has to be kept in mind that the "parameter-set space" for alloys is fundamentally different than the one for a single metal. Looking at the history and developments in Fe and Fe related alloys, it can be said that these techniques are rather appropriate for single metals (e.g. another success the Ti pot. by Ackland & Mendelev [147]), alloys, like Fe-Y, require techniques, such as the used combination (RF-MEAM&GA).

4.2.3 Fitting phases of Fe-Y

After the improvements of the potentials in the last chapter 4.2.2, one could easily get the impression that pot. A is now an ideal candidate to describe Fe-Y in liquid states, which is of particular interest for ODS. Unfortunately, that is, simply speaking, as too often in the "potential development business" not enough, especially in the rather complicated case of Fe-Y. This has to do with the complicated behaviour of the phases in Fe-Y – the high number of possible phases, seven (five diatomic ones, see next page on RHS, plus Fe and Y as described in detail before), is a first indication. A lot can be said about these. But, when only considering smaller amounts of dissolved Y in ht or melted Y this content can be limited as a handy simplification up to 20%. As a direct consequence, principally only $Fe_{17}Y_2$ needs to be precisely incorporated (appended phase diagram A.3 in 7.1 by Kardelass [16]). By coincidence, this happens also to be the only Fe-Y phase for which reliable EXAFS data for experimental validations are available (by our collaborating-group of Prof. Purans at ISSP, Riga). Nevertheless, for a clear separation to the adjacent phases the direct neighbouring phase $Fe_{23}Y_6$ needs to be included in such accuracy, that the energetic sequence wrt. $Fe_{17}Y_2$ is maintained – this, as addressed before, is the key point about phases in the context of this work and the main focus is placed on these two phases. So, these two iron rich phases are of interest[77].

$Fe_{17}Y_2$ & $Fe_{23}Y_6$: $Fe_{17}Y_2$ as presented in the table on the RHS corresponds to an amount of ≈10 % Y in Fe, and $Fe_{23}Y_6$ to ≈20%, all three (including α & β phase for the first) are pretty closely interlinked considering the corresponding cohesive energies and structures – these phases are separated by very fine differences, as highlighted before: $Fe_{17}Y_2$ is a complex phase with a unit cell of 19 atoms, existing in two phases (states) α and β with the same cohesion energies but slight differences in the structure. At low temperature [148] the rhombohedral α state is preferred, both potentials reproduce the structure and lattice constant (within 3% see RHS) and the cohesion energy very accurately, as desired, within 1% at low temperatures (around 40K). At higher temperatures, e.g. room temperature, the hcp α phase is dominant, which is accurately represented by both potentials within 3% and 1%. Only in pot. type B but not type A the exact same energy for both phase, α and β, is hit, but in pot. type A deviations of ≈0.015eV appear. It has to be stressed beforehand here, that the exact nature of the transition from β to α is not well known yet and the transition temperature is more or less speculated, some say 20K some even say high temperature [149], some suggest mixed phases ([150] & Mihalkovic [142]). As a lookahead of chapter 5: by indirectly including magnetic influences with AIMD it becomes apparent, that $Fe_{17}Y_2$ at room temperature seems to appear as a mixture of both phases, which depends on the temperature influencing the magnetic states.

This "mixing" behaviour supposedly plays an important role for a clear distinction to the structure of the $Fe_{23}Y_6$ phase (fcc) with a very similar cohesion energy (phase difference only 0.05eV) and *a* lattice parameter. This phase is reproduced by both potentials with the same accuracy as for $Fe_{17}Y_2$. But, even 1% accuracy in cohesion energies cannot ensure, that the represented cohesion energy of $Fe_{23}Y_6$ is always more negative (-4.29 eV) than of $Fe_{17}Y_2$ (-4.24 eV). In Pot B, when putting less weight on the defects and allowing higher inaccuracies, this fine difference can be accurately modelled, in Pot A with very accurate defect properties however this seems to be impossible. Pot A correctly models $Fe_{17}Y_2$ with E_c -4.26 eV but $Fe_{23}Y_6$ with a less negative E_c of -4.23 eV (this is assumed to be the best result in this formalism with a defect accuracy of 5-10%) – though the detailed correct defects are interesting for Y diffusion, this wrong sequence in Pot A has meaningful consequences in the next section 4.2.4, when looking at the *bigger picture*.[78] Probably the right order of the two phases without magnetism (though it seems to be exactly the reason for the two-phased existence) contradicts the occurrence of some defect configurations.

Having clarified this major point about the two phases of interest, for the sake of completeness few general remarks about the other phases and the fitting accuracy are made:

[77] B*efore including Fe_3Y and increasing the modelled Y content up to ≈35%, challenges in these two systems need to be resolved*

[78] both pots might assume that the α state exists purely at room temperature, which might be in contrast to some defect formations.

Fe_3Y: When increasing the Y content this is the next phase after $Fe_{23}Y_6$ with 25% Y content. From the purely practical ODS point of view, this phase is of technical importance, because it is used as a main Y donator (and to form ODS particles) in the production process of austenitic ODS steel [8]. As $Fe_{17}Y_2$ it has rhombohedral structure with an E_c of -4.37eV and a distinct structure (lattice parameters) causing sufficient differences to all other phases. Thus, all pots. can reproduce this phase and surely do not "mix up" this phase (e.g. confuse $Fe_{23}Y_6$ as this one). Though quite accurately reproduced, E_c within 2.5% and the lattice parameters within 5% (*a* within 2%, *c* within 5%), no further investigations including this phase were conducted (for further reasons see footnote 78 on LHS).

Fe_2Y: This is kind of the most complicated phase, because it is a Laves phase with a C15-type crystal structure [149], causing various magnetic states with strong influences, the energy contribution by magnetism is around 0.15eV (compared to 0.02-0.05eV for the other phases) [151], making it hard to model in these non-magnetic potentials, and leading to deviations in the cohesion energy of up to 10%. Luckily, this phase seems to be of no significance in ODS applications. So, it's acceptable.

Fe_5Y: According to experimentalists Fe_5Y apparently does not exist at all [137], while ab initio predicts it as a metastable phase [142]– so, it is in dispute. Regardless of that, it was included in the fit data base because it has the same hcp stacking as $Fe_{17}Y_2$ and is very useful to support a reasonable melting behaviour of it.

Phase	DFT	Exp. [152]	*Type A*	*Type B*	ABOP [132]
	Targets		Own		
α-$Fe_{17}Y_2$ ($P6_3/mmc$)					
a	8.31	8.46	8.58	8.56	8.62
c	8.24	8.28	8.40	8.35	8.33
E_c	4.24	n.a.	-4.26	-4.25	-4.25
β-$Fe_{17}Y_2$ ($R\bar{3}m$)					
a	8.31	8.46	8.60	8.56	8.63
c	12.45	12.41	12.58	12.54	12.48
E_c	-4.24	n.a.	-4.23	-4.25	-4.27
Fe_6Y_{23} ($Fm\bar{3}m$)					
a	11.87	12.08	12.11	12.04	12.21
E_c	-4.29	n.a.	-4.23	-4.30	-4.23
Fe_3Y ($R\bar{3}m$)					
a	5.12	5.14	5.26	5.32	5.21
E_c	-4.37	n.a.	-4.29	-4.33	-4.22
Fe_2Y ($Fd\bar{3}m$)					
a	7.29	7.36	7.93	7.61	7.73
E_c	-4.37	n.a.	-4.03	-4.15	-4.20
Fe_5Y ($P6/mmm$)					
a	5.05	not	5.16	5.12	5.10
E_c	-4.35	observed	-4.16	-4.22	-4.24

Table 4.1 Modelled Phases of Fe-Y with structure indices, units for energies are eV and Å for lat. const.

4.2.4 Applied Result – Melting Y in bcc Fe and cool down

Finally, all these previous rather theoretical results can be joined together to perform, at last some insightful (ODS) experiment-related MD simulations with these fitted RF-MEAM pots. about melting, solubility and to a certain extent phase reactions. For melting and solubility liquid (molten) mixtures of Fe and Y with concentrations ranging from 0.1% to ≈2.5% Y at T_m were considered[79]. For the phases specific liquid mixtures of Fe with dissolved Y at concentrations of 10.5% and 19.75% (corresponding to $Fe_{17}Y_2$ and $Fe_{23}Y_6$) will be cooled down below T_m to specific temperatures, where phases formations are observed in experiments [153] (and can be compared). So, the following MD runs with both pot. types were performed, yielding the afterwards presented results:

- melting run: For the examination of melting the usual procedure used for the determination of T_m in MD is applied here: A cell of 250000 atoms (50x50x50 bcc Fe unit cells (each side ≈145 Å)) with 2.5% Y atoms, which randomly replace single Fe atoms at regular sides (thus substitutional atoms), is divided into two halves. Part one is the non-molten half Y and part two is the molten half, both with the 2.5% Y substitution. Before starting the run, both halves need to be jointly relaxed (lattice relaxation) by: the solid half is fixed and the other one is relaxed at 2300K for 10ps, then the whole system is cooled down and quenched to 0K, to generate the initial relaxed state of the liquid-solid interface (one half solid, one half liquid) – for these steps the Berendsen thermostat and associated quench procedure was used [21]. Then at several temperatures this set-up was allowed to relax for 1.5 ns in the Nose-Hover thermostat (NVT) and the melting point of this mixture was determined to be around 1730 K (+/- 15K). Then two runs were performed: 1. at first the system is relaxed at 1650 K, so safely below the previously determined melting point, for 1ns (preparation for following solubility run), 2. relaxed slightly above T_m (around 1750 K) for 1.5 ns yielding the melting results, shown graphically on the next page.
- solubility run: This run was started with the relaxed cell at 1650 K, in addition this aforementioned procedure was repeated in several runs with different Y contents ranging from 0.1% to 1.25% (in cells with only 10000 atoms, also Parinello-Rahman barostat was tried out here). In these solubility runs the aforementioned relaxation run before the quenching was slightly changed: 20-30 ps. at 1800-2000° K allowing some more relaxation and possible mixing. After the quenching as in the melting run (1.), the cell was cooled from 1650 K within 10 ns down to 700 K (to reach the α phase domain of Fe) to check for recrystallisation and/or dissolution of the Y atoms to decide whether the at the corresponding concentration the Y atoms are dissolved (or partly) and/or precipitation of Y indicating that it did not dissolve.[80]
- phase creation run: Here in close orientation to the above mentioned phase diagrams (more details p. 97), the same is done as before but without a solid-liquid interface.

Melting results:

Finally, by looking at Fig. 4.6 (p. 95), snapshots after the 1.5 ns relaxation at around T_m (1750 K) the tendencies of the used types are immediately clear, pot. type A and pot type B have different outcomes:

- *Type B* (bottom) predicts diffusion of Y as a uniform distribution across the cell leading to kind of a *complete dissolution of Y* resulting in one single mixed phase.
- *Type A*, on the other hand, predicts the *complete* opposite case. Type A confirms the observations by experiments [20] and during ODS production [6, 7] : the *formation of clusters*, which creates two separate phases of Fe and Y.

Comparing with experiments [6], the behaviour of type A agrees and type B is rather unphysical.

[79] The addition of Y to Fe decreases T_m (since T_m of Y is lower), more details in [132] – relevant alternated T_m is determined.
[80] Obviously, a cool down from 1650 K to 700 K within few ns is quite unrealistic, but these are the MD time scales. And, this speed up procedure clearly promotes the tendency towards precipitation. Thus, if dissolution occurs this shows a clear wrong tendency.

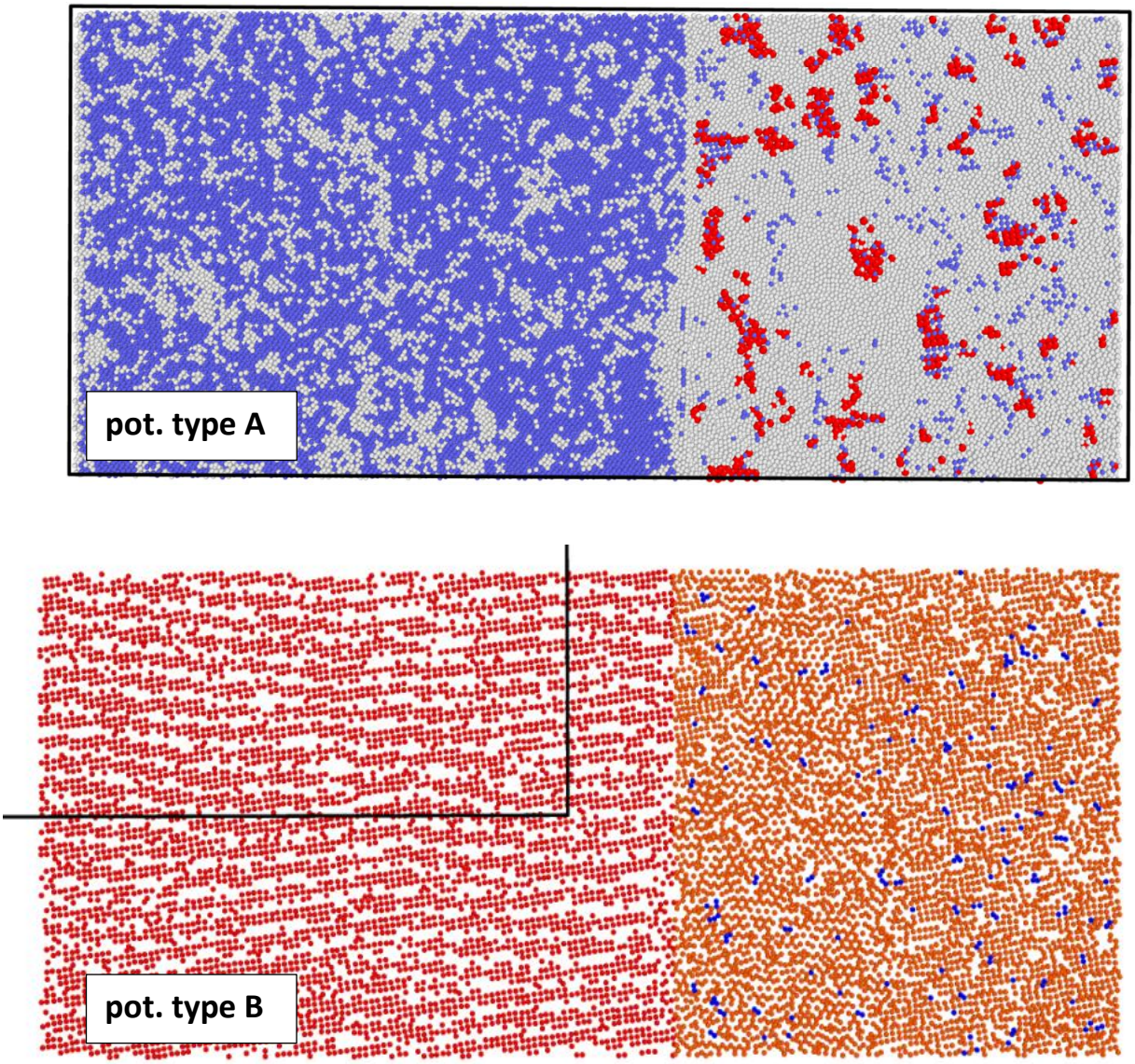

Fig. 4.6 Slices in z-direction of simulation cells at the end of the melting runs – solid-liquid cell with 2.5% Y at 1750K

Top: Results by pot. type A:

coloured **by CNA (Common Neighbour Analysis) with blue as bcc and grey as no structure (melt), red denotes the Y atoms.**

melt: clearly **visible "waving" behaviour (see text), which effectively shifts the border, solid-liquid interface. Also isles of melt (grey atoms in the blue (bcc) region) clearly indicate that cell is at T aorund T_m.**

Behaviour of Y: **firstly, in both pot types (LHS & RHS) Y prefers to "stay" in the liquid phase, realistic due to solubility of Y. But, what is very beneficial on the LHS by type A is the reproduction of the experimentally observed clustering behaviour of Y leading to precipitation when cooling the mixture below T_m.**

Bottom: Results by pot. type B:

Here, for better visibility representation is slightly changed by: 1. only showing 3-4 layers of atoms (in the slice) and 2. taking Centrosymmetry, this serves to better visualise the molten and solid state: on the bottom a clear order is visible indicating the solid state (bcc red), at the top the orange colouring representing the disordered, molten state as seen by eye dominates. Attention has to be paid to the fact, that dominating still includes little cells on the RHS to be in between both states, but the liquid state overweighs. The blue Y atoms unphysically dissolve despite a too high concentration.
The melting runs were started with the procedure of the halved cells as presented on p. 94. PBC are applied.

As said before in 4.2.1 the reason for this inaccuracy in pot. type B, the tendency for dissolution of the Y atoms, is probably interconnected with the incorrect binding energies, the incorrect signs (above the 2NN in pot type B) to be more precise. This error leads to an unrealistic tendency for repulsion between the Y atoms at distances above the 2NN rather than attraction (which is actually taking place in reality, though).

This behaviour is of particular importance because it is linked to further processes about the phases. This preference for clustering or dissolution is one of the key drivers for the solubility of Y in Fe. Consequently, when cooling the mixture below T_m (as explained before and the corresponding results are next), this behaviour and the associated solubility have significant influences during the ODS particle formation and is one of the main reasons for the expensive effort, as explained in the introduction (1.1).

Before moving on with this important question, three further observations are worth mentioning:
It was noted that quite simply one of the main parameters influencing the size and shape of the formed clusters of type A is the vacancy formation energy of the Y-Y pot. This was noted when comparing this to principal tendencies by M. Mock's Fe-Y ABOP pot [132], which has a lower E_{vac} (1.25 eV vs. ≈1.7eV) leading in theory to bigger clusters (this pot. is only able to reproduce molten Fe in liquid Y, the here considered mixture is unstable due to the wrong melting point of 2200 K for Fe (but enforcing stability by hypothetical pressures leads to this statement about the cluster size)).

Pot. B. exhibits an incorrect and problematic behaviour regarding the clustering of Y in Fe (with some even more serious consequences, s.b.). At least, though, in the solid-liquid runs (on p. 95) the Y diffused to the molten phase and preferred a presence in the liquid state, that's kind of reassuring and makes sense, since in solid Fe, as discussed below, the solubility of Y in Fe is severely limited. Besides, this shows a correct tendency in the diffusion behaviour, which is a more advanced question to be considered after these more essential and fundamental issues (when keeping a close link to applied ODS questions). Nevertheless, Pot B has serious shortages in these regards, but at least it gets this basic thing right (and to be fair only the here developed pot. and the ABOP one by M. Mock [132] gets this right, which is essential and basic though).

Last but not least, both potential types showed a reasonable behaviour around the melting temperature in form of the typical "melt waves" – when the system is close to melting, the molten half starts to move into the solid half. This implies that the former molten half recrystallises and the solid half becomes amorphous and eventually liquid. Than this waving is repeated until the whole cell is liquid (if T is high enough). The behaviour of the Y atoms during these rapid changes of liquid and solid state would be an interesting question to pursue further (provided solubility, phases and structures (incl. subtleties) are correct, which needs to be ensured before). Though, it is questionable, whether these changes between the states are also that rapid in reality, and if not, how can this faster succession be related to reality.

Solubility results:
The direct more practical implications of these previous melting results are evidently seen when cooling down the liquid part of the previous melting results, leading to solidification by recrystallisation. The pivotal question is: what happens with the added Y atoms? Is there a tendency for dissolution and subsequent inclusion into the newly formed crystals as one phase or will the added Y form a separate phase by precipitation as Y clusters? The clear and definite answer by experiments in reality is that the solubility of Y in Fe is extremely low [6, 15] – it is certainly below 0.1% (at 700-900°K) [13], that's an irrevocable fact. Therefore, a too high dissolution of Y in in the recrystallised solid mixture below 900°K is definitely out of the question and cannot be tolerated in any Fe-Y or ODS potential, which is used in application-orientated metallurgy. Having said this, to the greatest despair of the author Pot B makes this "unforgiveable mistake" – around half of the 2.5% Y is dissolved and forms with Fe one phase. Serendipitously, pot. type A allows only around 0.1% (+/- 0.05%) of the Y to be dissolved, the rest forms sensibly sized Y-clusters as precipitates. Therefore, Pot A remains and the pure, sole application of type B potentials is *out of the race* (but is still useful as a *"pot. ingredient"*).

4.2.5 Key-reactions in the Fe-Y Phase diagram– estimative reproduction

After these exp. observation-orientated considerations, only pot. type A is left in principle for further computations. In addition to the solubility and melting/clustering behaviour, potential type A should ideally be able to reproduce some of the relevant processes regarding the possible creation and transformation of the (Fe-Y) phases (e.g. phase creation during solidification, s.b.). To say in advance, pot. type A struggles with this (as expected since the out-ruled pot. B is better at phases), leading to the following discussion (in chapter 5) for essential improvements.
This accuracy in modelling of phases is highly desirable, because phase transformations in Fe-Y during the multistep ODS production could be the counterbalancing "conqueror" of the cluster-formation limiting consequences by the low solubility of Y in Fe. As said before, the presented low solubility of Y in Fe can be considered as one of the main issues, necessitating a possible interplay of phase creation and transformation with defect formations and diffusions as an alternative mechanism to incorporate Y into the Fe based alloy for the desired ODS cluster formation – and that is one of the main reasons why *useful* simulations regarding ODS particle formation should include both (phases & defects) at the same time.
In actual ODS alloying in reality, this could is concretely realised by adding certain Fe-Y phases (such as Fe_3Y in austenitic ODS [8]) or other components leading to the (still controversial but at least hypothetical) formation of such phases, which could then possibly act as a kind of an Y-donor stimulating ODS particle formation (via the disassembly of solute Y from these Y containing alloys, $Fe_{23}Y_6$ [8] for instance is a promising candidate).
These supplied free Y atoms are then distributed by diffusion and defect processes controlling the concentrations. But, as said before, this assumes a hypothetical mutual complementation of phases and defects. In order to solve this question and settle the ongoing debate about the possibility and relevance of such a hypothetical mutual interplay, the phase creation and transformation needs to be correctly modelled (in a potential with accurate defect properties).
In this model with the restriction to only consider Y contents up to 20% relevant phase processes include the (phase) creation of $Fe_{23}Y_6$ and $Fe_{17}Y_2$ from a liquid mixture which is cooled down to specific, *observed and measured* points of the corresponding phase diagram. Consulting experiments and CALPHAD (calculating phase diagrams) proceedings about Fe-Y, the results by Kardelass (2014) [16] and Saenko (2017) [153] are of particular interest because they contain two appropriate phase reactions (further called 'reac'), which are validated by experiments *and* modelling.

$$Liq.(10.5\%\ Y, 89.5\%\ Fe) \xrightarrow{cooling\ down\ (cd) to\ T_1} Fe_{17}Y_2$$ congruent reac(1) at 1650°K (T_1)

$$Liq.(19.75\%\ Y, 80.25\%\ Fe) \xrightarrow{cd\ to\ T_2} Fe_{17}Y_2\ (9.5\%) + Fe_{23}Y_6(90.5\%)$$ eutectic reac(2) at 1600°K (T_2)

Trying to reproduce these processes and its reactions with both types (tough type B is out), as expected, the opposite situation (wrt. to solubility and defects) occurs: type B is considerably superior to type A:

- *Reac (1)* is correctly reproduced by pot. type B, conveniently, nearly all Fe and Y is transformed to $Fe_{17}Y_2$, no considerable amounts of precipitates are formed. Pot. type A on the other hand completely fails at this: nearly no $Fe_{17}Y_2$ is formed *and* simply two distinct phases at the same concentration as before exist after the cool down from 2000 K to 1650 K. Seemingly, $Fe_{17}Y_2$ cannot be formed in this congruent reaction by pot type A, which would be a serious obstacle.
- This is confirmed by *reac (2)*, while pot B can reproduce most of it (a little bit less of $Fe_{23}Y_6$ and instead some additional Y precipitates, but all in all a mixture of both phases), type A fails again and does not reproduce the desired $Fe_{17}Y_2$ phase, only $Fe_{23}Y_6$ with some pure Fe.
- All in all, pot. A fails to reproduce the formation of the first Fe-Y phase (mixed phase, $Fe_{17}Y_2$, with lowest Y content, see phase diagram in the appendix A.3 in 7.1), unacceptable.

Again, this is not meant to be a known and observed process in the ODS formation, but this test should demonstrate the principal ability to reproduce the phase formation, which could be of considerable relevance for the broader goal in the framework of ODS developments.

4.3 Chapter conclusion & achievements in chapter 4

So, summarising it can be said, that these advanced MD results confirm as an irrefutable fact (at least in Fe-Y), that every MD pot. is always a (limiting) compromise – obviously, this is no surprise and simply confirms one of the universal rule of MD potential development. Unfortunately, it could be proven here that this compromise implies that the requirements of practical experimental relevant MD potentials are very hard to meet and this evolved technique still seems not good enough. But, the ultimate goal to model all phases and defects accurately at the same time remains.[81] However, it is best to "stop" here trying to reach these over ambitious goals – this RF-MEAM framework got the most out of the current state of the art techniques (ML is still not able to reproduce such accurate Fe-Fe potentials, as of now in June 2019). Plainly, the available infrastructure is incapable at the moment.

Nevertheless, the here encountered border can be stretched a bit further by pursuing the answer why pot. A failed, leading to a quite interesting and useful discussion in the next chapter (5) by linking the results to evolved experimental techniques in the form of EXAFS. These wider links show that this formalism is, the ODS problem withstanding, already remarkably accurate with some unparalleled abilities.

<u>All in all, this section offered the following achievements, such as</u>

- The fundamental preliminary result for these achievements is the application of here developed RF-MEAM fit techniques, which allowed to include the previously obtained EAM parameters as start parameters – this is essential, since without support by these well-reasoned start parameters the GA fitting stage is not able to find the global minimum (by linearly decoupled sets).
- Improved the MEAMfit performance by factor of ≈20, by better harmonisation between GA algorithm and explicit analytical RF-MEAM parametrisation functions (including extensive debugging, leading to cooperation in the development of MEAMfit v 2.0 (launched 2018))
- Independent development of software MD module for LAMMPS, which simulates screening factors of RF-MEAM (where S=1) in each situation to complete RF-MEAM pot. parameters for the use of the existing 2NN MEAM interface in LAMMPS. Used analytical restraining technique from 3.2 – screening parameters orientate towards (bounded by) physical quantities, similar to 3.2 – turned out to be a good match! Still, some performance issues of the module remain.
- All in all, by these first time developments reasonable fitting of all data with RF-MEAM
- Identification of the pot. type A / pot. type B dilemma (either very accurate in phases or defects)
- Result I: pass of binding energy test developed in chapter 3 (3.3.5) – accurate representation of various Y-vac clusters incl. tendency to double occupation (underlying properties are fitted) and accurate representation for the first time of all basic properties (E_c, a_0, B) of all Fe-Y phases
- (Main) Result II: first time successful simulation of molten Y in liquid Fe reproducing experimentally observed clustering behaviour of solute Y in Fe (in addition solubility estimations)
- Result III: Principal reproduction of two phase forming reactions in the phase diagram (solidifying the *explosiveness* of the type A/type B dilemma)

[81] *Maybe not many colleagues raise such points, but this stage clearly also raises the question, is an MD simulation for ODS possible at all? – the encountered obstacles in the last section of this chapter (4) provide a suggestive indication, that even GA based techniques are simply too weak for this "mammoth- task"(but predominantly it shows the need for more exp. input, see 5)* .

5 Discussion by including EXAFS spectra

By the insightful results and discovered challenges in chapter 3 and 4 this work encounters at this stage an actual *fork in the road* – either to stick to the kind of over-ambitious requirements of the challenges in ODS or simply omitting the aforementioned issues of the unfulfilled pre-condition, to model all phases and defects very accurately at the same time (=”phase/defect requirement”), and posing the incomplete model as a solution to ODS related problems, yielding potentially misleading or inapplicable results.
An insightful example is given by [132] which results in the rather disputable claim, that the ODS particle formation is associated with pipe diffusion, a type of diffusion occurring along edge dislocation cores [14]. Consequently, this assumes the countless occurrence of dislocations as edge dislocations at the corresponding conditions at which the formation of ODS particles occurs. Taking the practical point of view into account, the supposed ODS particle forming production process is HIPping with high T [20]– this limits the likelihood of the existence and relevance of (edge) dislocations for this particle formation hypothesis drastically, simply because of the necessary production condition of high T at around 1000° C. At these temperatures plain bulk diffusion and GB processes (movement of GBs for instance) dominate and dislocations vanish (cannot form due to the diffusion dominant dynamics) – the absence of dislocations at such high T is the main objection to [132]. A secondary objection is, that pipe diffusion possibly results in a too low flow of atoms, though individual atoms are faster, a quantitative issue.[82]
This issue originates from the fact that associated simulations [132] only considered the low temperature regime (up to 300K). The presumable reason, why higher temperatures were avoided is that at temperatures above 800K phase transformation- or phase destabilising processes (as shown before) are likely to take place and the energies (E_c) of the phases and their structures have to be extremely accurate for correct dynamics of phases (existence, stabilisation and transformation) beside the defect accuracy.
So, this work [132], even though in ABOP, has encountered the same typA/typeB dilemma as here, which as presented above creates a kind of *dead end* in the pursuit of MD simulation of ODS particle formation.

As a consequence, the *only* upright approach is the *first junction at the fork in the road* to respect the phase/defect requirement and as a first step to understand in-depth, why this problem occurs.
A helpful assumption was raised in section 4.2, that in the *fit dynamics* (mutual fit parameter dependence) exists apparently a strong correlation between the accuracy in the Y-vacancy binding energy and the energy difference caused by fine structure differences in E_c between $Fe_{23}Y_6$ and $Fe_{17}Y_2$ as well as the α & β phase of the latter one. This is a fundamental link between accuracy in defects and phases.
By the examination of the phases (see 4.2.3) it is supposed that without the inclusion of magnetism (as this model has no direct parametric dependence on it) these decisive fine energy differences in the phases and structures are probably missing. Supposedly, a phase accurate potential (type B) compensates during the fitting these weaknesses by changing the Y-vacancy energy, causing this dilemma! So, at the cost of these binding energies the phase properties are improved, and the weighting during fitting controls this tendency. In addition, considering the energy difference between the considered phases and the order of magnitude of magnetism, this seems very reasonable since they match (by 0,05 eV, detailed calculations by Coehoorn [151]). By comparisons to experimental EXAFS spectra the potential will be further improved (mainly to avoid this compensating mechanism) with the help of AIMD references with astonishing consequences.

So, the answer and suggestion to the opening dilemma of this introduction is – Dig deeper!

[82] Could be used for a further potential to validate that ODS particle formation is not taking place during the ball milling (at low T)

5.1 Using EXAFS spectra to examine atomic structures

The aim of the discussion is the indirect inclusion of magnetism by more details in phase associated DFT fitting data (AIMD, s.b.) in order to stop the fitting process falsifying the Y-vac. binding energies for better phase properties, supposedly the main cause of this central dilemma.
This requires the ability to check the correct (at least indirect) adherence to magnetic influences – an extremely elegant experimental tool to check this are EXAFS spectra, because these cover nearly all details of the fine structure, including effects on the structure by magnetism, which are represented here.

5.1.1 EXAFS experiment, general idea and link to sim. by electron waves

EXAFS experiment and general idea:

EXAFS spectra are obtained by exposing a sample to x-ray photons of suitable high energies (few keV up to 30 keV [154], depending on the examined material) – this can be ideally realised with synchrotron radiation, with an intense flux and continuous spectrum [155] .
Generally speaking, the following processes during photon irradiation cause the resulting EXAFS spectra: The irradiated X-ray photons are absorbed by the probed material during the experiment and the fraction of transmitted photons, $\mu(E)$, is determined by comparing the incident and transmitted flux, described by:

$$I_t(E) = I_0 e^{-\mu(E)x} \rightarrow \mu(E) = \frac{-\ln\left(I_t(E)/I_0\right)}{x} \quad (5.1)$$

Where I_0 and $I_t(E)$ are the incident and the transmitted photon flux and x describes the thickness of the sample, which for best results should be a fine powder in an ideally 10 µm thick sample [156]. The fraction of absorbed x-ray photons is described by µ(E), the (X-ray) absorption coefficient [107].
Normally, when considering a single atom absorption edge (meaning the binding energy of an electron (E_b) is matched by the incident energy of incoming photons), one would expect that the intensity decays exponentially wrt. to the incident energy of the X-ray photons [157] – simply a straight exponential curve, as in the appended Fig. A.9 (p. 125), labeled as $\mu_0(E)$, but instead a modulated curve is observed, labelled as $\mu(E)$. The reason for this lies in the scattering behaviour [158], which leads to the EXAFS principle described by the variation of the absorption coefficient past the absorption edge of orbital type l as $\chi^l(k)$:

$$\chi^l(k) = \frac{\mu(E) - \mu_0(E) - \mu_B}{\mu_0(E)} \quad \text{with k} = \sqrt{(2m_e/\hbar)^2(E - E_b)} \quad (5.2)$$

This $\chi^l(k)$ can be determined experimentally by measuring the transmitted photon flux leading to a $\mu(E)$ by eq. (5.1) at a certain energy of the photons, E. This energy is then mapped to a wavenumber in the material by using the wave-energy relationship (eq. 5.2) and linking it to the binding energy, threshold respectively, for the electrons in the considered orbital edge, E_b. This obtained k is then mapped to the obtained data point by eq. (5.2) in the EXAFS graph.
By considering the cause of this behaviour, this modulation, conclusions about the detailed structure can be drawn from the EXAFS spectrum [155]. In order to get to the bottom of this modulation the scattering processes need to be considered step-by-step:

- incident X-ray photons eventually hit an electron belonging to an atom of the irradiated sample, the x-ray photon is absorbed by this electron, which is then exited and leads to the ejection of an emitted photo-electron. The missing electron in the shell creates a core hole.
- This core hole, a missing electron of an lower energy electron state, is unstable and decays after 10^{-15} -10^{-16} s, implying that it is filled by some other electron, for instance another photo electron.

- the excited free photon-electron also decays in a similar time span as the core hole. This lifetime essentially depends on the absorbed kinetic energy obtained by the knocking-on x-ray photon and essentially influences the scattering behavior (which in turn depends on the adjusted irradiation energy, E in eq. 5.1 and 5.2). At the end of the lifetime the photo electron will be absorbed at another atomic side (filling another core hole for instance).

This is a very simplified explanation of these scattering processes, especially as one can imagine that multiple scattering processes are possible (details by Rehr in [159]). Summarising, using the wave like understanding of photons and photoelectrons by de Broglie [107], the scattering behaviour is caused by the atoms of the irradiated material acting like point scatterers of propagating electron waves, →Fig 5.1.

Modelling EXAFS with electron waves

These point scatterers, the atoms, which are excited by scattered photons, eventually eject photon electron waves. Very simplified a forward propagating electron wave can be imagined to form an interference pattern with the back scattering electron waves (caused by other excited atoms), as seen in Fig. 5.1. This causes an interference pattern, which depends on the wave length, described by k, and the structure (linked to specific binding energies, measurable in experiments, or structure factors, which can be modelled). Obviously, since k is dependent on E of the incident photons, the interference patterns change, more precisely the amplitude and phase of the waves. This leads to a variation in absorption coefficients.
These scattering processes with all these amplitudes and phases of these electrons can be described by the use of quantum mechanical states, leading to ab-initio simulations by solving these quantum mechanical equations in tools, like the used FEFF code [160]. Basically, the FEFF code is solving the following eq.:

$$\mu(E) \propto \sum_f \left|\langle f|\hat{H}|i\rangle\right|^2 \delta(E_f - E_i - \hbar\omega) \rightarrow \chi^l(k) \overset{T\neq 0}{\Longrightarrow} S_0^2 \langle \chi^l(k)\rangle_{diff\ conf} = \chi^l_{conf\ aver.}(k) \quad (5.3)$$

First, the LHS is considered: The scattering process is here represented by the transition from an initial state (i) of the hit electron to the final state (f), which is only happening if the incident photon matches the energy of these states $E_f - E_i$, which is closely linked to E_b (therefore if the energy of the photon is far away from E_b then no modulation takes place). Then for the one point of the EXAFS spectrum at a given Energy or k respectively all processes, implying all possible states and transitions at that k, need to be considered – it's like each process is one wave, and all processes are an superposition of different waves (at a given k) and a pattern is formed leading to a specific modulation of the absorption, which is then described as one dimensionless number by $\chi^l(k)$, as indicated by the arrow. This exact QM description assumes that the point scatterers, the atoms, are not moving. However, the movement of the atoms causes phase differences in the electron waves and these change the scattering pattern considerably (clearly since the movement of the atoms influences the chances of collisions) – a*nd that's where MD comes in and helps to complete the simulation to enable the link to the measured transmission coefficients in the exps.*

This is what is described on the RHS of eq. 5.3: for one ideal structure at zero temperature the aforementioned FEFF code is able to calculate the EXAFS value wrt. to k as a static picture (LHS). In order to illustrate the inclusion of thermal vibrations schematically, the thermal vibrations and the vibrations due to the scattering, are decoupled in a simplified manner for these explanatory illustrative purposes: $\Delta u_{\parallel}$ in Fig. 5.1 represents the *pure* diffraction pattern, like in standard XRD measurements. The presented distance R_{diff} causes phase differences of the electron waves leading to the same kind as the previously described interference patterns (these standard patterns by XRD for instance can be used to determine the lattice constant, which is the same as R_D, and before using an MD pot. for EXAFS this, the lattice constant(s), has to be right).

In EXAFS, however, this is not all. The relevant R in EXAFS, R_{EXAFS}, is more sensitive due to an additional component. The movement in perpendicular direction, $\Delta u_{\perp}$, causes the additional component, which needs to be added to $R_{Diffraction}$ in order to obtain R_{EXAFS} as shown in Fig. 5.1 (next page).

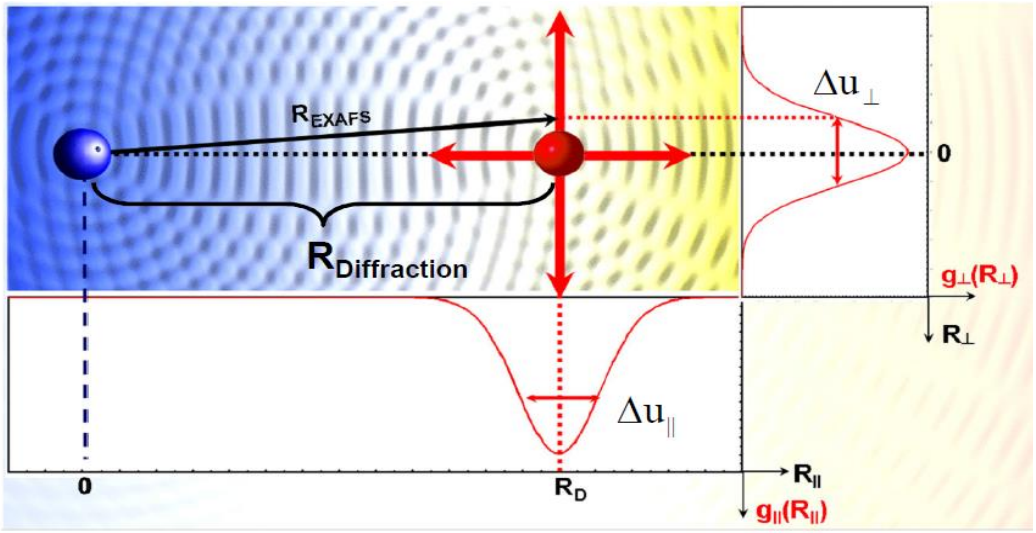

Fig. 5.1 Representation of the two mentioned components $\Delta u_{\parallel}$ & $\Delta u_{\perp}$, which form the EXAFS spectrum, at 0K both components converge to 0 and one would obtain an XRD – so, illustratively, EXAFS is kind of an XRD with the lattice dynamics, extracted graph from Fornasini paper [156]

Using the idea of decomposition for an interplay of MD and DFT in EXAFS simulations:

This additional component is the reason for the modulation of the EXAFS curve. In this simplified representation this $\Delta u_{\perp}$ component is interpreted as thermal motion (R_{thermo}), but care has to be taken, that magnetism and or (ion-like) charges for instance can also influence this component (the later is of high interest in yttrium oxide, and the first in $Fe_{17}Y_2$ as mentioned in the introduction). So, summarising it can be said, that the relevant phase shift causing distance R_{EXAFS} is a superposition of R_{thermo} and R_D. Naturally, on average this R_{thermo} component is zero, but looking at the time scales an interesting rather useful fact occurs: The scattering processes of $\Delta u_{\parallel}$, as described before, take place at least within 10^{-15} s, so fs, or faster. Thermal motions or also vibrations of the atoms are significantly slower, "the fastest" are of the order of magnitude of 10^{-13} s, so 10 ps – it is a difference by a factor of 100. Now, this fact allows a very helpful trick in the simulation of the EXAFS spectra as the concept of configuration averaging, which helps to split the EXAFS simulation in an apposite manner between the DFT FEFF code and MD (LAMMPS) code [60] with the in this work developed RF-MEAM Fe-Y potential.

In practice this means the following: since EXAFS is much "faster" than the atomic vibrations (caused by thermal motion for instance) the scattering processes of the incoming photons can be calculated in a "frozen snapshot" of the atomic configurations (representing the atomic vibrations). This allows to perform FEFF calculations yielding one $\chi^l(k)$ corresponding to one frozen atomic configuration at a given k (and k needs to be varied to obtain the whole spectrum). If one would only use one of these frozen snapshots as the atomic reference to calculate the EXAFS spectra, this would lead to an exclusion of the details about what has been interpreted previously as $\Delta u_{\perp}$ and linked to thermal motion.

In order to include this motion and simulate $T \neq 0$, *what EXAFS is kind of about*, the previous considerations with the help of Fig. 5.1 justify to represent temperature as the average of many different MD simulated configurations, each representing a snapshot of thermal vibrations. So, in FEFF for all the individual configurations a $\chi^l(k)$ is calculated and then averaged leading to the configuration averaged (ca) $\chi^l_{conf\ aver.}(k)$ in eq (5.3) [which is done by the software EDACA by Kuzmin [160]], which can be then readily compared to the experimental results, provided the assumed atomic input structure and the modelled vibrations in the MD simulation are correct – only very few MD potentials are accurate enough to suffice the high requirements for correct details in EXAFS.

5.1.2 Exact implementation in MD and improvements in RF-MEAM pot.

Choice of potential and upgrade by split technique:
Considering the aforementioned complexity, it is no surprise, that it is the very first time at all that an EXAFS spectrum of a metallic alloy, such as Fe-Y, is successfully modelled by a MD assisted simulation.
Even with no further improvements and adaptations, without explicit references about EXAFS, a principal good agreement is yielded by the fitted RF-MEAM Fe-Y potential of type B, see EXAFS I (5.2.1).
By this principal reproduction and further comparison of the corresponding experimental EXAFS spectrum for $Fe_{17}Y_2$ pot. type B reveals the possible influences of magnetism on the structure and further details about the fine structure – see appended flowchart A.9 in 7.1. These influences are principally confirmed by AIMD calculations, see 5.2.2. These AIMD calculations serve as an additional fitting reference (with the used ones) for the refit of selected fit parameters in pot. type B. The change in the selected fit parameters should leave the accuracy in phases, as shown in 4.2.3, unaffected and should not reduce accuracy in defects. This complex task can be conducted by a split-up technique in the style of Hu's Analytic MEAM (AMEAM) pot. developed in 2001 [90] – as said in the literature review, these pots. "as a whole" are unsuitable, but the basic idea is of great value for this particular task. The idea of AMEAM is to represent a MEAM potential simplified as an EAM potential with an angular dependant extra modification term, effectively splitting the potential into an angular and non-angular part. The trick is the angular dependant modification term is 0 at equilibrium, see extracted illustrative graph A.10 in 7.1.
This sparks the idea to construct the parameter changes in such a manner, that only the change itself is split into an angular and non-angular part (not the underlying potential which is improved). Now, only angular parameters (l>0) out of equilibrium are changed leaving the equilibrium phase properties in the non-angular part (l=0) unaffected. Since the AMEAM modification term and l>0 terms in RF-MEAM are different, a thorough condition for the RF-MEAM (angular.-part, l>0) changes is implemented, so that at equilibrium (phases at ideal spacing) the change in (angular) parameters (l>0) has no effect on the resulting energy of the angular part. Only the out of equilibrium properties associated to the angular part (l>0) are changed, leading to better defect properties (and more see 5.3). This (AIMD) improved version of potential type B is called pot type C. This directly leads to excellent EXAFS results in 5.2.3 and improved defect properties up to R= 0.1while maintaining accurate phase properties of type B.

Details of MD run: Having improved the performance of the LAMMPS Module (4.1.2, after numerous trial and error sessions) finally the EXAFS MD runs were performed with the following specifications: in Lammps [60] with this developed module a NVT MD simulation was performed at 300K for 20ps with 40.000 steps (each time step 0.5 fs). Every 10-th step the atomic configuration was recorded as a snapshot in the form of an XYZ file describing the structure of the simulation cell, which contained 3x3x3 unit cells (so 27 cells of $Fe_{17}Y_2$ resulting in 513 atoms in 25 $Å^3$). This yielded 4000 snapshots. The trick to improve accuracy was to repeat this procedure 5 times with the same configuration but to replace every time parts of the simulation cell with 2-3 FeY defect clusters. This corresponded to a defect concentration of 1-2% and significantly improved the amplitudes and also little wiggles. High concentrations above 2% worsened the result (with still the question left open, whether also concentrations of up to 5% are realistic). In total out of the 24000 snapshots (6x4000), 10000 were randomly picked and used by the FEFF code (version 8.0 [159]) to calculate the $\chi_{ca}^{l}(k)$ at a given k – and then the FEFF code repeated this for various k's ranging from 0 to 120 (as indicated by the experiments). Final results in the following section, EXAFS spectra, were yielded by Kuzmin's EDACA software [160], linking xyz- and FEFF files.

Comparison: By A. Kuzmin's group during investigations of Yttria for ODS steels this one Fe alloy phase ($Fe_{17}Y_2$) was measured in several synchrotron facilities, like at the ESRF in Grenoble, and experimental EXAFS spectra have been obtained. For the alloy of interest, $Fe_{17}Y_2$, it was measured at 200, 300,400, 600 and 800 K. The sample was *standard material*, metallurgically (by melting) produced $Fe_{17}Y_2$ with a purity of about 99,9%. Unfortunately, no further measurements have been performed with this sample.

5.2 Results

The EXAFS spectra reveal fine structure issues in pot. type B by the supposedly magnetism driven mixture of the α & β phase in $Fe_{17}Y_2$. The inclusion of AIMD (containing information about the effect on magnetism onto the structure more details see 5.2.2) overcomes this issue with astonishing consequences.

5.2.1 EXAFS I

Finally, after all these numerous preparations and the last fine tuning conducted in section 5.1 the following EXAFS spectra at room temperature (300K) on p. 105 on the RHS were obtained by EDACA, combining MD&FEFF, and compared to the available experimental spectra, raising the following points:

- Test with known EXAFS spectrum for pure bcc Fe [110]: Before the calculated EXAFS spectra with the help of the FEFF code were used, the correct application of the FEFF code was ensured by performing a calculation for a spectrum of pure bcc Fe and comparing it with the corresponding published successful EXAFS spectra [110]. Conveniently, the used Fe potential by Ackland [76] has been shown numerous times to be in excellent agreement with experimental EXAFS spectra [63] (another indication of its high accuracy and supporting the use of forces of liquid like states, see 4.2.2). Therefore, any errors in the calculated EXAFS spectrum would stem from mistakes in the calculation and not from faults in the used MD potential (since it correctness for EXAFS has been already shown).
  After the relatively simple MD run to create the necessary XYZ files, by a careful application of the FEFF code [159], with the XYZ files as input in EDACA, the corresponding EXAFS spectrum was reproduced with the same accuracy as in previous works and publications (see Fig. 5.2 on RHS). It even agreed to the same level as a cutting edge ML reverse approach [63], later more about that. So, the test was passed, the FEFF code is correctly applied.

- $Fe_{17}Y_2$ in general: all in all, the agreement between the experiment (dots in Fig. 5.4 on RHS) and MD simulations (black line) is good. The amplitudes and nearly all phases (position of the peaks) match in principal. Especially the agreement with the positions of the peaks is very important. This matters most, since it indicates that the assumed structure, here α $Fe_{17}Y_2$ (hcp, more exactly $Ni_{17}Th_2$ structure type, see page 93) and the used MD pot. are mostly correct (more details second half of this section). What can be definitely said though, is the fact, that the assumed α $Fe_{17}Y_2$ (hcp) is dominant and the main component shaping the EXAFS spectrum.

- Details of the peak positions: Except of two small phase shifts (indicating additional minor influences on the structure) all peaks generally agree, at least by significant overlapping.
  The first five peaks in Fig. 5.2, occurring at k≈ 33, 45, 55, 70 and 78 are in exact agreement (amplitude is separately considered below).
  One phase shift occurs at 85 to 90 (k) causing some revealing disagreement in the peak positions, to be more exact it is just one peak out of phase (will be discussed in more detail at the end of the section). Again, for values between 100 and 120 (for k) a good agreement in the peak positions is reached. At k=120 positions are correct, but amplitudes are drastically different. All in all, the most parts of the peaks in the experimental curves overlap with the simulations (amplitude discussed in the point after the next one)

- In addition, the width of the peaks, linked to the atomic vibrations (see Fig. 5.1) is in considerable agreement with the experimental data, indicating that the potential well and its slope of the used MD pot. are well fitted (shows that the considerations in chapter 3 to take care to fit a good slope kind of pays off).

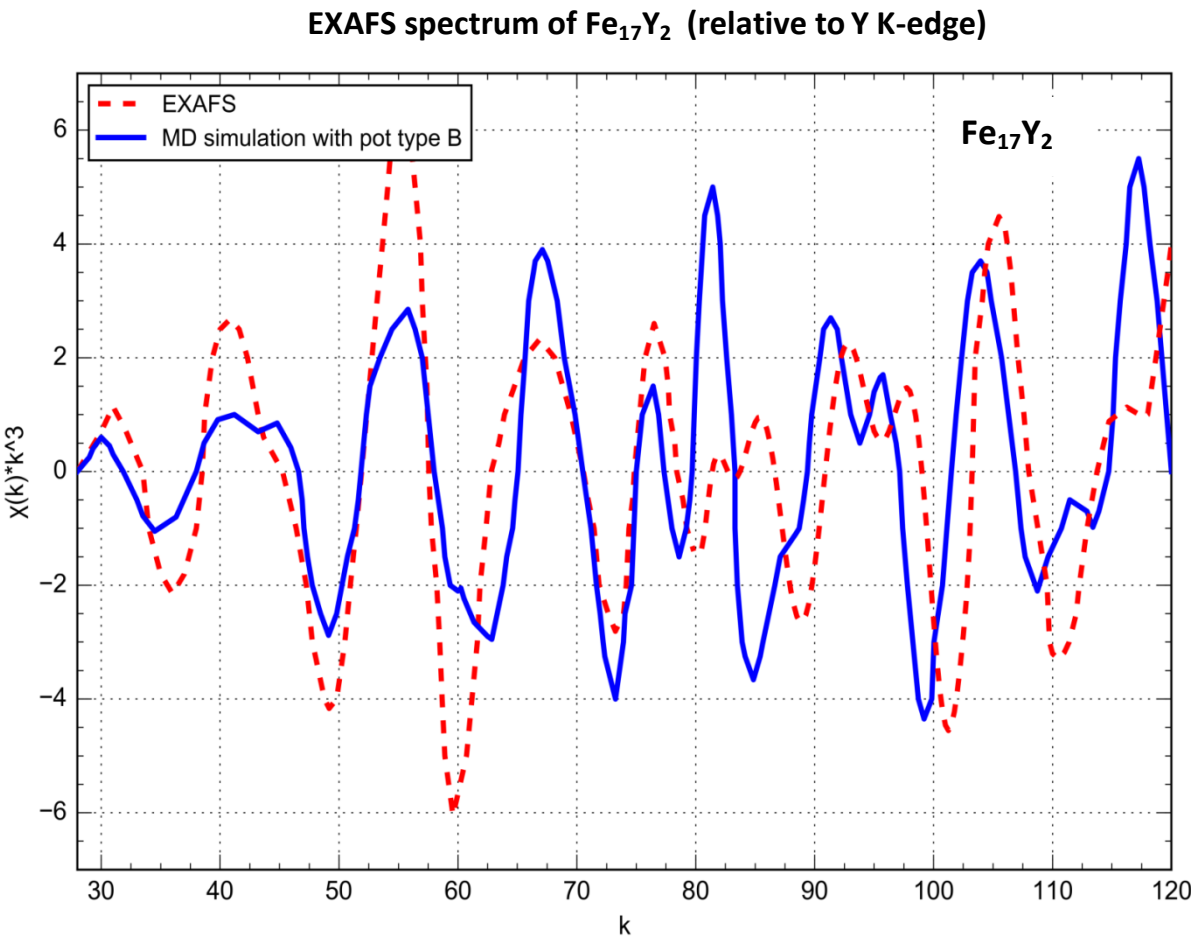

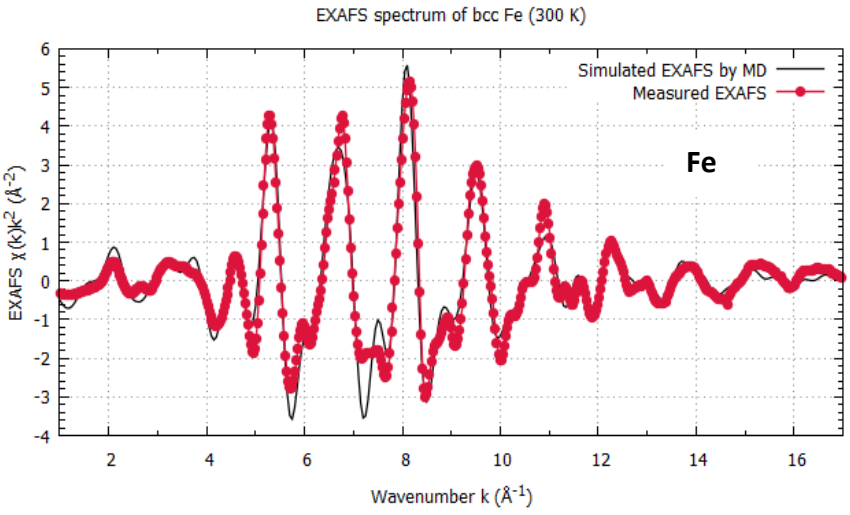

Fig. 5.2 Comparison of MD assisted simulation (line) and experimental measurements (dotted) of EXAFS spectra for $Fe_{17}Y_2$ (top) and pure bcc Fe at room temperature (300K) –

bcc Fe perfectly agrees as by previous works and confirmed that the applied technique is OK.

$Fe_{17}Y_2$ agrees in principle and shows a striking phase shift at k=90, which is the main observation providing important supportive indications to clarify the *actual* structure of $Fe_{17}Y_2$.

- Amplitudes: the order of magnitude of the simulated peak amplitudes agrees with the experimental ones, but disagreements up to a factor of 2 (with 2 exceptions) occur. Interestingly, a pattern in the disagreements seems to appear: if the MD simulated peaks exhibit too high amplitudes (in comparison to the experimental values) than an underestimation of the amplitudes, too low peaks, follow. For instance up to 70 (k) three times too high simulated amplitudes occur. Then one underestimation follows. This can be interpreted as the influence of defects in the sampled alloy. Presumably, at the first three peaks missing atoms in the form of vacancy defects decrease the amplitude and then at the fourth interstitials cause an increase in the amplitude, which the low defect density model (2-3% defects) cannot cover. Since the experiment sample has been produced by melting, a considerable number of defects can be assumed within the sample causing these effects and therefore these disagreements are tolerable. Including these influences of the defect in a more accurate way would require detailed experimental knowledge about the exact defect concentrations, which are not available by any experiment (especially quantifying point defects resembles a great challenge, neither positron annihilation experiments or resistivity measurements at low T could solve this [161])
- At higher Temperatures, the agreement is not convincing. The reasons will be further discussed in 5.2.2, 5.2.3 and concluded in 5.3.

The most *valuable* observation with EXAFS in the pursuit of a better understanding of the $Fe_{17}Y_2$ structure is the significant phase shift at k=85, revealing one particular disagreement of the experiment with the assumed pure hcp structure in the model (used structure for the MD runs). By considering other experiments with similar aims about this particular structure by others, one study stands out: a polarised neutron diffraction study by Moze [150]. This study beneficially supports the assumptions in the introduction and the end of chapter four, which could be drawn because of the informative behaviour of the potentials regarding $Fe_{17}Y_2$ and $Fe_{23}Y_6$. Alongside our findings, more detailed DFT calculations by Mihalkovic [142] and in this paper it seems like that the α state is stabilised by magnetism and that this influence of magnetism causes slight alternations in the structure leading to these observable differences to the assumed pure Th_2Ni_{17} hcp structure [150]. With the help of the detailed neutron diffraction studies Moze suggests in his paper, that certain, sporadic layers in c direction in $Fe_{17}Y_2$ at room temperature are in fact of rhombohedral structure as the β phase of $Fe_{17}Y_2$. This occurs while the majority remains in the anticipated hcp structure, extracted chart A.5 appended in 7.1. Looking at RDFs of these two states (α&β) this seems like a reasonable explanation for the phase shift at 85(k), since both structures exhibit quite a number of similarities. The only significant difference in amplitudes is at 3 and 5 Å, which would exactly explain the phase shift (the other differences seem rather small).

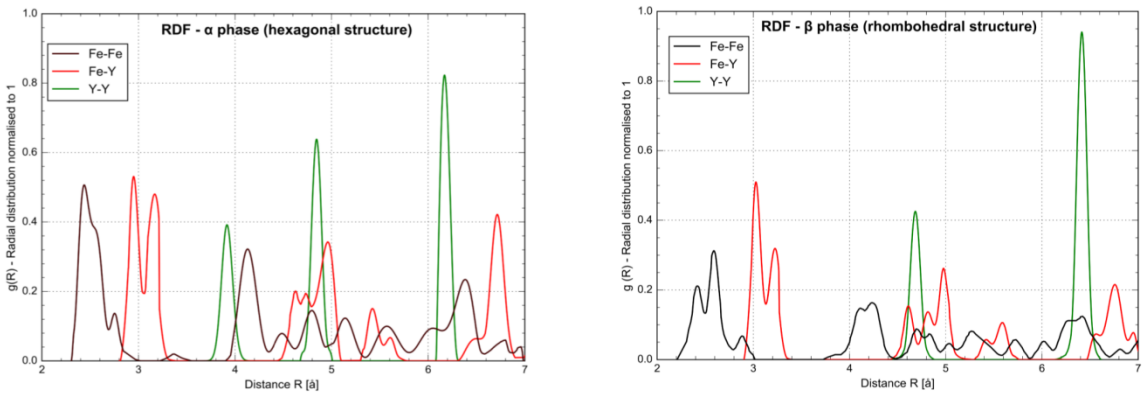

Fig. 5.3 RDF spectra of α-Fe17Y2 (LHS) which is hcp ($P6_3/mmc$) and resembles Th_2Ni_{17} and β-Fe17Y2 (RHS) which is rhombohedral (R3m) and resembles $Mn_{12}Th$ extracted from used XYZ files and normalised for comparison. The colours denote the different components. The atomic cells of both structures are visualised in the appendix A.8 in 7.1 (p. 124).

A closer look reveals, both peaks at 3 and 5 Å in Fig. 5.3 look like a superposition of two peaks, so in total consist of four peaks, and two out of these four are significantly different in amplitudes. This means a higher or lower likelihood of the existence of atoms at two specific distances. Exactly these differences could be the cause of the disagreement in the aforementioned EXAFS peak (these atomic distances seem to match to values obtained by transforming the k values of the waves of the EXAFS graphs to atomic distances). What is essential is the fact that the position of all RDF peaks in the rhombohedral and hcp structures are the same – this ensures that the corresponding EXAFS spectra of both structures are very similar (a difference in the peak positions would cause drastic differences). In combination with Moze's hypothesis that only certain layers are affected by this different structure, this seems very plausible and a likely explanation justifying a new EXAFS calculation. Performing this calculation, another MD run with the exact structure as supposed by Moze and then using it for EXAFS calculations, show that this idea is kind of the "right direction". The disagreeing peak at 85 (k) shifts to the right, but too far. Probably, this set up contains too many rhombohedral components in the structure. However, these rhombohedral components cause a shift at the correct peak and thus are likely to exist at room temperature in the major hcp structure of $Fe_{17}Y_2$. But there are not as many rhombohedral components as anticipated by Moze.[83] However, the idea of a mixture of a major hcp and minor rhombohedral component seems to be the right idea, which is followed up by confirming AIMD calculations in the next section.

Before doing so, a look up in the previous chapters 4.2.3 and 4.2.4 also proves to be very helpful: looking at the properties of the phases (in table 4.1 on page 93) it can be seen that the difference in cohesion energies between $Fe_{17}Y_2$ and $Fe_{23}Y_6$ is only of about 0.05eV – a *very small gap*. Considering the fact, that as shown by principal DFT calculations about magnetism (magnetic moments) in Fe-Y phases by Coehoorn [151] magnetism can influence up to 0.05-0.07eV in these structures and phases. Since the developed and used potentials do not include magnetism and tend to mix up the difference in energy between these two phases, in particular pot type A. as shown in 4.2.3, the following conclusion can be drawn: without magnetic influences, including its effects respectively, this gap gets smaller. It is even possible that the order of the two adjacent phases $Fe_{17}Y_2$ (hcp) and $Fe_{23}Y_6$ (fcc), the energetic sequence respectively, is mixed up exactly due to this missing magnetic component. Including the additional fact that hcp and fcc are quite similar, or in other words, that hcp and fcc can be easily transformed by few transformations (also plays a role in Bain-path calculations) and what happens without magnetism in the simulations it could be that that magnetism is even stabilising the hcp structure of α-$Fe_{17}Y_2$. The magnetism could cause a kind of ordering of structure which leads to parts of the cell to be in the rhombohedral (more ordered) structure β, since both α and β phase have the same cohesion energy and have similarities. So, this mixing of the two states could be significantly facilitated via ordering processes controlled by magnetism.

All in all, more detailed conclusions and accurate answers can only be drawn by overcoming the problem of missing magnetism in the model, in the Fe-Y potential. Instead of reformulating the potential, the fitting data base, will be simply "upgraded" by including advanced DFT fitting references which include details about the relationship between structure, temperature and magnetism. These advanced DFT fitting references are computed by state of the art ab-initio MD (AIMD) runs representing exact calculations of the structure at room temperature (300K) instead at 0K as in classical DFT with its magnetic moments.

Including these details in a refit of the previously used MD potential should improve the capability to represent this mixture accurately, and thus should lead to the desired correction in the EXAFS spectrum of this chapter. Therefore, in the next section 5.2.2 the performed AIMD run in cooperation with Prof. G. Ackland's group at the university of Edinburgh is briefly introduced and then applied in section 5.2.3 (an example of their and particularly M. Marques' expertise in AIMD Fe techniques can be found in [162]).

[83] However, to be fair though, without exact knowledge about magnetism (and the influence on the structure) by atomistic simulations, it is nearly impossible to üpredict the right mixture. It should be kept in mind, that current state of the art ab-initio MD calculations were not available in the 90's for such atomic systems by computional limitations.

5.2.2 Ab initio MD simulation of $Fe_{17}Y_2$ & development of pot. type C

As planed in the previous section the idea of Ab-initio MD (AIMD) (see 2.3.3) is employed: $Fe_{17}Y_2$ was modelled in a small cell consisting of two unit cells (38 atoms in hcp structure) for 20 ps (20000x1fs time steps) in AIMD with an NVT thermostat at 300K. The enabling underlying assumption, is a stable ferromagnetic state supported by an initial alignment of all individual spins pointing in the same direction (during the NVT run though few individual spins sometimes flipped). Indeed, this ferromagnetic representation of this phase is realistic, according to the early DFT calculations by Coehoorn [151] confirming that $Fe_{17}Y_2$ is weakly ferromagnetic (mainly due to Fe, which has a magnetisation of μ_B=2.4 and for Y, μ_B= –0.4). In order to achieve a stable magnetisation a quite evolved equilibration procedure in several preliminary NPT runs was performed by M. Marques (many alternations until stable behaviour and magnetisation has been reached). Afterwards a NVT run for these fitting purposes was performed together with M. Marques at G. Ackland's group. In Fig. A.4 (7.1, appended) the total magnetic moment (per atom) and volume is plotted. This shows two essential facts:

1. All curves confirm a successful equilibration at 300 K with stable behaviour of the runs, because there are no discontinuities, esp. in volume and temperature. So, these runs are suitable for fitting.
2. Although jumps in the magnetic moment occur, magnetism also behaves plausibly with an explainable pattern: the jumps of magnetism correspond to the flipping of individual spins of Fe atoms and the change in total magnetism can be exactly tracked back to such flippings. Checking the individual spins in the DFT output files it can be seen that 1-2 atoms change their spin from -1/2 to +1/2 and vice versa. This is a change by 1, and linking this to the magnetic moment and averaging over 17 Fe atoms in the unit cell, a change of ≈0.12-0.13 is anticipated and looking at Fig. A.4, this is exactly the case the changes are a multiple of that number. After having ensured that this behavior is physical, it is also interesting to investigate the links: looking at the output of the structure, it can be seen that these changes result in a slight change of the structure, consequently on a broader scale a change in volume can be noted.

Point 2 exactly confirms by these findings quantitatively the previous assumptions about an influence of magnetism on the structure – it is linked and some mutual stabilisation seems to take place. Having a closer look at the structures, some possible interesting pattern seems to appear: some of the Fe atoms change their positions with magnetism and there is a preference. The Fe atoms which are closest to the Y atom, which kind of makes the difference to between the rhombohedral and hcp structure (because of their similarities only 2-3 atoms are different) start to move towards these atoms with increasing magnetic moments. Astonishingly, this exact movement has been already assumed by Moze in the 90's, it exactly coincides with the atoms labeled as "Fe 4f" and "Fe 4e" by Moze (see Fig. A.5 in 7.1 from the article in the appendix). But the "swap" with the Y atom, as anticipated in that paper, is not observed. However, this is no surprise since the simulation cell with only 38 atoms is apparently much too small for these effects. That is where MD comes in, as done in the next section with more modelled atoms.

For the following improved EXAFS spectrum the more accurate phase modelling potential type B was refitted with the previous fit-database expanded including by the aforementioned AIMD data (see 5.1.1) – leading to pot. type C. During the tests to ensure that the previously achieved properties are maintained, an astonishing, more extensive improvement has been discovered: pot. type C seems to be able to overcome the dilemma of pot. type A and B. Pot. type C has accurate properties of phases and defects at the same time leading to a total R of 0.078 without any overfitting (confirmed by test references). As a result, type C has the exactness of type A and type B at the same time: it reproduces correctly the cluster formation of the liquid mixture as in 4.2.4 (as type A) and at the same time the correct energetic order of the phases reproducing the congruent melting reaction of chapter 4.2.5 correctly (as type B). Even without the updated EXAFS spectra this alone settles the most pushing matter, the type A/B dilemma. However, the question remains whether the EXAFS spectra improves, too.

5.2.3 Development of pot. type C and using it for EXAFS II

And on top of the improvement by the development of type C with the help of AIMD in 5.2.2, the EXAFS (and thus fine-structure) accuracy is increased, too. The previously highlighted phase shift around 85 (k) (in section 5.2.1) is corrected by this new pot. type C and an extraordinary agreement is reached, clearly indicating that pot. type C models $Fe_{17}Y_2$ at room temperature accurately in (nearly) all details. More generally, it is the combination of a perfect representation of the ideal pure phases, as discussed in 4.2.3, and a versatile accurate defect and also binding behavior, which can be linked to the mixing mechanisms (appearance of rhombohedral components in the dominating hcp structure). By AIMD magnetic influences were indirectly included, though the model does not explicitly depend on magnetism. This crucial advancement will put into a wider perspective with the help of more detailed links to the previous conclusions and key points of this work.

Coming back to EXAFS and examining the agreement in more detail, by looking at Fig. 5.4 the blue curve representing the MD simulated EXAFS spectrum at 300K and the red dotted curve showing the experimental results, both perfectly match in the positions of the peaks, leading to an excellent overall agreement. The peak widths are not exactly the same, leading to little areas which do not overlap, but that does not matter since the majority of the peaks overlap. More significantly, apart from mainly negligible differences, occasionally, two to three (at k= 55 and at 65) amplitudes significantly do not agree, but as said in 5.2.1 this can be accounted to the defects and as said before this would require experimental data on defect densities, which are not available, especially for the prominent point defects.

The final interesting step of this EXAFS examination would be to understand how these rhombohedral components are formed, how they exist/stabilise and the amount of them. Unfortunately, no exact formation behaviour, for instance the suggested swap of Fe and Y atoms, could be seen. What could be seen though, that the aforementioned specific Fe atoms ("Fe 4f" and "Fe 4e") oscillate between these two (the next Y atom and the original Fe atom positions). This seems to cause similarities to the rhombohedral structure – so maybe the statement of rhombohedral components is not quite correct and instead, the statement should be: by magnetic influences the pure hcp structure becomes disordered in a way that certain areas of the crystal exhibit similarities to the rhombohedral structure. Presumably, these similarities should become stronger with decreasing temperature and eventually lead to the transformation to pure rhombohedral structure. This would require different temperatures (following concluding section).

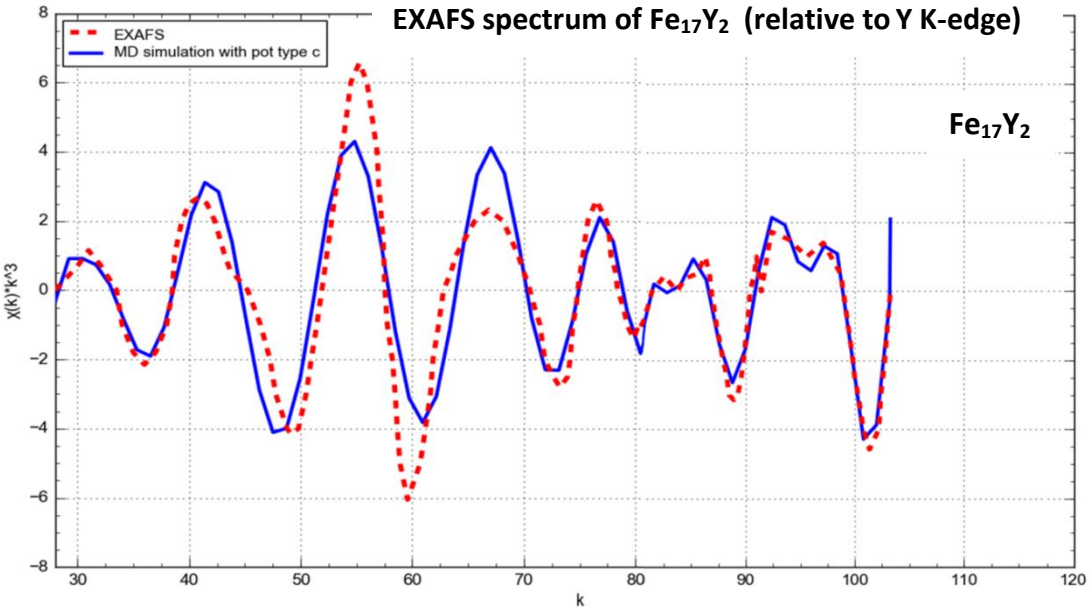

Fig. 5.4 Perfect reproduction of the $Fe_{17}Y_2$ EXAFS spectrum at 300K by pot. type C – k value was cut around k=105

5.3 Limitations, chapter specific conclusions & outlook

The final ability to precisely model the EXAFS spectrum of the rather complicated structure in $Fe_{17}Y_2$ marks the end of this work. Though the exact transformation process to rhombohedral or rhombohedral similar structures could not be found (reasons will be explained in more detail below), the major and paramount achievement of this work is the development of techniques to develop potentials with abilities of type C, which unites phase and defect properties in a rather complex alloy. Quantitatively, accuracies in Fe-Y measured as R values up to 0.078 for phases (with up to 20% Y content) and defects has been reached. This is the first time that a MD potential related to ODS materials can accomplish such an accuracy, as required in the introduction (R=0.1 was there the target). In the conclusion of the whole work (next chapter 6) this point will be revisited and deepened.

Considering the development of pot. type C in this chapter, the main question is why including AIMD references in the fit-database promoted solving some of the dilemmas of pot. type A and B ("type A/type B dilemma").

Before doing so, it is important to remind oneself, that this chapter focused on $Fe_{17}Y_2$ (since this is the only phase experimental EXAFS data is available). Considering phases in pot. type C, the limitation Y contents up to 20% allows very accurate simulations of $Fe_{17}Y_2$ or at most $Fe_{23}Y_6$, which can be considered too with satisfactory accuracy due to its similarities.

As a consequence not all dilemmas while modelling Fe-Y could be solved, for instance the congruent melting reaction considered in section 4.2.4 on p. 97 could also be reproduced by pot. type C like in pot. type B while also keeping the desired accuracy in defects as type A. But, when considering the second chosen (eutectic) reaction $Fe_{23}Y_6$ is not properly formed using pot. type C. So, this indicates that some dilemmas regarding other phases with higher Y content still remain, more in the final chapter 6.

Nevertheless, even with these limitations, a meaningful and helpful conclusion could be drawn by coming back to the question why pot. type C with AIMD has overcome the type A/B dilemma:

The main difference between AIMD and classical DFT is, that DFT is kind of the rigid picture at 0K with no vibrations and thus leading to a very restricted representation of the modelled phase (here $Fe_{17}Y_2$). AIMD on the other hand, models the thermal disorder with its vibrations (at T>0K) – this leads to a much more versatile and detailed description of a phase, because now the vibrations and exited states are included too. For the fitting this practically means, that during the fitting more possible states of the phase (including the excited ones) are considered. Each state is linked to a physically sensible choice of parameter sets (and more possibilities, a greater number of various states to verify) and thus makes the fitting more flexible by a broader choice of parameter sets. In contrast to the classical LSM fitting tools like POTFIT parameter sets here do not denote any arbitrary parameter set, but a selection of parameter sets belonging to certain states (so each available parameter set is checked to be suitable for at least one state, and this is possible by AIMD and GA techniques). These different (pre-chosen) possibilities resemble to a higher content of the real states – this makes it easier for GA techniques during the manipulation of the parameter set to distinguish the best suitable parameter sets, since there are more possible combination of parameter sets leading to the best combination satisfying all of these possible states (though the fitting itself gets more advanced by the need for more refined techniques such as GA).

Simply speaking, the pure 0K DFT description seems too rigid and *offers* too few suitable parameter sets, proving insufficient combination possibilities for the GA code. This enhanced representation of the states of the phase can be also better linked to magnetism and defects: it can be assumed that this more versatile and flexible representation of the phases can be better linked to the defects. More concrete, the details are the vibrations and these vibrations can sometimes also be similar or even resemble certain defect formations (or at least tendencies) – considering 0K it is clear at once, because at 0K in theory no defects exist. So, AIMD configurations are configurations where defects can exist at these non-zero temperatures. While in classical DFT defects represent out of equilibrium states, which normally do not exist at the considered temperature of 0K (however, defects can be artificially built in and forced to exist).

So, in AIMD references a representation of the phase and defects (or defect like formations in the form of vibrations) can kind of exist at one time in one configuration, while before there had to be separate configurations for defects (by clusters) and phases (by equilibrium configurations and out-of-equilibrium configurations (showing volume/energy relationship leading to EOS) without defects). Such an enhanced representation then helps the GA to better link the phase configurations and the defect clusters. The thermal vibrations increase the versatility in the atomic positions of the phase leading to more flexibility, which supports the occurrence of defects.

On top of that, these vibrations are not just thermal vibrations. The vibrations are also mutually dependant on magnetism, which is also considered in AIMD (and was realistic because spins were not fixed (enforced) in the used AIMD configurations) – so these states with atoms out of exact equilibrium also indirectly include magnetic contributions. So, it can be said that fitting with AIMD indirectly includes magnetism (whether that is enough more in conclusion in chapter 6) and this inclusion helps to exactly model the structure of $Fe_{17}Y_2$, where the fine structure as shown by comparisons to EXAFS is influenced by magnetism. And since the MD model precisely agrees, the MD model represents at least partly the magnetic influences on the structure (at least for $Fe_{17}Y_2$,). This solves the raised issue at the end of chapter 4, where it was assumed that missing magnetism could be a reason why either the phase energies are slightly inaccurate (by 0.05 eV) or the binding energies (same order of magnitude) leading to problems in defect properties. By this new technique EXAFS in combination with AIMD fitting references this problem was solved.

However, when considering what happens at higher temperatures by performing AIMD runs at these higher temperatures, like at 500K, the stabilisation failed and the runs could not be performed. The reason was that during stabilisation the initial magnetism always totally vanished and this led to critical destabilisation of the structure causing the stop of the AIMD run. One of the most probable reasons lies in the fact that the experimentally anticipated hcp structure is incorrect, as already shown in Mihalkovic's published DFT calculations about a wide range of possible structures of $Fe_{17}Y_2$ [142] (which were at 0K, but by considering enthalpies and energies it was tried to draw conclusion for exited states, which resemble higher temperatures). Consequently, the AIMD runs were repeated with the supposed structures by Mihalkovic, but none of them could fix this issue (thus for details it is referred to the paper [142]).
What can be said, that both experimental and DFT modelling cannot predict the exact, atomistic stable structure of $Fe_{17}Y_2$ at higher Ts. Another reason why the pure hcp structure is probably incorrect, is that even with the pure MD runs at 500K with an hcp (and the other structures) structure the experimental EXAFS spectra at higher temperatures could not be modelled (= not reproduced by simulation).
On the other hand, this is also good news, because the view from 300K predicts a structure which is stabilised by magnetism. However, the structure at higher temperatures (when considering the EXAFS spectrum at 800K) is stable without or at least a very weak magnetism (since 800K approaches the Curie temperature in Fe-Y which is around 250K lower than the curie temperature of Fe). Therefore, at higher temperatures there seems to be an unknown (different!) structure which is stable without magnetism and it seems neither to be this hcp/rhombohedral mixture or pure hcp. Some experiments still insist on pure hcp – maybe they are right and one effect at high T might tamper the EXAFS spectra – the defects and impurities in the examined $Fe_{17}Y_2$ EXAFS sample, which become more relevant for the resulting EXAFS spectrum by enhanced diffusion processes due to the higher Ts. These are hard to trace (wrt. direction and tendencies) bulk diffusion processes and this could kind of take over at higher temperatures.
What would be really needed beside the EXAFS spectra at different T, but is not available, would be an XRD at very low temperatures, room temperatures and high temperatures. This would help to identify structures, locate at which temperatures the transitions take place and would help to interpret the change with temperature in the EXAFS spectra – but without XRD in this rather complicated case a clarification of this transition seems impossible. Thus, these additional XRD measurements are the out-looking perspective of this chapter with a special focus on the structure of $Fe_{17}Y_2$.

Nevertheless, even without these additional XRD some interesting mixture of hcp/rhombohedral was discovered and validated at room temperature and it was shown that the previous descriptions of the structure of $Fe_{17}Y_2$ at higher temperatures are rather inaccurate. Three final remarks for this chapter:

1. it is quite a great surprise that the effects of contaminations seemed to be quite weak (at room temperature, at least), much more disagreement with the EXAFS spectrum due to these were expected (but maybe at higher T that's the case, see p. 110). Some defects caused some deviation in the peak overlapping, but this is expected and was explained in 5.2.1.
2. Though only some of the uncertainties about the structure of $Fe_{17}Y_2$ could be resolved to a satisfactory level, the principal new tool a precise MD potential can be ranked as an even better result. This successful comparison of simulated alloy structures to experimental EXAFS, required the development of a specific fitting technique, which employed the state of the art RF-MEAM format, with a goal orientated use of AIMD references, to fit this new potential class type C (main result), which will be put into perspective in the outlook.
3. Already from the point of view of this chapter, this new type was necessary for the EXAFS simulations. MD is necessary because of the required cell sizes. This becomes clear, when one gives in to the notion, to try to model the EXAFS spectrum and its processes directly in AIMD. Unfortunately, up to now this would take much too long – at least a simulation cell with 512 atoms is required for EXAFS simulation. The here used AIMD run was only 38 atoms and took 4-6 weeks, a suitable cell would run for years.

So, this new pot. type C served as a valuable structure examination potential and can additionally model defects, what can be done in more general with this is shown in the outlook in the next chapter 6.

5.4 Achievements in chapter 5

- The main underlying theoretical achievement, and result as an obtained technique, is the adaption of W. Hu's splitting technique to the change in parameters during the fit from type B to type C. This saved a lot of time, because instead of fitting the whole potential from scratch it was only slightly amended, but with significant outcomes within 2 instead of 6 months. [enabled by the detailed knowledge and results in potential fitting and formalism mainly by chapter 3]
- Successful use of own developed LAMMPS module to obtain a large MD data-set for EXAFS
- Independent implementation and application of the high-end EDACA software in combination with an evolved ab-initio scattering code FEFF, required careful checks at multiple stages (the presented check for bcc Fe in EXAFS I was only at the final level after numerous checks before).
- With these necessary preliminary results: principal simulation of an EXAFS spectrum of a complex metallic alloy for the first time (will be published after the hand-in of this dissertation).
- Independent interpretation of the EXAFS spectra leading to a clarification of the fine structure in $Fe_{17}Y_2$ at 300K as mainly a hcp structure with occasional random rhombohedral components, which could be principally linked to magnetism
- Successful cooperation for the implementation of a supportive cutting-edge AIMD run
- Successful pot. improving AIMD assisted refit with the aforementioned developed technique
- Exact reproduction of EXAFS spectrum for $Fe_{17}Y_2$ at 300K in a never before achieved accuracy, which confirmed the above statements about the fine structure of $Fe_{17}Y_2$ at 300K
- Identification of sample contaminations as obstacles for higher temperature EXAFS comparisons
- Exact identification of improving extensions and determination of long-term goals towards ODS

6 General Conclusions & Outlook

6.1 Conclusions

The developed techniques and obtained results by used Fe-Y interaction potential scheme can be summarised as threefold evolution: firstly, EAM techniques with LSM, where underlying universal parameter restraining techniques for the whole work with basic starting fit parameter and MD results were obtained. Then, secondly, development of RF-MEAM fitting techniques by employing GAs yielding enhanced RF-MEAM potentials with advanced results which can be linked to state of the art experiments regarding properties and behaviour of Y in ODS production relevant processes. And finally, to overcome the type A/B dilemma and enhance the accuracy in modelled Fe-Y structures an EXAFS spectrum at 300K was successfully reproduced with assistance by extension of the refit database with AIMD references. This completely new and innovative approach yielded a never before achieved accuracy in EXAFS simulation of metallic alloys. The overall outcomes of the development and results in these steps are:

- In EAM based fits, techniques were developed to better understand and control parameter sets, since these were identified as a key factor in the development of alloy potentials. This led to analytical constraints for the base properties (such as elastic constants), two flexible but necessary URs (α/β and r_e) with inevitable affiliations to the Rose eq. and an additional UR in the form of the key driver η (with the 2^{nd} key driver F_0), which was used by a systematic scan of the parameter sets within the UR restrained parameter space. The results by the developed Y-vac test in 3.3.7 clearly showed the absolute need to abolish the links to the Rose eq.. Regardless of this issue, this EAM technique was able to reproduce the basic single metal properties within 1% for the lattice constants and E_c, 5% for elastic constants (except C_{44} 8%) and as a *novelty* beside the acceptable vacancy defect formation energies, the accurately reproduced SIA energies correctly identified BO as the most stable position for the first time in (M)EAM (with E_f 2.17 eV vs. 2.03-2.10 (literature, DFT)). As an additional surprise, the developed EAM potential reproduced the first pressure derivative of the bulk modulus (B') more accurately (6.6 vs 7.5 by ZW and lit. values 5.0-6.5) though it was not included as a fitting target. This shows a significantly improved transferability and contributes to a better description of the associated energetic differences btw. the bcc and fcc phase as well as T_m (which in single metals not alloy pots. can be well fixed by this discovered alternative route). In this fitting scheme these Rose linked URs, successful in single metals, failed evidently in alloys (at least in Fe-Y), but these URs could not be simply omitted, a suitable replacement by
- RF-MEAM was necessary, which could reproduce for the first time all references within ≈ 11% on average and could successfully fit alloys, as confirmed by the passed Y-vac. test, which even shows potential to capture the famous double vacancy occupation mechanism of Y (SCD). Instead of these defect subtleties, the improvement of the Fe-Fe interaction by successfully including an existing Fe-Fe potential as a replacement was more pushing, because this improved defects (R was around 9%) and especially the accuracy of T_m improved to 3% (instead of 11% before (≈200K off)). While checking this replacement the remarkable discovery of the electron density as a parameter set indicator, how well potentials suit each other, was made – all of this is based on the in-detail study of parameter sets in EAM. This enhancing Fe-Fe inclusion enabled by the resultant pot. type A the first successful simulation of the Y cluster formation in liquid Fe at 1750K, the clusters are few nm in size and a dependence of the cluster size on the reproduced

E^f_{vac} was observed. When cooling this mixture down, it stayed stable and accurately predicted a low 0.1% solubility of Y in Fe leading to precipitation processes, as expected. It was found that, the DFT assisted correction of the vacancy formation energy from 1.25 eV to around 1.6-1.8 eV reproduces more realistic cluster sizes. Additionally, the binding energies of Y-vac. clusters, respectively their associated sign (+/-), plays an important role for this cluster formation: this energy needs to be negative for distances above the 2NN, resulting in an attraction, which acts as an important initiation for the Y atom accumulation leading to this cluster formation. This binding behaviour has been identified during the fitting in competition with minor difference in E_c btw. $Fe_{17}Y_2$ and $Fe_{23}Y_6$ in this non-magnetic model. Apparently, accuracy in these binding energies results in missing components in this phase difference (which consulting DFT and AIMD, as done later, shows links to magnetism). The tendency of either preferring accurate binding energies or phase differences is controlled by the weighting of atomic references during the fitting. Focusing on this energy difference leads to another type, type B, which was able to reproduce all structures of Fe-Y phases (a_0, c) and their energies (E_c) within 5% (up to 20% Y-content, 1% in E_c, 2.5% in a_0), leading to a principal ability to reproduce the congruent phase creation of $Fe_{17}Y_2$ at 1650K and in principal an eutectic reaction of a mixture of $Fe_{17}Y_2$ and $Fe_{23}Y_6$. Nevertheless, the resulting type A/B dilemma impedes the required modelling of phase and defect processes *at the same time* (in ball milling defects dominate, while in HIPping it is phase associated processes).

- EXAFS & AIMD: Originally, the use of EXAFS comparisons was planned to understand magnetism and its effect on the fine structure. And indeed, a principal existence of a magnetically induced rhombohedral component in the $Fe_{17}Y_2$ structure dominated by hcp has been shown at 300K (as predicted by EXAFS, supported by AIMD and confirmed by an AIMD assisted refit leading to type C), resulting in an excellent agreement of the MD model (and its RF-MEAM pot. (type C)) with an EXAFS spectrum of a metallic alloy for the first time. This finding provided an improvement of previous structure examinations by polarised neutron diffraction studies by Moze, which overestimated the amount of rhombohedral components. So, this AIMD assisted technique is of considerable use in the fine structure clarification in complicated cases (because potential candidates can be modelled and then compared with EXAFS). Unexpectedly and surprisingly this evolution by type C also overcomes the central theme of this work the type A/B dilemma. The whole development is summed up in table 6.1 (p. 116 on p. 116).

This newly developed RF-MEAM potential class, namely pot. type C, provides an excellent reliable starting point for further MD examinations of ODS. For more applications by an active interplay with experiments the following suggested extension in next section are advisable. Nevertheless, as a foundation for this desired deeper insight into ODS steels a substantially more accurate potential scheme for both phase and defect properties, at the same time accurately without lacking quickness, has been established in this work (more details see table 6.1).

6.2 General Outlook

As said in the conclusion pot type C is a reliable basis for further MD examination of the “ODS mystery”, how ODS particles are actually formed. The paramount and most pushing follow-up task in RF-MEAM is a required extension of the MEAMfit code by screening factors, for two reasons: Firstly, for the inclusion of CTIP to be potentially able to include oxides and secondly it significantly increases transferability wrt. module (see note at parameter section in 7.0.1). Nevertheless, it shouldn’t be overseen, that the problem for the slower than anticipated progress in this question not only lies in the modelling complications this work dealt with, but also lies in a considerable amount of required additional experimental data, which essentially needed for a successful modelling to deal with these extreme and complicated requirements.

Needed additional reference data by experiments

Starting from the last chapter the most desired missing experimental data are comprehensive XRD spectra for $Fe_{17}Y_2$ at various temperatures to clarify this mixture in the structure and to clarify the transition (supposedly from rhombohedral at T_{low} to the mixture (T_{room}) to some unknown structure (T_{high})).
In order to clarify the structure from the modelling side a dependence of the EXAFS spectra on magnetism would be of tremendous use – so, various EXAFS spectra of the same material with different external magnetic fields. This would make the AIMD runs easier and would extend the database for a better indirect inclusion of magnetism and could solve the issue of vanishing magnetism at higher temperatures (especially this point is a great surprise and underlines the complexity).
More generally, it has to be noted, that this basic EXAFS data (and AIMD) was only available for $Fe_{17}Y_2$, to fully cover EXAFS spectra of all Fe-Y phases, such as $Fe_{23}Y_6$ and especially Fe_3Y, are necessary. Though, the $Fe_{23}Y_6$ is the most pushing one, because pot. type C has weaknesses to reproduce the creation this phase – the type A/ B dilemma for Y contents up to 20% is practically solved here, but this issue remains and can be only solved by the additional EXAFS data. And the Y-content limitation might be lifted by the EXAFS spectra of all phases. With new EXAFS spectra and the here developed split technique this could be in principal done in an effective manner within 6 months.
Two practical issues when comparing to EXAFS data remain though: 1. Contaminations and 2. Defects. The latter can be hypothetically well handled by including defects into the AIMD runs and try various defect densities (since unfortunately experiments are not able to provide these, particularly the point defects) – but since due to the performance the cell size in AIMD is severely limited to 100 atoms and defect densities in reality are expected to not exceed 5 % (which is already a strong overestimate) – only 5 defects could be modelled in months long runs. So, it is a time issue. With contamination in general, this should be handled by using very "clean" powder metallurgical samples, which are rather costly.

Extensions to the potential framework of RF-MEAM and GAs

All the previous suggestions and the further experimental effort is only justifiable, if modelling of complete ODS (Fe-Y-O) is in reach. Within this developed and used framework this extension is readily possible by adding a Charge Ionic Transfer Potential (CTIP) – as Lazic [95] did. But CTIP requires for stability turned on screening factors, which then in turn makes the fitting and the GA adaption much harder (and is plagued by instability) – another exceedingly time consuming step.[84] COMB models, as shown before have even higher requirements for the GA optimisation techniques. All of this advocates for one option: machine learning, the author firmly believes in one simple but decisive benchmark to determine when ML is *ready*: as presented in the lit. review, the latest and best ML Fe pot. [100] is still not totally convincing (keyword T_m) – but once this obstacle in ML is cracked, ML can definitely be considered as a promising and probably *less painful* alternative for ODS modelling. However, as with the experiments, it is still not entirely certain which tech. will progress quicker in the next year. In any case, this work and its techniques act as a useful bridge to ML modelling.

Possible further simulations for now

But for now, before implementing these extensions another concrete immanent example is a readily possible study of interactions of Y-vacancy clusters with dislocations in iron and solute Y. By upscaling the simulation cell size to millions of atoms due to the computational efficiency of RF-MEAM it could be further investigated with novel accuracy at these large cell sizes for the first time, whether solute Y is playing a significant role in the Yttria formation process in ODS steels. The accuracy of this study will be characterised by the ability to also regard changes related to the amount of dissolved Y atoms by phase changes, which will provide a complete new technologically relevant picture in detail for the effect of solution hardening of Y dissolved in Fe which in combination with vacs. represents substantial obstacles to dislocations – thus resulting in hardening by adding Y solutes, *a great outlook to metallurgy*.

[84] requires further information about the valence states of Y-O and an answer to the discussed question of the existence of YO

EAM – „Classical Approach“	**RF-MEAM – „Analytically reduced approach“**	**RF-MEAM – „Systematic, fast approach“**
1.5 Year (2014-2016)	**1.5 Year (2016-2017)**	**1.5 Year (2018) incl. 1 year for EXAFS & AIMD**
Form: $E_i = \sum_i F(\rho_i) - \frac{1}{2}\sum_{ij} \Phi(\overrightarrow{r_{ij}})$	Form: $E_i = \sum_i F(\rho_i, \theta_{ijk}) - \frac{1}{2}\sum_{ij} \Phi(\overrightarrow{r_{ij}})$	Form: $E_i = \sum_i [F(\rho_i) + F(\theta_{ijk})] - \frac{1}{2}\sum_{ij} \Phi$
Approach: • *Tool: Potfit* • Seperate fits needed -> time consuming • Requires involvement of Rose equation • Rose -> inability to fit defects (s. e.g. II) • Matching of species potentials cumbersome • Overfitting -> not enough parameters • *But* more parameters cannot be fitted without extended fitting programmes using GA – genetic algorithms	Approach: • Tool: MEAMfit (v 1.0 & v2.0) (e.g. III) • Fitting at the same time with analytical constraints (e.g. IV & V) and 1x fixed pot [Fe-Fe fixed, Y-Y constrained, Fe-Y free] • Reasonable cluster defects (e.g. VII) • Very good at self interstitial and vacancy formation energy (s. e.g. VI) • Clusters need to be improved (R<0.1 & better Crosss validation see e.q. VII) • pot type A/type B dilemma	Approach: • Similar to LHS but: ○ Y-Y basic properties fixed by AMEAM pot. at eq. (r_0) (-> VIII) ○ Y-Y defect and additional properties fixed by angular part • **Separate ang. And non-ang. Part** • **Faster technique and better cluster energies – final technique** • **Inclusion of more details by AIMD and improvement by pot. type C**
Basic EAM potentials for Fe-Fe, Y-Y and Fe-Y **Skill to fit to DFT data or analytic rules or Mix**	**Framework (lammps module, fitting speed up (20x) in v2.0), extended potentials (RF-MEAM)**	**Intelligent Rapid technique using analogies (3x) and improvement for Fe-Y clusters**
Para: 12x Fe-Fe • 15x Y-Y • 8x Fe-Y [45-14=31]	**Para: 32x Fe-Fe • 26x Y-Y (*-18*) • 28x Fe-Y [36]**	**Para: 32x Fe-Fe • 16x Y-Y • 28x Fe-Y [46]**
Fitting time: 1.5 years **Quality: medium (R>0.15)**	**Fitting time: 1 – 1.5 years** **Quality: high (R: 0.1-0.15)**	**Fitting time: 0.5 years** **Quality: very high (R ≈ 0.1, up to 0.07 with AIMD)**

Table 6.1 Summary of evolution in potential development techniques during the project

7 Appendix

7.0 Final fitting results - POTENTIAL parameters

7.0.1 Single Fe and Y in POTFIT – ZW formalism (as in 3.1)

Para	bcc Fe	Para	Bcc Fe	Para	bcc Fe	Para	Bcc Fe
A	0.39099	κ	0.1703	F_2	0.20063	F_{n2}	0.19291
B	0.641091	f_e	1.88595	F_3	-0.14877	F_{n3}	-2.2825
β	5.23811	F_0	-2.54	F_{n0}	-2.53496	F_e	-2.558
r_e	2.48	η	0.3926	F_{n1}	-0.05952	ρ_e	20.05

Para	hcp Y	Para	hcp Y
F_2	0.9298	F_{n2}	-0.8452
F_3	0.9665	F_{n3}	-2.5426
F_{n0}	-5.448	F_e	5.0631
F_{n1}	-1.326		

Para	hcp Y	Para	hcp Y
A	0.022984	κ	-0.4529
B	0.00665	λ	-0.2554
β	6.1168	m	8.0261
r_e	6.4262	n	24.5582

These are solely the parameters for the single potentials, for the Fe-Y alloy potential there is no need to present these faulty parameters, because the RF-MEAM ones actually work, the ones (for Fe-Y) in POTFIT do not work. These parameters were transformed by tabulated potentials for use as start parameters in RF-MEAM (these POTFIT parameters are an extract of an own conference poster presentation).

7.0.2 Fe-Y final parameters in MEAMfit – RF-MEAM formalism (as in 4.1)

$$f_{\mathrm{A}}^{(l)}(r) = \sum_{n=1}^{n_{max}} a_{\mathrm{A}}^{(n,l)} \left(r_{\mathrm{A}}^{(n,l)} - r\right)^3 \Theta \quad (4.10) \qquad \varphi_{\mathrm{AB}}^{(l)}(r) = \sum_{n=1}^{n_{max}} b_{\mathrm{AB}}^{(n)} \left(s_{\mathrm{AB}}^{(n)} - r\right)^3 \Theta \quad (4.11)$$

Pot. type A

Parameter	Fe-Fe	Y-Y	Fe-Y
density:			
$a^{1,0}(r_{spec})$	11.686859407970 (2.4)	0.4003763188 (5.75)	
$a^{2,0}(r_{spec})$	-0.0147107400988 (3.2)	6.7764893964 (1.84)	
$a^{3.0}(r_{spec})$	0.4719352707594 (4.2)		
$a^{1,1}(r_{spec})$		-1.6608073927 (2.84)	
$a^{2,1}(r_{spec})$		-2.18157329575 (3.3)	
$a^{1,2}(r_{spec})$		13.137494756 (4.15)	
$a^{2,2}(r_{spec})$		-42.847360132 (3.11)	
$a^{1,3}(r_{spec})$		-1.8264243214 (4.38)	
$a^{2,3}(r_{spec})$		4.541862517 (3.93)	
EMB:			
a	1.000	1.0364420712735	
b	-0.00035387096577929	0.00040088627	
c		0.00000001334	
pair:			
$b^1(r_{spec})$		-4.399262342 (3.45)	-1.207932007 (1.65)
$b^2(r_{spec})$	-24.028204854115 (2.2)	-4.303296788 (1.87)	-11.10281487 (2.85)
$b^3(r_{spec})$	11.300691696477 (2.3)	4.839374135 (2.59)	-7.574291623 (4.45)
$b^4(r_{spec})$	5.3144495820462 (2.4)	2.385531283 (3.83)	-33.52648217 (3.45)
$b^5(r_{spec})$	-4.6659532856049 (2.5)		-0.543311986 (5.82)
$b^6(r_{spec})$	5.9637758529194 (2.6)		-4.8266986526 (5.81)
$b^7(r_{spec})$	*-1.771026200606 (*2.7)*		7.5334362484 (4.86)
$b^8(r_{spec})$	0.8591383076873 (2.8)		52.824298831 (3.16)
$b^9(r_{spec})$	-2.1845362968261 (3.0)		8.752624907 (3.90)
$b^{10}(r_{spec})$	2.6424377007466 (3.3)		3.1012628316 (6.14)
$b^{11}(r_{spec})$	-1.0358345370208 (3.7)		9.1721496486 (4.80)
$b^{12}(r_{spec})$	0.3354826495158 (4.2)		-2.7395473880 (5.45)
$b^{13}(r_{spec})$	-0.0464485821493 (4.7)		-15.027675855 (2.84)
$b^{14}(r_{spec})$	-0.0070294963048 (5.3)		-6.8568745984 (4.45)
Tau:			
t^1		-8.582181247040	
t^2		0.91482747199735	
t^3			

* "-" sign was missing in original publication [76], thank to M. Mendelev for the corrective info

Pot. type B

Parameter	Fe-Fe	Y-Y	Fe-Y
density:			
$a^{1,0}(r_{spec})$	11.686859407970 (2.4)	5.1705906979 (1.91)	
$a^{2,0}(r_{spec})$	-0.0147107400988 (3.2)	1.6669032257 (5.09)	
$a^{3.0}(r_{spec})$	0.4719352707594 (4.2)		
$a^{1,1}(r_{spec})$		-9.319161129 (1.60)	
$a^{2,1}(r_{spec})$		2.4623964222 (7.82)	
$a^{1,2}(r_{spec})$		-19.052027620 (1.60)	
$a^{2,2}(r_{spec})$		-0.3832583347 (8.03)	
$a^{1,3}(r_{spec})$		3.8607197755 (2.11)	
$a^{2,3}(r_{spec})$		11.044797755 (1.94)	
EMB:			
a	1.000	22.481739246443	
b	-0.00035387096577929	0.001.677506747	
c		-0.0000009588649	
pair:			
$b^{1}(r_{spec})$		80.906560431 (7.73)	3.7791918194 (8.23)
$b^{2}(r_{spec})$	-24.028204854115 (2.2)	-4.045796405 (1.73)	19.767738989 (8.21)
$b^{3}(r_{spec})$	11.300691696477 (2.3)	-87.65524828 (7.65)	131.38364466 (4.31)
$b^{4}(r_{spec})$	5.3144495820462 (2.4)	18.790689435 (5.27)	-9.487901329 (7.62)
$b^{5}(r_{spec})$	-4.6659532856049 (2.5)		-5.561878783 (8.40)
$b^{6}(r_{spec})$	5.9637758529194 (2.6)		-14.73929049 (6.42)
$b^{7}(r_{spec})$	*-1.7710262006061* (2.7)		3.1891273688 (6.61)
$b^{8}(r_{spec})$	0.8591383076873 (2.8)		-13.18082561 (7.85)
$b^{9}(r_{spec})$	-2.1845362968261 (3.0)		-6.458212978 (8.40)
$b^{10}(r_{spec})$	2.6424377007466 (3.3)		-63.162173819 (5.05)
$b^{11}(r_{spec})$	-1.0358345370208 (3.7)		-110.66939029 (4.22)
$b^{12}(r_{spec})$	0.3354826495158 (4.2)		48.519553846 (5.28)
$b^{13}(r_{spec})$	-0.0464485821493 (4.7)		-2.554916977 (1.93)
$b^{14}(r_{spec})$	-0.0070294963048 (5.3)		16.8988367 (7.24)
Tau:			
t^1			
t^2		-1.180094987561	
t^3		-0.799314219298	

Pot. type C

Parameter	Fe-Fe	Y-Y	Fe-Y
density:			
$a^{1,0}(r_{spec})$	11.686859407970 (2.4)		
$a^{2,0}(r_{spec})$	-0.0147107400988 (3.2)		
$a^{3.0}(r_{spec})$	0.4719352707594 (4.2)		
$a^{1,1}(r_{spec})$			
$a^{2,1}(r_{spec})$			
$a^{1,2}(r_{spec})$			
$a^{2,2}(r_{spec})$			
$a^{1,3}(r_{spec})$			
$a^{2,3}(r_{spec})$			
EMB:			
a	1.000	31.352479906718983	
b	-0.00035387096577929	0.000241121068662	
c			
pair:			
$b^{1}(r_{spec})$		-4.2794581292 (8.40)	-1.8035622629 (7.49)
$b^{2}(r_{spec})$	-24.028204854115 (2.2)	7.4816793100 (8.29)	7.9613368315 (7.96)
$b^{3}(r_{spec})$	11.300691696477 (2.3)	-3.0684743195 (8.06)	-1.6477101423 (7.10)
$b^{4}(r_{spec})$	5.3144495820462 (2.4)	-18.939367679 (3.01)	-10.531133107 (7.50)
$b^{5}(r_{spec})$	-4.6659532856049 (2.5)		6.8252706089 (4.59)
$b^{6}(r_{spec})$	5.9637758529194 (2.6)		1.8330312696 (6.19)
$b^{7}(r_{spec})$	*-1.7710262006061* (2.7)		-4.4844683653 (7.67)
$b^{8}(r_{spec})$	0.8591383076873 (2.8)		3.8854563937 (3.87)
$b^{9}(r_{spec})$	-2.1845362968261 (3.0)		-9.4385307535 (5.42)
$b^{10}(r_{spec})$	2.6424377007466 (3.3)		9.2248768346 (5.32)
$b^{11}(r_{spec})$	-1.0358345370208 (3.7)		-7.2191958498 (4.42)
$b^{12}(r_{spec})$	0.3354826495158 (4.2)		-1.9165050241 (4.75)
$b^{13}(r_{spec})$	-0.0464485821493 (4.7)		10.193345388 (7.63)
$b^{14}(r_{spec})$	-0.0070294963048 (5.3)		-0.4994350122 (6.54)
Tau:			
t^{1}			
t^{2}		-0.16438819123335	
t^{3}		-0.68397979324355	

N.B: *The resulting potential properties by these presented parameters are unfortunately still critically influenced by the code implementation of the necessary LAMMPS (RF-MEAM)module – in other words: other RF-MEAM modules than the one used in this work can lead to different results, due to different associated screening factors. By the launch of MEAM v 3.0 (≈2020) with a planned integrated LAMMPS module and included screening factors in the fitting (extension of formalism) this issue is likely to be settled for better transferability.*

7.1 Appended “extra” fig./graphs/tables A.1-A.10

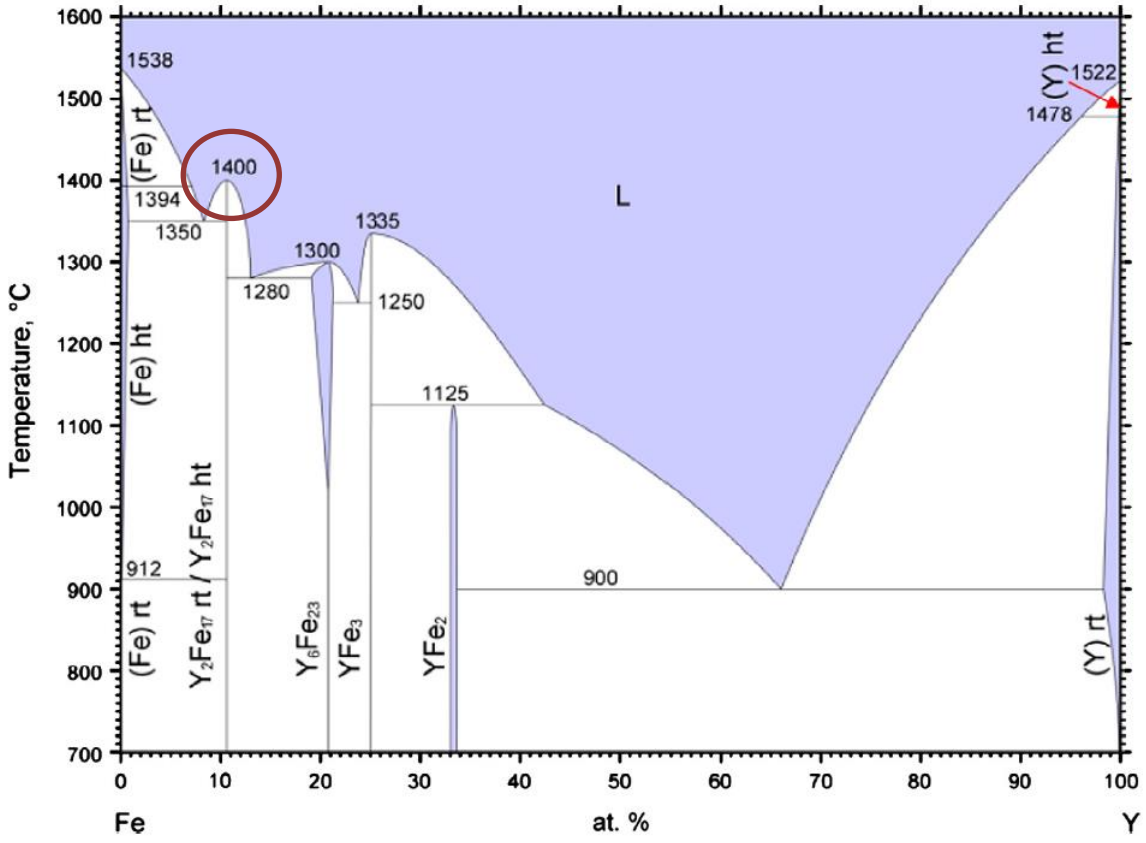

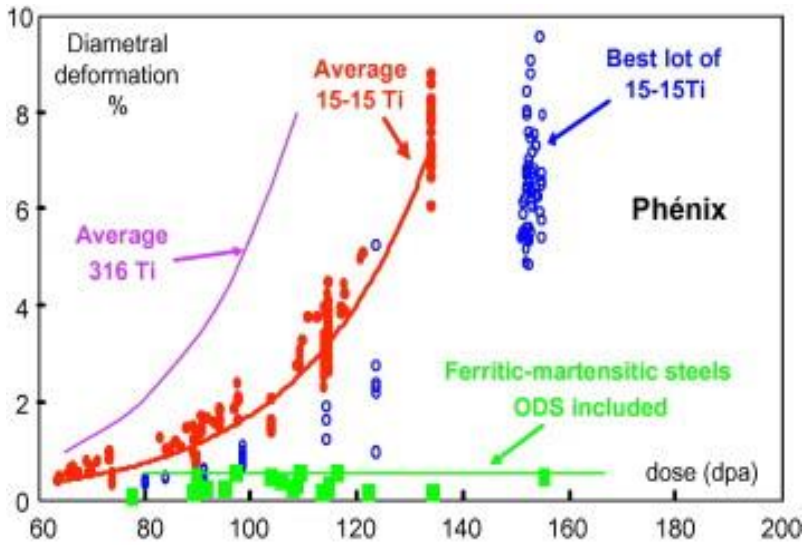

A.1 (bottom, p. 121) Comparitave illustration of swelling behaviour in different materials from [6]. The x-axis shows neutron irradiation measured in dpa. 316 denotes an „standard steel“ with Mb, 15-15 Ti is an austenitic steel with very high content of Cr – ODS is clearly superior in Swelling. 2-4 % Swelling is rated as *crictical*.

A.2 (LHS bottom) removed

A.3 (top p. 121) phase diagramm of Fe-Y by Kardelass [16], most relevant point is red-circled.

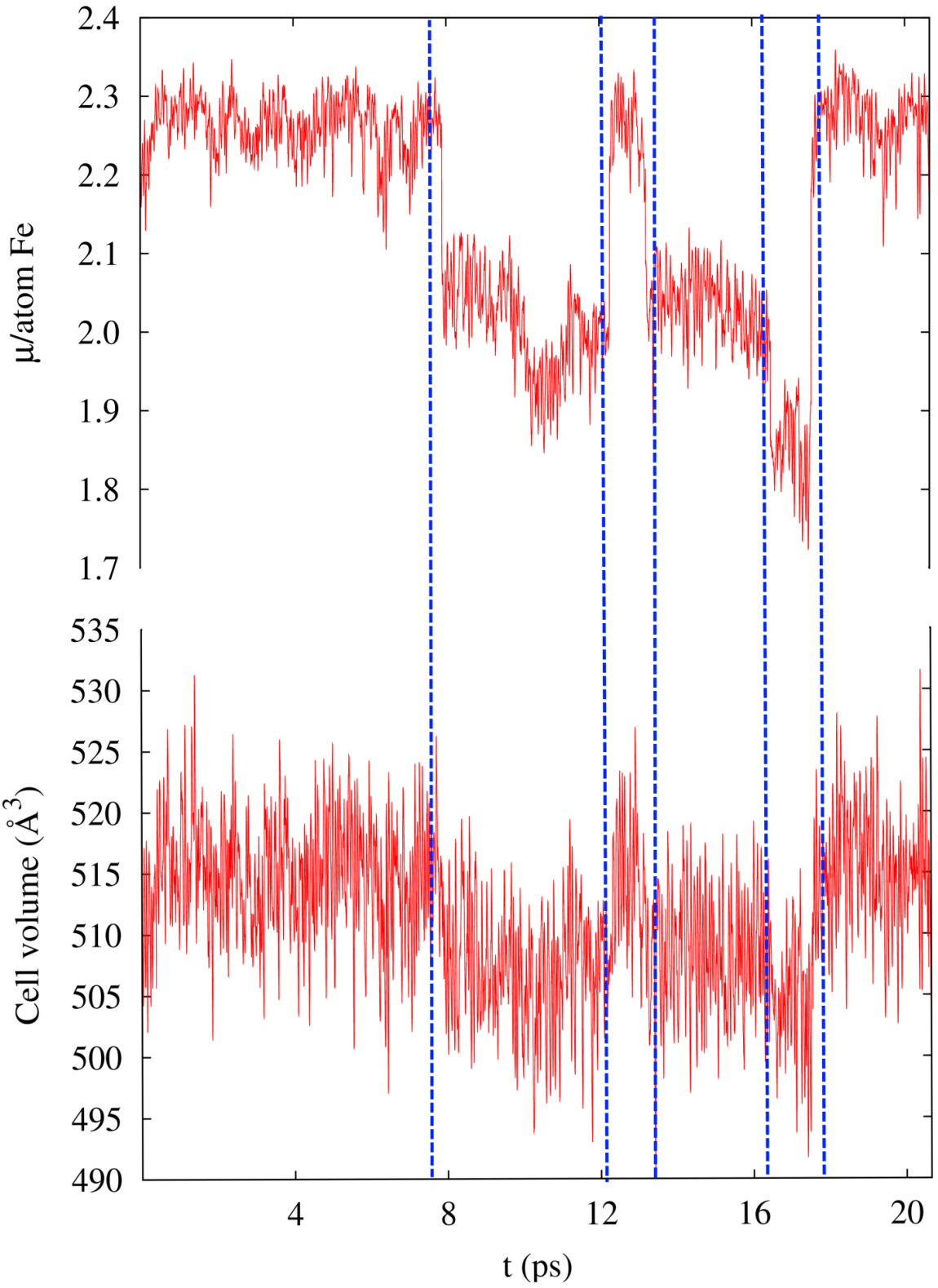

A.4 (top) diagramm showing stability of AIMD run, by magnetisation and volume in comparison, stable and mag. and vol. are related indicating the correlation – runs and graph with assistance of M. Marques (UoE).

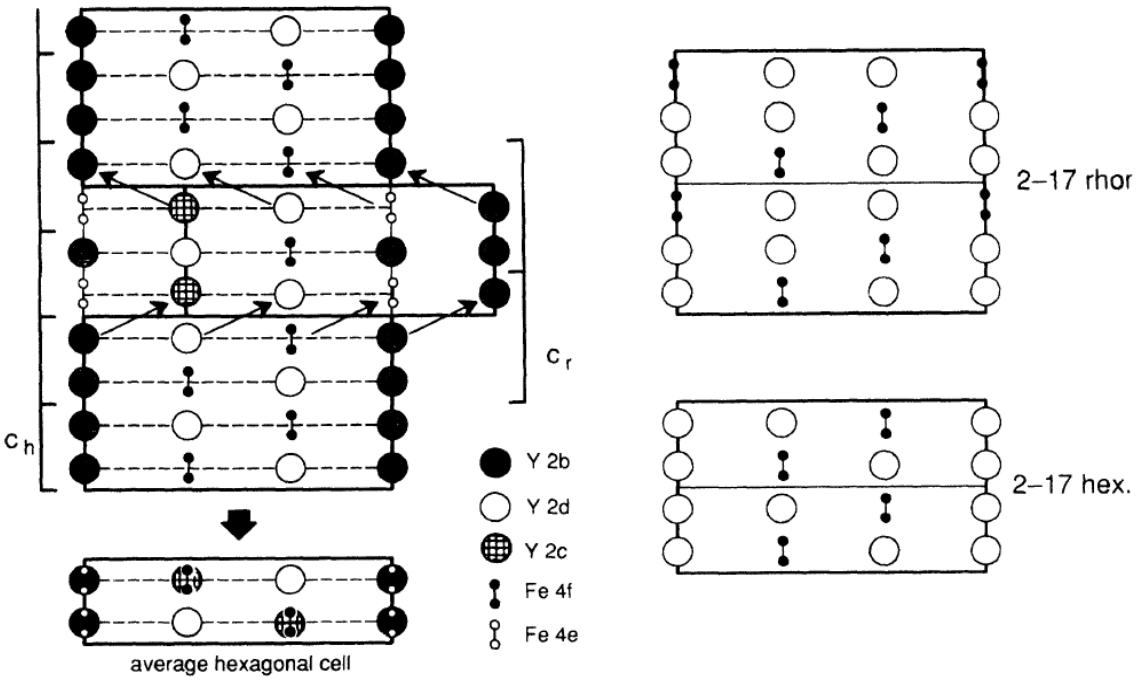

P.123: A.5 (top) & A.6 (bottom)

A.5 Schematic illustration how the mixture and possible transition of the α and β state in $Fe_{17}Y_2$ takes place. Of particular importance is the shift in the Fe atoms labled Fe „4f“ and „4e“ as observed in AIMD, the shift in the Y was not observed and would have consequented in stronger rhombohedral components, which were not observed by EXAFS, extract from paper of Moze [150]

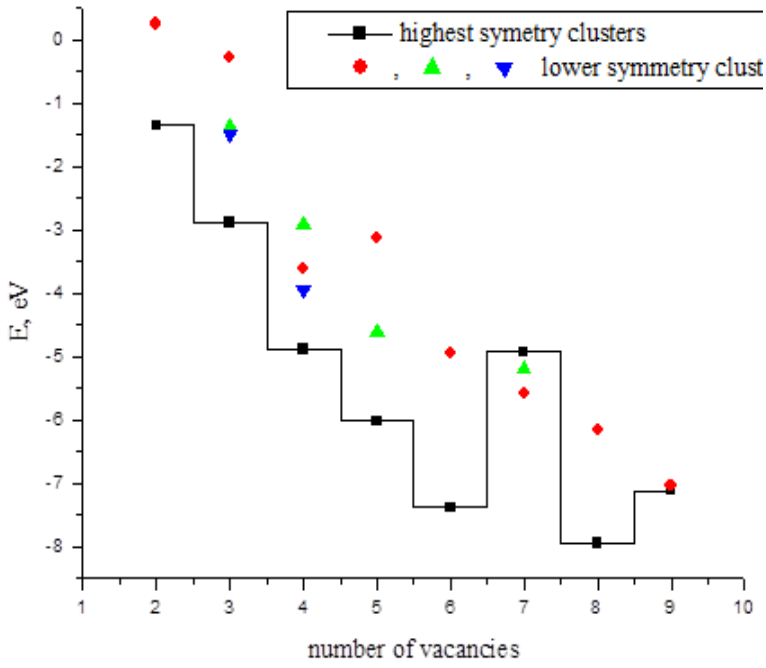

A.6 Illustration of different formation energies of defect clusters depending on the symmetry associated with the defect, these different points , which were all included in the fit databasecan be also found in the tables in 7.2, taken with permission from Y. Mastrikov‘s presentation [144].

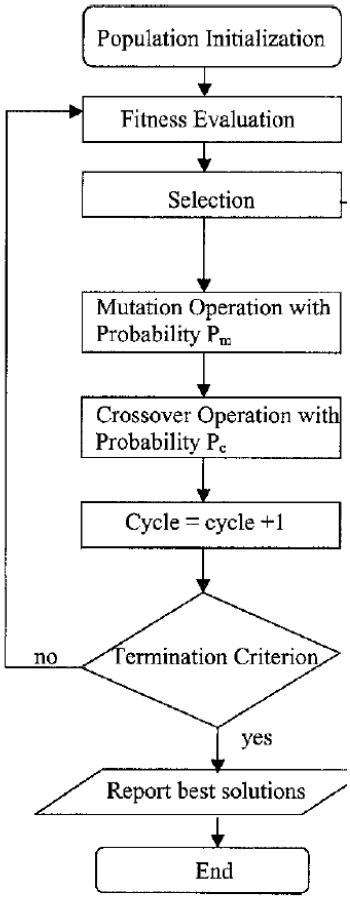

Table A.11 Binding energies of Y-vac clusters

Distance	DFT	Type A	Type B
1 NN	1.22	1.21	1.46
2 NN	0.23	0.18	0.01
3 NN	0.13	0.11	-0.11
4 NN	0.04	0.06	-0.07
5 NN	0.18	0.15	-0.05

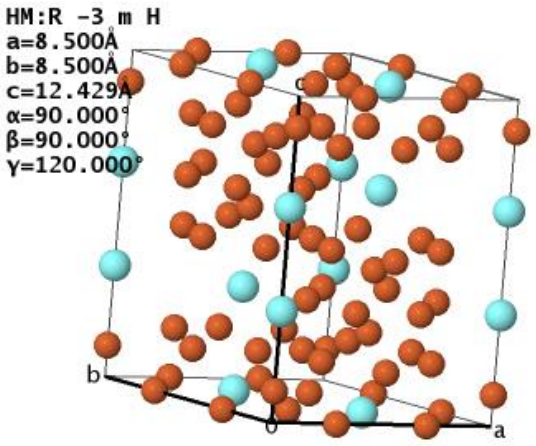

A.7 (top) & A.8 (RHS middle & bottom)

A.7 Flow diagram deepening info about the process of the GA based optimisation: suitable parameter sets are selected and the best are noted and then the prsented GA operations are conducted leading to improvements, which are performed until the termination criterion is reached from introduction evolutionary comp. [102].

A.8 Snapshot of corresponding $Fe_{17}Y_2$ crystals representing rhomobohedral (top) and hcp (bottom) from ICSD (Leibniz Institute crystal database) .

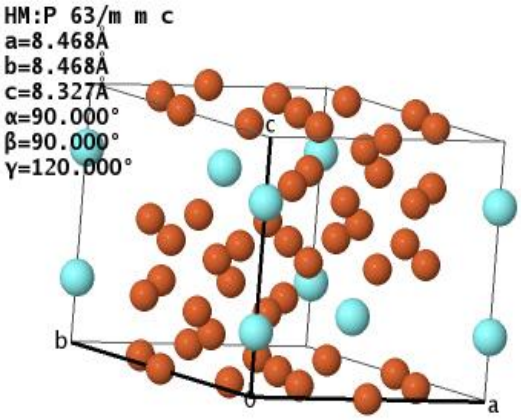

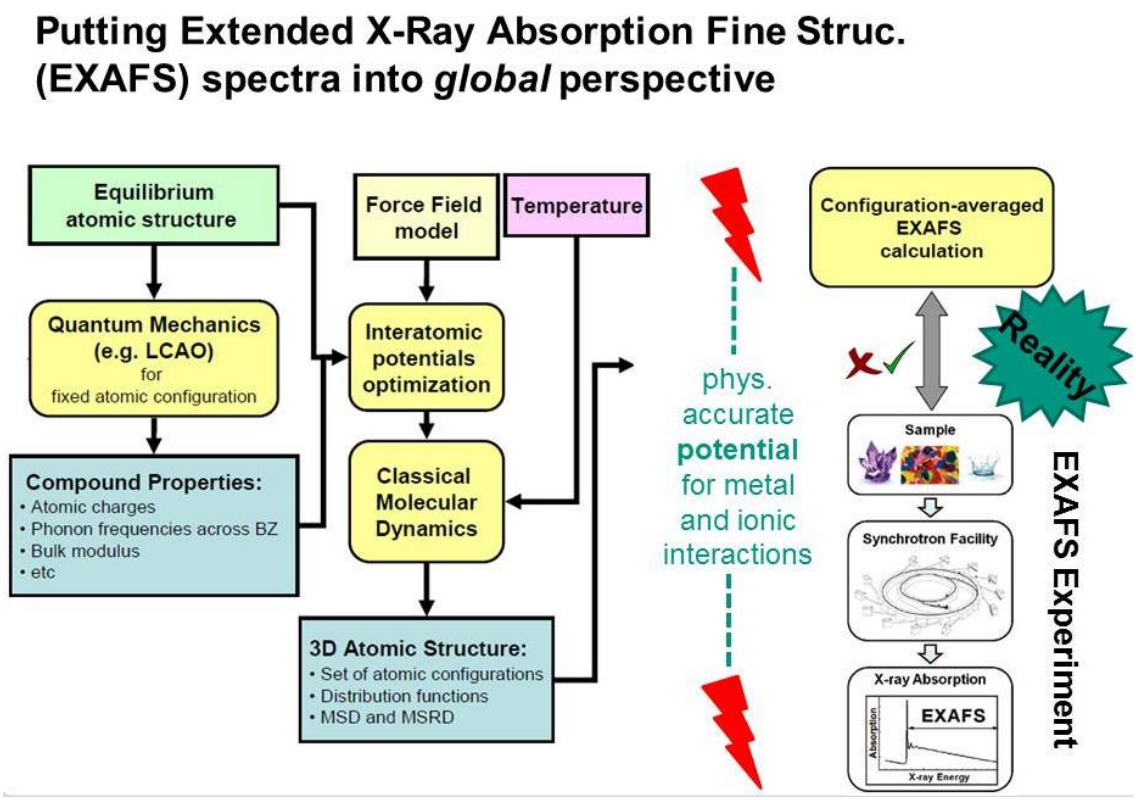

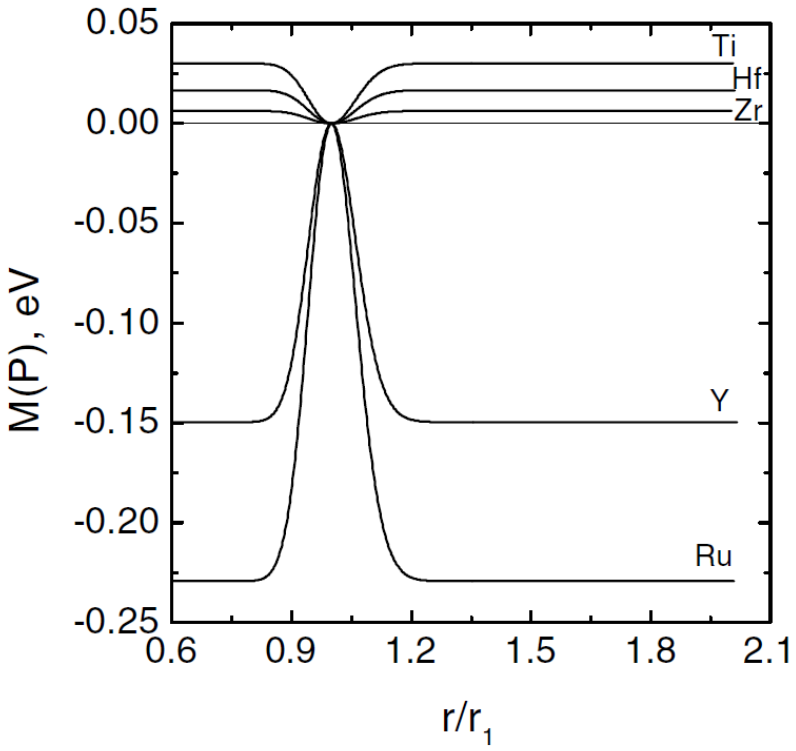

A.9 (top) & A.10 (LHS)

A.9 Flowdiagram of EXAFS evaluation (from left to right): first step the pot. development by the „ingredients“ on the LHS, then MD run with LAMMPS module and simulating thermal vibrations and more, yielding xyz files and these yield by FEFF and EDACA the CA EXAFS calc (top RHS), which are compared to real measurements (bottom shows typical graph of intensity)

A.10 Illustration angular dependant modification function within the splitting concept by W. Hu , extract from his paper [90]. Main point: At equilibrium (at 0) the modification term is zero, making it very useful for the amendments by AIMD in 5.2.

7.2 Appended tables defect cluster used as a fit-reference

Table 7.2 Single defects energies (eV), formation for V_{Fe} and self-interstitials, binding between Y_{Fe} and O_{Fe} solutes and V_{Fe}. Higher values correspond to less favourable states.

	defect			
site	V_{Fe}	Fe	Y	O
2*a*	2.16(2.15[1])	0	ref. state	ref. state
8*c*			-1.35[*]	3.01
6*b*		5.31(5.29[1])	15.06	0.51
12*d*		4.40(4.44[1])	8.40	1.01
dumbbell <100>		5.19(5.13[1])		
dumbbell <110>		4.05(4.02[1])		
dumbbell <111>		4.78(4.72[1])		

Table 7.3 Y solute at 8*c* site, combined with two nearest V_{Fe}.

	Y_{8c}	V_{Fe}	V_{Fe}
Y_{8c}	0	1(2*a*-8*c*)	1(2*a*-8*c*)
V_{Fe}		0	1(2*a*-2*a*)
V_{Fe}			0

Table 7.4 Pair-wise interaction of V_{Fe}, Y_{Fe} and O_{6b}.

	Self-interaction				
	V_{Fe}(2*a*-2*a*)	Y_{Fe}(2*a*-2*a*)	O_{6b}(6*b*-6*b*)	V_{Fe}-Y_{Fe}(2*a*-2*a*)	V_{Fe}-O_{6b}(2*a*-6*b*)
0				unstable	-0.58
1	-0.14(-0.14[1])	0.02(0.04[2])	0.70(0.73[3])	-1.35[*](-1.27[2,3],-1.45[4])	-1.63(-1.69[3],-1.65[5])
2	-0.23(-0.28[1])	-0.12(-0.06[2])	0.49(0.46[3])	-0.20(-0.20[2,3],-0.26[4])	-0.69(-0.73[3],-0.75[5])
3	0.01(0.02[1])	-0.10(-0.08[2])	0.00(0.11[3])	-0.12(-0.13[2,3],-0.24[4])	-0.11(-0.14[3])
4	-0.05	0.00(0.04[2])	1.81/1.59/-0.13[3])	-0.06(-0.04[2,3],-0.15[4])	-0.34(-0.37[3])
5	-0.06	0.12(0.11[2])	0.27(0.23[3])	-0.19(-0.20[2,3],-0.25[4])	0.12(-0.01[3])
6	-0.02	-0.02	0.17(0.12[3])	-0.07	0.03

[*]Stable as the configuration in

Table 7.5 Binding energy between multiple vacancies

	vacancy cluster size	configuration	binding energy, eV
a)	1		0.00
b)	2		-0.23(-0.28[1])
c)	3		-0.65(-0.64[1])
d)	4		-1.38(-1.34[1])
e)	5		-2.19
f)	6		-3.18
g)	7		-2.94

		V_{Fe}						0	2(2*a*-2*a*)			
		V_{Fe}							0			
h)	7		V_{Fe}	V_{Fe}	V_{Fe}	V_{Fe}	V_{Fe}	V_{Fe}	V_{Fe}			-3.32
		V_{Fe}	0	1(2*a*-2*a*)	1(2*a*-2*a*)	1(2*a*-2*a*)	1(2*a*-2*a*)	1(2*a*-2*a*)	1(2*a*-2*a*)			
		V_{Fe}		0	2(2*a*-2*a*)	2(2*a*-2*a*)	3(2*a*-2*a*)	3(2*a*-2*a*)	5(2*a*-2*a*)			
		V_{Fe}			0	3(2*a*-2*a*)	2(2*a*-2*a*)	5(2*a*-2*a*)	3(2*a*-2*a*)			
		V_{Fe}				0	2(2*a*-2*a*)	2(2*a*-2*a*)	3(2*a*-2*a*)			
		V_{Fe}					0	3(2*a*-2*a*)	2(2*a*-2*a*)			
		V_{Fe}						0	2(2*a*-2*a*)			
		V_{Fe}							0			
i)	8		V_{Fe}	V_{Fe}	V_{Fe}	V_{Fe}	V_{Fe}	V_{Fe}	V_{Fe}	V_{Fe}		-4.23
		V_{Fe}	0	2(2*a*-2*a*)	3(2*a*-2*a*)	1(2*a*-2*a*)	4(2*a*-2*a*)	3(2*a*-2*a*)	5(2*a*-2*a*)	9(2*a*-2*a*)		
		V_{Fe}		0	2(2*a*-2*a*)	1(2*a*-2*a*)	1(2*a*-2*a*)	2(2*a*-2*a*)	3(2*a*-2*a*)	5(2*a*-2*a*)		
		V_{Fe}			0	1(2*a*-2*a*)	1(2*a*-2*a*)	3(2*a*-2*a*)	2(2*a*-2*a*)	3(2*a*-2*a*)		
		V_{Fe}				0	2(2*a*-2*a*)	1(2*a*-2*a*)	1(2*a*-2*a*)	4(2*a*-2*a*)		
		V_{Fe}					0	1(2*a*-2*a*)	1(2*a*-2*a*)	1(2*a*-2*a*)		
		V_{Fe}						0	2(2*a*-2*a*)	3(2*a*-2*a*)		
		V_{Fe}							0	2(2*a*-2*a*)		
		V_{Fe}								0		
j)	9		V_{Fe}	V_{Fe}	V_{Fe}	V_{Fe}	V_{Fe}	V_{Fe}	V_{Fe}	V_{Fe}	V_{Fe}	-5.34
		V_{Fe}	0	2(2*a*-2*a*)	2(2*a*-2*a*)	3(2*a*-2*a*)	1(2*a*-2*a*)	2(2*a*-2*a*)	3(2*a*-2*a*)	3(2*a*-2*a*)	5(2*a*-2*a*)	
		V_{Fe}		0	3	2(2*a*-2*a*)	1(2*a*-2*a*)	3(2*a*-2*a*)	2(2*a*-2*a*)	5(2*a*-2*a*)	3(2*a*-2*a*)	
		V_{Fe}			0	2(2*a*-2*a*)	1(2*a*-2*a*)	3(2*a*-2*a*)	5(2*a*-2*a*)	2(2*a*-2*a*)	3(2*a*-2*a*)	
		V_{Fe}				0	1(2*a*-2*a*)	5(2*a*-2*a*)	3(2*a*-2*a*)	3(2*a*-2*a*)	2(2*a*-2*a*)	
		V_{Fe}					0	1(2*a*-2*a*)	1(2*a*-2*a*)	1(2*a*-2*a*)	1(2*a*-2*a*)	
		V_{Fe}						0	2(2*a*-2*a*)	2(2*a*-2*a*)	3(2*a*-2*a*)	
		V_{Fe}							0	3(2*a*-2*a*)	2(2*a*-2*a*)	
		V_{Fe}								0	2(2*a*-2*a*)	
		V_{Fe}									0	

Table 7.6 Binding energies of single solute Y atom and cluster of vacancies

	Configuration	Binding energy, eV
a)		-1.35
b)		-0.19
c)		-0.11
d)		-2.89
e)		-0.30
f)		-1.37
g)		-1.51
h)		-4.89

	V_{Fe}		0	2(2*a*-2*a*)	1(2*a*-2*a*)	1(2*a*-2*a*)		
	V_{Fe}			0	1(2*a*-2*a*)	1(2*a*-2*a*)		
	V_{Fe}				0	2(2*a*-2*a*)		
	V_{Fe}					0		
i)		Y_{Fe}	V_{Fe}	V_{Fe}	V_{Fe}			-3.62
	Y_{Fe}	0	1(2*a*-2*a*)	1(2*a*-2*a*)	1(2*a*-2*a*)			
	V_{Fe}		0	2(2*a*-2*a*)	3(2*a*-2*a*)			
	V_{Fe}			0	2(2*a*-2*a*)			
	V_{Fe}				0			
j)		Y_{Fe}	V_{Fe}	V_{Fe}	V_{Fe}			-2.92
	Y_{Fe}	0	1(2*a*-2*a*)	1(2*a*-2*a*)	1(2*a*-2*a*)			
	V_{Fe}		0	2(2*a*-2*a*)	3(2*a*-2*a*)			
	V_{Fe}			0	5(2*a*-2*a*)			
	V_{Fe}				0			
k)		Y_{6b}	V_{Fe}	V_{Fe}	V_{Fe}	V_{Fe}		-3.95
	Y_{6b}	0	2(2*a*-6*b*)	1(2*a*-6*b*)	1(2*a*-6*b*)	2(2*a*-6*b*)		
	V_{Fe}		0	1(2*a*-2*a*)	1(2*a*-2*a*)	3(2*a*-2*a*)		
	V_{Fe}			0	2(2*a*-2*a*)	1(2*a*-2*a*)		
	V_{Fe}				0	1(2*a*-2*a*)		
	V_{Fe}					0		
l)		Y_{6b}	V_{Fe}	V_{Fe}	V_{Fe}	V_{Fe}	V_{Fe}	-6.02
	Y_{6b}	0	2(2*a*-6*b*)	2(2*a*-6*b*)	1(2*a*-6*b*)	1(2*a*-6*b*)	2(2*a*-6*b*)	
	V_{Fe}		0	2(2*a*-2*a*)	1(2*a*-2*a*)	1(2*a*-2*a*)	2(2*a*-2*a*)	
	V_{Fe}			0	1(2*a*-2*a*)	1(2*a*-2*a*)	3(2*a*-2*a*)	
	V_{Fe}				0	2(2*a*-2*a*)	1(2*a*-2*a*)	
	V_{Fe}					0	1(2*a*-2*a*)	
	V_{Fe}						0	
m)		Y_{Fe}	V_{Fe}	V_{Fe}	V_{Fe}	V_{Fe}		-3.13
	Y_{Fe}	0	1(2*a*-2*a*)	1(2*a*-2*a*)	1(2*a*-2*a*)	1(2*a*-2*a*)		
	V_{Fe}		0	3(2*a*-2*a*)	2(2*a*-2*a*)	5(2*a*-2*a*)		

	V_{Fe}			0	5(2*a*-2*a*)	2(2*a*-2*a*)	
	V_{Fe}				0	3(2*a*-2*a*)	
	V_{Fe}					0	

n)		Y_{Fe}	V_{Fe}	V_{Fe}	V_{Fe}	V_{Fe}	-4.61
	Y_{Fe}	0	1(2*a*-2*a*)	1(2*a*-2*a*)	1(2*a*-2*a*)	1(2*a*-2*a*)	
	V_{Fe}		0	2(2*a*-2*a*)	2(2*a*-2*a*)	3(2*a*-2*a*)	
	V_{Fe}			0	3(2*a*-2*a*)	2(2*a*-2*a*)	
	V_{Fe}				0	2(2*a*-2*a*)	
	V_{Fe}					0	

o)		Y_{6b}	V_{Fe}	V_{Fe}	V_{Fe}	V_{Fe}	V_{Fe}	V_{Fe}	-7.39
	Y_{6b}	0	1(2*a*-6*b*)	2(2*a*-6*b*)	2(2*a*-6*b*)	2(2*a*-6*b*)	2(2*a*-6*b*)	1(2*a*-6*b*)	
	V_{Fe}		0	1(2*a*-2*a*)	1(2*a*-2*a*)	1(2*a*-2*a*)	1(2*a*-2*a*)	2(2*a*-2*a*)	
	V_{Fe}			0	2(2*a*-2*a*)	2(2*a*-2*a*)	3(2*a*-2*a*)	1(2*a*-2*a*)	
	V_{Fe}				0	3(2*a*-2*a*)	2(2*a*-2*a*)	1(2*a*-2*a*)	
	V_{Fe}					0	2(2*a*-2*a*)	1(2*a*-2*a*)	
	V_{Fe}						0	1(2*a*-2*a*)	
	V_{Fe}							0	

p)		Y_{Fe}	V_{Fe}	V_{Fe}	V_{Fe}	V_{Fe}	V_{Fe}	-4.95
	Y_{Fe}	0	1(2*a*-2*a*)	1(2*a*-2*a*)	1(2*a*-2*a*)	1(2*a*-2*a*)	1(2*a*-2*a*)	
	V_{Fe}		0	2(2*a*-2*a*)	2(2*a*-2*a*)	3(2*a*-2*a*)	2(2*a*-2*a*)	
	V_{Fe}			0	3(2*a*-2*a*)	2(2*a*-2*a*)	3(2*a*-2*a*)	
	V_{Fe}				0	2(2*a*-2*a*)	3(2*a*-2*a*)	
	V_{Fe}					0	5(2*a*-2*a*)	
	V_{Fe}						0	

q)		Y_{Fe}	V_{Fe}	V_{Fe}	V_{Fe}	V_{Fe}	V_{Fe}	V_{Fe}	-4.94
	Y_{Fe}	0	1(2*a*-2*a*)	1(2*a*-2*a*)	1(2*a*-2*a*)	1(2*a*-2*a*)	1(2*a*-2*a*)	1(2*a*-2*a*)	
	V_{Fe}		0	3(2*a*-2*a*)	2(2*a*-2*a*)	3(2*a*-2*a*)	2(2*a*-2*a*)	5(2*a*-2*a*)	
	V_{Fe}			0	2(2*a*-2*a*)	3(2*a*-2*a*)	5(2*a*-2*a*)	2(2*a*-2*a*)	
	V_{Fe}				0	5(2*a*-2*a*)	3(2*a*-2*a*)	3(2*a*-2*a*)	
	V_{Fe}					0	2(2*a*-2*a*)	2(2*a*-2*a*)	

	V_{Fe}						0	3(2*a*-2*a*)		
	V_{Fe}							0		
r)		Y_{Fe}	V_{Fe}	V_{Fe}	V_{Fe}	V_{Fe}	V_{Fe}	V_{Fe}		-5.58
	Y_{Fe}	0	1(2*a*-2*a*)	1(2*a*-2*a*)	1(2*a*-2*a*)	1(2*a*-2*a*)	1(2*a*-2*a*)	1(2*a*-2*a*)		
	V_{Fe}		0	2(2*a*-2*a*)	2(2*a*-2*a*)	3(2*a*-2*a*)	3(2*a*-2*a*)	5(2*a*-2*a*)		
	V_{Fe}			0	3(2*a*-2*a*)	2(2*a*-2*a*)	5(2*a*-2*a*)	3(2*a*-2*a*)		
	V_{Fe}				0	2(2*a*-2*a*)	2(2*a*-2*a*)	3(2*a*-2*a*)		
	V_{Fe}					0	3(2*a*-2*a*)	2(2*a*-2*a*)		
	V_{Fe}						0	2(2*a*-2*a*)		
	V_{Fe}							0		
s)		Y_{Fe}	V_{Fe}	V_{Fe}	V_{Fe}	V_{Fe}	V_{Fe}	V_{Fe}		-5.21
	Y_{Fe}	0	1(2*a*-2*a*)	1(2*a*-2*a*)	1(2*a*-2*a*)	1(2*a*-2*a*)	1(2*a*-2*a*)	1(2*a*-2*a*)		
	V_{Fe}		0	3	2(2*a*-2*a*)	3(2*a*-2*a*)	2(2*a*-2*a*)	3(2*a*-2*a*)		
	V_{Fe}			0	2(2*a*-2*a*)	3(2*a*-2*a*)	5(2*a*-2*a*)	3(2*a*-2*a*)		
	V_{Fe}				0	5(2*a*-2*a*)	3(2*a*-2*a*)	2(2*a*-2*a*)		
	V_{Fe}					0	2(2*a*-2*a*)	3(2*a*-2*a*)		
	V_{Fe}						0	2(2*a*-2*a*)		
	V_{Fe}							0		
t)		Y_{6b}	V_{Fe}	V_{Fe}	V_{Fe}	V_{Fe}	V_{Fe}	V_{Fe}	V_{Fe}	V_{Fe}	-7.96
	Y_{6b}	0	1(2*a*-6*b*)	2(2*a*-6*b*)	2(2*a*-6*b*)	2(2*a*-6*b*)	2(2*a*-6*b*)	1(2*a*-6*b*)	4(2*a*-2*a*)	4(2*a*-2*a*)	
	V_{Fe}		0	1(2*a*-2*a*)	1(2*a*-2*a*)	1(2*a*-2*a*)	1(2*a*-2*a*)	2(2*a*-2*a*)	1(2*a*-2*a*)	4(2*a*-2*a*)	
	V_{Fe}			0	2(2*a*-2*a*)	2(2*a*-2*a*)	3(2*a*-2*a*)	1(2*a*-2*a*)	5(2*a*-2*a*)	2(2*a*-2*a*)	
	V_{Fe}				0	3(2*a*-2*a*)	2(2*a*-2*a*)	1(2*a*-2*a*)	3(2*a*-2*a*)	3(2*a*-2*a*)	
	V_{Fe}					0	2(2*a*-2*a*)	1(2*a*-2*a*)	3(2*a*-2*a*)	3(2*a*-2*a*)	
	V_{Fe}						0	1(2*a*-2*a*)	2(2*a*-2*a*)	5(2*a*-2*a*)	
	V_{Fe}							0	4(2*a*-2*a*)	1(2*a*-2*a*)	
	V_{Fe}								0	9(2*a*-2*a*)	
	V_{Fe}									0	
u)		Y_{Fe}	V_{Fe}	V_{Fe}	V_{Fe}	V_{Fe}	V_{Fe}	V_{Fe}	V_{Fe}		-6.15
	Y_{Fe}	0	1(2*a*-2*a*)	1(2*a*-2*a*)	1(2*a*-2*a*)	1(2*a*-2*a*)	1(2*a*-2*a*)	1(2*a*-2*a*)	1(2*a*-2*a*)		

	V_{Fe}		0	2(2*a*-2*a*)	2(2*a*-2*a*)	3(2*a*-2*a*)	2(2*a*-2*a*)	3(2*a*-2*a*)	5(2*a*-2*a*)		
	V_{Fe}			0	3(2*a*-2*a*)	2(2*a*-2*a*)	3(2*a*-2*a*)	2(2*a*-2*a*)	3(2*a*-2*a*)		
	V_{Fe}				0	2(2*a*-2*a*)	3(2*a*-2*a*)	5(2*a*-2*a*)	3(2*a*-2*a*)		
	V_{Fe}					0	5(2*a*-2*a*)	3(2*a*-2*a*)	2(2*a*-2*a*)		
	V_{Fe}						0	2(2*a*-2*a*)	3(2*a*-2*a*)		
	V_{Fe}							0	2(2*a*-2*a*)		
	V_{Fe}								0		
v)		Y_{Fe}	V_{Fe}	V_{Fe}	V_{Fe}	V_{Fe}	V_{Fe}	V_{Fe}	V_{Fe}	V_{Fe}	-7.12
	Y_{Fe}	0	1(2*a*-2*a*)	1(2*a*-2*a*)	1(2*a*-2*a*)	1(2*a*-2*a*)	1(2*a*-2*a*)	1(2*a*-2*a*)	1(2*a*-2*a*)	1(2*a*-2*a*)	
	V_{Fe}		0	2(2*a*-2*a*)	2(2*a*-2*a*)	3(2*a*-2*a*)	2(2*a*-2*a*)	3(2*a*-2*a*)	3(2*a*-2*a*)	5(2*a*-2*a*)	
	V_{Fe}			0	3(2*a*-2*a*)	2(2*a*-2*a*)	3(2*a*-2*a*)	2(2*a*-2*a*)	5(2*a*-2*a*)	3(2*a*-2*a*)	
	V_{Fe}				0	2(2*a*-2*a*)	3(2*a*-2*a*)	5(2*a*-2*a*)	2(2*a*-2*a*)	3(2*a*-2*a*)	
	V_{Fe}					0	5(2*a*-2*a*)	3(2*a*-2*a*)	3(2*a*-2*a*)	2(2*a*-2*a*)	
	V_{Fe}						0	2(2*a*-2*a*)	2(2*a*-2*a*)	3(2*a*-2*a*)	
	V_{Fe}							0	3(2*a*-2*a*)	2(2*a*-2*a*)	
	V_{Fe}								0	2(2*a*-2*a*)	
	V_{Fe}									0	

Table 7.6 Interaction of a single solute atom Y_{Fe} with the V_{Fe}-Y_{8c}-V_{Fe} complex

	Configuration	Binding energy, eV	Configuration
a)	<table><tr><td></td><td>Y_{Fe}</td><td>Y_{Fe}</td><td>V_{Fe}</td></tr><tr><td>Y_{Fe}</td><td>0</td><td>2 (2*a*-2*a*)</td><td>1 (2*a*-2*a*)</td></tr><tr><td>Y_{Fe}</td><td></td><td>0</td><td>1 (2*a*-2*a*)</td></tr><tr><td>V_{Fe}</td><td></td><td></td><td>0</td></tr></table>	-0.30	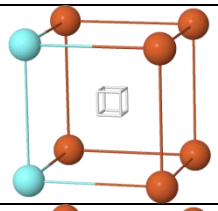
b)	<table><tr><td></td><td>Y_{Fe}</td><td>Y_{Fe}</td><td>V_{Fe}</td></tr><tr><td>Y_{Fe}</td><td>0</td><td>3 (2*a*-2*a*)</td><td>1 (2*a*-2*a*)</td></tr><tr><td>Y_{Fe}</td><td></td><td>0</td><td>1 (2*a*-2*a*)</td></tr><tr><td>V_{Fe}</td><td></td><td></td><td>0</td></tr></table>	-1.03	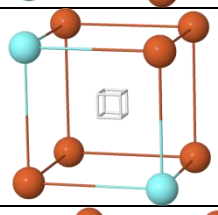
c)	<table><tr><td></td><td>Y_{Fe}</td><td>Y_{Fe}</td><td>V_{Fe}</td></tr><tr><td>Y_{Fe}</td><td>0</td><td>4 (2*a*-2*a*)</td><td>1 (2*a*-2*a*)</td></tr><tr><td>Y_{Fe}</td><td></td><td>0</td><td>2 (2*a*-2*a*)</td></tr><tr><td>V_{Fe}</td><td></td><td></td><td>0</td></tr></table>	-0.27	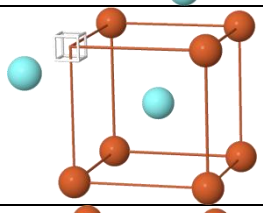
d)	<table><tr><td></td><td>Y_{Fe}</td><td>Y_{Fe}</td><td>V_{Fe}</td></tr><tr><td>Y_{Fe}</td><td>0</td><td>5 (2*a*-2*a*)</td><td>1 (2*a*-2*a*)</td></tr><tr><td>Y_{Fe}</td><td></td><td>0</td><td>1 (2*a*-2*a*)</td></tr><tr><td>V_{Fe}</td><td></td><td></td><td>0</td></tr></table>	-1.16	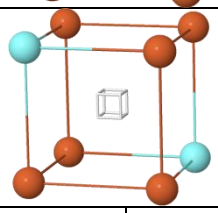
e)	<table><tr><td></td><td>Y_{Fe}</td><td>Y_{6b}</td><td>V_{Fe}</td><td>V_{Fe}</td></tr><tr><td>Y_{Fe}</td><td>0</td><td>5(2*a*-6*b*)</td><td>3(2*a*-6*a*)</td><td>4(2*a*-6*a*)</td></tr><tr><td>Y_{6b}</td><td></td><td>0</td><td>1(2*a*-6*b*)</td><td>1(2*a*-6*b*)</td></tr><tr><td>V_{Fe}</td><td></td><td></td><td>0</td><td>1 (2*a*-2*a*)</td></tr><tr><td>V_{Fe}</td><td></td><td></td><td></td><td>0</td></tr></table>	-0.01	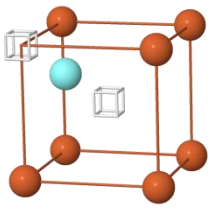 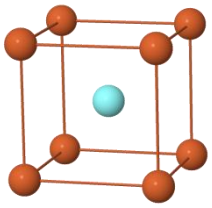
f)	<table><tr><td></td><td>Y_{Fe}</td><td>Y_{6b}</td><td>V_{Fe}</td><td>V_{Fe}</td></tr><tr><td>Y_{Fe}</td><td>0</td><td>6(2*a*-6*b*)</td><td>4(2*a*-6*a*)</td><td>5(2*a*-6*a*)</td></tr><tr><td>Y_{6b}</td><td></td><td>0</td><td>1(2*a*-6*b*)</td><td>1(2*a*-6*b*)</td></tr><tr><td>V_{Fe}</td><td></td><td></td><td>0</td><td>1 (2*a*-2*a*)</td></tr><tr><td>V_{Fe}</td><td></td><td></td><td></td><td>0</td></tr></table>	0.13	
g)	<table><tr><td></td><td>Y_{Fe}</td><td>Y_{6b}</td><td>V_{Fe}</td><td>V_{Fe}</td></tr><tr><td>Y_{Fe}</td><td>0</td><td>7(2*a*-6*b*)</td><td>4(2*a*-6*a*)</td><td>6(2*a*-6*a*)</td></tr><tr><td>Y_{6b}</td><td></td><td>0</td><td>1(2*a*-6*b*)</td><td>1(2*a*-6*b*)</td></tr><tr><td>V_{Fe}</td><td></td><td></td><td>0</td><td>1 (2*a*-2*a*)</td></tr><tr><td>V_{Fe}</td><td></td><td></td><td></td><td>0</td></tr></table>	0.04	
h)	<table><tr><td></td><td>Y_{Fe}</td><td>Y_{6b}</td><td>V_{Fe}</td><td>V_{Fe}</td></tr><tr><td>Y_{Fe}</td><td>0</td><td>7(2*a*-6*b*)</td><td>3(2*a*-6*a*)</td><td>7(2*a*-6*a*)</td></tr><tr><td>Y_{6b}</td><td></td><td>0</td><td>1(2*a*-6*b*)</td><td>1(2*a*-6*b*)</td></tr><tr><td>V_{Fe}</td><td></td><td></td><td>0</td><td>1 (2*a*-2*a*)</td></tr><tr><td>V_{Fe}</td><td></td><td></td><td></td><td>0</td></tr></table>	-0.07	

Table 7.7 Interaction of two V_{Fe}-Y_{8c}-V_{Fe} complexes

	configuration							Binding energy, eV	Configuration
a)		Y_{8c}	Y_{8c}	V_{Fe}	V_{Fe}	V_{Fe}	V_{Fe}	0.84	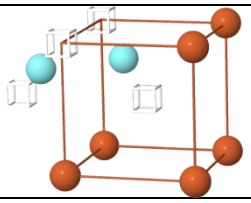
	Y_{8c}	0	3(8*c*-8*c*)	1(2*a*-8*c*)	1(2*a*-8*c*)	2(2*a*-8*c*)	2(2*a*-8*c*)		
	Y_{8c}		0	2(2*a*-8*c*)	2(2*a*-8*c*)	1(2*a*-8*c*)	1(2*a*-8*c*)		
	V_{Fe}			0	1 (2*a*-2*a*)	1 (2*a*-2*a*)	2 (2*a*-2*a*)		
	V_{Fe}				0	2 (2*a*-2*a*)	1 (2*a*-2*a*)		
	V_{Fe}					0	1 (2*a*-2*a*)		
	V_{Fe}						0		
b)		Y_{8c}	Y_{8c}	V_{Fe}	V_{Fe}	V_{Fe}	V_{Fe}	-1.29	
	Y_{8c}	0	4(8*c*-8*c*)	1(2*a*-8*c*)	1(2*a*-8*c*)	2(2*a*-8*c*)	4(2*a*-8*c*)		
	Y_{8c}		0	4(2*a*-8*c*)	2(2*a*-8*c*)	1(2*a*-8*c*)	1(2*a*-8*c*)		
	V_{Fe}			0	1 (2*a*-2*a*)	2 (2*a*-2*a*)	4 (2*a*-2*a*)		
	V_{Fe}				0	1 (2*a*-2*a*)	2 (2*a*-2*a*)		
	V_{Fe}					0	1 (2*a*-2*a*)		
	V_{Fe}						0		
c)		Y_{8c}	Y_{8c}	V_{Fe}	V_{Fe}	V_{Fe}	V_{Fe}	-1.24	
	Y_{8c}	0	5(8*c*-8*c*)	1(2*a*-8*c*)	1(2*a*-8*c*)	2(2*a*-8*c*)	5(2*a*-8*c*)		
	Y_{8c}		0	4(2*a*-8*c*)	3(2*a*-8*c*)	1(2*a*-8*c*)	1(2*a*-8*c*)		
	V_{Fe}			0	1 (2*a*-2*a*)	2 (2*a*-2*a*)	4 (2*a*-2*a*)		
	V_{Fe}				0	1 (2*a*-2*a*)	3 (2*a*-2*a*)		
	V_{Fe}					0	1 (2*a*-2*a*)		
	V_{Fe}						0		
d)		Y_{8c}	Y_{8c}	V_{Fe}	V_{Fe}	V_{Fe}	V_{Fe}	-1.37	
	Y_{8c}	0	6(8*c*-8*c*)	1(2*a*-8*c*)	1(2*a*-8*c*)	2(2*a*-8*c*)	6(2*a*-8*c*)		
	Y_{8c}		0	4(2*a*-8*c*)	4(2*a*-8*c*)	1(2*a*-8*c*)	1(2*a*-8*c*)		
	V_{Fe}			0	1 (2*a*-2*a*)	2 (2*a*-2*a*)	4 (2*a*-2*a*)		
	V_{Fe}				0	1 (2*a*-2*a*)	5 (2*a*-2*a*)		
	V_{Fe}					0	1 (2*a*-2*a*)		
	V_{Fe}						0		

Table 7.8. Used Core PAW PBE potentials.

core potential for	valence electrons	Cut-off energy, eV
Fe	$3d^6 4s^2$	267.883
Y	$4s^2 4p^6 4d^1 5s^2$	211.641

7.3 POTFIT code extract to illustrate analytic restraints

```
/*************************************************************
 * newpot potential
 *************************************************************/

void csw3_value(double r, double *p, double *f)
{
 static double x, y,fe,re, power, lambda,beta;

  re = 2.48199;
  fe = 1.885957;
  lambda = 0.340613;
  x = (r/re-lambda);
  y = 20.0;
  beta = p[0];

  power_1(&power, &x, &y);

  *f = fe * exp(-beta*(r/re-1))/(1+power);
}

/*************************************************************
 * newpot potential
 *************************************************************/

void ljcsw_value(double r, double *p, double *f)
{
```

```
 static double A, B, re,a0, alpha,lambda, kappa, x[11], y[11], power[11], c, delta, gamma, eta, d, kappa2, g1, a2, a3,
g2, g3, p2NN, a2NN, ga, gb, gc, gd, da, db, dc, dd;


  re = 2.48199;

  a0 = 2.865;

  lambda = 0.340613;

  //printf(" a0 = %8.6f, a0/2.866 = %8.6f, a0/2.866*3.159851 = %8.6f \n", a0, a0/2.866, a0/2.866*3.159851);

  alpha = 1.875 * p[0];

  kappa = lambda/2;

  x[0] = (a0/re-kappa);

  x[1] = (a0/re-lambda);

  x[2] = (a0/re-lambda);

  x[3] = (a0/re-lambda);

  x[4] = (1-kappa);

  x[5] = (lambda-a0/re);

  x[6] = (kappa-a0/re);

  x[7] = (a0/re-kappa);

  x[8] = (a0/re-kappa);

  x[9] = (r/re-kappa);

  x[10] = (r/re-lambda);

  y[0] = 20.0;

  y[1] = 20.0;

  y[2] = 19.0;

  y[3] = 18.0;

  y[4] = 20.0;

  y[5] = 20.0;

  y[6] = 20.0;

  y[7] = 19.0;

  y[8] = 18.0;

  y[9] = 20.0;
```

```
 y[10] = 20.0;

power_m(11, power, x, y);

d = a0*3.159851/2.866;

c = a0*0.852261/2.866;

a2 = alpha*alpha;

a3 = (power[0]+1)*(power[0]+1);

g1 = re*re;

g2 = p[0]*p[0];

g3 = (power[1]+1)*(power[1]+1);


kappa2 = a2/(g1*(power[4]+1));

eta = g2/g1;


p2NN = exp(-p[0]*(a0/re-1));

a2NN = exp(-alpha*(a0/re-1));


ga = g2*p2NN/(g1*(power[1]+1));

gb = 40*p[0]*power[2]*p2NN/(g1*g3);

gc = (800*power[2]*power[2]/(g1*g3*(power[1]+1))-380*power[3]/(g1*g3))*p2NN;

gd = p2NN*(-p[0]*(power[5]+1)-20*power[2])/(a0*re*(power[5]+1)*(power[5]+1));


gamma = -ga - gb - gc + gd;


da = a2*a2NN/(g1*(power[0]+1));

db = 40*alpha*power[7]*a2NN/(g1*a3);

dc = (800*power[7]*power[7]/(g1*a3*(power[0]+1))-380*power[8]/(g1*a3))*a2NN;

dd = a2NN*(-alpha*(power[6]+1)-20*power[7])/(a0*re*(power[6]+1)*(power[6]+1));


delta = - da - db - dc + dd + 0.03;
```

```
  B = -(-c*kappa2/delta-d)/(gamma*kappa2/delta-eta);

  A = -(c-B*gamma)/delta;

  //A= 0.39281;
  //B= 0.64624;
 printf("%8.6f %8.6f %8.6f %8.6f %8.6f %8.6f %8.6f\n", A, B, p[0], alpha, kappa,lambda, re);
 //printf(" a0 = %8.6f, a0/2.866 = %8.6f, a0/2.866*3.159851 = %8.6f \n", a0, a0/2.866, a0/2.866*3.159851);

  *f = (A * exp(-alpha*(r/re-1))/(1+power[9]))-(B * exp(-p[0]*(r/re-1))/(1+power[10]));
}


/*****************************************************************
 * newpot potential
 *****************************************************************/

void oef_value(double r, double *p, double *f)
{
  static double rhosqua[5], rhocub[5];

  rhosqua[0] =(r/54.62910-1)*(r/54.62910-1);
  rhosqua[1] =(r/64.26953-1)*(r/64.26953-1);
  rhosqua[2] =(r/66.21202-1)*(r/66.21202-1);
  rhosqua[3] =(r/66.92391-1)*(r/66.92391-1);
  rhosqua[4] =(r/74.23105-1)*(r/74.23105-1);

 if (0.0<r && r<54.62910)
```

```
{
 *f = p[0]+p[1]*(r/54.62910-1)+p[2]*rhosqua[0]+p[3]*rhosqua[0]*(r/54.62910-1);
}
if (54.62910<=r && r<65.24078)
{
 *f = p[4]+p[5]*(r/64.26953-1)+p[6]*rhosqua[1];
}
if (65.24078<=r && r<66.56797)
{
 *f = p[7]+(r/66.21202-1)*p[8]+rhosqua[2]*p[9];
}
if (66.56797<=r && r<=70.57748)
{
 *f = p[10]+(r/66.92391-1)*p[11]+rhosqua[3]*p[12];
}
if (r>70.57748)
{
 *f = p[13]+(r/74.23105-1)*p[14]+rhosqua[4]*p[15];
}
}
/*****************************************************************
 * newpot potential
 *0.85 re =rn for first shell.....an rs=re!!!
 *****************************************************************/
void fef_value(double r, double *p, double *f)
{
  static double rhoe,rho,rn,c,rhosqua[2],w[5],
y[5],peta,re,r2,r3,powere[5],powerF[2],fx[2],fy[2],f1,fac12,fac22,fac13,fac23,Fn0,Fn1,F1,Fn2,Fn3,F2,F2de,F3,F0,rhos
,fe,f0,lambda,x0,beta,Fe;
```

```
 re = 2.481987;

 r2 = 2.866;

 r3 = 4.04;

 fe = 1.885957;

 lambda = 0.340613;

 w[0]=(1.0-lambda);

 w[1] = (r2/re-lambda);

 w[2] = (r3/re-lambda);

 w[3] = (lambda-r2/re);

 w[4] = (lambda-r3/re);

 y[0] = 20.0;

 y[1] = 20.0;

 y[2] = 20.0;

 y[3] = 20.0;

 y[4] = 20.0;


 power_m(5, powere, w, y);


 rhoe = 20.041463;

 F0 = -2.54;

 beta=(rhoe-8*fe)/(6*fe)*(powere[1]+1);

 x0=-1.0*log(beta)/(r2/re-1.0);
// lopp iterations ...
unsigned int K = 1;
unsigned int k;
for(k = 0; k < K; ++k) {
```

```
 f0=8.0*fe/(1+powere[0]) + 6.0*fe* exp(-x0*(r2/re-1.0))/(1.0+powere[1]) + 12.0*fe* exp(-x0*(r3/re-
1.0))/(1.0+powere[2]);


 f1=-6.0*fe*(r2/re-1.0)*exp(-x0*(r2/re-1.0))/(1.0+powere[1])-12.0*fe*(r3/re-1.0)*exp(-x0*(r3/re-
1.0))/(1.0+powere[2]);


x0=x0 - (f0-rhoe)/f1;


}

//x0=p[3];

  //8.0*fe/(1+powere[0]) + 6.0*fe* exp(-p[3]*(r2/re-1.0))/(1.0+powere[1]) + 12.0*fe* exp(-p[3]*(r3/re-
1.0))/(1.0+powere[2]);

  //printf("%8.6f %8.6f %8.6f %8.6f\n", x0, f0, f0-rhoe,f1);

  rhos = rhoe;

  Fe = -2.539945; //p[0];//

  F2de = fe*x0*(r2/re)*((r2/re)+exp(-x0*((r2/re)-1)));

  F2 = (0.028185/4.0)*rhoe*rhoe*r2*r2*r2/(F2de*F2de);

  F1 = 0;

  F0 = -2.54;

  peta = 0.391750;


 fx[0] = 1.15;

  fx[1] = r/rhos;

  fy[0] = peta;

  fy[1] = peta;

  power_m(2, powerF, fx, fy);


unsigned int L = 2;

unsigned int l;

for(l = 0; l < L; ++l) {
```

```
 f0=(-20+peta/1.15)*Fe*powerF[0]*log(powerF[0])+20*Fe*powerF[0]+50.7699595;


 f1=powerF[0]*Fe*(0.121532*peta+(0.121532*peta-1.92567)*log(powerF[0]));


//if (peta - (f0)/f1 > 0.1 && peta-(f0)/f1 < 1.5)
            //{


peta=peta - (f0)/f1;
//printf("%8.6f %8.6f %8.6f\n", f0, peta,f1);
      /**}
            else { }**/
}


 fx[0] = 1.15;
 fx[1] = r/rhos;
 fy[0] = peta;
 fy[1] = peta;
 power_m(2, powerF, fx, fy);


 F3= (Fe*(1-log(powerF[0]))*powerF[0]-0.0225*F2-F0)/0.003375;


 //F3 = ((/0.85)+F2*0.3)/0.0675;
  Fn1 = 0.85*(F3*0.0675-F2*0.3);
  Fn2 = 0.7225*(F2-0.45*F3);


 //c = (1.15/Fe)*(0.3*F2+0.0675*F3);
 //peta= (2/log(1.15))*gsl_sf_lambert_W0(0.5*sqrt(fabs(c*log(1.15))));
```

```
   //F0 = -2.54 F0 = p[1]*(1-log(powerF[0]))*powerF[0]-0.0225*F2-0.003375*F3;

 //Fe = F0 + 0.0225*F2 + 0.003375*F3 / ((1-log(powerF[0]))*powerF[0]);


 Fn0 = F0+F2*0.0225-0.003375*F3;

 Fn3 = Fn0-Fn1+Fn2;


 rn = 0.85*rhoe;

 rhosqua[0] =(r/rn-1)*(r/rn-1);

 rhosqua[1] =(r/rhoe-1)*(r/rhoe-1);

  //printf("%8.6f %8.6f %8.6f %8.6f %8.6f %8.6f %8.6f %8.6f %8.6f %8.6f\n",
rhoe,F1,F2,F3,Fn0,Fn1,Fn2,Fn3,Fe,peta);


 if (rn>r)

 {

  *f =Fn0+Fn1*(r/rn-1)+Fn2*rhosqua[0]+Fn3*rhosqua[0]*(r/rn-1);

 }

 if (rn<=r && r<1.15*rhoe)

 {

  *f =F0+F1*(r/rhoe-1)+F2*rhosqua[1]+F3*rhosqua[1]*(r/rhoe-1);

 }


 if (1.15*rhoe<=r)

 {

  *f = Fe*(1-log(powerF[1]))*powerF[1];

 }

}


/*************************************************************

 * newpot potential

 *************************************************************/
```

```
void newpot_value(double r, double *p, double *f)

{

  *f = r * p[0] + p[1];

}

/*****************************************************************

 * end of analytic potentials

 *****************************************************************/

//calc beta

/**

double apot_grad(double fe, double rhoe,double lambda,double re, double r2, double r3, double power1, double
power2, double power3, void (*function) (double, double *, double *))

{

  static double beta

   beta=(rhoe-8*fe)/(6*fe)*(powere[1]+1);

  x0=-1.0*log(beta)/(r2/re-1.0);

// lopp iterations ...

unsigned int K = 1;

unsigned int k;

for(k = 0; k < K; ++k) {

 f0=8.0*fe/(1+powere[0]) + 6.0*fe* exp(-x0*(r2/re-1.0))/(1.0+powere[1]) + 12.0*fe* exp(-x0*(r3/re-
1.0))/(1.0+powere[2]);

 f1=-6.0*fe*(r2/re-1.0)*exp(-x0*(r2/re-1.0))/(1.0+powere[1])-12.0*fe*(r3/re-1.0)*exp(-x0*(r3/re-
1.0))/(1.0+powere[2]);

x0=x0 - (f0-rhoe)/f1;

}

  return x0;

} **/
```

8 References

8.1 List of Cited Literature

1. Energiebedarf steigt weltweit bis 2035 um mehr als ein Drittel: Heise online [cited 15th June 2018]. Available from: URL: https://www.heise.de/newsticker/meldung/Energiebedarf-steigt-weltweit-bis-2035-um-mehr-als-ein-Drittel-2552871.html.

2. Gruss P, Schüth F. Die Zukunft der Energie: Die Antwort der Wissenschaft. München: Verlag C.H. Beck; 2008. (p. 7-48; 295-312).

3. Hepburn DJ, MacLeod E, Ackland GJ. Transition metal solute interactions with point defects in fcc iron from first principles. Phys. Rev. B 2015; 92(1).

4. Xavier Morel. Evaluation of equations of state for helium and tritium gas mixture bubbles formed in beryllium under neutron irradiation: Introductory Chapter (p. 2-10). Karlsruhe, Germany: KIT; 2018.

5. Mastrikov YA, Sokolov MN, Koch S, Zhukovskii YF, Gopejenko A, Vladimirov PV et al. Ab initio modelling of the initial stages of the ODS particle formation process. Nuclear Instruments and 8 Methods in Physics Research Section B: Beam Interactions with Materials and Atoms 2018; 435:70–3.

6. Cayron C, Rath E, Chu I, Launois S. Microstructural evolution of Y2O3 and MgAl2O4 ODS EUROFER steels during their elaboration by mechanical milling and hot isostatic pressing. Journal of Nuclear Materials 2004; 335(1):83–102.

7. Klimiankou M, Lindau R, Möslang A. Direct correlation between morphology of (Fe,Cr)23C6 precipitates and impact behavior of ODS steels. Journal of Nuclear Materials 2007; 367-370:173–8.

8. Gräning T. Herstellung, Charakterisierung und Optimierung von austenitischen ODS Stählen. (Schriftenreihe des Instituts für Angewandte Materialien, Karlsruher Institut für Technologie; vol 79).

9. Ault GM. HM Burte. Oxide Dispersion Strengthening 1968; 47:4 ff.

10. Smallman RE, Bishop RJ. Modern physical metallurgy and materials engineering: Science, process, applications. 6th ed. Oxford: Elsevier Butterworth Heinemann; 1999.

11. Fischer J.**J.**, et al., „Dispersion strengthened ferritic alloy for use in liquid metal fast breeder reactors (LMFBRS)“ U.S. Patent 4,075,010, February 21, 1978.

12. Ukai S, Harada M, Okada H, Inoue M, Nomura S, Shikakura S et al. Alloying design of oxide dispersion strengthened ferritic steel for long life FBRs core materials. Journal of Nuclear Materials 1993; 204:65–73.

13. Alinger MJ, Odette GR, Hoelzer DT. On the role of alloy composition and processing parameters in nanocluster formation and dispersion strengthening in nanostuctured ferritic alloys. Acta Materialia 2009; 57(2):392–406.

14. Hull D, Bacon DJ. Introduction to dislocations. 5th ed. Oxford, Burlington, MA: Butterworth-Heinemann; 2011.

15. Lindau R, Möslang A, Schirra M, Schlossmacher P, Klimenkov M. Mechanical and microstructural properties of a hipped RAFM ODS-steel. Journal of Nuclear Materials 2002; 307-311:769–72.

16. Kardellass S, Servant C, Selhaoui N, Iddaoudi A, Amar MA, Bouirden L. A thermodynamic assessment of the iron–yttrium system. Journal of Alloys and Compounds 2014; 583:598–606.

17. Hoffmann J. Ferritische ODS-Stähle - Herstellung, Umformung und Strukturanalyse. Karlsruhe: KIT Scientific Publishing; 2014. (Schriftenreihe des Instituts für Angewandte Materialien; vol 32).

18. Okuda T, Fujiwara M. Dispersion behaviour of oxide particles in mechanically alloyed ODS steel. J Mater Sci Lett 1995; 14(22):1600–3.

19. Yu X, Zhou J, Liang H, Jiang Z, Wu L. Mechanical metamaterials associated with stiffness, rigidity and compressibility: A brief review. Progress in Materials Science 2018; 94:114–73.

20. Klimiankou M, Lindau R, Möslang A. TEM characterization of structure and composition of nanosized ODS particles in reduced activation ferritic–martensitic steels. Journal of Nuclear Materials 2004; 329-333:347–51.

21. Frenkel D, Smit B. Understanding molecular simulation: From algorithms to applications. 2. rev. ed. San Diego [u.a.]: Academic Press; 2002. (Computational science series; vol 1).

22. Tadmor EB, Miller RE. Modeling materials: Continuum, atomistic and multiscale techniques. Reprinted with corr. Cambridge: Cambridge Univ. Press; 2014. (p. 262-334).

23. Hammond KD, Voigt HL, Marus LA, Juslin N, Wirth BD. Simple pair-wise interactions for hybrid Monte Carlo–molecular dynamics simulations of titania/yttria-doped iron. J. Phys.: Condens. Matter 2013; 25(5):55402.

24. Mishin Y, Asta M, Li J. Atomistic modeling of interfaces and their impact on microstructure and properties. Acta Materialia 2010; 58(4):1117–51.

25. Murali D, Panigrahi BK, Valsakumar MC, Sundar CS. Diffusion of Y and Ti/Zr in bcc iron: A first principles study. Journal of Nuclear Materials 2011; 419(1-3):208–12.

26. Mishin Y, Farkas D, Mehl MJ, Papaconstantopoulos DA. Interatomic potentials for monoatomic metals from experimental data and ab initio calculations. Phys. Rev. B 1999; 59(5):3393–407.

27. Malerba L, Ackland GJ, Becquart CS, Bonny G, Domain C, Dudarev SL et al. Ab initio calculations and interatomic potentials for iron and iron alloys: Achievements within the Perfect Project. Journal of Nuclear Materials 2010; 406(1):7–18.

28. Materials Science and Engineering Division of the Material Measurement Laboratory (MML) at the National Institute of Standards and Technology (NIST). Available from: URL: https://www.ctcms.nist.gov/potentials/.

29. Plimpton SJ, Thompson AP. Computational aspects of many-body potentials. MRS Bull. 2012; 37(5):513–21.

30. Jones JE. On the Determination of Molecular Fields. II. From the Equation of State of a Gas. Proceedings of the Royal Society A: Mathematical, Physical and Engineering Sciences 1924; 106(738):463–77.

31. Fermi E., Pasta J., Ulam S. Los Alamos report LA-1940; (1955).

32. Frenkel J. Zur Theorie der Elastizitaetsgrenze und der Festigkeit kristallinischer Koerper. Z. Physik 1926; 37(7-8):572–609.

33. Orowan E. Zur Kristallplastizitaet. III. Z. Physik 1934; 89(9-10):634–59.

34. Rodriguez P. Sixty years of dislocations. Bull. Mater. Sci. 1996; 19(6):857–72.

35. Hirsch & Horne. Dislocations and stacking faults in stainless steel. Proc. R. Soc. Lond. A 1957; 240(1223):524–38.

36. Daw MS, Baskes MI. Embedded-atom method: Derivation and application to impurities, surfaces, and other defects in metals. Phys. Rev. B 1984; 29(12):6443–53.

37. Alder BJ, Wainwright TE. Studies in Molecular Dynamics. I. General Method. The Journal of Chemical Physics 1959; 31(2):459–66.

38. Verlet L. Computer "Experiments" on Classical Fluids. I. Thermodynamical Properties of Lennard-Jones Molecules. Phys. Rev. 1967; 159(1):98–103.

39. Finnis M. Interatomic forces in condensed matter. [Online-ausg.]. Oxford [u.a.]: Oxford Univ. Press; 2003. (Oxford Scholarship Online; vol 1).

40. Fellinger MR. “First Principles-Based Interatomic Potentials for Modeling the Body-Centered Cubic Metals V, Nb, Ta, Mo, and W.” [PhD Thesis]: University of Ohio; 2013.

41. Marx D, Hutter J. Ab initio molecular dynamics: Basic theory and advanced methods. Cambridge, New York: Cambridge University Press; 2009. (p. 5-53).

42. Stillinger FH, Rahman A. Improved simulation of liquid water by molecular dynamics. The Journal of Chemical Physics 1974; 60(4):1545–57.

43. Mills R. Self-diffusion in normal and heavy water in the range 1-45.deg. J. Phys. Chem. 1973; 77(5):685–8.

44. Harrison DE, Kelly PW, Garrison BJ, Winograd N. Low energy ion impact phenomena on single crystal surfaces. Surface Science 1978; 76(2):311–22.

45. Meyers MA, Mishra A, Benson DJ. Mechanical properties of nanocrystalline materials. Progress in Materials Science 2006; 51(4):427–556.

46. Wolf D, Yamakov V, Phillpot SR, Mukherjee A, Gleiter H. Deformation of nanocrystalline materials by molecular-dynamics simulation: relationship to experiments? Acta Materialia 2005; 53(1):1–40.

47. Daw MS, Baskes MI. Semiempirical, Quantum Mechanical Calculation of Hydrogen Embrittlement in Metals. Phys. Rev. Lett. 1983; 50(17):1285–8.

48. Kohn W, Sham LJ. Self-Consistent Equations Including Exchange and Correlation Effects. Phys. Rev. 1965; 140(4A):A1133.

49. Finnis MW, Sinclair JE. A simple empirical N -body potential for transition metals. Philosophical Magazine A 2006; 50(1):45–55.

50. Daw MS, Foiles SM, Baskes MI. The embedded-atom method: a review of theory and applications. Materials Science Reports 1993; 9(7-8):251–310.

51. Brenner DW. Relationship between the embedded-atom method and Tersoff potentials. Phys. Rev. Lett. 1989; 63(9):1022.

52. Yip S. Handbook of materials modeling: Introduction (p. 3-38) & (M)EAM chapter by Mishin (p. 400-480). Dordrecht: Springer; 2005.

53. Brommer P, Kiselev A, Schopf D, Beck P, Roth J, Trebin H. Classical interaction potentials for diverse materials from ab initio data: a review of potfit. Modelling Simul. Mater. Sci. Eng. 2015 [cited 2019 Jun 12]; 23(7):74002.

54. Johnson RA. Alloy models with the embedded-atom method. Phys. Rev. B 1989; 39(17):12554–9.

55. Johnson RA, Oh DJ. Analytic embedded atom method model for bcc metals. J. Mater. Res. 1989; 4(5):1195–201.

56. Oh DJ, Johnson RA. Simple embedded atom method model for fcc and hcp metals. J. Mater. Res. 1988; 3(3):471–8.

57. Zhou XW, Johnson RA, Wadley, H. N. G. Misfit-energy-increasing dislocations in vapor-deposited CoFe/NiFe multilayers. Phys. Rev. B 2004; 69(14):1358.

58. Rose JH, Smith JR, Guinea F, Ferrante J. Universal features of the equation of state of metals. Phys. Rev. B 1984; 29(6):2963–9.

59. Ercolessi F, Adams JB. Interatomic Potentials from First-Principles Calculations: The Force-Matching Method. Europhys. Lett. 1994; 26(8):583–8.

60. Plimpton S. Fast Parallel Algorithms for Short-Range Molecular Dynamics. Journal of Computational Physics 1995; 117(1):1–19.

61. Schiøtz J, Di Tolla, Francesco D., Jacobsen KW. Softening of nanocrystalline metals at very small grain sizes. Nature 1998; 391(6667):561–3.

62. Tateyama S, Shibuta Y, Suzuki T. A molecular dynamics study of the fcc–bcc phase transformation kinetics of iron. Scripta Materialia 2008; 59(9):971–4.

63. Timoshenko J, Anspoks A, Cintins A, Kuzmin A, Purans J, Frenkel AI. Neural Network Approach for Characterizing Structural Transformations by X-Ray Absorption Fine Structure Spectroscopy. Phys. Rev. Lett. 2018; 120(22):66.

64. Gunkelmann N, Bringa EM, Kang K, Ackland GJ, Ruestes CJ, Urbassek HM. Polycrystalline iron under compression: Plasticity and phase transitions. Phys. Rev. B 2012; 86(14):631.

65. Ackland GJ. Simulation of martensitic microstructure. J Mater Sci 2005; 40(12):3205–8.

66. Osetsky YN, Bacon DJ. An atomic-level model for studying the dynamics of edge dislocations in metals. Modelling Simul. Mater. Sci. Eng. 2003; 11(4):427–46.

67. Stewart DM, Osetsky Y, Stoller RE, Golubov SI, Seletskaia T, Kamenski PJ. Atomistic studies of helium defect properties in bcc iron: Comparison of He–Fe potentials. Philosophical Magazine 2010; 90(7-8):935–44.

68. Juslin N, Nordlund K. Pair potential for Fe–He. Journal of Nuclear Materials 2008; 382(2-3):143–6.

69. Stewart D, Osetskiy Y, Stoller R. Atomistic studies of formation and diffusion of helium clusters and bubbles in BCC iron. Journal of Nuclear Materials 2011; 417(1-3):1110–4.

70. Ackland GJ, Mendelev MI, Srolovitz DJ, Han S, Barashev AV. Development of an interatomic potential for phosphorus impurities in -iron. J. Phys.: Condens. Matter 2004; 16(27):S2629.

71. Stoller RE, Odette GR, Wirth BD. Primary damage formation in bcc iron. Journal of Nuclear Materials 1997; 251:49–60.

72. Jang J, Lee B, Hong J. Influence of Cu, Cr and C on the irradiation defect in Fe: A molecular dynamics simulation study. Journal of Nuclear Materials 2008; 373(1-3):28–38.

73. Shibuta Y, Takamoto S, Suzuki T. Dependence of the grain boundary energy on the alloy composition in the bcc iron–chromium alloy: A molecular dynamics study. Computational Materials Science 2009; 44(4):1025–9.

74. Anand RS, Patra K. Modeling and Simulation of Mechanical Micro-Machining—A Review. Machining Science and Technology 2014; 18(3):323–47.

75. Healy C, Koch S, Siemers C, Mukherji D, Ackland GJ. Shear Melting and High Temperature Embrittlement: Theory and Application to Machining Titanium. Phys. Rev. Lett. 2015; 114(16).

76. Mendelev MI, Han S, Srolovitz DJ, Ackland GJ, Sun DY, Asta M. Development of new interatomic potentials appropriate for crystalline and liquid iron. Philosophical Magazine 2003; 83(35):3977–94.

77. Proville L, Rodney D, Marinica M. Quantum effect on thermally activated glide of dislocations. Nature Mater 2012; 11(10):845–9.

78. Müller M, Erhart P, Albe K. Analytic bond-order potential for bcc and fcc iron—comparison with established embedded-atom method potentials. J. Phys.: Condens. Matter 2007 [cited 2019 Jun 12]; 19(32):326220.

79. Pettifor D. New many-body potential for the bond order. Phys. Rev. Lett. 1989; 63(22):2480–3.

80. Baskes MI. Modified embedded-atom potentials for cubic materials and impurities. Phys. Rev. B 1992; 46(5):2727–42.

81. Behler J. Perspective: Machine learning potentials for atomistic simulations. The Journal of Chemical Physics 2016; 145(17):170901.

82. Moore AP, Deo C, Baskes MI, Okuniewski MA, McDowell DL. Understanding the uncertainty of interatomic potentials' parameters and formalism. Computational Materials Science 2017; 126:308–20.

83. Mock M, Albe K. Modelling of dislocation-solute interaction in ODS steels: Analytic bond-order potential for the iron-yttrium system. Journal of Nuclear Materials 2018; 509:102–13.

84. Fan K, Yang L, Tang J, Sun Q, Dai Y, Peng S et al. Analytical Bond-order Potential for hcp-Y. Chinese Journal of Chemical Physics 2013; 26(5):526–32.

85. Borodin VA, Vladimirov PV. Vacancies and interstitials in yttrium. J. Phys.: Condens. Matter 2019; 31(18):185401.

86. Bartók AP, Csányi G. Gaussian approximation potentials: A brief tutorial introduction. Int. J. Quantum Chem. 2015; 115(16):1051–7.

87. Liang T, Shan T, Cheng Y, Devine BD, Noordhoek M, Li Y et al. Classical atomistic simulations of surfaces and heterogeneous interfaces with the charge-optimised many body (COMB) potentials. Materials Science and Engineering: R: Reports 2013; 74(9):255–79.

88. Lee B, Baskes MI, Kim H, Koo Cho Y. Second nearest-neighbor modified embedded atom method potentials for bcc transition metals. Phys. Rev. B 2001; 64(18):2666.

89. Goryaeva AM, Maillet J, Marinica M. Towards better efficiency of interatomic linear machine learning potentials. Computational Materials Science 2019; 166:200–9.

90. Hu W, Zhang B, Huang B, Gao F, Bacon DJ. Analytic modified embedded atom potentials for HCP metals. J. Phys.: Condens. Matter 2001; 13(6):1193–213.

91. Pei Z, Zhu L, Friák M, Sandlöbes S, Pezold J von, Sheng HW et al. Ab initio and atomistic study of generalized stacking fault energies in Mg and Mg–Y alloys. New J. Phys. 2013; 15(4):43020.

92. Ko W, Lee B. Modified embedded-atom method interatomic potentials for pure Y and the V–Pd–Y ternary system. Modelling Simul. Mater. Sci. Eng. 2013; 21(8):85008.

93. Baskes MI, Johnson RA. Modified embedded atom potentials for HCP metals. Modelling Simul. Mater. Sci. Eng. 1994; 2(1):147–63.

94. Timonova M, Thijsse BJ. Optimizing the MEAM potential for silicon. Modelling Simul. Mater. Sci. Eng. 2011; 19(1):15003.

95. Lazic I. Atomic scale simulation of oxide and metal film growth.[Doctoral Thesis]. Netherlands: TU Delft; 2009.

96. Zhou XW, Wadley, Haydn N G. A charge transfer ionic–embedded atom method potential for the O–Al–Ni–Co–Fe system. J. Phys.: Condens. Matter 2005; 17(23):3619–35.

97. Wadley H, Zhou X, Johnson R, Neurock M. Mechanisms, models and methods of vapor deposition. Progress in Materials Science 2001; 46(3-4):329–77.

98. Scopece D, Thijsse BJ. Comment on: "An improved molecular dynamics potential for the Al–O system" Computational Materials Science 53, 483 (2012). Computational Materials Science 2015; 104:143–6.

99. Duff AI, Finnis MW, Maugis P, Thijsse BJ, Sluiter MH. MEAMfit: A reference-free modified embedded atom method (RF-MEAM) energy and force-fitting code. Computer Physics Communications 2015; 196:439–45.

100. Dragoni D, Daff TD, Csányi G, Marzari N. Achieving DFT accuracy with a machine-learning interatomic potential: Thermomechanics and defects in bcc ferromagnetic iron. Phys. Rev. Materials 2018; 2(1):1939.

101. Brommer P, Gähler F. Potfit: effective potentials from ab initio data. Modelling Simul. Mater. Sci. Eng. 2007; 15(3):295–304.

102. Introduction to Evolutionary Computing. [Erscheinungsort nicht ermittelbar]: Springer; 2015. (Natural computing series).

103. Wang K, Zhu W, Xiao S, Chen J, Hu W. A new embedded-atom method approach based on the p th moment approximation. J. Phys.: Condens. Matter 2016; 28(50):505201.

104. S. Koch. Polycrystalline iron under extreme shear in Molecular Short Range Dynamics Simulations [Master thesis]: University of Edinburgh; 2014.

105. Leonid Zhigilei. Introduction to Atomistic Simulations. MSE 4270/6270; 2010 [cited 2014 Apr 3, last time visited 23. April 2019].

106. G.J. Ackland. Empirical Potentials: Summary; 2013; teaching material, available on https://www2.ph.ed.ac.uk/~gja/ (last time visited 15. July 2015) .

107. Ashcroft NW, Mermin ND. Solid state physics. Belmont (USA); Brooks/Cole, 1976.

108. Koch W, Holthausen MC. A Chemist's Guide to Density Functional Theory., Weinheim (Germany); John Wiley & Sons; 2nd edition (July 11, 2001)

109. Clementi E, Roetti C. Roothaan-Hartree-Fock atomic wavefunctions. Atomic Data and Nuclear Data Tables 1974; 14(3-4):177–478.

110. Jonane I, Lazdins K, Timoshenko J, Kuzmin A, Purans J, Vladimirov P et al. Temperature-dependent EXAFS study of the local structure and lattice dynamics in cubic Y 2 O 3. J Synchrotron Rad 2016; 23(2):510–8.

111. Zope RR, Mishin Y. Interatomic potentials for atomistic simulations of the Ti-Al system. Phys. Rev. B 2003; 68(2):30.

112. Zhou LG, Huang H. Controversy Over Elastic Constants Based on Interatomic Potentials. J. Eng. Mater. Technol 2013; 135(1):11010.

113. Mishin Y, Mehl MJ, Papaconstantopoulos DA. Phase stability in the Fe–Ni system: Investigation by first-principles calculations and atomistic simulations. Acta Materialia 2005; 53(15):4029–41.

114. Pasianot R, Farkas D, Savino EJ. Empirical many-body interatomic potential for bcc transition metals. Phys. Rev. B 1991; 43(9):6952–61.

115. Lenosky TJ, Sadigh B, Alonso E, Bulatov VV, Rubia, Tomas Diaz de la, Kim J et al. Highly optimised empirical potential model of silicon. Modelling Simul. Mater. Sci. Eng. 2000; 8(6):825–41.

116. Nguyen-Manh D, Horsfield AP, Dudarev SL. Self-interstitial atom defects in bcc transition metals: Group-specific trends. Phys. Rev. B 2006; 73(2):67.

117. Dudarev SL, Derlet PM. A 'magnetic' interatomic potential for molecular dynamics simulations. J. Phys.: Condens. Matter 2005; 17(44):7097–118.

118. Ackland GJ. Two-band second moment model for transition metals and alloys. Journal of Nuclear Materials 2006; 351(1-3):20–7.

119. Schrödinger E. An Undulatory Theory of the Mechanics of Atoms and Molecules. Phys. Rev. 1926; 28(6):1049–70.

120. Kaxiras E. Atomic and electronic structure of solids. Transferred to digital printing. Cambridge: Cambridge Univ. Press; 2011.

121. Tuckerman ME. Ab initio molecular dynamics: basic concepts, current trends and novel applications. J. Phys.: Condens. Matter 2002; 14(50):R1297.

122. Fock V. Naeherungsmethode zur Loesung des quantenmechanischen Mehrkoerperproblems. Z. Physik 1930; 61(1-2):126–48.

123. C. Stihl. Skalenübergreifende Simulation von Wasserstoffisotopen auf (0001) Berylliumoberflächen: PhD Thesis [DOI: 10.5445/IR/1000090436]: KIT; 2019 [cited 2019 May 15]. Available from: URL: https://publikationen.bibliothek.kit.edu/1000090436/22466268.

124. G.Kresse. VASP the Guide: Computational Materials Physics, Faculty of Physics, Universität Wien; 2016 [cited 2017 May 30]. Available from: URL: http://cms.mpi.univie.ac.at/vasp/vasp.pdf.

125. Blöchl PE. Projector augmented-wave method. Phys. Rev. B 1994; 50(24):17953–79.

126. Kresse G, Joubert D. From ultrasoft pseudopotentials to the projector augmented-wave method. Phys. Rev. B 1999; 59(3):1758–75.

127. Perdew JP, Burke K, Ernzerhof M. Generalized Gradient Approximation Made Simple. Phys. Rev. Lett. 1996; 77(18):3865–8.

128. Car R, Parrinello M. Unified Approach for Molecular Dynamics and Density-Functional Theory. Phys. Rev. Lett. 1985; 55(22):2471–4.

129. Banerjea A, Smith JR. Origins of the universal binding-energy relation. Phys. Rev. B 1988; 37(12):6632–45.

130. Jalkanen J, Müser MH. Systematic analysis and modification of embedded-atom potentials: case study of copper. Modelling Simul. Mater. Sci. Eng. 2015; 23(7):74001.

131. Stukowski A, Fransson E, Mock M, Erhart P. Atomicrex—a general purpose tool for the construction of atomic interaction models. Modelling Simul. Mater. Sci. Eng. 2017; 25(5):55003.

132. Mock M, Albe K. Diffusion of yttrium in bcc-iron studied by kinetic Monte Carlo simulations. Journal of Nuclear Materials 2017; 494:157–64.

133. G.J. Ackland. Non-pairwise potentials and defect modelling for transition metals: ISNI: 0000 0001 3393 0990 [Doctoral Thesis]. United Kingdom: University of Oxford; 1987.

134. Raju S, Mohandas E, Raghunathan VS. The pressure derivative of bulk modulus of transition metals: An estimation using the method of model potentials and a study of the systematics. Journal of Physics and Chemistry of Solids 1997; 58(9):1367–73.

135. Yuan X, Chen N, Shen J. Construction of embedded-atom-method interatomic potentials for alkaline metals (Li, Na, and K) by lattice inversion. Chinese Phys. B 2012; 21(5):53401.

136. Li JH, Liang SH, Guo HB, Liu BX. Four-parameter equation of state of solids. Appl. Phys. Lett. 2005; 87(19):194111.

137. Lide DR. CRC handbook of chemistry and physics, 2003-2004: A ready-reference book of chemical and physical data. 84th ed. Boca Raton, Fla: CRC Press; 2003.

138. Smithells CJ, Gale WF, Totemeier TC. Smithells metals reference book. 8th ed. / edited by W.F. Gale, T.C. Totemeier. Amsterdam, Boston: Elsevier Butterworth-Heinemann; 2004.

139. Barrett CS, Massalski TB. Structure of metals: Crystallographic methods, principles and data. 3. rev. ed., repr. Oxford u.a: Pergamon Pr.; 1992. (International series on materials science and technology; vol 35).

140. Murali D, Posselt M, Schiwarth M. First-principles calculation of defect free energies: General aspects illustrated in the case of bcc Fe. Phys. Rev. B 2015; 92(6):245.

141. Boer, Frank R. de. Cohesion in metals: Transition metal alloys. 2nd corrected printing. Amsterdam [etc.]: North-Holland; 1989. (Cohesion and Structurevol. 1).

142. Mihalkovic M. Cohesive energies of Fe-based glass-forming alloys. 2004.

143. OGOLEM. Mol. Phys. 2010, 108, 279: B. Hartke. Available from: URL: http://www.ogolem.org/.

144. Y. Mastrikov, *E.A. Kotomin, P.V. Vladimirov, and A. Möslang and et. al., "Modeling of Y-O precipitation in bcc-Fe and fcc-Fe lattices." – Abstract: OR-35.*, Presentation on *9th International Conference "Functional Materials and Nanotechnologies" FM&NT-2013 (Tartu, Estonia, April, 2013)* - graphs taken from presentation with author's permission.

145. Carlsson AE. Beyond Pair Potentials in Elemental Transition Metals and Semiconductors. In: Carlson, editor: Elsevier; 1990. p. 1–91 [Solid State Physics].

146. Il'inskii A, Slyusarenko S, Slukhovskii O, Kaban I, Hoyer W. Structure of liquid Fe–Al alloys. Materials Science and Engineering: A 2002; 325(1-2):98–102.

147. Mendelev MI, Underwood TL, Ackland GJ. Development of an interatomic potential for the simulation of defects, plasticity, and phase transformations in titanium. The Journal of Chemical Physics 2016; 145(15):154102.

148. Koyama K, Fujii H. Nitrogen gas–solid reaction process and basic magnetism of the interstitially modified rare-earth 3d transition-metal nitrides R2Fe17N3(R=Y,Ce,Nd,Sm) and Y2Co17N3. Phys. Rev. B 2000; 61(14):9475–93.

149. Goldbeck OK von. IRON—Binary Phase Diagrams: p. 172-177 & 304-311. Berlin, Heidelberg: Springer Berlin Heidelberg; 1982.

150. Moze O, Caciuffo R, Gillon B, Calestani G, Kayzel FE, Franse, J. J. M. Polarized-neutron-diffraction study of the magnetization density in hexagonal Y2Fe17. Phys. Rev. B 1994; 50(13):9293–9.

151. Coehoorn R. Calculated electronic structure and magnetic properties of Y-Fe compounds. Phys. Rev. B 1989; 39(18):13072–85.

152. Zhang BW, Liu G, Han K. The Fe-Y (iron-yttrium) system. JPE 1992; 13(3):304–8.

153. Saenko I, Fabrichnaya O, Udovsky A. New Thermodynamic Assessment of the Fe-Y System. J. Phase Equilib. Diffus. 2017; 38(5):684–99.

154. Kuzmin A, Chaboy J. EXAFS and XANES analysis of oxides at the nanoscale. IUCrJ 2014; 1(6):571–89.

155. Kuzmin A, Anspoks A, Kalinko A, Timoshenko J. The Use of X-ray Absorption Spectra for Validation of Classical Force-Field Models. Zeitschrift für Physikalische Chemie 2016; 230(4).

156. Fornasini P. Study of lattice dynamics via extended x-ray absorption fine structure. J. Phys.: Condens. Matter 2001; 13(34):7859–72.

157. Teo BK, Joy DC. EXAFS Spectroscopy. Boston, MA: Springer US; 1981.

158. Kuzmin A, Evarestov RA. Quantum mechanics–molecular dynamics approach to the interpretation of x-ray absorption spectra. J. Phys.: Condens. Matter 2009; 21(5):55401.

159. Rehr JJ, Albers RC. Theoretical approaches to x-ray absorption fine structure. Rev. Mod. Phys. 2000; 72(3):621–54.

160. Alexei Kuzmin. EDA: EXAFS Data Analysis Software Package: User's Manual.

161. Chui CP, Liu W, Xu Y, Zhou Y. Molecular Dynamics Simulation of Iron — A Review. SPIN 2015 [cited 2019 Jun 12]; 05(04):1540007.

162. Marqués M, González LE, González DJ. Pressure-induced changes in structural and dynamic properties of liquid Fe close to the melting line. An ab initio study. J. Phys.: Condens. Matter 2016; 28(7):75101.

163. Kunal Jain. Analytics Vidhya: leading [online] knowledge portal for [data] analysts in India [cited May ‘19]. URL: www.analyticsvidhya.com/blog/2017/07/introduction-to-genetic-algo/.

164. Healy C, Koch S, Siemers C and Ackland, G.J. Shear Melting and High Temperature Embrittlement: Application to Machining Titanium. Phys. Rev. Lett., 2015; 114(16):165501

165. MRS proceedings 2016, arXiv:1605.05514

8.2 Author's References

Due to the generous scientific founding by the Helmholtz foundation within the HRJG 411 ODS- HITs project a short list of the scientific contribution in its various kinds is appended:

Publications

as first author:

- **internal KIT intermediate PhD project status report**
- **own publication of "*EXAFS spectrum simulation of a complex metallic alloy ($Fe_{17}Y_2$) by an AIMD assisted RF-MEAM potential"* is in progress and expected to be published**

as Co-author:

- "Shear Melting and High Temperature Embrittlement: Theory and Application to Machining Titanium" in **Physical Review Letters (2015)** [164] **and MRS Proceedings (2016) [165]**
- "Ab initio modelling of the initial stages of the ODS particle formation process" **in Nuclear Instruments and Methods in Physics Research Section B: Beam Interactions with Materials and Atoms (2018) [5]**

Conferences

talks:

- **Eurofusion progress meeting, Riga, Dec 2017**
- **Gordon Research Conference, Boston, Seminar talk, July 2017**
- **ODISSEUS conference, Dreseden (HZDR), Mai 2016**

poster:

- **DGM MSE conference, Darmstadt, September 2018**
- **8th Multiscale Materials Modelling Conference, Dijon, October 2016**
- **13th COSIRES (Simulating radiation effects), Loughborough, 06/2016**
- **Modelling Force fields workshop, Jülich, November 2015**

Visits

- **Prof. G.J. Ackland Group (UoE), AIMD calcs, 09/18–11/18**
- Prof. Purans, Kuzmin and Mastrikov ISSP (Riga), DFT&EXAFS, various visits
- FG Materialmodellierung (TU Darmstadt), AtomiCrex, occasional visitis
- **EXAFS measurement session at ESRF (Grenoble), with Purans, 12/15**

About the Author

Sascha Koch was born in Rostock, Germany, on February 11, 1991 and moved to Hamburg before starting school. In 2010 he finished as salutatorian his Abitur (average 1.0) with focus on Maths and Physics with a parallel successful completion of junior-studies in Physics at the University of Hamburg. In addition to English he learned Russian and Chinese during high school and spent 3 months in Shanghai Da Tong High school as well as an active participant in several exchange projects with Russia.

With this background the author was attracted to study Physics at the University of Edinburgh, a lively multifaceted first class institution with a history of an excellent balance of research activities and a holistically engaged student body. Consequently, the author was awarded the Klaus Murmann scholarship by the German Business Foundation (Stiftung der deutschen Wirtschaft) and actively travelled through Europe for numerous seminars in several cooperations and NGOs putting the laborious Physics studies into a rewarding broader context.
These activities led to his first internship as a Data Analyst in the Data Warehouses of Lufthansa Technik in Germany. Afterwards during the internship next summer (2012) the data collection was more hands-on in an industrial research project by Scottish Renewables: researching the impact on carbon cycles and CO_2 emissions of Scottish windfarms near Glasgow. This work included lab-work, as well as measuring device and statistics work.
Nevertheless, during the specialisation in third year of his studies, the author excelled in the advanced experimental courses as well as in his Bachelor project in experimental nuclear Physics and finished these as second best out of his cohort. For more variety and due to his interest for multi-cultural exchange, he additionally engaged as a RA (Resident Assistant) for 2 years at the international university accommodation (hosting over 40 nations in his section).

Regardless of all these activities the author shortened his duration of undergraduate studies to four years (instead of five for a Master degree in Physics) and entered the last year in fourth year. For his Master project he transitioned from experimental Physics to Computational Material Science/Physics, which attracted him due to its importance for energy by fusion (a field of Physics with high impact on society). This change led him to studies in Molecular Dynamics about nanocrystaline materials supervised by Prof. G.J. Ackland. He finished his project with distinction and a publication as well as his Physics Master degree with First class honours (highest distinction, 1.3 average).

Subsequently, the Karlsruhe Institute of Technology was the right choice to do a PhD in an institution, which applies science on highest level in a beneficial way to society. At the institute of applied materials physics and under the supervision of Prof. A. Möslang the author developed new ways to model materials of interest for fusion and high temperature applications in molecular dynamics, the research profile is on the previous page (p. 158).

After this successful PhD project the author is expected to continue his applied research in a more industry minded setting at a Fraunhofer Institute in Karlsruhe (as of December 2019).